MELT GENERATION, MIXING AND DEGASSING AT EL HIERRO, CANARY ISLANDS

A THESIS SUBMITTED TO THE UNIVERSITY OF MANCHESTER
FOR THE DEGREE OF DOCTOR OF PHILOSOPHY
IN THE FACULTY OF SCIENCE AND ENGINEERING

2020

Zoltán Taracsák
School of Natural Sciences
Department of Earth and Environmental Sciences

Contents

Word count 51474

The University of Manchester

Zoltán Taracsák
Doctor of Philosophy
Melt generation, mixing and degassing at El Hierro, Canary Islands
September 17, 2020

The formation of ocean islands and the cause of melt generation in the mantle beneath them is of great interest to geoscientist. Much of our current understanding of deep Earth processes and phenomena, such as mantle plumes and long term cycling elements, including volatiles (H, C, S, halogens), between the surface and the mantle derive from the study of ocean island basalts (OIBs). The Canary Islands is one of the most studied ocean island chain on Earth, yet processes driving melt generation underneath it are still debated. The main focus of this work is to investigate the driving forces of generation beneath El Hierro, located in the Western Canary Islands, using a source to surface approach. In my thesis I present major, trace, volatile element, and sulfur isotope data from samples representing the past ~20000 years of volcanic activity on the island of El Hierro and use these to further increase our understanding of melt formation and evolution of OIBs erupting at the Western Canary Islands and beyond. Major, trace and volatile element data from El Hierro melt inclusions indicate prevalent carbon and sulfur enrichment in young El Hierro magmas. Primary mantle-derived melt CO_2 contents may be as high as 4 wt%. Trace and volatile element ratios indicate C and S enrichment at El Hierro is either caused by extremely low melting degrees or by addition of S and C to the mantle source from recycled lithosphere. F/Nd ratios of melt inclusions point to the presence of recycled F in the mantle source, indicating volatiles can survive subduction and be effectively recycled into the mantle source of OIBs. Sulfur isotope ratios measured in melt inclusions using a novel microanalytical technique reveal that primary El Hierro magmas are enriched in heavy ^{34}S compared to normal upper mantle. Modelling the composition of the mantle source using primary magma sulfur content, sulfur isotope ratios, and trace element contents indicate that the El Hierro mantle source is up to three times more enriched in sulfur than the primitive upper mantle. The presence of such a large amount of excess S in the mantle source can only be explained if the original asthenospheric mantle reacted with volatile-rich metasomatic melts originating from a recycled lithosphere. Magma temperature, magma storage pressure, and melt oxygen fugacity estimates from El Hierro point to a long and complex pre-eruptive history. Magma residence times of ~400 years calculated by diffusion modelling enabled extensive chemical re-equilibration of minerals and melt inclusions, obscuring primary magma temperature and oxygen fugacity conditions. Olivine-spinel pairs reveal that El Hierro magmas are among the most oxidised OIBs on Earth. Oxidising conditions combined with near-ambient mantle potential temperature estimates from the Canary Islands contradict the hypothesis of a deep, thermal mantle plume origin for the Canary Islands.

These observations, together with extreme carbon and sulfur enrichment observed in El Hierro magmas, point to a melt generation process where volatile-enrichment of the mantle is the main driving force of melt generation at the Canary Islands, caused by the addition of metasomatic melt/fluid to the asthenospheric mantle originating from previously subducted material. The transfer of oxidised volatiles, sulfur in particular, could be a major pathway for oxidised surface material to be introduced into the mantle. Results presented in the thesis have implications for mantle dynamics, as volatile-rich plumes may originate from shallower depth than suggested for deep thermal plumes, and also point to the importance of previously subducted material in the generation of OIBs. Both hypotheses of volatile and temperature induced melting could be correct at different ocean island locations, with volatiles likely playing a primary role in melt formation at ocean islands with low melt fluxes, such as the Canary Islands and Cape Verde.

Declaration

No portion of the work referred to in the thesis has been submitted in support of an application for another degree or qualification of this or any other university or other institute of learning.

Copyright Statement

i. The author of this thesis (including any appendices and/or schedules to this thesis) owns certain copyright or related rights in it (the “Copyright”) and s/he has given The University of Manchester certain rights to use such Copyright, including for administrative purposes.

ii. Copies of this thesis, either in full or in extracts and whether in hard or electronic copy, may be made **only** in accordance with the Copyright, Designs and Patents Act 1988 (as amended) and regulations issued under it or, where appropriate, in accordance with licensing agreements which the University has from time to time. This page must form part of any such copies made.

iii. The ownership of certain Copyright, patents, designs, trade marks and other intellectual property (the “Intellectual Property”) and any reproductions of copyright works in the thesis, for example graphs and tables (“Reproductions”), which may be described in this thesis, may not be owned by the author and may be owned by third parties. Such Intellectual Property and Reproductions cannot and must not be made available for use without the prior written permission of the owner(s) of the relevant Intellectual Property and/or Reproductions.

iv. Further information on the conditions under which disclosure, publication and commercialisation of this thesis, the Copyright and any Intellectual Property and/or Reproductions described in it may take place is available in the University IP Policy

Acknowledgements

Among the many people who helped me through my now close to nine year-long journey that cumulated in the submission of this work, first and foremost I have to thank my PhD supervisor, Margaret Hartley, for her support in both scientific and personal matters over the last four years. Margaret aided both my personal and professional development as a researcher during my Manchester years, and I'm most grateful for the support I received.

Other members of my supervisory team, Ray Burgess, Marie Edmonds and Marc-Anotione Longpré, were extremely helpful during my PhD years and I'm grateful for their support. Advice from Ray on many matters, both scientific and personal, were tremendously helpful. I would like to express my thanks to Marie in helping me connect with other members of the magmatic volatiles community at various meetings and conferences. Marc-Anotine's extensive knowledge and insight on Canary Island volcanism was especially helpful during my PhD work. I also would like to thank my examiners, Brian O'Driscoll and Eleanor Jennings for carefully evaluating my PhD thesis, enduring my rather long viva, and for providing valuable comments on my thesis that no doubt made this document a more digestible and whole piece of work.

I would like to thank members of Williamson building room 1.23, most notably Ben, Emma and Matthew for the occasional scientific, and more common non-scientific discussion that kept the days entertaining. I'm grateful to the members of the Isotope and Cosmochemisrty research group for their support over the years. The many social

events, public engagement events, and pub visits were maybe the most memorable parts of the last four years. Members of the EAO NERC DTP were also important part of my Manchester years and I would like to thank the many nice memories that resulted from the many events we attended together as a group. Pub visits with Elliot, Jess and Joshi were most entertaining.

One should not forget his/her roots either. I would like to thank my many Hungarian colleagues with whom I studied together, and from whom I learned a lot during my first five years at university, including my BSc and MSc supervisor Szabolcs Harangi for his help. I also would like to thank Évi Jankovics, who introduced me to many research practices early on, when I was still a BSc student. I'm grateful for Csaba Szabó for first introducing me to the world of geochemistry when I was a second year student. I'm thankful for István Kovács at the Geophysical and Geodetic Institute for his help and advice during my three month internship in the summer of 2019. And the list could go on.

I would like to thank the support of colleagues who taught me the art of geochemical microanalysis, most notably Jonathan Fellows, who trained me to use the EPMA in Manchester, and John Craven and Cees-Jan De Hoog in Edinburgh for his help with the SIMS development work and analyses during my PhD. I also have to thank John for the tea and biscuits; they were quite nice!

On a more personal note I have to thank my fiancée Boglárka for the continues personal support she provided and for enduring the many challenges over the years that arose due to my career, including a move from Hungary to the United Kingdom. And last but not least, I have to thank my family members for their support during my university studies and for enduring my absence from Budapest in the last four years.

Chapter 1

Introduction

Volcanic rocks erupted at ocean islands are among the most studied geological materials. While extensive field observations and geochemical data have been collected from numerous locations, fundamental processes, such as the cause of melt generation in the mantle beneath ocean islands are still debated. Thermal plumes, or hotspots, have been long proposed as the cause of melt generation in intraplate settings, including ocean islands (Morgan, 1971). Mantle heterogeneity and the presence of previously subducted material in the source of many ocean island magmas (Hofmann and White, 1982; Hofmann, 1997) complicates modelling melt generation processes at ocean islands.

In the last 50 years considerable efforts have been made to characterise the major element, trace element, and isotopic composition of magmas erupting on ocean islands. However, their volatile contents have been relatively understudied; only a couple of estimates exist for the carbon, water and sulfur content of ocean island magmas. This complicates the estimation of global volcanic gas fluxes, such as CO_2 and SO_2, as ocean islands may emit more of these gases per mass unit compared to those erupting at mid-ocean ridges. Links between mantle source heterogeneity and the volatile content of ocean island magmas are not well-understood even though volatiles may play a key role in melt generation processes as they decrease mantle solidus temperatures (e.g.

Dasgupta et al., 2007; Green et al., 2010). Whether recycled volatiles are present in the ocean island mantle source is ambiguous; more and better estimates of ocean island magma volatile contents are required if we want to understand the long-term cycling of volatile elements between the surface and the deeper spheres of Earth.

1.1 Aims and Objectives

In my thesis I aim to contribute to our understanding of magmatism at the Canary Islands and to provide some answers on the still debated topics, such as the cause of melt generation at the Canary Islands, through the petrological and geochemical study of some of the youngest volcanics erupted on the island of El Hierro, Western Canary Islands. Topics of broad interest to petrologist and earth scientists are discussed, such as the role of mantle heterogeneity, particularly volatile element heterogeneity, during melt generation in the asthenosphere.

In my thesis I investigate the cause of melt generation, mantle source geochemistry, magma fractionation, degassing processes, and fluxes of volatiles at El Hierro, which is thought to be one of the most volatile-rich ocean island basalts (OIBs) currently erupting on Earth (Longpré et al., 2017), and place my results into the wider context of global ocean island volcanism. I present geochemical data from glassy El Hierro melt inclusions, found in young (<20000 years old) tephra samples, including major, trace, and volatile elements in chapter four. From these data volatile fluxes and mantle volatile contents are estimated for El Hierro and compared with other locations to emphasise the importance of smaller volcanic systems on global volcanic volatile fluxes. The possible role of excess volatiles, originating from recycled lithospheric materials, during melt generation is discussed at El Hierro and other locations. Magma degassing at ocean islands, including early carbon degassing in the deeper parts of the magma plumbing system and the challenges of carbon budget estimation, are also discussed.

In chapter six of the thesis I use sulfur isotope ratio data collected from the same samples presented in chapter four to further investigate the effect of recycled volatiles on mantle melting and long-term surface to mantle cycling of volatile elements, primarily sulfur. Modelling in this chapter enables better estimation of sulfur contents of the El Hierro mantle source. Analyses are carried out using novel procedures that enable the high precision measurement of sulfur isotope ratios in glassy materials using secondary ion mass spectrometry. This technique is detailed in chapter five, including the viability of sulfur isotope ratio analyses on different sample sets.

In chapter seven I present results derived from various mineral-mineral and mineral-melt thermometric, barometric and oxybarometric calculations from El Hierro together with crystallisation modelling. For this study I use the same tephra samples that were utilised in chapters four and six together with lava samples collected from adjacent lava flows. Melt evolution and magma storage processes are discussed in this chapter. A comparison of global OIB and Atlantic mid-ocean ridge basalt mantle potential temperatures and melting pressures are also provided, with implications on the thermal condition of the Canary Islands mantle source and beyond. An overall summary of the results of my PhD thesis is presented in chapter eight, detailing how the aims listed here are met. A model for magmatism at El Hierro, more broadly applicable to the Canary Islands and low melt flux ocean islands, is presented. This model is put in the context of the mantle plume theory most commonly used to explain ocean island volcanism on Earth. Volatile recycling into the mantle during slab subduction, a topic of broad interest for geoscientists, and the role of volatiles in the generation of ocean island basalts, are discussed and suggestions are given for further research.

1.2 The structure of the thesis

As the thesis is written in "alternative format" the structure is somewhat different from what would be expected from a classic PhD thesis. In this short section an explanation is provided to the reader, which may help navigating the thesis. An alternative format thesis is expected to be written in a way that individual chapters form separate and well-defined pieces of research publishable in scientific journals. In my thesis chapters four, five, six, and seven are pieces of work intended to be published in journals (one is currently under review, one is already accepted and published). However, parts of the original manuscripts have been moved to different chapters in the thesis, notably the geological background and the methods sections, to avoid excessive repetition. The geodynamical and volcanological background of the Canary Islands and El Hierro are provided in chapter two, together with background information on topics that are discussed in the thesis in detail, such as mantle heterogeneity, melt generation at ocean islands, and study of volatile elements through melt inclusions. Details of analytical methods used in most research chapters are provided in chapter three. One exception is the description of analytical methods used to measure sulfur isotope ratios in glasses by secondary ion mass spectrometry; this is discussed chapter five as it is a piece of original research accomplished during the PhD studies. A list of all the samples used in the thesis is presented in chapter three, with relevant sample details given in each chapter. The final chapter of the thesis aims to synthesise and connect the results and conclusions of the journal format chapters.

Chapter four mostly contains text from the article with the same title authored by myself, Margaret E. Hartley, Ray Burgess, Marie Edmonds, Fiona Iddon and Marc-Antoine Longpré and published in Geochimica et Cosmochimica Acta volume 258 p. 19-36 in 2019. My contributions to the articles included carrying out sample preparation, SIMS, EPMA, and Raman spectroscopic measurement of melt inclusions and their host crystals. Interpretation of the data was carried out by me and Margaret

E. Hartley. I led the writing of the paper, with contributions from all other authors. The analytical methods section describing how major, trace and volatile elements were measured are found in chapter three of the thesis. The geological background is covered in chapter two, hence it have been removed. A paragraph containing speculative calculations on the long volatile-fluxes from El Hierro, originally present in the manuscript which was later taken out during the review process have been re-added to the text of the thesis. The original article can be accessed using the following link: DOI:10.1016/j.gca.2019.05.020

In chapter five chapter I discuss analytical procedures and matrix effect correction methods during sulfur isotope analysis of glasses by multi-collector secondary ion mass spectrometry. Chapter five is based on the draft of a manuscript with the same title intended to be submitted to Chemical Geology in September 2020. This work was carried out in collaborations with multiple laboratories/groups, including Shuhei Ono's lab at Massachusetts Institute of Technology (bulk sulfur isotope ratio analyses of glasses was carried out by Patrick Beaudry), Sasha Turchyn's lab at the University of Cambridge (bulk sulfur isotope ratio analyses of doping anhydrite), Andri Stefánsson/Saemi Halldórsson's group at the University of Iceland, who provided natural Icelandic glass chips and bulk sulfur isotope data for these samples, the experimental petrology laboratories at the Universität Hannover (production of synthetic glasses in collaboration with David Neave), and the Edinburgh Ion Microprobe Facility. My contribution to this work includes carrying out SIMS analyses in Edinburgh and EPMA/FTIR analyses in Manchester, preparing the materials used to make the synthetic glass standards, helping out with experiments in Hannover, data processing, interpretation, and producing the manuscript. Co-authors of this work are Margaret E. Hartley, David Neave, Ray Burgess, Marie Edmonds, Marc-Antoine Longpré, Saemi Halldórsson, Jóhann Gunnarson-Robin, Saemundur Ari Halldórsson, Andri Stefánsson, Eemu Johannes Ranta, Patrick Beaudry, Shuhei Ono, Alexandra V. Turchyn, and was carried out in collaboration with the Edinburgh Ion Probe Facility.

Chapter six is based on sulfur isotope data collected from El Hierro melt inclusions and matrix glasses at the Edinburgh Ion Microprobe Facility in November 2019. This chapter is a draft version of the manuscript intended to be submitted later in 2020 to a short format journal such as Earth and Planetary Science Letters, Geology, Geochemical Perspectives Letters, or Proceedings of the National Academy of Sciences of the United States of America. Analytical procedures for lava samples are detailed in chapter three (analyses carried out in collaboration with Sasha Turchyn at the University of Cambridge), while SIMS analysis are detailed, including matrix effect corrections, in chapter five. Trace element data used here are presented in chapter four. Co-authors for this manuscript Margaret E. Hartley, Ray Burgess, Marie Edmonds, Marc-Antoine Longpré, and Alexandra V. Turchyn.

Chapter seven is based on the manuscript with the same title, authored by Zoltán Taracsák, Margaret E. Hartley, Marc-Antoine Longpré, Ray Burgess and Marie Edmonds, originally submitted for review in Journal of Petrology on the 1st of April, 2020. All authors contributed to the writing of the manuscripts. My contribution to the manuscript was carrying out data collection and processing, including thermometric, barometric and oxybarometric calculations, data interpretation, and producing the first draft of the manuscript, including all the figures and supplements. As with previous chapters, to avoid repetition analytical methods (EPMA analytical conditions) were moved to chapter three.

Chapter 2

Ocean island volcanism at El Hierro, the Canary Islands and beyond: plumes, mantle heterogeneity and the role of volatiles

Ocean islands, along with mid-ocean ridges and volcanic arcs located behind subduction zones, are one of the main locations where volcanism occurs on Earth today. In contrast to the other two locations, ocean islands volcanism does not necessarily takes place along or in vicinity of plate boundaries; many ocean islands can be found far from any current tectonic plate boundary. A number of volcanic ocean islands have active volcanoes away from plate boundaries today: these include Hawaii and Galapagos Islands in the Pacific Ocean, Réunion in the Indian Ocean, and the Azores, Cape Verde, and the Canary Islands in the Atlantic Ocean. Many more currently inactive volcanic ocean islands can be found on the surface, mostly in the Pacific and Atlantic Oceans.

Due to their distance from tectonic plate boundaries, the formation of ocean islands and in particular the cause of melt generation in the mantle underneath them, are topics of great interest. At mid-ocean ridges decompression melting of an upwelling mantle due to spreading provide suitable explanation for melting (e.g. Langmuir et al., 1992). At convergent plate margins volatile transfer from the subducting slab into the mantle wedge and subsequent decrease in the solidus temperature (e.g. Grove et al., 2006; Green et al., 2010) is though to cause melt formation. However, no single process can be attributed as the cause of melting under ocean islands. One of the first modern (i.e. after the establishment of plate tectonics theory) solution was the mantle plume theory proposed by Morgan (1971), who suggested thermal plumes arising from the deeper mantle cause positive temperature anomalies and melting in the mantle under ocean islands. Since then countless studies, utilising both geochemical and geophysical data from various locations, have been published on the topic, with many favouring the thermal plume theory for OIB genesis (e.g. Sleep, 1990; Hart et al., 1992; Hofmann, 1997; Montelli et al., 2004; French and Romanowicz, 2015) while some partially questioning (e.g. Fitton, 2007; Pilet et al., 2008) or totally rejecting it (e.g. Anderson, 2000).

Geochemical study of OIBs have revealed that their composition, most notably in terms of radiogenic isotope ratios such as ^{87}Sr/^{88}Sr, ^{206}Pb/^{204}Pb and ^{207}Pb/^{204}Pb, is distinct from those measured in mid-ocean ridge basalts (MORBs), which thought to originate from the melting of a depleted upper mantle material. These finding indicate that the mantle is heterogeneous and the source of this heterogeneity is material being introduced back into the deeper parts of the mantle at subduction zones (Hofmann and White, 1982). These recycled materials have been grouped based on their radiogenic isotope composition (Zindler and Hart, 1986): EM1 and EM2 (enriched mantle 1 and 2) are thought to represent recycled sedimentary material while HIMU is a ^{206}Pb-rich mantle component often associated with recycled basaltic ocean crust (e.g. Day et al., 2010), albeit the origin of this HIMU component is debated (e.g. Kogiso et al., 1997; Takamasa et al., 2009; Jackson et al., 2018). These recycled components are mixed into the ambient mantle, represented by the BSE (the bulk silicate Earth) and DMM (depleted MORB) components. The presence of non-peridotitic lithologies in the mantle beneath ocean islands, and in other geodynamic settings, such as mid-ocean ridges and large igneous provinces, is a topic that have been extensively studied for the bast 30 years due to its importance in governing melt composition and melting processes (e.g. Kogiso et al., 1998; Dasgupta et al., 2007; Herzberg and Asimow, 2008). Melt-solid and solid-solid reactions between recycled crust or lithosphere and ambient mantle may result in the formation of pyroxenites (Herzberg, 2011), which has a lower the solidus temperature than peridotite (Hirschmann et al., 2003) and therefore may serve as an explanation for the cause of melting beneath ocean islands (Sobolev et al., 2005).

Volatile elements, including hydrogen, carbon, sulfur, and halogens, are of extreme importance when discussing mantle heterogeneity, but unlike radiogenic isotopes, volatiles have been considerably less studied in magmatic systems due to various challenges restricting their direct measurement, such as their low solubility at low pressure. The importance of volatiles is due to the effects they have on the physical properties of the mantle: higher volatile contents result in lower seismic velocity, lower viscosity, and higher electric conductivity. For petrologist, the most important change caused by volatile addition to the mantle is the decrease in solidus temperature, possibly by several hundred degrees (Katz et al., 2003; Hirschmann et al., 2009; Green et al., 2010). Furthermore, volatiles elements influence the chemical composition of mantle melts (Dasgupta et al., 2007; Gaetani and Grove, 2013; Green et al., 2014), causing magmas with different chemical composition to erupt in various geodynamic settings. Whether volatile elements are recycled into the mantle during subduction have been investigated in detail during recent years (Evans et al., 2012; Kendrick et al., 2012; Jégo and Dasgupta, 2014; Kelemen and Manning, 2015; Plank and Manning, 2019; Walters et al., 2020), albeit many questions remain unanswered, such as in what phase and in what quantity are volatile added back into the mantle and whether these recycled volatiles are returned to the surface at ocean islands and other locations such as large igneous provinces, through the melting of heterogeneous mantle lithologies.

2.1 Geodynamic setting and the geology of the Canary Islands

The Canary Islands archipelago is located approximately 100 km west of the western African coast and is one of the many volcanic island groups located in the Eastern side of the Mid-Atlantic Ocean, together the island of Madeira, the islands of Cape Verde, and the Azores (Fig. 2.1). The Canary Islands is built up by a chain of seven major volcanic islands: Lanzarote, Fuerteventura, Gran Canaria, Tenerife, La Gomera, La Palma, and El Hierro, from east to west, respectively (Fig. 2.2). This 450 km-long island chain stretches deep into the abyssal plain of the Atlantic Ocean; the islands of Tenerife, La Gomera, El Hierro, and La Palma emerge from a depth of 4000 m below sea level to thousands of meters above sea level, making Teide, the central volcano of Tenerife, the largest active volcanic edifice on the Earth after the volcanoes of Hawaii.

Currently volcanism at the Canary Islands is characterised by low magma fluxes and few eruptions, similar to the Azores or the Cape Verde islands in the region. Since historic records began, 13 eruptions were recorded in the Canary Islands, most of them on La Palma and Tenerife. Volcanic activity at the Canary Islands can separated into three units (Schmincke, 1982): the first submarine phase begins by the formation of pillow lavas erupting in relatively deep water. Below the pillow lavas an extensive network of plutonic rock and dyke swarms also forms at this stage within turbiditic ocean floor sediments. As the island grows and reaches shallower depths, explosive volcanic activity forms hyaloclastics at the final stage of submarine volcanic activity. Such submarine sequences are exposed on the surface in the basal complexes of La Palma (Staudigel and Schmincke, 1984) and Fuerteventura (Stillman, 1999) and have

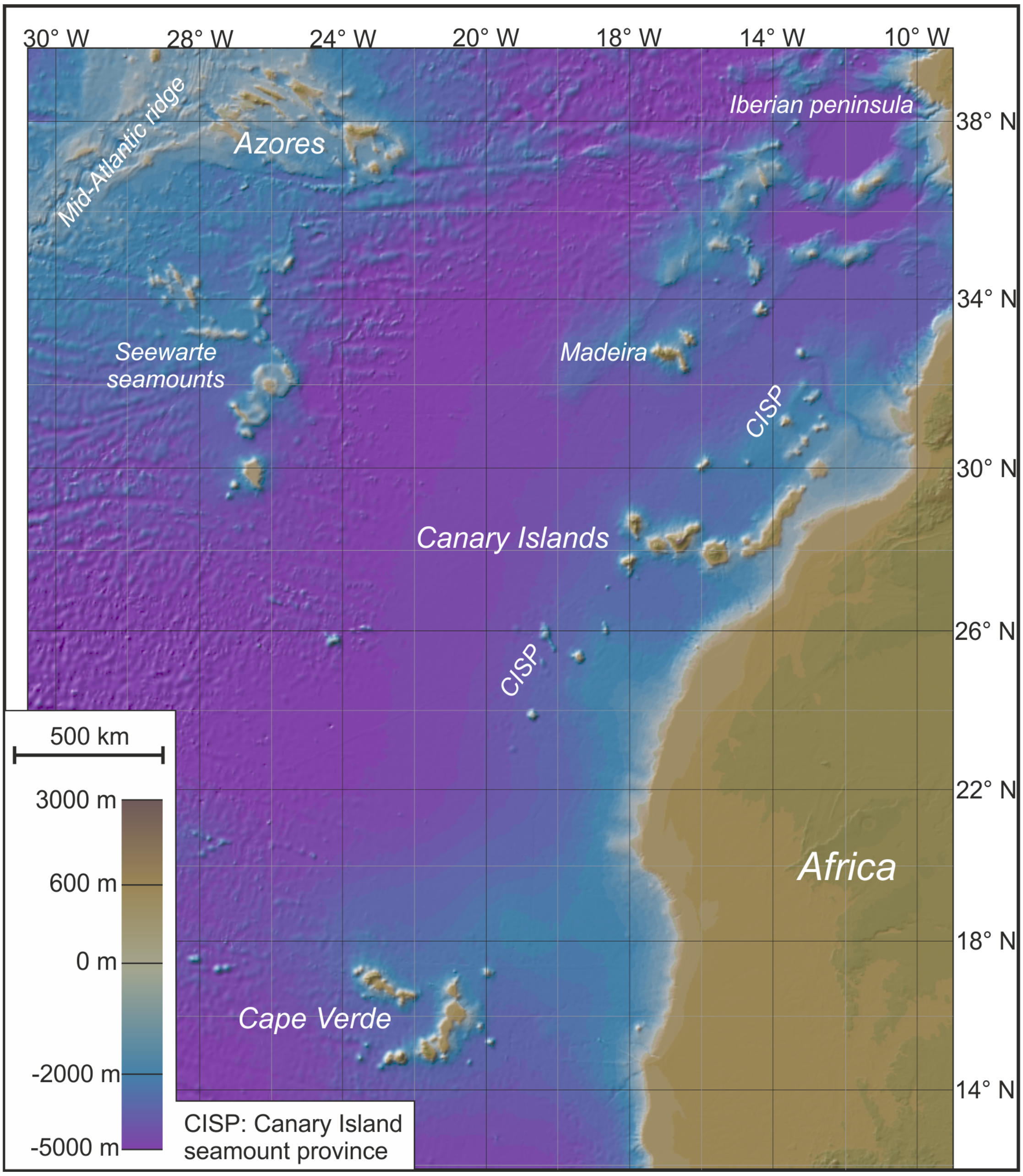

Figure 2.1: Topographic and bathymetric map of the Eastern-Central Atlantic Ocean, created using GeoMapApp (http://www.geomapapp.org/). Several volcanic ocean island chains and seamounts are located in the region, including the Canary Islands, the Azores, Madeira, and Cape Verde. In the vicinity of the Canary Islands, along the M25 geomagnetic polarity, a chain of seamounts can be found called the Canary Island seamount province, which are thought to have been volcanically active since the early Cretaceous (Van Den Bogaard, 2013). South of the Azores another seamount province is located called the Seewarte Seamounts.

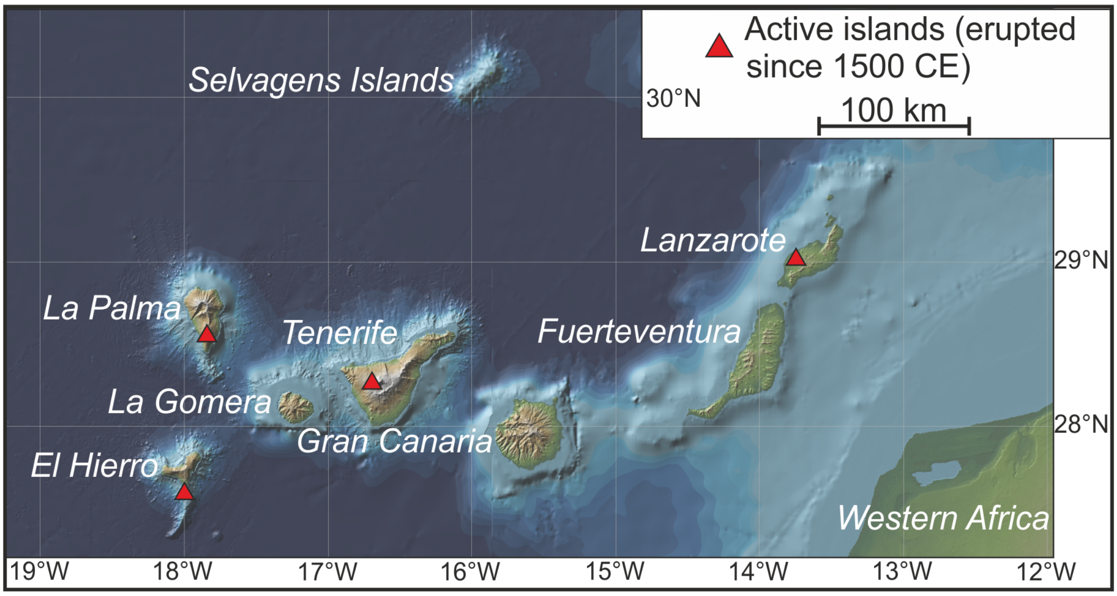

Figure 2.2: Topographic map of the Canary Islands, created using GeoMapApp, indicating the locations of historic eruptions (red triangles). A red triangle can indicate either one eruption, like in the 2011-2012 eruption of El Hierro, or multiple eruptions like in the case of Cumbre Veija in La Palma, which erupted eight times since 1470.

been described in core samples drilled underwater (Schmincke and von Rad, 1979).

The submarine phase is followed by a subaerial shield-building stage during which mafic magmas form thin lava flows and scoria cones such as those observed on the western islands of La Palma and El Hierro today. Finally the islands reach the differentiated stage (Schmincke, 1982), characterised by explosive eruptions of more evolved magmas like phonolites and trachytes. Currently the island of Tenerife is in this stage. A common feature in the subaerial sequences is the presence of collapse scars, separating different volcanic complexes from each other (e.g. Carracedo et al., 2001). These scars are formed by large flank collapse events during which a volcanic edifice collapses under its own weight; scars are currently present on the surface on El Hierro, La Palma, and Tenerife (e.g. Masson et al., 2002). Different classifications for stages of volcanism on the Canary Islands have also been proposed: Carracedo et al. (2001) identifies a juvenile shield building stage at the western island of El Hierro and La Palma to separate these relatively small and young islands from larger Tenerife, while Stillman (1999) classifies the eastern islands of Lanzarote and Fuerteventura into a post-erosional stage due to their low altitude topography.

The Canary Islands are located close to the passive margin of Africa (see bathymetry in Fig. 2.1) on 150-180 Ma Jurassic oceanic lithosphere (Müller et al., 2008). Using the half-space cooling model of Steinberger and Becker (2018) this age corresponds to a lithospheric thickness of 120-135 km. Geophysical measurements, such as seismic tomography, also indicates a thick (>90 km) lithosphere in the region (Fullea et al., 2015). This large lithospheric thickness, together with the proximity of the African passive margin, makes the Canary Islands a unique location among ocean island chains. A significant gravitational anomaly is present around each island, caused by the thickening of the oceanic crust in the region due to volcanic activity. The Mohorovičić discontinuity beneath the volcanic islands is suggested to be in the range of 10 to 15 km (e.g. Watts et al., 1997), considerably thicker than the average oceanic crustal thickness (~6 km).

Based on ocean floor magnetic anomalies in the region, half spreading rates in the mid-Atlantic can be estimated between 15-20 mm/year (Müller and Roest, 1992; Müller et al., 2008), and have been relatively constant since the Cretaceous. This is considerably slower compared to what is observed in the Pacific (usually >40 mm/year, up to 100 mm/year today). Slow spreading has been accompanied by various degrees of rotation since the early Cretaceous (Duncan, 1981; Morgan, 1983). Due to the slow spreading rate and rotation, the Canary Islands display distinctive features that are different compared to other ocean island chains, like the Hawaii-Emperor chain. The islands forming the Canary Islands are closer to each other and older islands like Fuerteventura and Lanzarote do not fall along a straight line with the other islands. Slow spreading rates strongly influence the current landscape of the islands: the western islands of El Hierro and La Palma only recently started erupting subaerial magmas while islands in the east are already highly eroded (Carracedo et al., 2001), often exposing intrusive basal complexes (e.g Balogh et al., 1999; Stillman, 1999). This presents an opportunity to study different units and the structure of oceanic islands within one island chain: deeper parts of the magmatic system, like plutonic bodies (often characterised by rocks of extreme composition, like carbonatites) and fresh lava flows and pyroclastics are both present at the surface of the Canary Islands.

All seven islands have been predominantly erupting mafic alkaline magmas such as basanites (olivine-phyric alkaline basalts) and tephrites (olivine-poor alkaline basalts) since their formation (Fig. 2.3). On the western islands of El Hierro and La Palma, volcanism has been exclusively alkaline, while on the islands of Gran Canaria and Lanzarote tholeiites are also present (e.g. Hoernle and Schmincke, 1993b; Sigmarsson et al., 1998). Mafic volcanism is occasionally interrupted by more evolved magmas, like trachytes and phonolites, most notably during the differentiation stage of the island formation (Schmincke, 1982). Evolved magmas are exclusively alkaline in composition (Fig. 2.3) and are commonly found on the island of Tenerife and Gran Canaria (Fig. 2.3). The widespread evolved volcanism, together with nearly exclusive alkaline volcanism, sets Canary Islands apart from other active ocean islands such as Hawaii and Réunion, where evolved volcanics are less common and tholeiites are far more typical during the shield building stage.

2.1.1 The timescale of magmatism in the Canary Islands and surrounding seamounts

Subaerial volcanism on the Canary Islands began during the late Oligocene or the early Miocene on the island of Fuerteventura, approximately at 20-25 Ma (Le Bas et al., 1986b; Geldmacher et al., 2005). However, there are multiple indications of magmatism present in the region considerably earlier than this based on ages determined from plutonic rocks exposed on the surface of the islands and from dredged samples of surrounding seamounts (Fig. 2.1). In the case of the basal plutonic complex of Fuerteventura ages of 63-64 Ma have been determined by $^{40}Ar/^{39}Ar$ dating syenites (Balogh et al.,

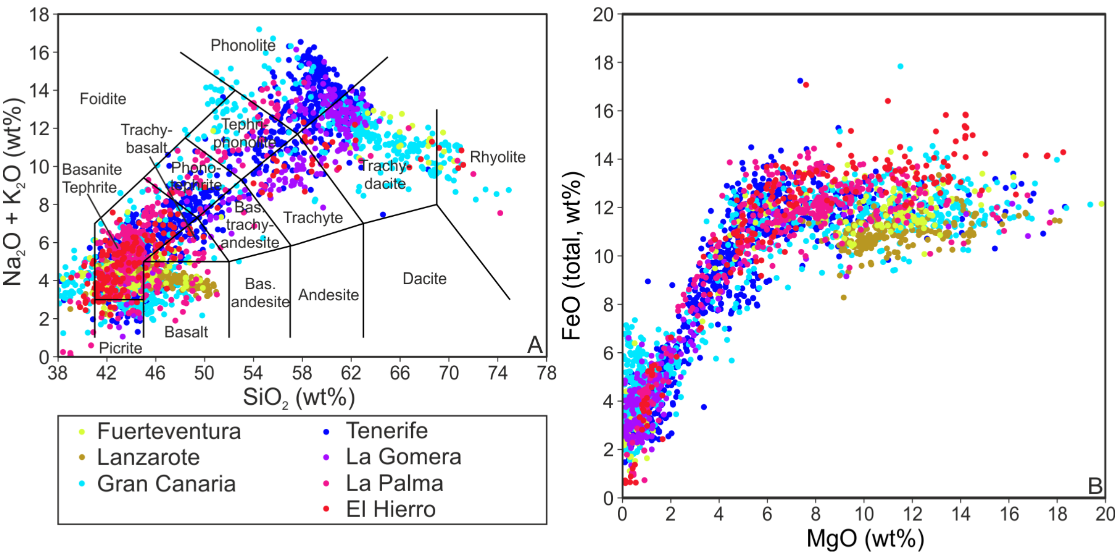

Figure 2.3: (A) Whole-rock geochemistry of Canary Island samples on total alkali-silica (TAS diagram) using the classification of Le Bas et al. (1986a), indicated by the black solid lines, and on (B) total FeO vs. MgO diagrams. Data is taken from GeoROC FeO vs. MgO diagram shows that magma evolution in the Canary Islands is first controlled by olivine fractionation, causing a decrease in MgO at constant FeO, followed by extensive crystallisation of clinopyroxene + oxides after MgO is <6 wt%, causing a decrease in FeO content. The colour scheme used classifies islands into groups based on their location: yellow/bronze = eastern, blue/purple = central, red/magenta = western.

1999), indicating alkaline magmatism has been present in the region, at least in the form of intrusive rocks, since the beginning of the Paleogene. Ages of seamounts found in the region indicate that subaerial volcanism was preceded by considerably older submarine activity. Seamounts located northeast of Lanzarote, called Lars, Anika, Dacia and Conception, formed between 68 Ma and 17 Ma (in a north to south order, Geldmacher et al. 2005), i.e. between the late Cretaceous and the early Miocene. Seamounts scattered across the region (Fig. 2.1) have been dated up to 142 Ma, with the oldest seamounts located south of El Hierro (Van Den Bogaard, 2013). These results indicate that intraplate volcanism has been occurring in this part of the Atlantic Ocean since the early Cretaceous, just a few tens of million years after the opening of the Central-Atlantic Ocean.

The formation of Fuerteventura was followed by the islands of Lanzarote to the north and Gran Canaria to the west in the Miocene at 15.5 Ma (Coello et al., 1992) and 13.9

Ma (McDougall and Schmincke, 1976), respectively. A considerable part of the current edifice of Gran Canaria is thought to have formed at around 13.5 Ma (McDougall and Schmincke, 1976). Subaerial volcanism on Tenerife is thought to have commenced at 11.9 Ma (Guillou et al., 2004), indicating some degree of westward age progression in the eastern and central Canary Islands. Subaerial activity on La Gomera, the only currently inactive island of the Canary Archipelago, began at around 10 Ma, while volcanic activity ceased 4 to 2 Myr ago (Paris et al., 2005; Ancochea et al., 2006), before volcanism began on the western islands, restricting volcanic activity at La Gomera to the late Neogene.

The two youngest islands of La Palma and El Hierro, as opposed to their eastern neighbours, formed exclusively during the Quaternary. Subaerial volcanic activity at La Palma began at 1.8 Ma, while at El Hierro the oldest subaerial volcanics have been dated at 1.1 Ma (Guillou et al., 1996, 2001). Both El Hierro and La Palma have a similar volcanic history: the formation of a large volcanic edifice is followed by a flank collapse and the formation of a new volcanic edifice in its place; two such collapsed volcanoes can be found on both islands (the Tiñor and El Golfo volcanoes on El Hierro, and the Grafía and the Taburiente volcanoes on La Palma, Carracedo et al. 2001).

Based on these ages, a general east to west trend can be observed in the Canary Islands in terms of the onset of volcanism: young, Quaternary islands are located in the west, followed by older islands in the central section (La Gomera, Tenerife, Gran Canaria) formed during the mid- to late Miocene, while subaerial volcanism in the eastern islands began as early as the late Oligocene. However, age relationships become more complicated when the age of surrounding seamounts and historical volcanic activity is taken into account (Fig. 2.1, 2.2). While some ages from seamounts north of Lanzarote (Conception, Dacia, Anika, Lars, Geldmacher et al. 2005) follow the age trend outlined by subaerial volcanics, other seamounts, especially those associated with the M25 magnetic anomaly (CISP, Fig. 2.1, Van Den Bogaard, 2013), do not show any signs of linear age progression. Recent eruptions on the eastern islands indicate that while they are strongly eroded and several million years older than the islands in the central section and >10 million years older than the westernmost islands, they are still volcanically active. By far the largest (in terms of volume) and longest eruption in historic times in the Canary Islands occurred on Lanzarote, the easternmost islands of the archipelago. The Timanfaya eruption between 1730-1736 CE erupted ~1 km^3 magma to the surface, close to three times as much as the second largest eruption, which occurred on El Hierro between 2011-2012 and erupted 0.321 km^3 magma (Carracedo et al., 2015).

2.2 The formation of the Canary Islands: models for melt generation and magmatism

The causes of magmatism at the Canary Islands have been extensively studied since the 1960s resulting in numerous models being proposed to explain volcanic activity at the Canary Islands and more broadly in the Eastern Central-Atlantic Ocean. Early models associated the formation of the Canary Islands with various rifting processes, such as trans-Atlantic rift systems parallel with magnetic anomalies (Klerkx and de Paepe, 1971) or propagating faults related to the formation of the High Atlas Mountains (Anguita and Hernán, 1975). The Canary Islands was also one of the first oceanic islands suggested as a location of a thermal mantle plume, or a hotspot (Morgan, 1971; Wilson, 1973).

Various models derived from the original mantle plume model have been favoured by many publications as the most feasible model to explain volcanism at the Canary Islands archipelago in the past three decades. One such model, called the "blob model", was based on the compositional variation observed in Miocene Gran Canaria volcanics (Hoernle and Schmincke, 1993b). The "blob model" involves an up to 400 km wide heterogeneous mantle plume delivering a mixture of fertile and less fertile material (blobs)

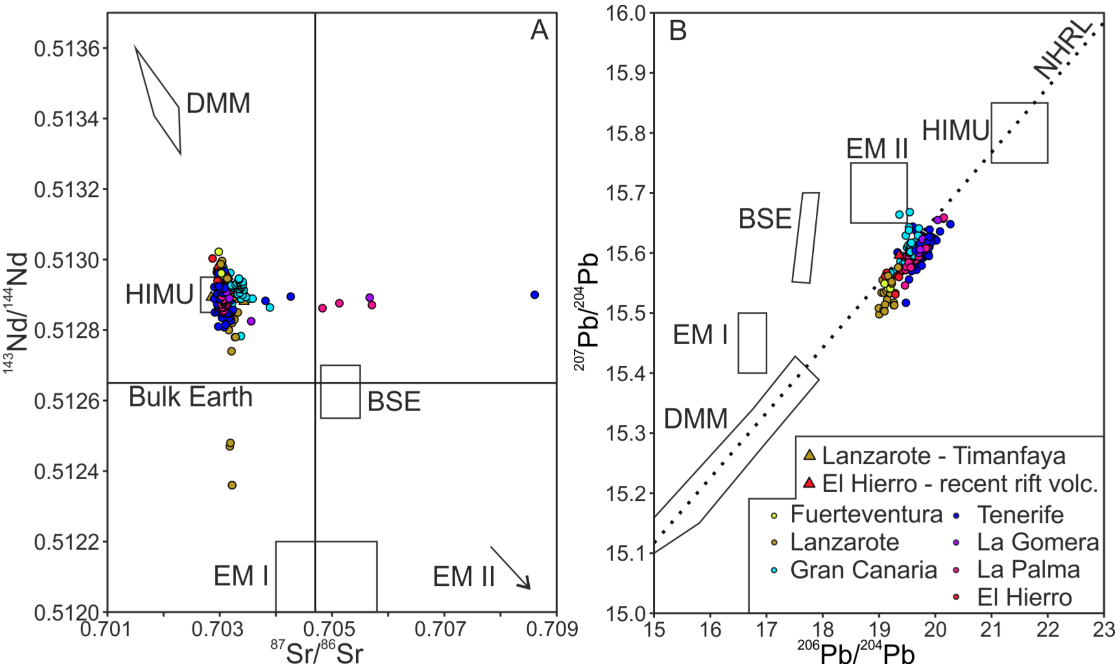

Figure 2.4: Sr-Nd and ^{206}Pb-^{207}Pb isotope systematics of Canary Islands volcanics, including basanites and phonolites. Dataset is taken from a number of publications (Thirlwall et al., 1997; Neumann et al., 1999; Thomas et al., 1999; Simonsen et al., 2000; Edgar et al., 2002; Lundstrom et al., 2003; Gurenko et al., 2006; Prægel and Holm, 2006; Aparicio et al., 2010; Aulinas et al., 2010; Day et al., 2010; Deegan et al., 2012; Turner et al., 2015) that cover all seven islands, including the tholeiites from the 1730-1736 Timanfaya eruption on Lanzarote and recent volcanics from El Hierro. Present bulk earth compostion in (A), show by solid lines are from O'Nions et al. (1979), while fields for bulk silicate earth (BSE), depleted MORB mantle (DMM), EM I, EM II and HIMU mantle end-members are from Zindler and Hart (1986). Northern hemisphere reference line (dotted line in B) is from Hart (1984).

into the mantle source of the Canary Islands, from which melts with different composition form. The presence of blobs with various compositions in the mantle source causes chemical heterogeneity (e.g. tholeiitic vs. alkaline basaltic) in magmas that erupted on Gran Canaria over time (Hoernle and Schmincke, 1993a); when refractory material is present in the source hiatuses in volcanism occur. The mantle plume model was also suggested by Carracedo et al. (1998) as the cause of magmatism in the region based on field observations on the islands of Tenerife, La Palma and El Hierro. The current volcanic edifices on these islands resemble a three-armed star, very similar to those found on the volcanoes of Hawaii (Manua Kea and Manua Loa), which they interpret as evidence for a common mantle plume origin for the Canary Islands and Hawaii. The east-west age relationship between the onset of volcanism on the seven major islands and seamount to the north of Lanzarote was used to argue for a thermal mantle plume origin, possibly combined with edge-driven convection along the African passive margin (Geldmacher et al., 2005). Ages recorded by foraminifera in sediments pre-dating volcanic island formation were also used to argue for a clear east-west age trend and a mantle plume origin in the Canary Islands (Zaczek et al., 2015). Seismic tomographic models based on s-wave velocities are also interpreted as deep thermally driven plumes originating at the core-mantle boundary (Montelli et al., 2004; French and Romanowicz, 2015). Integrated geophysical and petrological modelling (combining geodetic, seismic and mantle xenolith geochemical data) presented by Fullea et al. (2015) was used to strengthen the thermal mantle plume hypothesis, as these indicate that a mantle potential temperature (T_p, the temperature at the top of the asthenosphere adiabatically projected to surface) of >100 °C in excess that of the ambient mantle required to reproduce geodetic and seismic observations at the Canary Islands.

The isotopic composition of Canary Islands volcanics have been extensively used to decipher the causes of magmatism. Using uranium series isotope data, Lundstrom et al. (2003) suggested a purely mantle plume origin for basanites, while tholeiitic basalts (see Fig. 2.3), e.g. those erupted on Lanzarote between 1730-1736, form due to mixing of melts from the asthenosphere (plume origin) and the lithospheric mantle (formed by melting amphibole-rich veins). Lead isotopic compositions of rocks from the eastern Canary Islands are generally more depleted, which could imply a different origin for these magmas (Fig. 2.4). Both Marcantonio et al. (1995) and Day et al. (2010) presented extensive Sr, Nd, Os, Pb and O isotopic datasets from the western Canary Islands, and argued that the mantle source of Canary Islands magmas are heterogeneous, containing various portions of Proterozoic (1 to 2 Ga) recycled lithosphere. Day et al. (2010) suggested $<10\%$ of recycled lithospheric material is present in the mantle source of La Palma and El Hierro and that the enriched HIMU-signature, prevalent in rocks from all seven islands (Fig. 2.4), originates from recycled upper oceanic crust (i.e. basalts and gabbros) based on lava Pb and O isotopic composition.

The highly enriched nature of Canary Islands rocks compared to those erupted on some other ocean islands is evident in their trace element composition. High field strength elements, such as Nb, are especially enriched in Canary Island magmas (25-400 ppm, Fig. 2.5A), while Nb/U ratios cover a much wider range (around 30-110) compared to average OIBs (Fig. 2.5A, Hofmann et al. 1986). Trace element data suggest melting beneath the Canary Islands occurs mostly in the presence of garnet (Fig. 2.5B), in accordance with a deep, asthenospheric mantle source (e.g. Hoernle and Schmincke, 1993a; Day et al., 2010). Using melting models low melting degrees between 1 to 10% can be derived assuming a source with primitive mantle composition, which is somewhat lower than the 8-12% melting degree at Hawaii proposed by Feigenson et al. (2003); however, variations in melting degree estimates are large at Hawaii, especially between alkaline and tholeiitic rocks (e.g. Frey et al., 1991). This difference in melting degree and trace element enrichment between a typical mantle plume location such as Hawaii and the Canary Islands could be due to difference in mantle potential temperatures: modelling by Herzberg and Asimow (2008) shows that the temperature of the asthenosphere beneath the Canary Islands is lower (1410-1480 °C) compared to Hawaii (1520-1600 °C), which could be an explanation for low melting degrees at the Canary Islands.

While a thermally driven mantle plume originating from the core-mantle boundary is the most common model used to explain magmatism at the Canary Islands, and other surrounding ocean islands (Madeira, Cape Verde, the Azores), there are a number of observations that are inconsistent with such a model. If melting is due to a fixed mantle plume, a clear east-west age trend would be expected as the Atlantic plate moves slowly eastwards in the Canary Islands in the onset and end of volcanic activity. To some degree such a trend exists for the onset of volcanism, but more recent volcanic activity does not

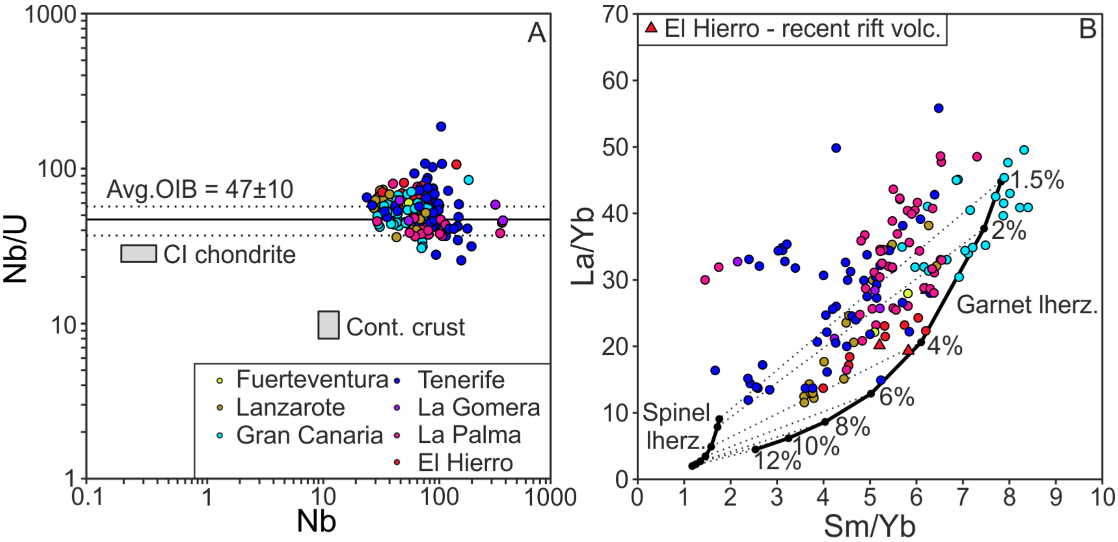

Figure 2.5: Trace element composition of Canary Islands volcanics on Nb/U vs. Nb (A) and La/Yb vs. Sm/Yb (B) diagrams, taken from the same publications listed in Fig. 2.4. CI chondrite, average OIB and continental crust Nb/U ratios and Nb contents are from Hofmann et al. (1986). Black curves in (B) are melting models assuming a primitive mantle source (Hofmann, 1988) and a garnet or spinel lherzolite lithology, calculated using the dynamic melting model of Zou (1998). More detail is provided in chapter 4 of the thesis on melting models shown in this figure.

support east-west age progression. Apart from La Gomera all islands have been active in the Holocene with the westernmost (El Hierro) and easternmost (Lanzarote) islands both erupting in the last 300 years, even though they are 450 km apart. Long hiatuses in magmatic activity occurred in some islands, such as Gran Canaria (inactive between 8.5-6 Ma, Hoernle and Schmincke 1993b) and La Gomera (inactive since 1.9 Ma, Paris et al. 2005); these hiatuses are longer than those observed on the islands of Hawaii (~1.3 Ma on O'ahu, Ozawa et al. 2005), and are not consistent with a fixed mantle plume origin, which should more or less continuously supply heat for melt generation. Surrounding seamounts, active since the Jurassic, do not show signs of age progression (Van Den Bogaard, 2013) either, although these could relate to a different volcanic phase in the region altogether (Zaczek et al., 2015). If we assume that the current location of the mantle plume is between El Hierro and La Palma and that the Atlantic plate is moving 15-20 mm/year eastwards it would mean that the part of the Atlantic-plate where Fuerteventura currently is located passed above the mantle plume at 20-26 Ma. The late Cretaceous ages measured in the basal complex of Fuerteventura (Balogh et al., 1999) are >30 Ma older than this, hence are in a disagreement with a fixed mantle plume model and indicate magmatism began in the Canary Islands well in advance of reaching the supposed mantle plume.

Geophysical data is also a source of ambiguity. A positive bathymetric, geoid and heat flow anomaly is expected to form above hotspots as excess heat is transferred towards the surface. However, such anomalies are absent or considerably weaker at the Canary Islands than other locations of suspected mantle plumes (e.g. Jung and Rabinowitz, 1986; Sleep, 1990; Canales and Dañobeitia, 1998). The mantle plume flux of ~1 Mg/s for the Canary Islands caclulated by Sleep (1990) is more than six times less than for Hawaii (6.3 Mg/s), which have been interpreted as a less buoyant mantle plume. While negative seismic velocity anomalies have been observed in the lower mantle beneath the Canary Islands (e.g. Montelli et al., 2004; French and Romanowicz, 2015), these anomalies are less prominent compared to those beneath Hawaii and Iceland, most notably at the top of the lower mantle (600-1000 km). On the other hand, low shear wave velocity anomalies are present at the top of the mantle transition zone, at < 500 km depth (French and Romanowicz, 2015).

Compositional trends in magma composition observed in Hawaiian volcanoes as the plate passes over a mantle plume, such as pre-shield alkaline volcanism, shield-stage tholeiitic volcanism, and post-shield stage alkaline volcanism (reflecting differences in melting degree, Frey et al. 1991) are lacking on the Canary Islands. Cyclical variation in magma composition can be observed on Gran Canaria (Hoernle and Schmincke, 1993a), but tholeiites are not restricted to the shield-building stage. Furthermore, tholeiites cannot be found on either El Hierro or La Palma, both currently in their shield-building stage, while tholeiites erupted on the highly eroded island of Lanzarote in historic times.

Due to these inconsistencies, many alternative models have been proposed to explain the formation of the Canary Islands since the birth of the mantle plume theory. Anguita and Hernán (1975) argued that magmatism at the Canary islands is controlled by shallower tectonic processes linked to the formation of the High Atlas Mountains during the Mesozoic and Neogene. They suggested propagating fracture zones as the cause of magmatism, which connect the Atlas mountains to the Canary Islands through the passive African margin. In this model, magmatism at the Canary Islands is linked to the three main tensional phases observed in the Atlas Mountains and hiatuses are due to compressional tectonics. While this model is a good alternative in explaining erratic age relationships observed in the Canary Islands, a crucial part of the model, i.e. tectonic connection between the Atlas mountains and the Canary Islands would require faults and other structures to be present in the African continental slope located between them. Seismic sections in the region do not indicate any structural connection between the High Atlas and the Canary Islands (Watkins and Hoppe, 1979). Furthermore, such a model would require hiatuses in volcanic activity to occur approximately the same time, which is not the case.

Araña and Ortiz (1991) also proposed a model implying volcanism is caused by the uplift of lithospheric blocks due to compression in the region with subsequent decompression melting in the asthenosphere. This model relies on the fact that the African plate is being pushed eastwards by spreading in the middle of the Atlantic and southwards by the European plate, causing a compressional tectonic regime in the region. Such a model would require evidence of extensive uplift around the islands, which is not observed in sediments around Tenerife (Watts et al., 1997).

A more complex model, incorporating different elements of above mentioned models was proposed by Anguita and Hernán (2000). This model involves remnants of a thermal plume, faults in the oceanic crust and lithospheric mantle (but not in the overlying sediments) and transgressive shear (i.e. compressional tectonics) to explain the formation of the Canary Islands. Most recent models argue that shallow mantle upwelling beneath the Atlantic (Van Den Bogaard, 2013) or small scale heterogeneous mantle convection (Belay et al., 2019) causes melt generation at the Canary Islands and more broadly in the eastern-central Atlantic.

While the topic of melt generation has been extensively studied at the Canary Islands from both a petrological and geophysical viewpoint, no consensus has been reached to date regarding the presence of a deep mantle plume in the region. The mantle plume model (e.g Fullea et al., 2015) and models favouring shallower processes (e.g Van Den Bogaard, 2013; Belay et al., 2019) also have been proposed in the last decade. The unique geological location of the Canary Islands, positioned close to the passive margin of Africa on extremely old Atlantic oceanic lithosphere further complicates the interpretation of geochemical and geophysical observations or comparing those results to other, more typical ocean islands like Hawaii.

2.3 Volcanology and petrography of the island El Hierro

El Hierro is the westernmost, smallest, and youngest island of the Canary Islands. Its topography resembles a three-armed star with each arm representing a rift system. A similar structure can be found on other oceanic islands such at Hawaii and Tenerife (Dieterich, 1988; Carracedo et al., 2001, 2011; Walter et al., 2005). The three rifts face southwards, westwards and northeastwards, respectively (Fig. 2.6). The highest point of El Hierro, Pico del Malpaso, is located near the junction of the rifts and stretches 1502 m above sea level. Another distinct topographic feature on El Hierro is the presence of three, large embayments located between the rift arms. The largest is the El Golfo embayment, located in the northern part of the island, occupying around one fifth of El Hierro. The other two embayments are located in the southwestern and southeastern part of the island and are called El Julán and Las Playas, respectively. These embayments are assumed to be the results of gigantic landslide events (e.g. Masson, 1996; Masson et al., 2002) during which the excessive growth of a volcanic edifice leads to instability and subsequent gravitational collapse. Large volume landslide scars and their deposits are a common features in the western Canary Islands, including La Palma and Tenerife (e.g. Day et al., 1999; Longpré, 2009).

El Hierro emerges from the abyssal plain of the Atlantic Ocean found approximately 4000 meters below sea level (Fig. 2.6). If the underwater part of the volcanic edifice is taken into account, El Hierro is ~100 km in diameter from east to west, with only ~23 km of this section located above sea level. Along the south rift a ~25 km long positive bathymetric anomaly can be traced in the Atlantic Ocean, indicating that the south rift is continued below sea level (indicated as Hierro ridge in Fig. 2.6). Van Den Bogaard (2013) proposed that part of this underwater structure formed in the early Cretaceous and hence is much older than El Hierro (Fig. 2.6). The mid-Cretaceous Henry seamount, rising 600 m above the abyssal plain, is located approximately 40 km to the south-southeast of El Hierro, while the Bisabuelas seamount, rising 1600 m above the abyssal plain, is 80 km to the south-southwest. These seamounts are considered to have formed in the early Cretaceous (Van Den Bogaard, 2013).

2.4 Volcanology of El Hierro

The volcanic stratigraphy of El Hierro was extensively studied by Carracedo et al. (2001), who subdivided El Hierro volcanics into three distinct volcanic units (Fig. 2.7): the Tiñor volcano, the El Golfo volcano and the Rift volcanics. The Tiñor volcano is the oldest of the three: subaerial outcrops have K-Ar ages exceeding 1 Ma, with the oldest age of 1.11 Ma (Guillou et al., 1996). Most of the outcrops of the Tiñor volcano are located in the eastern part of the island and are part of the Ventejís group,

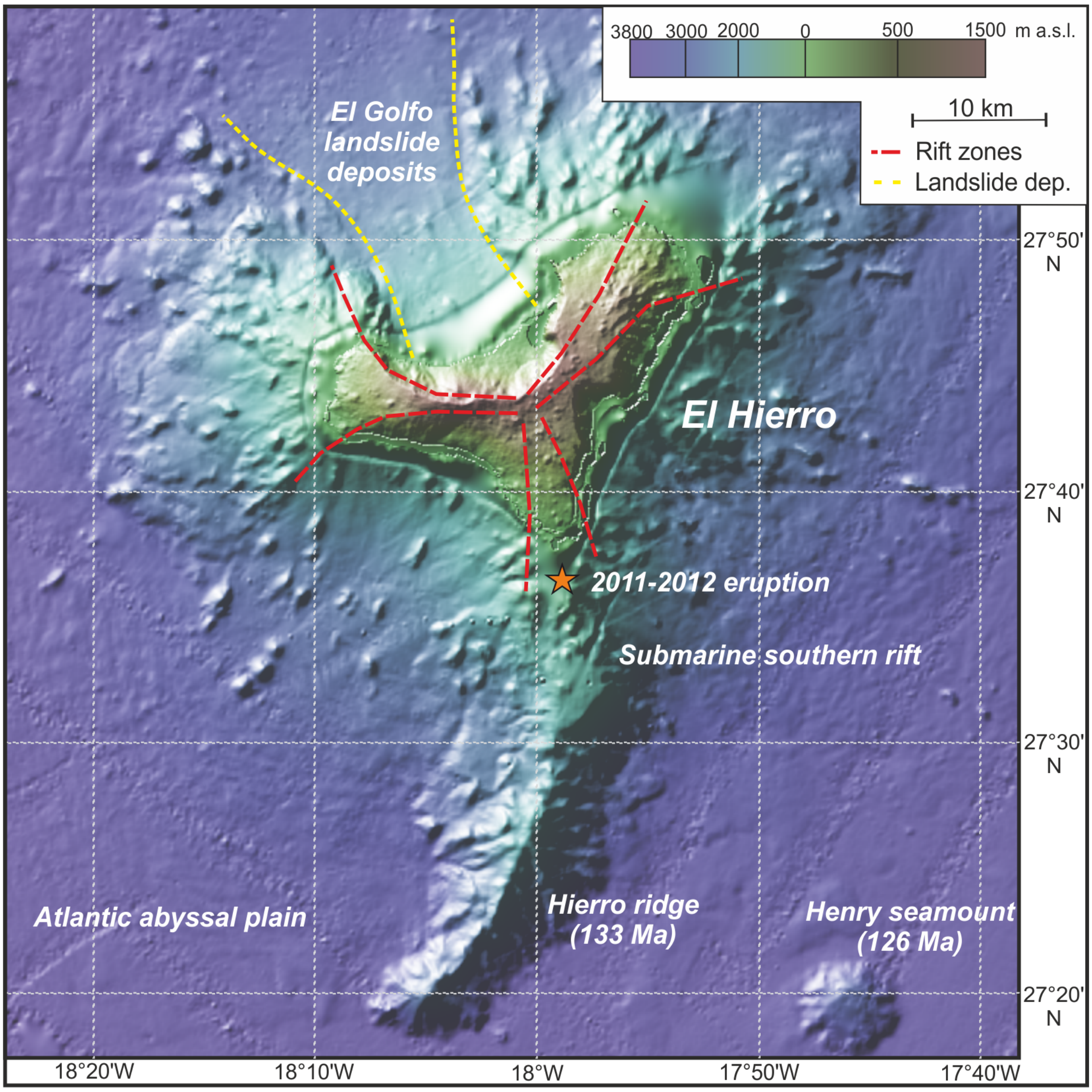

Figure 2.6: Bathymetric map of the Atlantic Ocean surrounding El Hierro (made using GeoMapApp), showing underwater features in the region, such as the Henry Seamount, numerous submarine volcanic cones around El Hierro, landslide deposits along the El Golfo embayment, and submarine parts of the southern rift zone. Ages for the Hierro ridge and the Henry Seamount are from Van Den Bogaard (2013).

which represent the youngest Tiñor volcano deposits, while other outcrops of the Tiñor volcano can be found in the southeast of El Hierro inside the Las Playas embayment. The oldest rocks of the Tiñor volcano are steeply dipping lava flows that formed during the early subaerial stage of the island. Younger Tiñor lavas have more gentle dips and often contain mantle xenoliths; this is a typical feature of the Ventejís lavas found in

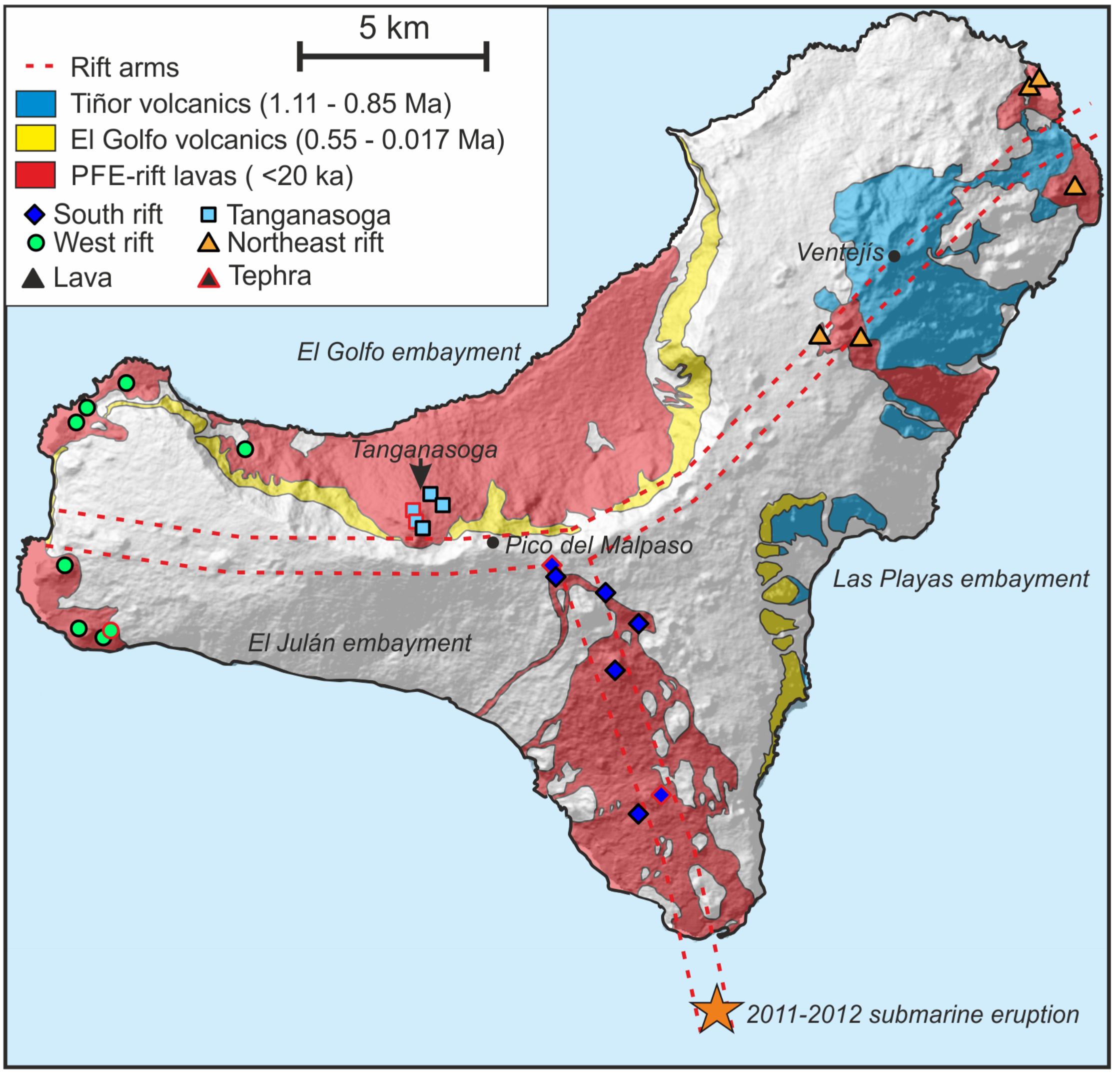

Figure 2.7: Geological map of El Hierro after Carracedo et al. (2001), showing the three distinct volcanic units (Tiñor, El Golfo and Rift volcanics). The map is superimposed on a digital elevation model taken from GeoMapApp. The approximate axis of the rift systems is indicated by the red dashed lines. The location of Tanganasoga, the current main vent of El Hierro, is also shown within the El Golfo embayment. Location of samples used in the thesis (listed in Table 2.1) are also shown on the map.

the eastern outcrops of Tiñor. Compositionally Tiñor volcanics are dominantly alkaline basaltic. Smaller volumes of explosive pyroclastics erupted by the Tiñor volcano are also exposed on the surface of El Hierro. The Tiñor volcano thought to have collapsed approximately 800-900 kyr ago (Carracedo et al., 2001).

The Tiñor volcano was followed by the El Golfo volcano, whose outcrops are located along the walls of the El Golfo embayment, and to some extent, along the Las Playas embayment (Fig. 2.7). The oldest K-Ar ages measured on El Golfo volcanics are ~550 ka (Guillou et al., 1996), indicating a hiatus of volcanic activity on El Hierro between the Tiñor and El Golfo volcanos. The initial products of the El Golfo volcano are dominated by mafic strombolian and surtseyan pyroclastics, while later stages are characterised by lava flows (Carracedo et al., 2001). During the last stage of its activity, more evolved volcanics (trachytes) were erupted from the El Golfo volcano, suggesting that a shallow magma storage system developed within the crust beneath El Hierro. Similarly to Tiñor, the El Golfo volcano also ended its activity with a gravitational collapse event, resulting in the formation of the present El Golfo embayment. The age of this event is somewhat controversial: K-Ar ages from the top of the collapse scar suggest an age of 134 ka (Guillou et al., 1996), while dating of turbidites associated with the landslide suggest a younger age of 13-17 ka (Masson, 1996; Gee et al., 2001). Ar-Ar ages put the landslide event between 87±8 ka and 39±13 ka (Longpré et al., 2011).

The El Golfo collapse event was followed by widespread volcanism along the three rift zones present today on El Hierro (Fig. 2.6, 2.7). This rift volcanism (Carracedo et al., 2001) is characterised by both effusive and explosive eruptions, producing basanitic lava flows and pyroclastics (products of Hawaiian and Strombolian-type eruptions, Fig. 2.8.). The Tanganasoga volcano, located in the western half of the El Golfo embayment (Fig. 2.7, 2.8), is the current main volcanic edifice of El Hierro. Several other vents can be found throughout the island that have been active at some point during the Holocene. The youngest materials erupted on El Hierro have been classified as platform-forming

---

Figure 2.8 (next page): Images of El Hierro rift volcanics, including a volcanic landscape typical of the western rift (A) with Hawaiian fissure eruption and lava flow deposits in the front and large scoria cone in the back. The plant in the right side of (A) is approximately 1 meter wide. (B) shows the Tanganasoga scoria cones from the east. On the left-hand side of the image (towards north) lava flows connecting to the scoria cones can be seen, overgrown with vegetation.

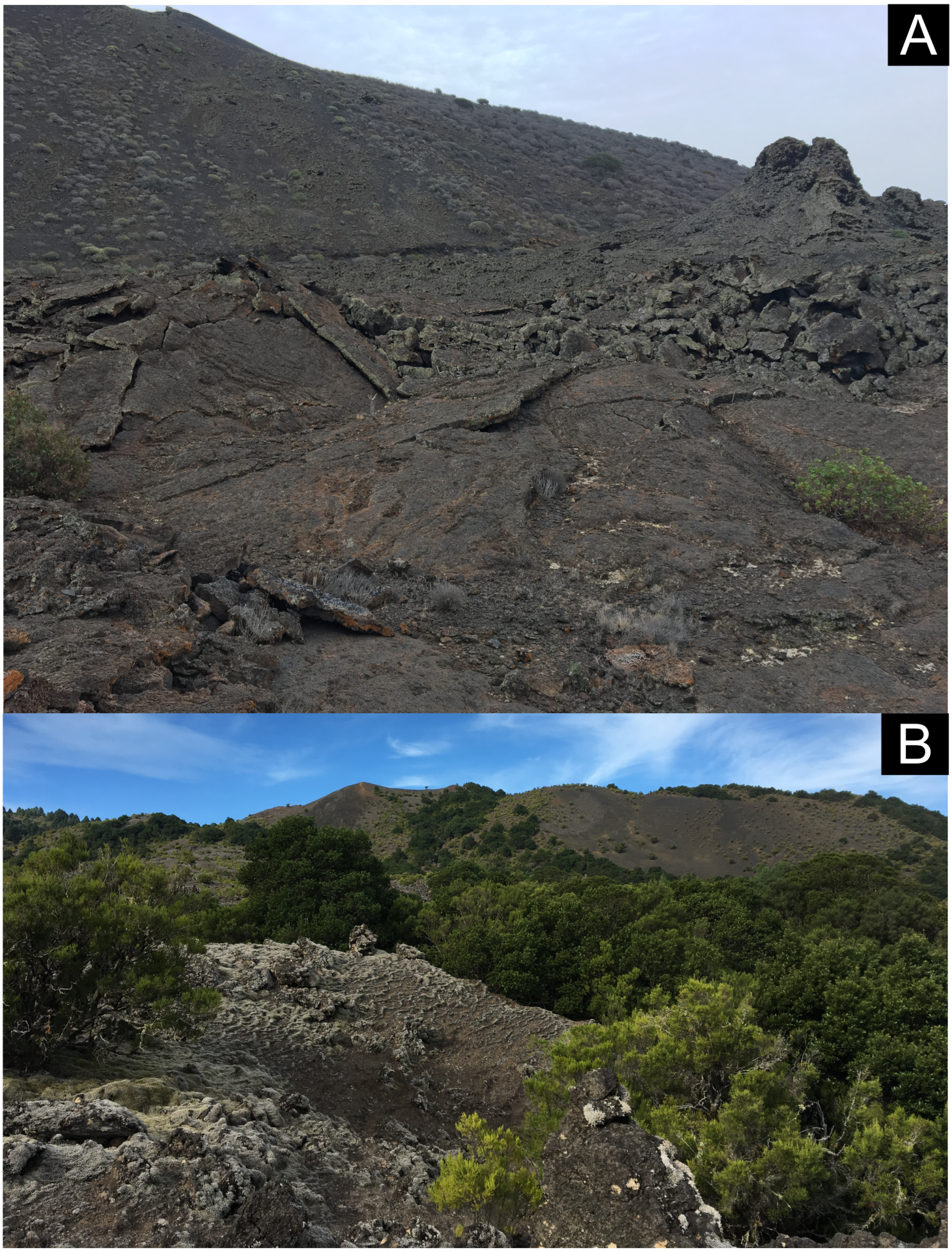
A
B

rift volcanics to distinguish them from the older "cliff-forming" rift volcanics (Carracedo et al., 2001) that cover most of El Hierro today (Fig. 2.8). Platform-forming rift volcanics are thought to post-date the last glacial maximum (Carracedo et al., 2001). Platform-forming rift lavas have partially filled up both the El Julán and the El Golfo embayments (Fig. 2.7). Magma supply of the rift volcanics is relatively small: no eruptions have been recorded in the last few hundred years apart from the submarine eruption along the underwater part of the south rift zone in 2011-2012 (Figs. 2.6 and 2.7).

2.4.1 The 2011-2012 eruption of El Hierro: volcanology, geophysics and petrology of the last eruption of the Canary Islands

The most recent eruption on the Canary Island archipelago occurred along the underwater section of the south rift between October 2011 and March 2012. Due to the extensive monitoring equipment present on the island at the time, this eruption was the first opportunity to study an eruption on the Canary Islands in real time and to integrate geophysical and petrological observations. An estimated 0.321 km^3 of volcanic material was erupted at depths ~300 meters below sea level (Carracedo et al., 2015). The eruption was preceded by seismic unrest between July 2011-October 2011. The earthquake hypocentre depths increased during the pre-eruption unrest period, with the highest levels of seismic activity observed a few weeks before the eruption, during the end of September and early October 2011 (López et al., 2012). Based on geophysical, volcanological, petrological and geochemical observations, the latter two carried out on highly vesicular floating rocks found on the surface of the Atlantic Ocean during the eruption, it was established that the magma feeding this eruption originated from the northern part of the island below the Tanganasoga volcano approximately 14 km north of the eruptive vents (Fig. 2.7). This indicates that significant lateral migration occurred priori to the eruption (Martí et al., 2013a,b).

Floating rock samples collected during the eruption were dominantly basanites. Smaller volumes of white pumice also erupted, later interpreted as either a remobilised, evolved melt (Sigmarsson et al., 2013) or xenoliths of sedimentary origin incorporated and partially melted by the magma (Troll et al., 2012). Both interpretations indicate long crustal residence times for the magma, enabling the assimilation of a large amount of sedimentary material. The basanites experienced both fractionation of olivine+clinopyroxene±plagoclase and mixing, the latter caused by the injections of several magma batches from a deeper upper mantle magma reservoir into a shallower, mid-crustal reservoir. The depth of the deep magma storage system is recorded by clinopyroxene-melt thermobarometry, while the shallow, lower crustal magma reservoir depth was determined by fluid inclusions barometry (Martí et al., 2013b; Longpré et al., 2014). Diffusion modelling indicates crystal residence times between one to five months for a first mixing event, and eight hours to 15 days for a second, shorter mixing event (Longpré et al., 2014). The one to five month-long crystal residence times overlap with the seismic unrest between July and October 2011. The later mixing event likely took place just before eruption at the time of the highest levels of seismic activity and corresponds to the ascent of the magma through the crust towards the surface (López et al., 2012; Longpré et al., 2014). These results indicate that El Hierro might have been fed by a complex magma plumbing system in the past, with possible stalling at crustal levels. Therefore, if the causes of melt generation are to be explored at El Hierro, a source to surface research approach is required that investigates any processes altering magma composition during its journey from the mantle to the surface.

2.5 Utilising melt inclusions for volatile studies

Melt inclusions (MIs) are droplets of melt that are entrapped within crystals during crystal growth or cleavage/crack formation. They can be various in size, but are generally small (<100 μm in diameter) and are found in most type of igneous crystals. In most cases, melt inclusions are ellipsoidal, but they can be sometimes elongated especially if captured during rapid, skeletal crystal growth. Melt inclusions can be primary or secondary: primary inclusions are entrapped during crystal growth, while secondary inclusions are entrapped when a crystal fractures and anneals allowing some melt to be trapped within the crystal. Primary inclusions generally form along crystal growth planes, while secondary inclusions tend to be parallel with cleavage directions. Larger melt inclusions often occur isolated within crystals, with no clear indication of their origin. Melt inclusions are either one phase (glass only), two phase (glass + solid or fluid), or multiphase with solid phases and fluid bubbles (Fig. 2.9).

The main advantage of studying MIs over whole-rock or matrix glasses is that they are expected to be less susceptible to modification by differentiation processes after entrapment. Therefore, they can provide insight into the state of the magmatic system at a specific point in time. Unlike matrix glasses MIs can retain their original magmatic volatile contents after entrapment, as they are not affected by decompression driven degassing. Therefore, MIs have been utilised to study magmatic volatile contents excessively during the last 30 years: most of our current understanding on deep magmatic volatile budgets rely on melt inclusion volatile data (e.g. Lowenstern, 2003; Métrich and Wallace, 2008). The only requirement for MIs to form is the presence of a host crystal, therefore the first inclusions can form close to liquidus conditions and the last just before eruption, covering the whole life of the magmatic system.

In reality, many processes complicate melt inclusions studies, as illustrated in Fig. 2.9. One of the most common process that changes melt inclusion composition is post entrapment crystallisation (PEC). During PEC a thin crystal rim made of the same material as the host forms along the wall of the inclusion (Fig. 2.9B). Bubbles can also form after melt inclusion entrapment due to changes in internal and external pressure conditions (Fig. 2.9C). One of the main driving force of bubble formation is PEC and daughter crystal formation, during which denser crystalline material forms from the melt, leading to a decrease in internal pressure within the inclusions and subsequent degassing. Volatiles, most notably CO_2 degasses into the bubble, leading to a decrease in melt CO_2 content (Steele-Macinnis et al., 2011; Hartley et al., 2014; Moore et al., 2015). Loss of H atoms via fast diffusion through the host crystal, such as olivine (Gaetani et al., 2012; Bucholz et al., 2013; Hartley et al., 2017) also causes issues in determining original magmatic H_2O contents. Hydrogen loss will cause oxidation and possibly oxide formation (Fig. 2.9E, Danyushevsky et al. 2002). Iron (as Fe^{2+}) can be lost in a similar way, through diffusion, which may result in sulfur saturation and sulfide precipitation (Fig. 2.9F). Melt inclusions can also decrepitate if the overpressure, defined as the difference between the internal MI pressure and external lithostatic pressure, reaches the threshold that the host mineral can withstand. Decrepitation could lead to exchange of material between the inclusion and the melt surrounding the host and cause the escape of vapour bubbles if present (Fig. 2.9H, Maclennan 2017). Nonetheless, while these complications may arise, no method have been proven to be as reliable as the geochemical analyses of melt inclusions in determining magma volatile contents. More detail, applicable specifically to El Hierro melt inclusions, is provided in chapter four and in the supplementary text (Supplementary text chapter four).

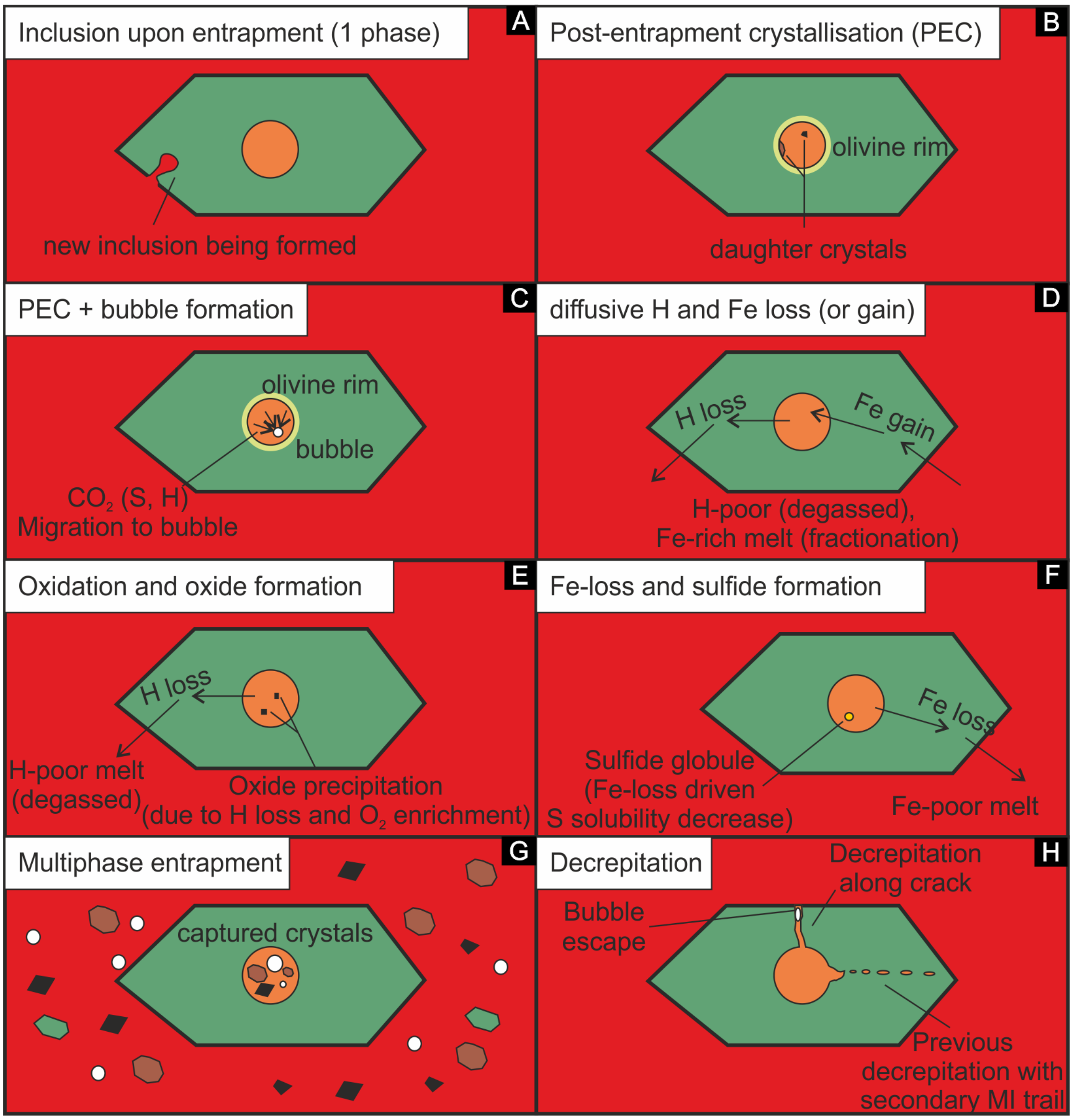

Figure 2.9: Small cartoons showing processes that could influence the composition of melt inclusions after entrapment. In (A) a melt inclusion containing only melt is shown, which have not been altered in anyway after entrapment. Along the edge of the olivine crystal a new inclusion is being formed from an embayment. After entrapment a number of processes can alter the composition of the melt within the inclusion including: post-entrapment crystallisation (B) during which an olivine rim crystallises along the inclusion wall; bubble formation after entrapment (C) due to volume/internal pressure change; diffusive H and Fe loss or gain (D) due to changes in H and Fe content of the surrounding melt; post-entrapment oxidation (E) and reduction (F) resulting in oxide and sulfide precipitation; decrepitation of the inclusion (H) due to overpressure reaching the strength of the host olivine crystal, resulting in partial or total volatile loss and possible material transfer in or out of the inclusion. Multiphase entrapment (G) may also occur, i.e. when not only melt but solids and fluids are also captured during time of entrapment.

Chapter 3

Samples and Analytical Methods

Samples used in the thesis were collected from material representing the platform-forming rift volcanism (Carracedo et al., 2001) stage, corresponding to the last ~20000 years of volcanic activity at El Hierro (Fig. 2.7). Both tephra and lava samples used in the thesis were collected in 2014 by Margaret E. Hartley. A second field trip in 2017 was also carried out, during which new lava and tephra samples were collected; however, these samples were not used in the thesis. Samples indicated on the map in figure 2.7 are listed in table 3.1. Details on sample petrography is provided in relevant chapters. Petrography of lava samples are given in chapter seven. Details on tephra samples and melt inclusion petrography are detailed in chapter four. Melt inclusions used in chapter six for sulfur isotope ratios analyses are a subset of the MIs that are analysed for trace- and volatile elements in chapter four. A few inclusions were also analysed for sulfur isotope ratios that are not presented in chapter four: these have been analysed for major elements using the same technique as for other MIs.

Table 3.1: List of samples used in the thesis.

Sample	Rift	Location	Type	Petrology	Latitude	Longitude
MCG14-01	South	near Mercade scoria cone	Lava	Ol-phyric, basanite	27°43’20.32"N	18° 1’33.06"W
MCG14-02	South		Tephra	Ankaramite	27°43’19.24"N	18° 1’26.33"W
MCG14-03	South		Lava	Ankaramite	27°43’9.77"N	18° 0’53.03"W
MCG14-04	South		Lava	Ankaramite	27°42’38.77"N	18° 0’19.26"W
ME14-01	South	Montaña la Empalizada scoria cone	Lava	Ol-phyric with cpx megacrysts	27°41’59.68"N	18° 0’32.87"W
MJ14-01	South	Montañas de Julán	Tephra	Ol-phyric, tephrite	27°40’18.01"N	17°59’55.54"W
MJ14-02	South		Lava	Ol-phyric, tephrite	27°39’50.18"N	17°59’58.92"W
WH14-01	West	Northwestern corner of El Hierro, west of Sabinosa	Tephra	Aphyric, tephrite	27°44’58.16"N	18° 6’7.63"W
WH14-02	West		Lava	Aphyric, tephrite	27°45’55.01"N	18° 7’58.91"W
WH14-03	West		Tephra	Aphyric, tephrite	27°45’29.77"N	18° 8’37.93"W
WH14-04	West		Lava	Aphyric, tephrite	27°45’42.05"N	18° 8’32.71"W
MN14-01	West	Montanita Negra, southwest El Hierro	Tephra	Ol-phyric, basanite	27°42’30.56"N	18° 8’13.49"W
MN14-02	West		Lava	Ol-phyric, basanite	27°42’29.56"N	18° 8’19.57"W
MN14-03	West		Lava	Ol-phyric, basanite	27°42’28.33"N	18° 8’25.91"W
MN14-04	West		Lava	Ankaramite (older)	27°43’2.96"N	18° 8’28.97"W
MN14-05	West		Lava	Aphyric, tephrite	27°43’32.45"N	18° 8’48.77"W
TSG14-01	Tanganasoga	Tanganasoga	Tephra	Ankaramite	27°43’47.86"N	18° 3’30.49"W
TSG14-02	Tanganasoga		Tephra	Ankaramite	27°43’54.44"N	18° 3’33.01"W
TSG14-02b	Tanganasoga		Tephra	Ankaramite (megacryst separate)	27°43’54.44"N	18° 3’33.01"W
TSG14-02c	Tanganasoga		Tephra	Ankaramite	27°43’54.44"N	18° 3’33.01"W
TSG14-03	Tanganasoga		Lava	Ol- and cpx-phyric, basanite	27°43’41.92"N	18° 3’21.31"W
TSG14-04	Tanganasoga		Lava	Ankaramite	27°44’28.86"N	18° 3’24.48"W
TSG14-05	Tanganasoga		Lava	Ankaramite	27°44’24.29"N	18° 3’4.07"W
TSG14-06	Tanganasoga		Tephra	Ol-phyric, tephrite	27°43’59.34"N	18° 3’39.82"W
TNR14-01	Northeast	North of San Andrés	Lava	Ol-phyric, basanite	27°46’29.68"N	17°57’18.40"W
TNR14-02	Northeast		Lava	Ol-phyric, basanite	27°46’28.27"N	17°56’49.67"W
TDE14-01	Northeast	Tamaduste, Montaña Huya del Diano	Lava	Ol-phyric, tephrite	27°49’52.36"N	17°53’50.50"W
TDE14-02	Northeast		Lava	Ol-phyric, tephrite	27°49’46.52"N	17°53’59.75"W
TDE14-03	Northeast	Tamaduste, quarry near Airport	Tephra	Ol-phyric, tephrite	27°48’25.70"N	17°53’36.31"W

3.1 Bulk chemical analysis

Fourteen powdered whole-rock lava samples from El Hierro platform-forming rift eruptions were analysed for major elements by X-ray fluorescence at the University of Edinburgh using a Panalytical PW2404 instrument, following the procedure described by Passmore et al. (2012) and references therein. Sample powders (2 to 4 g) were fused with lithium borate into glass pellets prior to analyses.

The same lava samples were also analysed for bulk sulfur isotope ratios ($^{34}S/^{32}S$) at the Godwin Laboratories, University of Cambridge. Sulfur isotope analyses were carried out using ~2 g of rock powder from each sample. As a first step a mixture 6

M HCl and $CrCl_2$ solution was added to the sample powders and boiled on a hotplate for approximately 2 hours. H_2S gas produced during this process was trapped in a Zn-acetate solution, precipitating the sulfur as ZnS. This step extracts reduced sulfur species (S^{2-} and S^0) from the samples by forming H_2S though reactions:

$$2H^+ + S^{2-} = H_2S \tag{3.1}$$

and

$$S^0 + 2Cr^{2+} + 2H^+ = H_2S + 2Cr^{3+} \tag{3.2}$$

After the first step, 30 ml Thode's solution (HI + H_2PO_3 + HCl mixture) was injected into the reaction vessel, and reacted with the sample for ~3 hours to extract any oxidised sulfur from the samples as H_2S via reaction:

$$SO_2{}^{4-} + 10H^+ + 8I^- = 4I_2 + H_2S + 4H_2O \tag{3.3}$$

The H_2S produced during the reaction was precipitated as ZnS in a separate bath of Zn-acetate solution into ZnS. Both ZnS precipitates were then mixed with $AgNO_3$ to form Ag_2S, which was then dried and weighted before combustion and analysis. $^{34}S/^{32}S$ measurements were carried out using a Thermo Finnegan Delta V Plus GS-IRMS. Blank extractions containing no sample powder were also carried out to check for any impurities in the chemical solutions used during the procedure. Blanks extractions contained <0.2 ppm sulfur, consideably less most bulk rock samples, which contained few 100 ppm S. Errors associated with the analyses are ±0.4‰(2σ).

Sulfur isotope ratios are conventionally expressed as $\delta^{34}S$ in permil relative to the Vienna Canyon Diablo Troilite standard ($^{34}S/^{32}S$ = 0.044162589, Ding et al. 2001), which is calculated as:

$$\delta^{34}S\ (‰) = ((^{34}S/^{32}S_{sample}) / (^{34}S/^{32}S_{standard}) - 1) * 1000 \tag{3.4}$$

In the following chapters S isotope ratios expressed in permil are calculated using the equation and V-CDT ratio.

Bulk sulfur contents of lava samples were measured using colorimetry. 200 μl of sample solution containing the precipitated ZnS was reacted with HCl and dimethyl-p-phenylenediamine. During the reaction methyline blue dye forms from S^{2-} containing solutions, causing a blue discolouration. The absorption of the sample at 445 nm was measured using an optical spectrometer. To convert measured absorption values into concentrations, a calibration curve was produced using Na_2S solutions with known dissolved S contents before unknown analysis.

3.2 Microbeam techniques

3.2.1 Electron probe microanalysis of glasses and minerals

Chemical analyses of crystal phases, melt inclusions, matrix glasses, and synthetic sulfur isotope glass standards used in chapter five were carried out by electron probe microanalysis (EPMA) using a Cameca SX100 instrument at the University of Manchester over several sessions between March 2017 and January 2020. All analyses were carried out using a 15 kV accelerating voltage, while beam size and beam current were varied depending on the analysed phase. I used a set of synthetic and natural minerals as primary standards, which included (elements in parentheses): pyrite (S), anhydrite (S), jadeite (Na, Al, Si), sodalite (Na, Cl), periclase (Mg), San Carlos olivine (Mg, Si), K-feldspar (K, Al), apatite (P), wollastonite (Ca, Si), rutile (Ti), V_2O_3 (V), Cr_2O_3 (Cr), tephroite (Mn), fayalite (Fe, Si), Fe_2O_3 (Fe), cobalt metal (Co), NiO (Ni). Glass and mineral reference material from the Smithsonian National Museum of Natural History were used from 2018 November onwards to monitor accuracy and inter-session reproducibility of the measurements. EPMA data including secondary standards, and analytical uncertainties, are provided as supplementary material in appendix A in a Mendeley Data folder.

Olivine compositions were analysed using a two-condition setting throughout all sessions to achieve high-precision data for trace elements while avoiding detector oversaturation for major elements. Magnesium, Fe, and Si were analysed at 3 or 5 nA beam current and a 5 μm beam diameter for 30 s. Trace elements, including Al, P, Ca, Ti, Cr, Mn, and Ni, were analysed using a 100 nA beam current and a 5 μm beam diameter. To achieve the best results for Al, at least two TAP crystals were used simultaneously for the measurements, with peak and background counting times at 120 s and 60 s, respectively. Other trace elements were measured for 30-60 s on peak. Relative uncertainties for major elements were generally below or close to 1% (1σ). Analytical uncertainty for Al in olivines was usually ~4% (1σ), similar to other trace elements. Reproducibility between sessions was monitored by repeat analyses of the San Carlos and Springwater olivine standards (Fig. 3.1).

Clinopyroxenes were analysed using either a 5 nA or 20 nA beam current and 5 μm beam diameter, using variable on peak counting times between 20-60 s. Spinels were analysed using two conditions: a 5 nA beam current and 1 μm beam diameter for major elements (Mg, Al, Ti, Fe, Cr) and a 25 nA beam current and 1 μm beam diameter for minor elements (V, Mn, Ni). Silicon was measured on peak for 20 s together with major elements to monitor any contamination from silicates during analyses. On peak counting times were between 20 and 80 s. Analytical uncertainties for major elements were usually around 1-2% (1σ), while for minor elements (such as Mn in oxides or Na in clinopyroxene) uncertainty was generally around 5-15%, depending on concentration.

Glasses were analysed using a 15 μm defocused beam. A beam current of 3 or 5 nA was used for Si, Al and Ca, and Fe to avoid detector saturation. A beam current of 20 nA was used for Na, Mg, P, S, Cl, K and Ti to achieve good counting statistics on elements <10 wt% concentration. On peak counting times were 20-80 s. Elements known to volatilise during sample-electron interaction (e.g. Na, S) were corrected for loss of signal using a time-dependent intensity correction. Analytical uncertainty using this set up was <1 wt% for Si and Mg, 1-2 wt% for Ca, Ti, and Fe K and 2-3% for

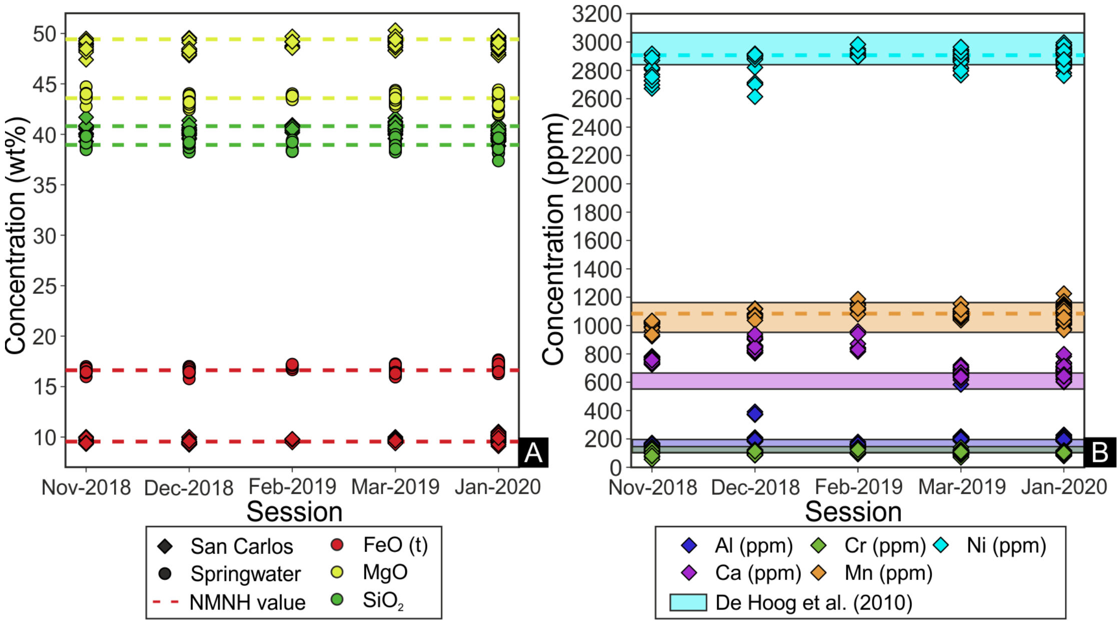

Figure 3.1: Data collected from the Smithsonian olivine standards over five EPMA sessions. Major elements from both the San Carlos and Springwater olivines are shown in (A), while trace elements measured in the San Carlos olivine are shown in (B). Al contents measured in the December 2018 session were slightly higher due to a three outlier analyses, hence olivine data from this session was not used in thermometric calculations in chapter seven. Dashed lines indicate preferred values published by the Smithsonian National Museum of Natural History. Shaded areas in (B) are trace element contents measured in the San Carlos olivine by De Hoog et al. (2010) using LA-ICP-MS and SIMS. Calcium is the only trace element not reproduced in most sessions within literature values. No accepted value or composition range is available currently for San Carlos olivine Ca content.

Na. Uncertainty in S was strongly dependent on concentration, varying between 3% for S-rich samples and 50% at just a few 100 ppm S content. Sulfur detection limit during EPMA analyses of glasses was ~50 ppm. Cl measurement errors were around 8 to 20% in glasses, with a detection limit of ~90 ppm.

3.2.2 Volatile and trace element analysis with Secondary Ion Mass Spectrometry

Water, carbon, halogen and trace element concentrations in El Hierro melt inclusions were measured using a Cameca IMS-4f secondary ion mass spectrometer (SIMS) instrument at the NERC Ion Micro-probe Facility, University of Edinburgh, using a negative ^{16}O beam with a primary beam current of 4-5.5 nA. Before analysis the beam was rastered above the measurement spot to avoid any secondary ion formation from contaminants found on the sample surface. Secondary ions were extracted using a voltage of +4500 V, minus an offset of 50 during carbon measurements and an offset of 75 during trace element and water measurements to avoid molecular interferences. Beam diameter was between 15-20 μm.

The instrument was operated in high-resolution mode during carbon measurement to separate the ^{12}C peak from the ^{24}Mg^{2+}/2 peak. Peak positions for the ^{12}C (10), ^{24}Mg^{2+}/2 (5), ^{26}Mg (2) and ^{30}Si (2) peaks were verified before every analysis (numbers in parenthesis are counting times on each peak in seconds). Each measurement comprised 10 cycles. For carbon analyses the first 4 cycles were always excluded. Relative standard deviation of the ^{12}C/^{30}Si signal was better than 5% for 97% of the analyses and between 6-13% for the remaining 3%, where C was above detection limit. The detection limit for carbon is better than 30 ppm. Data quality of the carbon measurements was monitored by a set of experimentally produced basaltic glasses (M5, M10, M40, M36. M21 and M47) and one natural MORB glass (519-4-1) with known water and carbon concentrations from Shishkina et al. (2010), while the carbon background was determined using a carbon-free glass standard (N-72), degassed matrix glasses, and measurements carried out on nominally volatile-free host crystals. Carbon calibration curves are shown in Fig. 3.2. Instrument drift was monitored by repeat measurements on the primary standards, and comparing it to literature values. Precision of CO_2 measurements is better than ±10% at low (<500 ppm) concentrations, and better than ±7% at high (>500 ppm)

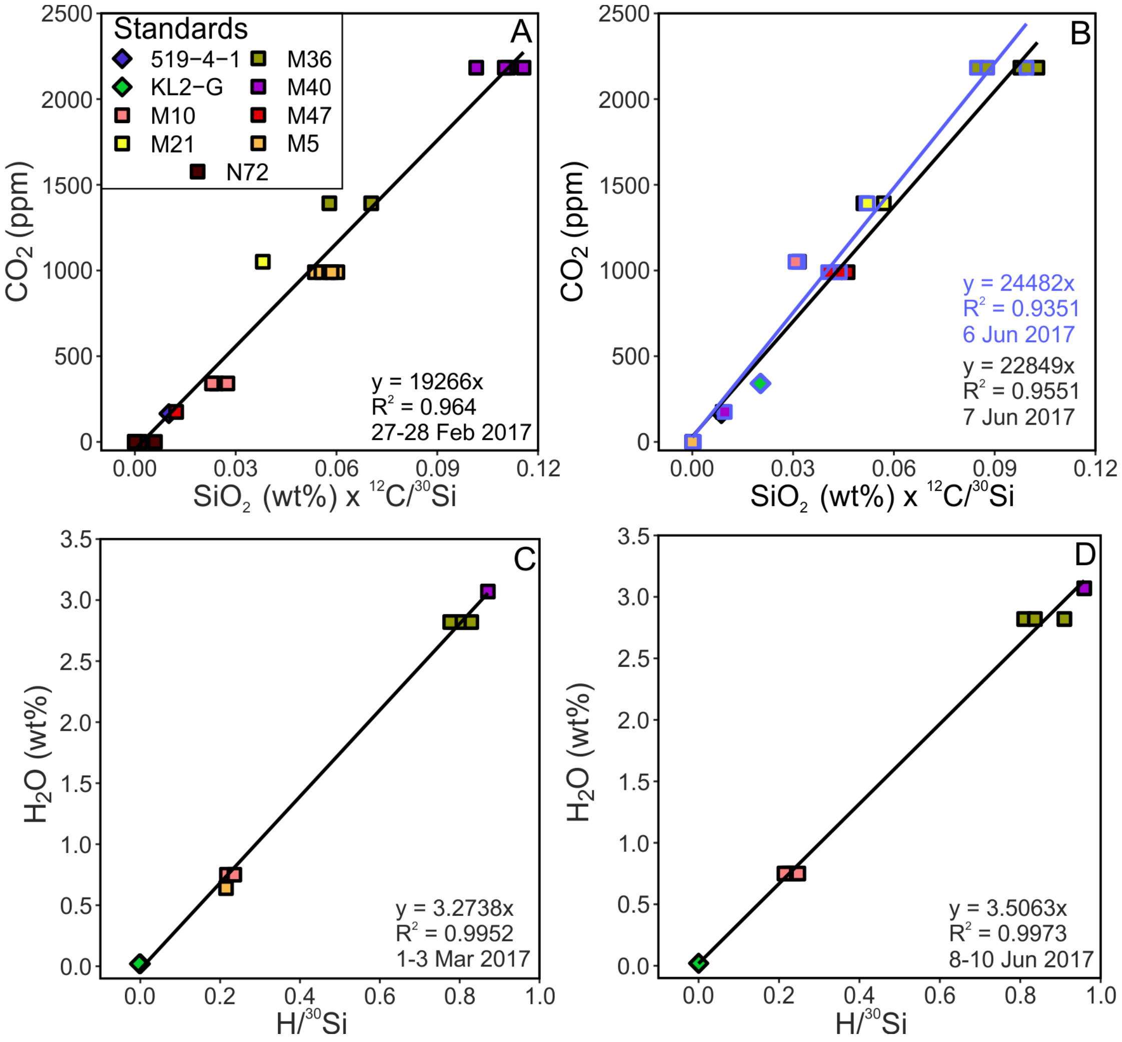

Figure 3.2: Carbon (A, B) and water (C, D) calibration curves showing known CO_2 and H_2O concentration vs. measured $^{12}C/^{30}Si$ times SiO_2 and $H/^{30}Si$ of the standard. Calibration curves are calcluiated using a simple linear regression with a fixed intercept though the origin. The above curves were used during session 1 (A, C; 27 February to 3 March 2017) and session 2 (B, D; 6-10 June 2017). Square symbols are standards from Shishkina et al. (2010); diamonds are other international glass standards whose composition can be found in the GeoRem database (http://georem.mpch-mainz.gwdg.de/). In B the two colours (blue and black) represent calibration curves used on the two different days within the same session.

concentrations. Accuracy is estimated to be better than ±10%.

Water and trace elements were measured together, in low-resolution mode. Peak positions were verified before each measurement. The following isotopes of each element were measured (counting time in seconds in parentheses): ^{1}H (4), ^{7}Li (4), ^{11}B

(4), ^{19}F (4), ^{30}Si (2), ^{35}Cl (5), ^{39}K (2), ^{47}Ti (2), ^{84}Sr (5), ^{85}Rb (5), ^{88}Sr (3), ^{89}Y (3), ^{90}Zr (3), ^{93}Nb (5), ^{138}Ba (5), ^{139}La (3), ^{140}Ce (3), ^{141}Pr (3), ^{143}Nd (3), ^{149}Sm (5), ^{151}Eu (8), ^{157}Gd (5), ^{159}Tb (5), ^{161}Dy (5), ^{165}Ho (8), ^{167}Er (8), ^{169}Tm (8), ^{171}Yb (8), ^{175}Lu (8). The background was determined by measuring masses of 0.7 (1) and 131 (3) and was shown to be negligible. Each measurement comprised six cycles. For ^{1}H only the last 4 cycles were used for quantification. Precision and accuracy of water concentrations were monitored using the same set of standards as for carbon measurements (Fig. 3.2); precision is better than ±6% for $H_2O<1$ wt% and better than ±3% for $H_2O>1$ wt%, while accuracy is ±1%. Precision and accuracy of trace elements were monitored using repeat measurements on glass standards with known composition: BCR-2G, KL-2G, T1-G and GSD-1G, while repeated analysis of the water standards M-10 and M-36 were used to monitor any changes in concentrations as a function of time during each session. The 1σ standard deviation for most trace elements is better than ±5%, while for LREE and HREE it increases to ±10% and ±15-20%, respectively. Accuracy varies between ±3-10%, with lowest values for Tb and Er. Errors for F and Cl were approximately around ±10% and ±20% respectively. However, errors for halogens are hard to evaluate during SIMS analysis, as only standards with low F and Cl concentrations were available (<400 ppm F, <100 ppm Cl). Silica contents of the glasses measured by EPMA were used as the internal reference element during the quantification of the data.

3.2.3 Determination of sulfur speciation in glasses by EPMA

The wavelength of X-rays emitted by some elements such as sulfur and iron during EPMA analysis are oxidation state dependent (Carroll and Rutherford, 1988; Fialin et al., 2001; Höfer and Brey, 2007; Hughes et al., 2018). In the case of sulfur, it has been demonstrated that a large shift in the Kα peak position occurs as a function of speciation that is thought to be linearly related to the $S^{6+}/\sum S$ ratio (Carroll and Rutherford, 1988; Wilke et al., 2011). Due to this phenomenon $S^{6+}/\sum S$ can be determined

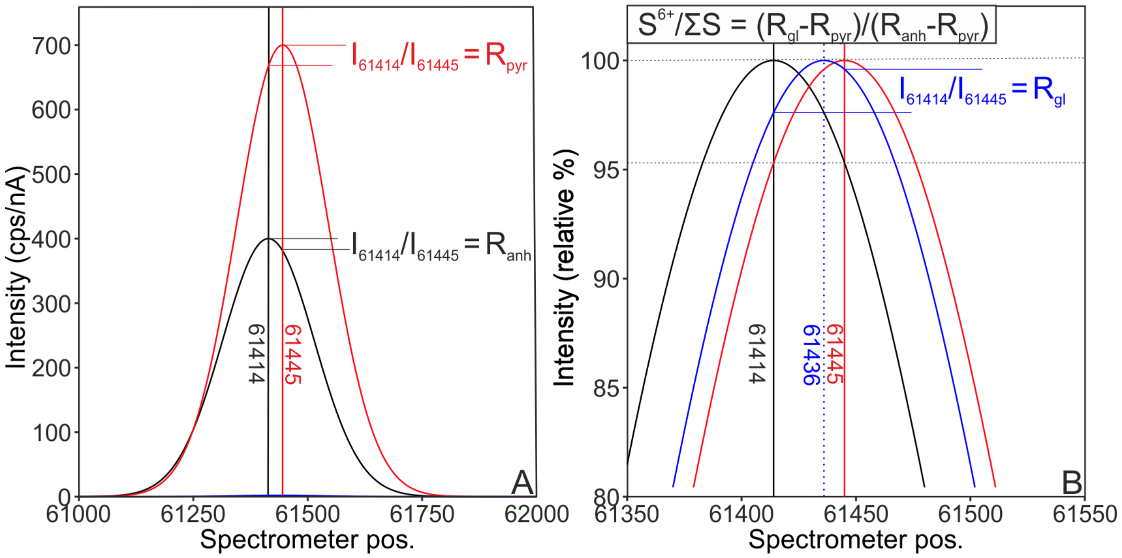

Figure 3.3: Determination of sulfur speciation by utilising the peak shift in sulfur Kα emission. In (A), idealised (i.e. perfect Gaussian distribution) peaks measured in a pyrite (red) and anhydrite (black) standards are shown, exhibiting a peak shift of 31 spectrometer units. In (B), three intensity-normalised peaks are shown: a pyrite, an anhydrite and a glass (blue). Theoretical peak maxima are also shown by the vertical lines. Measured intensities at 61414 (anhydrite maximum) and 61445 (pyrite maximum) are divided, with R_{pyr} corresponding to $S^{6+}/\sum S$ of 0 and R_{anh} to $S^{6+}/\sum S$ of 1. When a material containing both S^{2-} and S^{6+} is measured (such as the theoretical glass B), the ratio (R_{gl}) will be between R_{anh} and R_{pyr}. The difference between R_{gl} and R_{pyr} will be proportionate to $S^{6+}/\sum S$ in the glass and can be calculated using the equation in (B).

by EPMA either by scanning over the sulfur Kα peak or by fixing spectrometers at the maximum S^{6+} and S^{2-} peak positions. In the former case peak scans are carried out on both standards with known $S^{6+}/\sum S$ and unknown samples, followed by a Gaussian-peak fitting procedure on all measured peaks to determine $S^{6+}/\sum S$; in the latter method the two intensities measured on the maximum S^{6+} and S^{2-} peak positions are divided and converted to $S^{6+}/\sum S$ using the following equation:

$$S^{6+} / \sum S = (R_{gl} - R_{pyr}) / (R_{anh} - R_{pyr}) \tag{3.5}$$

where R_{gl} is the ratio of the S^{6+} peak and the S^{2-} peak in the unknown sample, R_{pyr} is the ratio of the S^{6+} peak and the S^{2-} in a pyrite ($S^{6+}/\sum S = 0$), and R_{anh} is the ratio of the S^{6+} peak and the S^{2-} in an anhydrite ($S^{6+}/\sum S = 1$; Fig. 3.3). It is noted that any other sulfide-sulfate pair may be used for this technique.

While both methods can be used in theory to determine $S^{6+}/\sum S$, the common practice is to scan over the sulfur Kα peak. However, data obtained in this thesis were obtained using the fixed peak position for the following reason: the Cameca SX100 EPMA at the Univeristy of Manchester is equipped with two LPET crystals and two PET crystals all of which are capable detecting the sulfur Kα peak, enabling the precise measurement of two sulfur peak positions and two background positions at the same time without the need of spectrometer movement during the analytical session. While this method is rarely used in the literature, it has multiple advantages: it does not require moving any parts of the instrument within the detector, changes in intensity can be monitored throughout the analysis (hence sample-beam interaction related oxidation/reduction can be detected), and is relatively rapid (~1 minute).

Chapter 4

High fluxes of deep volatiles from ocean island volcanoes: Insights from El Hierro, Canary Islands

4.1 Abstract

Basaltic volcanism contributes significant fluxes of volatiles (CO_2, H_2O, S, F, Cl) to the Earth's surface environment. Quantifying volatile fluxes requires initial melt volatile concentrations to be determined, which can be accessed through crystal-hosted melt inclusions. However, melt inclusions in volatile-rich mafic alkaline basalts, such as those erupted at ocean islands, often trap partially degassed melts, meaning that magmatic volatile fluxes from these tectonic settings may be significantly underestimated. We have measured major, trace element and volatile concentrations in melt inclusions from a series of young (<20 ka) basanites from El Hierro, Canary Islands. Our melt inclusions show some of the highest CO_2 (up to 3600 ppm) and S (up to 4290 ppm) concentrations measured in ocean island basalts to date, in agreement with data from the recent 2011-2012 eruption. Volatile enrichment is observed in melt inclusions with crystallisation-controlled major element compositions and highly variable trace element ratios such as La/Yb. We use volatile-trace element ratios to calculate original magmatic CO_2 contents up to 4.2 wt%, which suggests at least 65% of the original CO_2 was degassed prior to melt inclusion trapping. The trace element contents and ratios of El Hierro magmas are best reproduced by 1-8% partial melting of a garnet lherzolite mantle source. Our projected CO_2 (200-680 ppm) and S (265-450 ppm) concentrations for the source are consistent with upper estimates for primitive mantle. However, El Hierro magmas have elevated F/Nd and F/Cl in comparison with melts from a primitive mantle, indicating that the mantle must also contain a component enriched in F and other volatiles, most probably recycled oceanic lithosphere.

Our modelled original magmatic CO_2 contents suggest that, per mass unit, volatile fluxes from El Hierro magmas are up to two orders of magnitude greater than from typical mid-ocean ridge basalts and 1.5 to 7 times greater than from recent Icelandic eruptions, indicating large variability in the primary volatile content of magmas formed in different geodynamic settings, or even within different ocean islands. Our results highlight the importance of characterising mantle heterogeneity in order to accurately constrain both short- and long-term magmatic volatile emissions and fluxes from ocean island volcanoes.

4.2 Introduction

Volatiles (H_2O, CO_2, F, S, Cl) often constitute just a few weight percent of silicate melts, yet they impact a variety of processes in magmatic systems. In particular, volatiles strongly influence melt generation processes through changing the melting depth and degree of the source mantle (e.g. Dasgupta et al., 2007; Green et al., 2010), and also affect the order in which crystallising phases appear on the liquidus (e.g. Gaetani et al., 1993; Métrich and Rutherford, 1998).

The volatile-carrying capacity of a magma is strongly influenced by its major element composition (e.g. Dixon, 1997). Mid-ocean ridge basalts (MORB) constitute ~75% of the Earth's annual magmatic output (Schmincke, 2004) and typically contain <0.3 wt% total volatiles (Saal et al., 2002). Ocean islands basalts (OIB) represent just ~10% of erupted magmas, but as they can contain >5 wt% volatiles (Dixon et al., 1997) likely contribute disproportionately more to global volcanic gas emissions. Volatile enrichment is most prominent in trace element and radiogenic isotope-enriched (e.g. HIMU) OIBs (Cabral et al., 2014; Boudoire et al., 2018). A good understanding of the origin, storage and flux of volatiles from OIB magmas is crucial if we are to provide reasonable estimates of volcanic volatile fluxes into the environment (Burton et al., 2013).

Determining magmatic volatile contents is complicated by their low solubility in silicate melts at low pressures, with melt volatile contents being reduced by degassing as they ascend towards the surface. Formation of immiscible sulfide globules at high melt sulfur concentrations can also lower the melt sulfur content. These issues can be circumvented by measuring volatile contents in crystal-hosted melt inclusions (MIs), which are theoretically shielded from processes like crystallisation or shallow degassing from their carrier melt (e.g. Métrich and Wallace, 2008; Koleszar et al., 2009; Edmonds et al., 2013; Hartley et al., 2014; Cabral et al., 2014; Wallace et al., 2015). In practice, MI compositions are modified by post-entrapment crystallisation, diffusive re-equilibration with their external carrier melt, and sulfide formation due to melt reduction (Danyushevsky et al., 2002; Gaetani et al., 2012). These processes can often be corrected to establish original inclusion compositions (Danyushevsky et al., 2000; Danyushevsky and Plechov, 2011).

This work focuses on El Hierro in the Canary Islands, a location relatively understudied until the occurrence of a submarine eruption 2 km off the southern tip of the

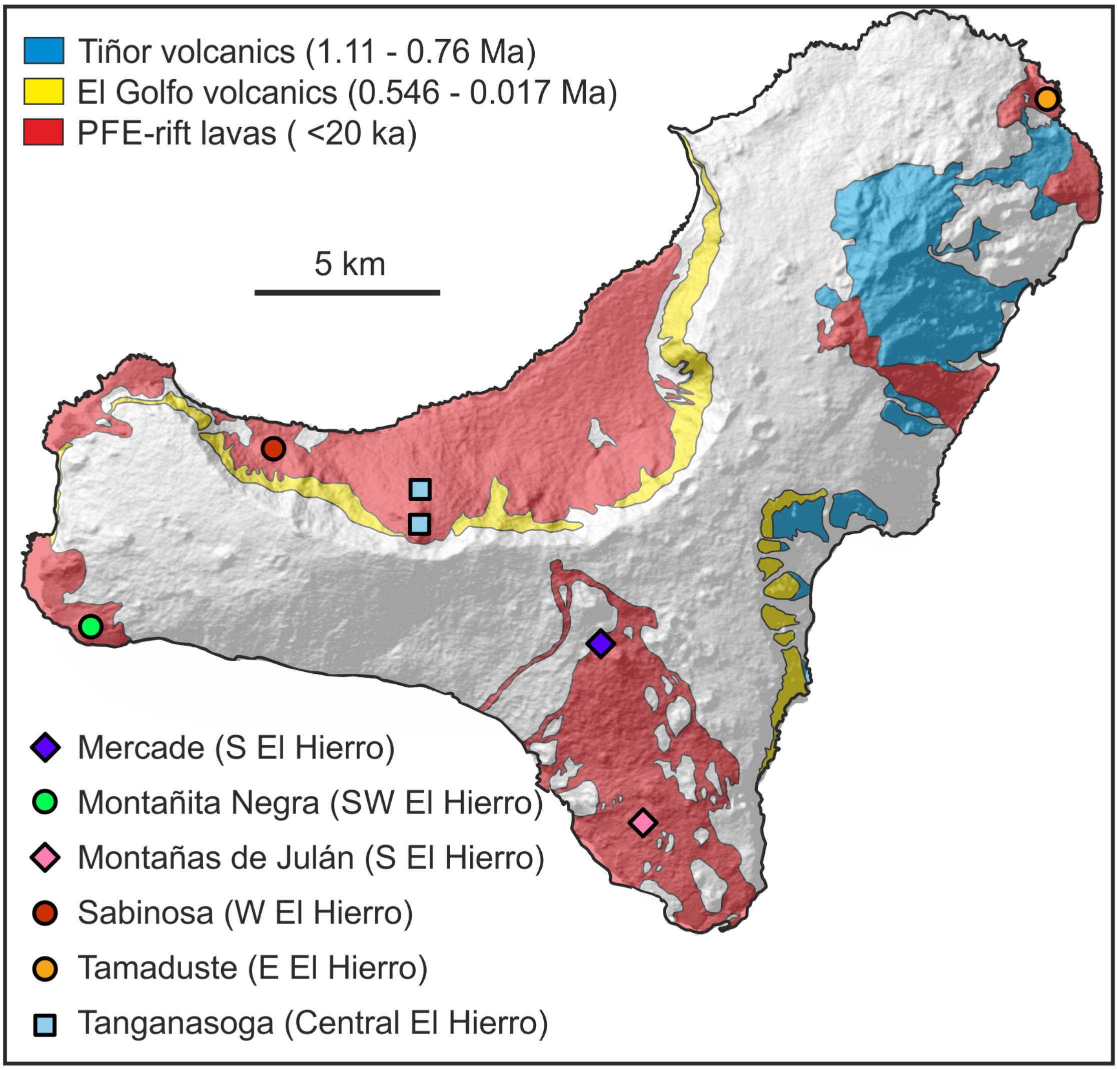

Figure 4.1: Simplified geological map of El Hierro, modified after Carracedo et al. (2001) with digital elevation model from GeoMapApp. The map shows the erupted products from the three main volcanic edifices: Tiñor, El Golfo, and the platform-forming (PFE) rift volcanics, that have built the island, and the sample locations for this study.

island, between October 2011 and March 2012. The eruption received significant attention from geoscientists due to abundant surface gas measurements and seismic data recorded pre-, syn- and post-eruption (López et al., 2012; Pérez et al., 2012; Melián et al., 2014; Klügel et al., 2015). Floating rocks collected from the ocean during the eruption enabled petrological studies of the magmatic plumbing system to infer the origin of the magma feeding the eruption (Troll et al., 2012; Martí et al., 2013a; Sigmarsson et al., 2013; Longpré et al., 2014). Volatile contents of MIs reveal that the erupted magma was one of the most CO_2- and S-enriched oceanic island basalts known to date. The estimated minimum volatile budget of the eruption is 1.3–2.1 Tg CO_2 and 1.8–2.9 Tg S (Longpré et al., 2017). However, it remains an outstanding question whether El Hierro magmas have been characterised by similar volatile enrichment over the past 20 ka.

Here we present major, trace and volatile element data from olivine- and clinopyroxene-hosted MIs from young (<20 ka) tephra samples collected from multiple locations on El Hierro. Melt inclusion compositions are discussed with an emphasis on melt genesis and evolution. Trace element data are used to identify mantle source characteristics, while volatiles combined with volatile and lithophile trace element ratios are utilised to estimate original magmatic volatile contents and the relative timing of their exsolution. The origin of volatile element enrichment in El Hierro magmas is also explored in detail. In this work, we highlight the importance of volatile-rich magmas erupting on ocean islands to both the global and local environment, and compare the volatile content of El Hierro magmas with other magmatic systems.

4.3 Samples, analytical techniques and data processing

Our samples comprise of glassy tephras collected from El Hierro pyroclastic deposits that post-date the last glacial maximum (<20000 years old, Fig. 4.1). The seven sampling locations cover all three rift systems on the island; details on sampling locations are provided in chapter two and three, while detailed petrography of lava thin sections are given in chapter seven. Tephra clasts were hand-crushed in a stainless steel mortar, and olivine crystals containing glassy melt inclusions were picked from sieved size fractions between 0.25 and 2 mm. Olivines were individually ground to expose MIs, then mounted in epoxy and polished for analysis. Clinopyroxene megacrysts >10 mm in length, collected near the summit of Tanganasoga, were cut, mounted in epoxy and polished to expose MIs.

Inclusions were typically ellipsoidal in shape, with diameters between 14 and 714 μm (mean diameter 117 μm) and had a glassy appearance (Fig. 4.2). While some inclusions only contained glass and were close to ellipsoidal (Fig. 4.2F), a number of inclusions had various phases and textural features. Some inclusion experienced crystallisation along their wall (Fig. 4.2E). Bubbles were observed in a large number of MIs: 47 MIs of the analysed 96 (52%) contained bubbles, which occupy between 0.3 and 59.2 vol% of the inclusion (Fig. 4.3). This feature indicates multiphase entrapment of melt and fluid occurred and that the magmatic system was fluid saturated during melt inclusion entrapment. Several inclusions contained crystals, generally Fe-Ti oxides, together with the glass and bubble (Fig. 4.2C). Olivine-hosted MIs from Tanganasoga ankaramites often contain abundant and large oxide crystals interpreted as "captured" crystals as their large size cannot be explained through crystallisation. Some inclusions showed patches with high reflectivity and a grainy appearance in reflected light: this may be due to polishing effects or devitrification (Fig. 4.2D). These grainy features are not present in backscattered electron images. Some melt inclusions had pointed "tails" that may indicate decrepitation occurred post-entrapment (Fig. 4.2D). Four analysed inclusions from Tanganasoga contained a sulfide globule ~2-10 μm in diameter. Such globules could form due to post-entrapment sulfide saturation after redox conditions change within the inclusion (e.g. Danyushevsky et al., 2002). Sulfides were not observed in the groundmass material. Small (<10 μm) fluid inclusions were present in some olivines. Reflected light images of most melt inclusions used in this chapter are provided in the supplementary material (chapter 4 melt inclusion images).

Trace and volatile (H_2O, CO_2, F and Cl) element concentrations in a total of 80

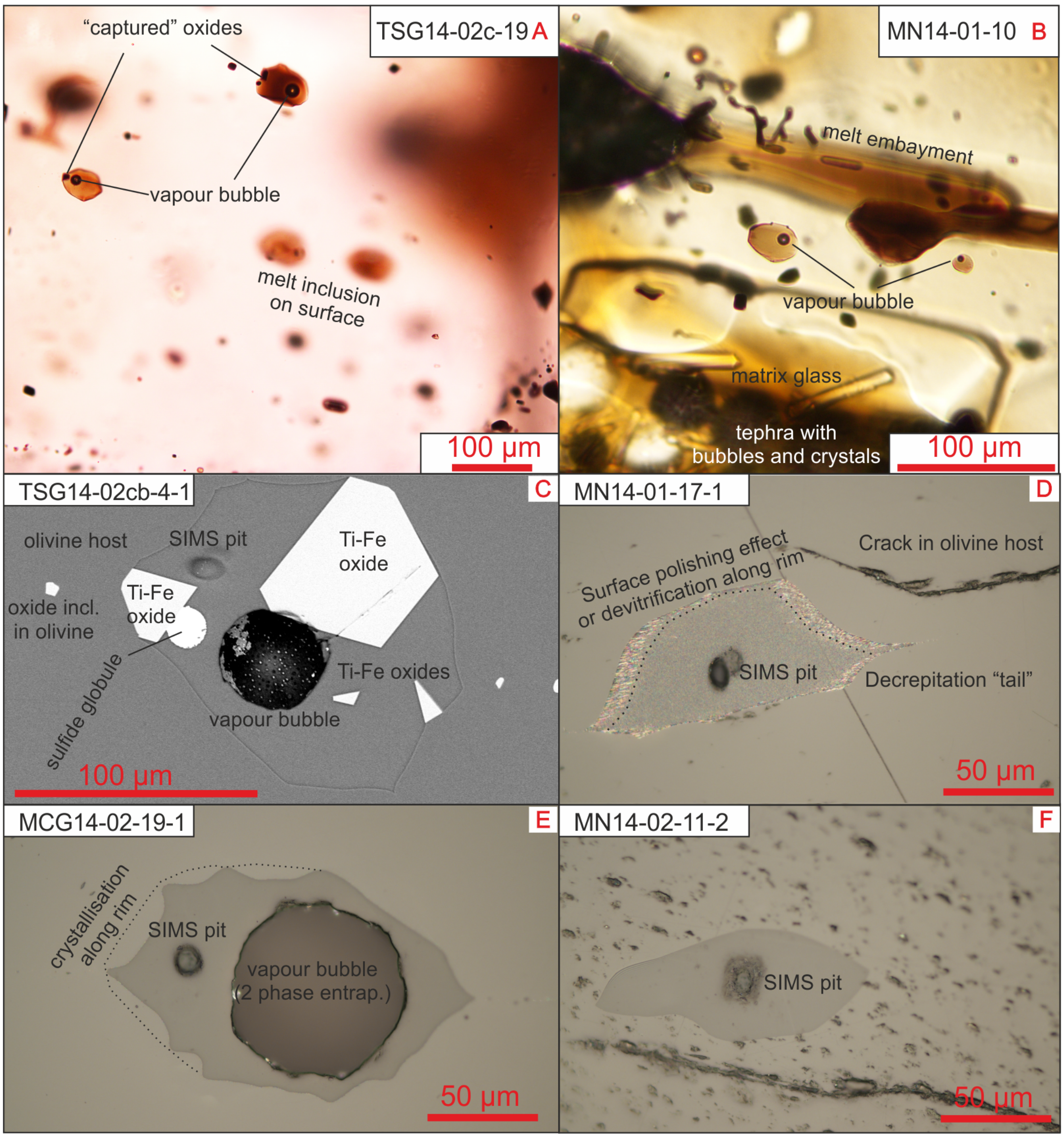

Figure 4.2: Petrographic microscope (A, B, D, E, F) and backscattered electron image (C) of melt inclusions found in El Hierro platform-forming rift tephra samples. In (A) multiple melt inclusions are shown, containing a vapour bubbles and "captured" oxide crystals that were entrapped together with the melt. In (B) a melt embayment, still connected to surrounding melt via a thin channel is shown, together with glassy melt inclusion. An opened up, polished MI is also shown in (C), containing a open vapour bubble, four Ti-Fe oxides captured together with the melt, a sulfide globule, and a SIMS analysis spot. In D, E, and F, reflected light images of MIs are shown, demonstrating various features that are characteristic of El Hierro melt inclusions, such as crystallisation along the inclusion wall, large vapour bubbles, and pointed glass "tails" that form due to inclusion decrepitation.

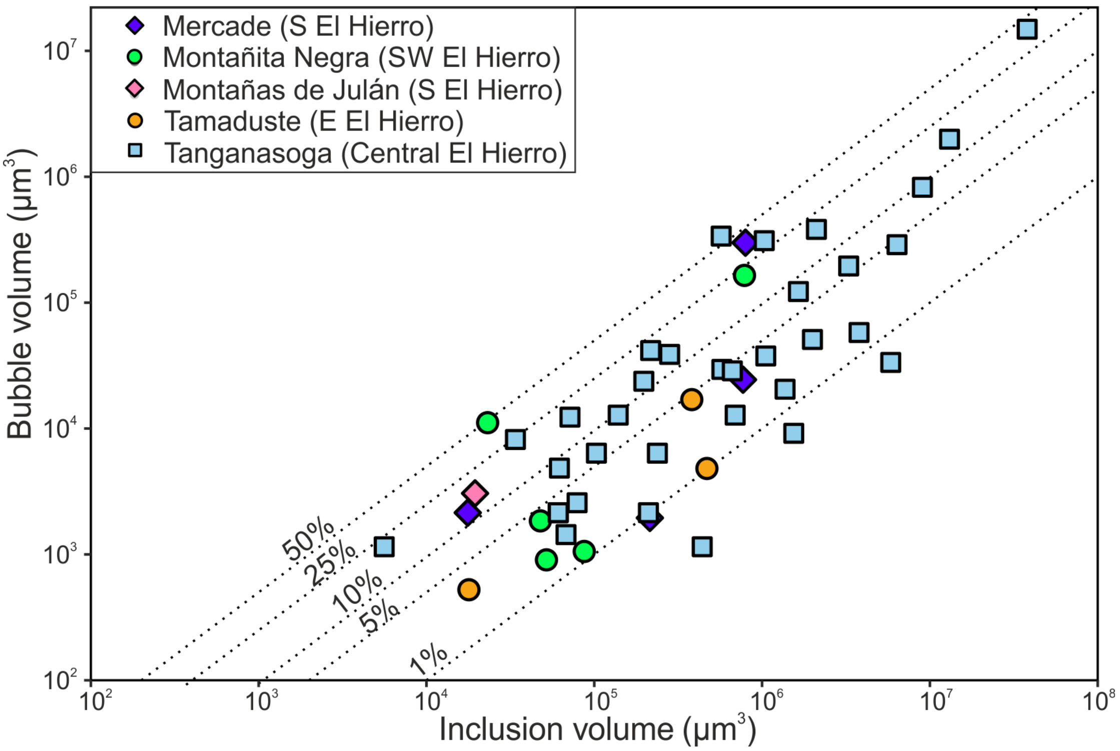

Figure 4.3: Bubble volume plotted against total MI volume (note the logarithmic scale). Dashed lines indicate constant bubble proportions of 1, 5, 10, 25 and 50%. MIs show large variation (0.3 to 59.2%) in bubble proportion, regardless of their size. The large number of MIs with large (>10%) bubble proportions provide a strong evidence that the magmatic system was volatile saturated during MI entrapment. Symbols are the same as Fig. 4.1.

olivine-hosted MIs, 10 clinopyroxene-hosted MIs, and 16 tephra glasses and embayments along crystal rims, were measured by secondary ion mass spectrometry (SIMS) using the CAMECA IMS-4f instrument at the University of Edinburgh, as described in chapter three of the thesis. Following SIMS analyses, glasses and minerals were analysed for their major, minor elements and volatiles S and Cl by electron microprobe (EPMA) using the CAMECA SX100 instrument at the University of Manchester, using analytical conditions described in chapter three. Fluorine concentrations in five MIs (covering a compositional range of 1500-2500 ppm F) were measured by EPMA at the using a Cameca SX100 EPMA at the University of Cambridge, using a large area TAP (LTAP) analysing crystal to resolve F (K_α) and Fe(L_α) lines to verify the SIMS fluorine data. EPMA and SIMS fluorine data agree within 1σ (more detail on F by SIMS and EPMA is provided in supplementary text chapter 4).

Inclusion-hosted bubbles were analysed by micro-Raman spectroscopy using a Renishaw inVia instrument at the University of Manchester. Spectra were acquired using a 514 nm laser at 50% power, with acquisition time 10 s over 10 accumulations. Of the 41 inclusion-hosted bubbles analysed, 27 bubbles in samples from Tanganasoga, Tamaduste or Sabinosa contained detectable CO_2. Raman spectra were processed by fitting Gaussian distributions to the Fermi diad peaks. Fitted peak positions were then used to determine the separation of the Fermi diad, which is proportional to the CO_2 fluid density. The CO_2 density was calculated using the calibration of Wang et al. (2011). Bubble CO_2 contents were obtained through mass balance calculations following the method of Steele-Macinnis et al. (2011) and using a melt density of 2750 kg/m^2. The CO_2-bearing bubbles occupied ≤11 vol% of their host inclusions.

4.4 Results

4.4.1 Major Elements

Measured melt inclusion compositions lie between 38.6-52.9 wt% SiO_2, 2.2-6.4 wt% MgO, 1.9-5.6 wt% Na_2O and 8.3-15.1 wt% $FeO_{(t)}$ (data are available as supplementary material). However, olivine-hosted MIs experience both post-entrapment crystallization (PEC) and diffusive Fe loss during cooling. Published whole-rock and glass SiO_2 and FeO contents from El Hierro are linearly correlated (R^2=0.938), yet measured inclusion compositions show Fe depletion up to 2 wt% relative to the FeO-SiO_2 correlation, indicative of diffusive Fe loss (Longpré et al., 2014). We used Petrolog3 (Danyushevsky and Plechov, 2011) to correct MIs for PEC and diffusive Fe loss. Calculations were performed using the olivine-melt equilibrium model of Putirka (2005) and Fe^{3+}/Fe^{2+} =

0.35, as calculated for the 2011-2012 erupted products using ilmenite-magnetite oxybarometry (Longpré et al., 2014, 2017). PEC corrections between 0 and 18.3% were required to restore inclusion compositions to equilibrium with their host olivine. The average PEC correction was 4.3%. Five olivine-hosted MIs required a PEC correction >10%. For 8 inclusions Petrolog3 predicts negative PEC values, i.e. olivine addition to the inclusion. The amount of olivine addition predicted is always <4.2%, and typically <2%, which is small in comparison to the Fe-loss correction for these inclusions. Following the PEC and Fe-loss corrections, trace element and volatile concentrations were corrected using the distribution coefficients listed in the supplementary material.

For clinopyroxene-hosted MIs, the measured Mg# of the host was generally lower than the Mg# of clinopyroxene calculated to be in equilibrium with the inclusion using $Kd^{Mg-Fe}_{cpx-liq}$=0.28 (Putirka, 2008b). Haloes surrounding the MIs were not observed in backscattered electron images, ruling out any PEC on the inclusion walls. Clinopyroxene-hosted inclusions were therefore only corrected for diffusive Fe loss.

Following PEC and Fe-loss corrections, the olivine- and clinopyroxene-hosted MIs contain 37.8-53.5 wt% SiO_2, 2.3-9.2 wt% MgO, and 8.3-15.5 wt% $FeO_{(t)}$ (Fig. 4.4).

4.4.2 Trace elements

Trace element concentrations in MIs generally fall within the range of published whole-rock compositions for El Hierro lavas (Fig. 4.5A) (Carracedo et al., 2001; Longpré, 2009; Day et al., 2010; Martí et al., 2013b). Concentrations of incompatible lithophile elements (ILE) such as Zr increase with decreasing MgO content (Fig. 4.5B). Trace element ratios cover a much wider range than previously published whole-rock and MI data: La/Yb varies between 5 and 70, and variation is high even within hosts with a narrow Mg# range (Fig. 4.5C). Inclusions from the Tanganasoga ankaramite hosted in Fo_{78-79} olivines have La/Yb between 15 and 58; this La/Yb variation is three times

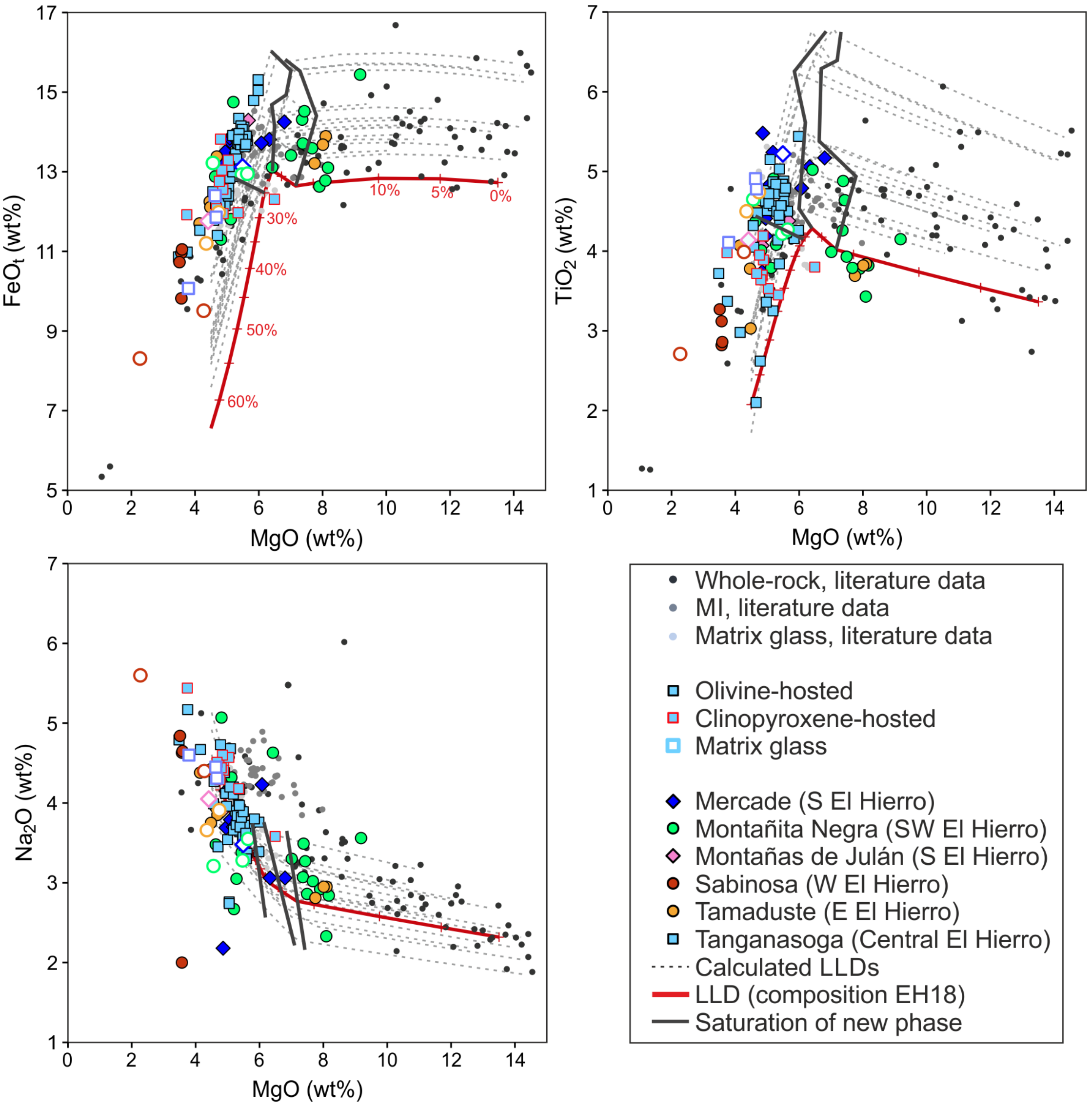

Figure 4.4: Major element composition of melt inclusions (filled symbols) and matrix glasses (open symbols), together with literature data from El Hierro (gray and black circles; Carracedo et al. (2001); Abratis et al. (2002); Stroncik et al. (2009); Longpré (2009); Day et al. (2010); Klügel et al. (2011); Martí et al. (2013a); Longpré et al. (2017)). Black dotted lines are liquid lines of descent (LLDs) calculated from primitive lava compositions from El Hierro using Petrolog3 (Danyushevsky and Plechov, 2011). The red dashed line is a LLD calculated from sample EH18 Longpré (2009), an olivine-phyric (Fo$_{90}$) alkaline basalt thought to represent a composition close to the primary melt; this sample is not thought to be affected by crystal accumulation. LLDs are calculated assuming 1 wt% initial H_2O and a Fe^{3+}/Fe^{2+} ratio of 0.35. Red crosses along this LLD represent 5% steps in crystallisation. Total crystallisation amount varies considerably between LLDs from 37% to 63%. Thin solid lines indicate the predicted positions of clinopyroxene, magnetite and plagioclase saturation on the liquidus, in order of decreasing MgO content. Symbol size is larger than the 1σ standard deviation.

larger than measured in MIs from the 2011-2012 eruption (Longpré et al., 2017). Similarly large variations in La/Yb are observed in other samples, especially those from eruption centres along the southern rift. Melt inclusions from the western rift zone are characterised by lower La/Yb between 5-27. Primitive MIs hosted in Fo>82 olivines have the most ILE-depleted compositions.

In addition to olivine-hosted MIs, we analysed 10 clinopyroxene-hosted MIs from Tanganasoga. We observe no systematic differences in the major and trace element concentrations of olivine- and clinopyroxene-hosted inclusions, although trace element ratios in clinopyroxene-hosted MIs are somewhat less variable, with 27<La/Yb<35. The small number of clinopyroxene-hosted MIs precludes statistical comparison with olivine-hosted MI, and any observed compositional differences might not persist if more clinopyroxene-hosted MIs were to be measured.

4.4.3 Volatiles

The studied inclusions have maximum glass CO_2 and S contents of 3610 ppm and 4290 ppm, respectively (Fig. 4.6). Most MIs from Tanganasoga contain >3000 ppm S. The matrix glasses contain 0-55 ppm CO_2 and 140-500 ppm S (except for one glass analysis with 1890 ppm S). H_2O concentrations vary between 0.06-2.22 wt% for MIs and 0.07-0.38 wt% for matrix glasses. Melt inclusions contain 970-3350 ppm F and 290-1500 ppm Cl. One MI has an anomalously high Cl content of 2450 ppm. Matrix glasses contain 1520-3220 ppm F and 380-1340 ppm Cl.

Of the 27 MIs containing detectable CO_2 in inclusion-hosted bubbles, nine were also analysed by SIMS. For these inclusions, it is possible to determine their total CO_2 by summing the glass and bubble CO_2 contents. The highest bubble CO_2 contents of 0.83-1.02 wt% were measured in MIs from Tanganasoga ankaramite samples; these inclusions also had the largest bubbles occupying 7.4-10.5 vol% of the inclusion. Inclusions with bubble proportions >10% likely formed due to heterogeneous trapping of melt and

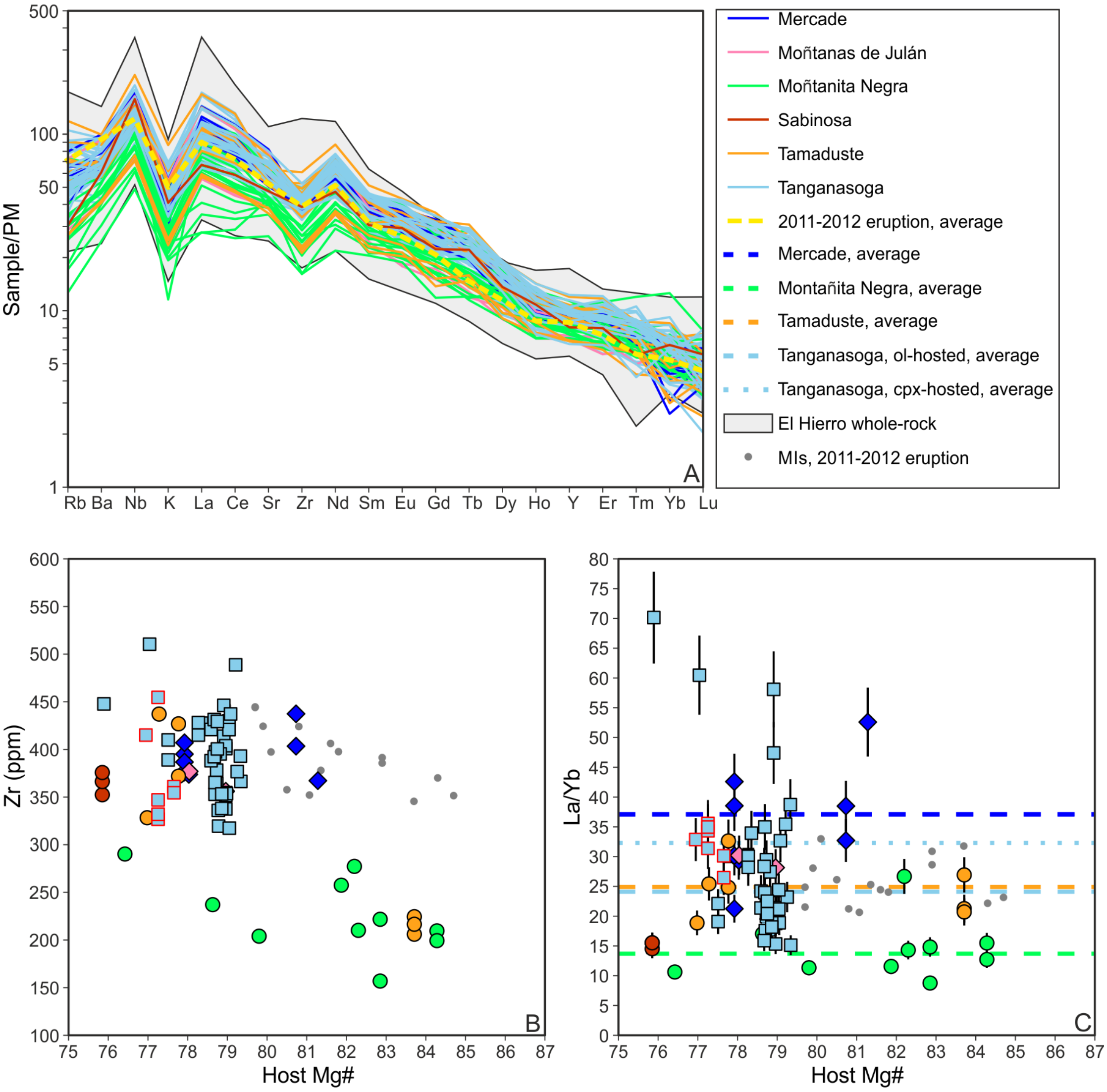

Figure 4.5: (A) Multi-element diagram for El Hierro matrix glasses and melt inclusions. Concentrations are normalised to primitive mantle (Hofmann, 1988). Samples fall within the range of previously measured whole-rock analyses from El Hierro (the grey shaded area includes alkali basalts and trachytes, Carracedo et al. (2001); Abratis et al. (2002); Day et al. (2010); Klügel et al. (2011); Martí et al. (2013a)) and show similar patterns to whole-rock samples and MIs from the 2011-2012 eruption. (B) Melt inclusion Zr and (C) La/Yb vs. Mg# of the host mineral (olivine Fo mol% or clinopyroxene Mg#). Error bars are 1σ and mostly smaller than the symbol size. The dashed coloured lines show the average La/Yb for MIs from single locations. Grey circles show MIs from the 2011-2012 eruption (Longpré et al., 2017). The broad overall increase in Zr with decreasing host Mg# is consistent with crystal fractionation, but the variation in Zr and La/Yb at constant host Mg# cannot be explained by crystallisation of a single initial melt composition. This may instead indicate that the magmatic systems beneath El Hierro is fed by variably enriched primary melts.

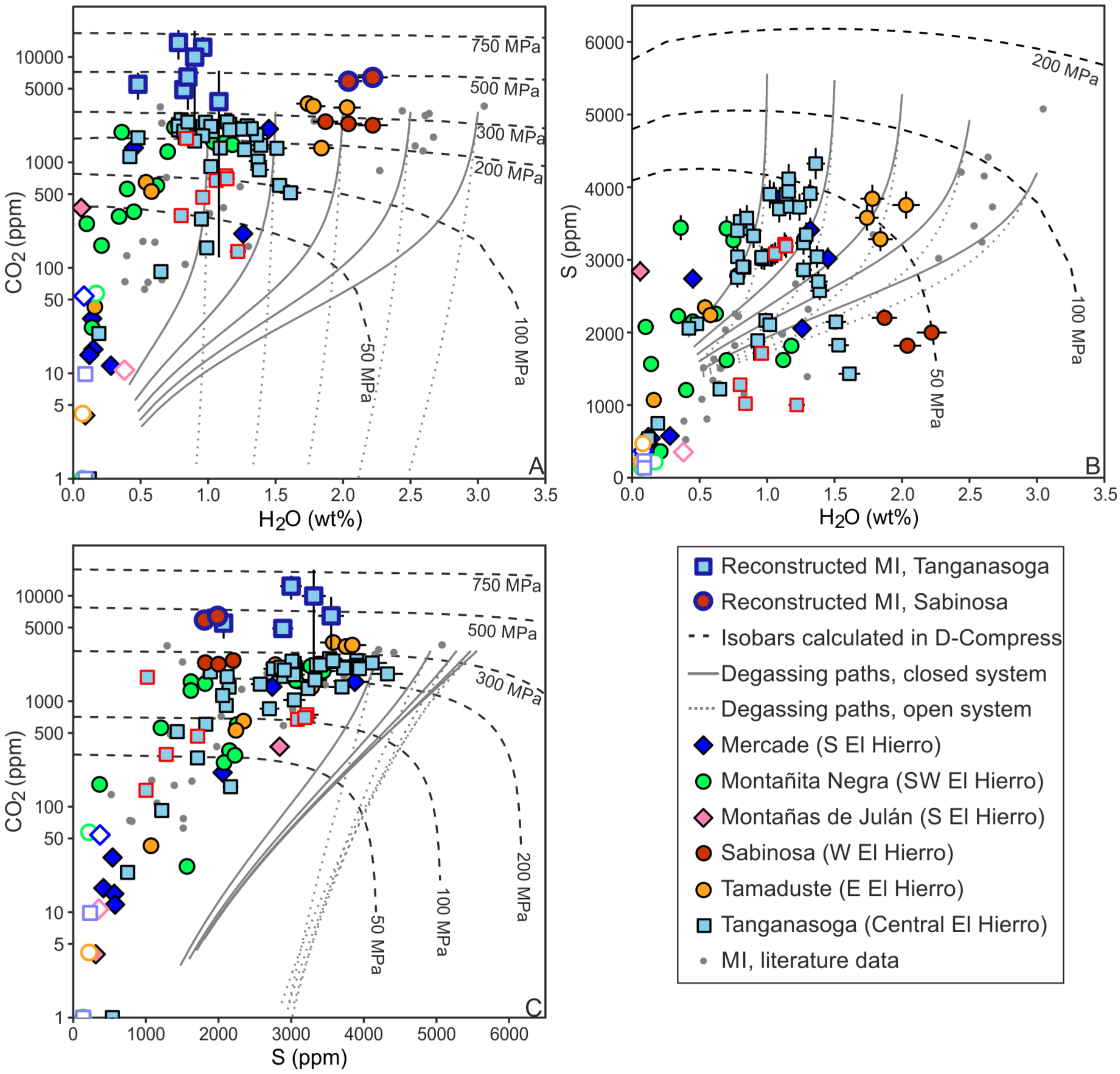

Figure 4.6: H_2O, CO_2 and S concentrations in the studied melt inclusions on CO_2 vs. H_2O (A), S vs. H_2O (B) and CO_2 vs. S (C). Literature data are MIs from the 2011-2012 eruption by Longpré et al. (2017). Dashed lines show isobars calculated for the H-C-O-S-Fe system using D-Compress (Burgisser et al., 2015). Isobars were calculated using a magma composition close to clinopyroxene saturation of the Tanganasoga ankaramite at a temperature of 1200 °C. fO_2 of ΔNNO=1.5 was used in the calculations. Degassing paths were calculated using D-Compress with the same input melt composition and temperature, a starting CO_2 of 3500 ppm, and water contents between 1 and 3 wt%. Black- and red-outlined symbols show volatile concentrations measured in the glass phase. Larger symbols with blue outlines show reconstructed total CO_2 contents, i.e. glass plus bubble. Error bars for reconstructed MI CO_2 contents are 1σ standard errors derived from the Raman peak fitting process. 1σ error bars for glass are mostly smaller than the symbol size. Volatile contents in our melt inclusions are similar to those of MIs from the 2011-2012 eruption (grey circles). Maximum volatile saturation pressures derived from glass CO_2 contents are 250-350 MPa. Using total inclusion CO_2 (glass plus bubble), maximum saturation pressures exceed 700 MPa. Isobars plotted in H_2O-S space (Fig. 4.6B) are much less pressure-sensitive, hence there are large uncertainties on their position.

fluid phases, such that their total inclusion CO_2 overestimates the true CO_2 content of the trapped melt (Moore et al., 2015; Steele-MacInnis et al., 2017). The two MIs with the largest bubble proportions have diameters <40 μm. If these MI radii are uncertain by just 10%, their calculated bubble could be reduced to 5.8-7.7 vol%, which in turn decreases their calculated total CO_2 contents by several thousand ppm. Estimation of true MI glass volumes is further complicated by the presence of included oxides. If MIs with bubbles <10 vol% are considered to represent homogeneously trapped melts, then up to 85% of the total inclusion CO_2 may be sequestered into the bubble. This is consistent with previous studies demonstrating that inclusion-hosted bubbles can sequester up to 90% of an inclusion's original CO_2 (Hartley et al., 2014; Wallace et al., 2015). Our reconstructed total CO_2 contents, i.e. glass plus bubble, in MIs with <10 vol% bubble fraction are between 3800 and 13700 ppm (Fig. 4.6). These results demonstrate the importance of CO_2 degassing into inclusion-hosted bubbles, and suggest that glass CO_2 contents measured in El Hierro MIs represent minimum melt CO_2 contents, in agreement with (Longpré et al., 2017).

4.5 Discussion

4.5.1 Crystallisation and mixing of El Hierro magmas

Melt inclusions can be trapped at any point along a crystallisation pathway. By modelling liquid lines of descent (LLDs) from primitive lavas representative of primary melt compositions, the extent of crystallisation at the time of entrapment can be determined. We used Petrolog3 (Danyushevsky and Plechov, 2011) to calculate possible LLDs for El Hierro magmas (Fig.4.4). Input starting compositions were 17 whole-rocks with MgO >10 wt% (Carracedo et al., 2001; Longpré, 2009; Day et al., 2010) that cover most compositional variation found in whole-rock data from El Hierro. Figure 4.4 shows LLDs calculated assuming an initial 1 wt% H_2O, consistent with our mean and median melt inclusion H_2O concentrations (0.9 and 0.95 wt%, respectively) and the 0.71-1.49 wt% H_2O concentrations based on clinopyroxene H_2O contents in the western Canary Islands (Weis et al., 2015). Oxygen fugacity was specified as an Fe^{3+}/Fe^{2+} ratio of 0.35 (Longpré et al., 2014, 2017). We used the mineral-melt equilibrium models of Putirka (2005) for olivine, Danyushevsky (2001) for clinopyroxene and plagioclase, and Ariskin and Barmina (1999) for magnetite. Further details of Petrolog3 calculations are provided as supplementary material.

In all calculated LLDs, the first crystallizing phase is olivine (Fig. 4.4). After 7.7–19.3% olivine crystallization, the melt reaches saturation in clinopyroxene and titaniferous magnetite. This is consistent with observed phase relations in our samples: crystals of Ti-rich magnetite are absent in MgO-rich MIs hosted in Fo>82 olivines, but are common in inclusions with $MgO \leq 6$ wt%. The calculated LLDs predict that plagioclase saturation is reached at melt MgO contents around 5-5.5 wt%. However, plagioclase is rarely present in our most MgO-poor tephra samples as a phenocryst phase, nor is it observed as an included crystal in any MI: it is mostly present as microlites in the groundmass. Plagioclase saturation is depressed to lower temperatures in melts with high H_2O contents, so it is possible that the 1 wt% H_2O assumed for our starting compositions underestimates the true H_2O content of some El Hierro primary melts (e.g. Sabinosa and Tamaduste) (Longpré et al., 2017). Using 0.5 to 2 wt% H_2O contents do not change the shape of LLDs and crystallising assemblage significantly, indicating this interval is the reasonable initial H_2O content for our crystallisation modelling.

Melt inclusion trace element contents are broadly consistent with crystal fractionation-dominated trends: concentrations of incompatible trace elements such as Zr increase with decreasing Mg# of the host mineral (Fig. 4.5B). However significant variability can be observed in the Zr content of MIs hosted crystals with similar Mg#. Large variability is observed in trace element ratios such as La/Yb, La/Y, Sm/Yb and Nb/Zr, both within individual samples and between samples from different eruptions (Fig. 4.5C), even though these ratios are not expected to vary significantly during crystal fractionation. Melt inclusions from Montañita Negra and Tamaduste show no significant variation in La/Yb as a function of olivine Fo content (Fig. 4.5C), as expected during crystal fractionation. The large variation in La/Yb (15-58) in Tanganasoga MIs is less straightforward to explain. Our data do not provide conclusive evidence that this variation is caused by mixing of magmas with differing La/Yb accompanied by crystallisation, since we do not observe decreasing variability in La/Yb with decreasing host Fo content: instead, the Tanganasoga MIs are largely restricted to host olivine compositions of $Fo_{79\pm1}$. A single crystallizing magma cannot explain the observed trace element ratio (La/Yb, La/Y, Sm/Yb and Nb/Zr) variations; it points to heterogeneity in mantle source composition or variations in melting degree, both of which can cause variation in La/Yb (these topics are discussed later in the chapter). We propose that the Tanganasoga MIs represent multiple magma batches, with each representing melts that were formed by variable melting degrees or originate from a heterogeneous mantle source. These magma batches were stored separately and were mixed just only together prior to eruption. In this scenario the most enriched and depleted endmembers must have La/Yb>50 and La/Yb<15 respectively, and similar major element compositions, since the Tanganasoga olivines are relatively uniform in composition and show no chemical zonation. Variations in melt inclusion La/Yb could also be achieved through restricted mixing between melts already stored in a chamber and new intruding batches of melt. A third possibility is that part of the Tanganasoga crystal cargo was entrained from one or more mush zones whose crystals trapped MIs with different La/Yb to the Tanganasoga carrier melt.

Magma storage depths of 10-30 km have been calculated using clinopyroxene-liquid thermobarometry on samples from the 2011-2012 eruption and dredged rock samples along the rift axis (Stroncik et al., 2009; Longpré et al., 2014; Klügel et al., 2015). These depth estimates suggest a vertically extensive magma storage system beneath El

Hierro: a suitable environment for magmas to evolve separately with little mixing. We suggest that the Tanganasoga magmatic plumbing system comprises multiple interconnected sills over a depth range of ~10-15 km, and that mixing between melts stored in these reservoirs, and possibly crystal entrainment, could reproduce the trace element characteristics observed in Tanganasoga MIs.

4.5.2 Volatile budget and degassing of El Hierro magmas

The presence of large bubbles (>10 vol.%) within our MIs suggest trapping from volatile-saturated melts. We used D-Compress (Burgisser et al., 2015) in the C-S-O-H-Fe system to calculate MI volatile saturation pressures. D-Compress requires oxygen fugacity as an input parameter, so it should be suitable for calculating volatile solubility in relatively oxidised alkaline melts. The isobars shown on Fig. 4.6 were calculated at 1200 °C using a melt composition representing the Tanganasoga ankaramite at clinopyroxene saturation. We assumed an fO_2 of ΔNNO=1.5 at 300 MPa and 1200 °C, based on the fO_2 estimate of Longpré et al. (2014, 2017). Isobars calculated using the most primitive and most evolved MI compositions differ by less than the 1σ analytical uncertainty on the measured MI H_2O and CO_2 contents.

Taking only glass CO_2 contents into account, the highest calculated volatile saturation pressures are between 150-355 MPa for individual samples. For MIs where both glass and bubble CO_2 contents were measured, calculated pressures using the total inclusion CO_2 reach 350-700 MPa (Fig. 4.6A, C). Applying the pressure-depth conversion of Longpré et al. (2014), these values corresponds to depths of 6-13 km (glass only) and 13-24 km (glass+bubble), respectively. These volatile saturation pressures should be regarded as minima, since the glass CO_2 content does not take into account any CO_2 degassed into a vapour bubble after inclusion trapping. Pressures calculated using the total CO_2 contents are consistent with both clinopyroxene-liquid barometry (400-900 MPa) and with fluid inclusion data (300-500 MPa) from previous studies (Hansteen et al., 1998; Stroncik et al., 2009; Longpré et al., 2014; Klügel et al., 2015). These pressures likely represent the main magma storage system beneath El Hierro.

D-Compress predicts sulfur solubility in the El Hierro melts to be up to 0.6 wt% at 200 MPa, and 1.1 wt% at 750 MPa, meaning MIs are unlikely to have experienced extensive S degassing. Our D-Compress calculations predict that MIs were trapped from melts dominated by S^{6+} rather than S^{2-}, consistent with the high melt inclusion S contents. Very few MIs contained sulfides (~ 4%), and sulfides were not observed in the tephra groundmass. No strong correlation is present between FeO and S content in MIs, and there is no difference between the S content of sulfide-bearing and sulfide-free inclusions. We suggest that inclusion-hosted sulfides could be formed after trapping, in response to decreasing sulfur solubility during diffusive Fe loss (Danyushevsky et al., 2002), or due to a decrease in MI fO_2 as a result of lattice diffusion and loss of Fe^{+2} via the host olivine (Gaetani et al., 2012).

The Tanganasoga melt inclusions show near-constant H_2O contents that do not decrease with decreasing sulfur (Fig. 4.6B). These near-uniform water contents suggest that diffusive re-equilibration has occurred between MI and the external melt, via H^+ diffusion through the host olivine. This process occurs on timescales of hours to days at magmatic temperatures (Gaetani et al., 2012). The H_2O contents of Tanganasoga MIs, and possibly those from other eruptions, likely record the water content of the pre-eruptive magma rather than their original trapped water contents (Hartley et al., 2015).

The observed H_2O-CO_2-S variations in El Hierro MIs are broadly consistent with calculated closed-system degassing pathways (Fig. 4.6A, C). There is a near-constant offset of ~1500 ppm S between the modelled degassing curves and our measured melt inclusion S contents (Fig. 4.6C): this may be an artefact of the D-Compress model, which predicts melt sulfur contents up to 2000 ppm higher than other volatile saturation models such as SolEx Witham et al. (2012). Matrix glasses contain <500 ppm S, indicating 85-90% is degassed during ascent and eruption.

Volatile-trace element ratios of an undegassed melt such as CO_2/Ba or CO_2/Nb are not expected to vary during melting or crystallisation, meaning that Ba and Nb can be used as proxies for the original melt CO_2 content (Saal et al., 2002; Rosenthal et al., 2015). Undegassed OIBs are expected to have CO_2/Nb=505±168, and CO_2/Ba=133±44 (Rosenthal et al., 2015). Our MIs have glass CO_2/Nb values <48 and CO_2/Ba<10 (Fig. 4.7A). Using reconstructed total CO_2, CO_2/Ba and CO_2/Nb increases to 9-31 and 51-181, respectively. We suggest that even reconstructed MI CO_2 contents represent a partially degassed melt. Exsolution of CO_2-rich fluid likely started at pressures >1 GPa, significantly deeper than melt inclusion trapping (Longpré et al., 2017; Boudoire et al., 2018). Assuming a primary melt CO_2/Ba of 89 and using the OIB mantle CO_2 content (600 ppm) of Rosenthal et al. (2015), we calculate that our inclusions represent melts that degassed at least 65% of their original CO_2. Using a CO_2/Nb instead of CO_2/Ba increases our estimate of pre-entrapment CO_2 degassing to >80%.

Several inclusion-hosted bubbles that occupied a large volume fraction (>10%) of the inclusion, therefore likely formed due to heterogeneous trapping of a fluid and a melt rather than by simple shrinkage (Steele-MacInnis et al., 2017), did not contain detectable CO_2. We suggest empty bubbles are formed due to MI decrepitation, whereby the fracturing of the host mineral causes loss of the vapour phase. Decrepitation is induced when internal MI and external melt pressure difference exceeds ~200 MPa (Maclennan, 2017), promoted by rapid magma ascent and low PEC. We suggest that the preservation of CO_2-rich bubbles in MIs from Tanganasoga, Sabinosa and Tamaduste could reflect relatively slow magma ascent or long residence times accompanied by cooling, which provides sufficient time for PEC to maintain the inclusion internal pressure below the decrepitation threshold. At other locations, faster magma ascent may have induced decrepitation, leading to CO_2 loss from the bubbles. Longpré et al. (2017) favoured CO_2 loss through decrepitation to explain low volatile saturation pressures (<260 MPa) for olivine-hosted MIs from the 2011-2012 eruption. We suggest that the

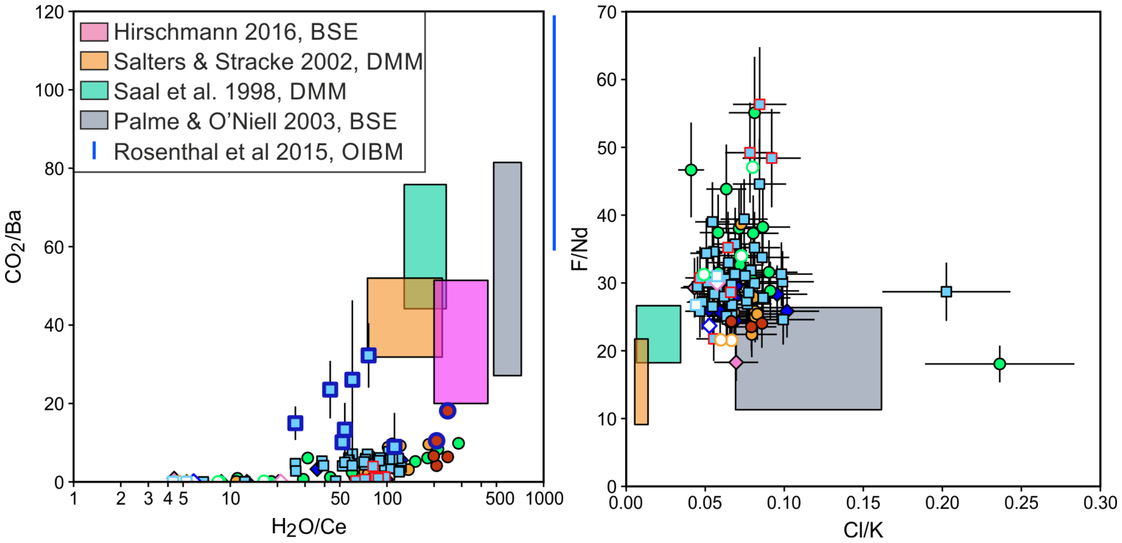

Figure 4.7: Volatile/trace element ratios of melt inclusions: (A) CO_2/Ba vs. H_2O/Ce (note the $\log_{10}$ x-axis), and (B) F/Nd vs. Cl/K. Symbols are the same as in Fig. 4.6. Literature estimates of volatile concentrations in primitive mantle (PM) and depleted MORB mantle (DMM) are taken from Saal et al. (2002), Palme and O'Neill (2003), Salters and Stracke (2004), Rosenthal et al. (2015) and Hirschmann (2016), while trace element concentrations are from Palme and O'Neill (2003) and Salters and Stracke (2004). Rosenthal et al. (2015) did not estimate mantle water concentrations; hence we show their CO_2/Ba range as bar outside of the x-axis instead of a field in (A). Error bars are 1 σ. All the El Hierro melt inclusions have lower CO_2/Ba than would be predicted for melts derived from a PM source. Melt inclusions have Cl/K just below the expected range for PM, but have elevated F/Nd compared to both DMM and PM. This could indicate the presence of a high-F/Cl component in the mantle source.

2011-2012 eruption and those of the Montañita Negra and Mercade cinder cones experienced similar magma ascent rates.

Melt inclusions and matrix glasses have very similar F and Cl contents, suggesting that the melts experienced minimal halogen degassing. Furthermore, the MIs have F/Nd and Cl/K (Nd partitions similarly to F during fractionation, while Cl partitions similarly to K Saal et al. 2002) either above or within the expected ranges for primitive mantle-derived melts (Fig. 4.7B). It has been suggested that fluorine in MIs is susceptible to diffusive re-equilibration with the surrounding melt (Koleszar et al., 2009; Le Voyer et al., 2014); however, reheating experiments do not appear to influence melt inclusion F contents (Portnyagin et al., 2008; Bucholz et al., 2013). Fluorine diffusivity in olivine has not been precisely measured, so we cannot calculate the possible effects of diffusive F exchange between our MIs and their carrier melts. However, we can rule out F enrichment through trapping of incompatible-enriched boundary layers: boundary layer effects are thought only to affect MIs smaller than 20 μm (Danyushevsky et al., 2002), and we observe no systematic change in F content as a function of inclusion size. The consistency between MI and matrix glass F/Nd values, and the fact that F and Cl are positively correlated, leads us to conclude that F concentrations in our MIs have not been modified by diffusion above analytical uncertainty.

4.5.3 Trace element characteristics of the El Hierro mantle

Canary Island magmas have been suggested to originate from a mantle source that is heterogeneous on the scale of the archipelago, with melting in asthenospheric and lithospheric mantle domains (Hoernle and Schmincke, 1993b; Lundstrom et al., 2003). Stable and radiogenic isotopic data from whole-rock samples suggest the presence of lithological heterogeneities beneath La Palma and El Hierro in the form of recycled oceanic crust and lithosphere (Day et al., 2010; Day and Hilton, 2011).

While whole-rock samples represent the mixed average composition of melts supplied to a magmatic system, melt inclusions may preserve records of diverse mantle-derived melts. To explore the significance of trace element variability of our MIs, we carried out melting calculations using various mantle source compositions (Fig. 4.8), including the primitive mantle (PM) estimate of Hofmann (1988). We then calculated possible enriched mantle compositions by adding an eclogite-derived melt to this PM composition. Eclogite represents a subducted oceanic crustal component in the source, and acts as a Si- and trace element-enriched metasomatising agent. Our eclogite-derived melt represents 15% melting of the median eclogite composition of Barth et al. (2001). This melt was mixed into a PM matrix in proportions of 5 and 10%. We assume that mixing occurs in a chemically closed system and that all melt reacts with peridotite to

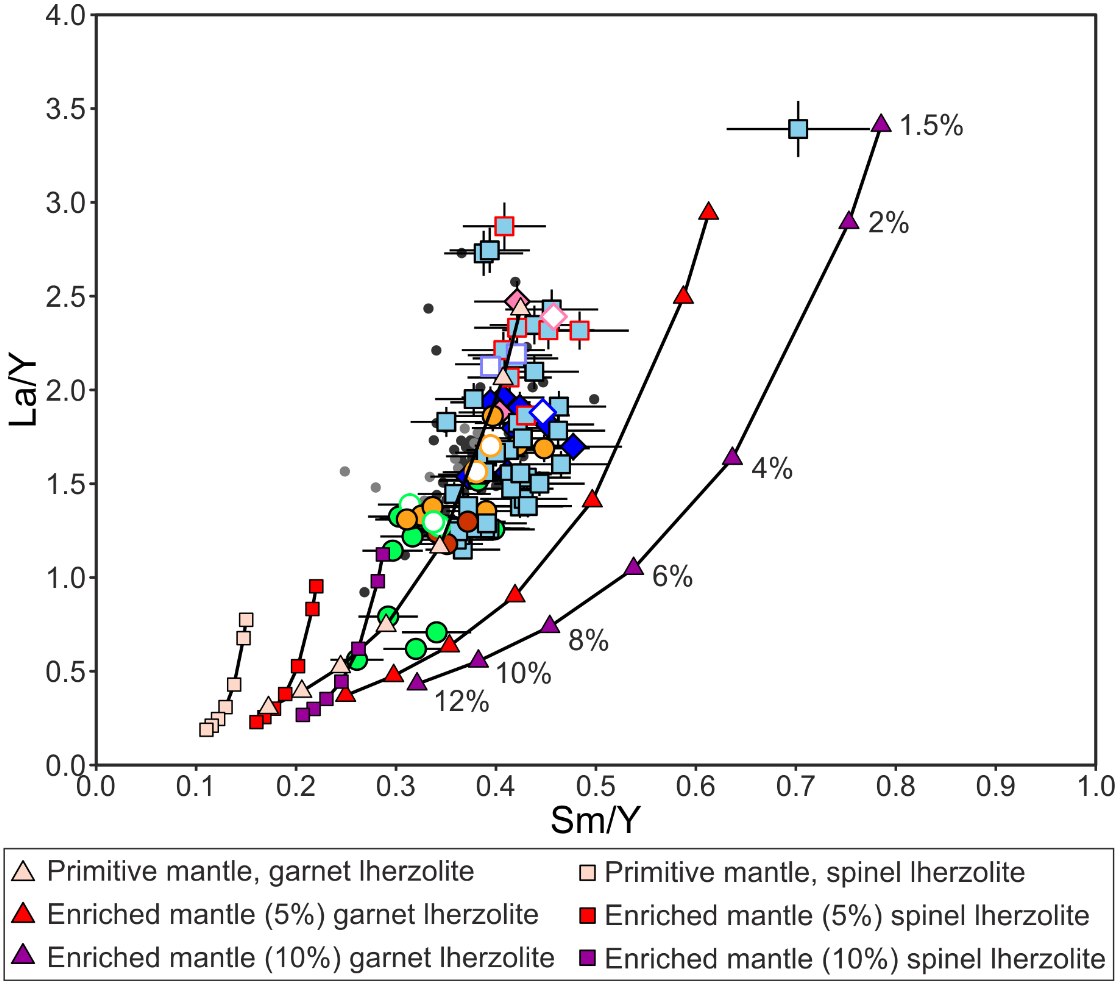

Figure 4.8: Mantle melting models compared with our MI dataset and whole-rock samples and melt inclusions from the 2011-2012 eruption, shown on a La/Y vs. Sm/Y diagram. Melt inclusions and literature data are shown using the same symbols as Fig 4.4. The primitive mantle (PM) composition is from Hofmann (1988). Enriched mantle compositions were calculated by adding 5 and 10% eclogite-derived melt to PM. Symbols on the model curves indicate the partial melt fraction (same fractions for every curve). Most El Hierro whole-rock and melt inclusion compositions fall along the garnet-bearing primitive mantle source curve. This indicates melting depth is restricted to <80 km, i.e. below the garnet-spinel transition, which is in accordance with the presence of a >90 km-thick Jurassic lithosphere beneath the island (Fullea et al., 2015).

form orthopyroxene from olivine. Detailed derivations of the enriched mantle compositions are provided as supplementary material.

Our calculations suggest that the trace and rare earth element (REE) contents and ratios of El Hierro MIs are best explained by 1-8% melting of a garnet lherzolite with composition close to PM (Fig. 4.8). Apart from one inclusion, all our data fall along the PM melting curve, or within the range covered by the PM and the 5% enriched mantle melting curves. The outlier MI is extremely depleted in heavy REEs and Y, and falls between the 5 and 10% enriched garnet lherzolite melting curves. Enriched spinel lherzolite-derived melts could match the compositions of some inclusions from Montañita Negra, but do not reproduce the compositions of any other samples. Our calculated melting degrees are lower than for Hawaiian alkaline basalts (8-12%; Feigenson et al. (2003)), which could reflect lower mantle temperatures in the Canary Islands compared to Hawaii (Herzberg and Asimow, 2008). Our melting degrees are more comparable to continental alkaline basalts (e.g. McGee et al., 2013). As melting seems to be restricted to the garnet stability field, it likely occurs below the spinel-garnet transition at 2.5 GPa (80 km at 1450 °C, Klemme and O'Neill (2000). This is consistent with melting of an asthenopheric source below >90 km-thick Jurassic lithosphere (Fullea et al., 2015), and is similar to previous estimates of melting depths beneath the western Canary Islands (Day et al., 2010). It is also consistent with the ~2-6% melting of a PM-dominated source (Day et al., 2010), with possible contribution from carbonated peridotites, suggested to explain the melt volatile systematics of the 2011-2012 eruption (Longpré et al., 2017). The 1-8% variability in melting degree either reflects minor variations in temperature in the source (mantle potential temperatures for the Canary Islands are estimated around 1420-1480 °C; Herzberg and Asimow 2008), or slight changes in mantle lithology, for example varying amounts of recycled lower lithospheric mantle (more refractory), primitive mantle, and recycled altered oceanic crust or uppermost oceanic mantle (more fusible).

4.5.4 Volatile characteristics of the El Hierro mantle

Determining the volatile element character of the source region of basalts is challenging. Both CO_2 and H_2O in our MIs have been modified through degassing, decrepitation and/or diffusion. However, the Ba concentrations of the most primitive MIs can be used alongside published CO_2/Ba values for the primitive mantle to estimate undegassed carbon contents for the primary magmas. We used three estimates of primitive mantle carbon content (241 ppm, Hirschmann 2016; 600 ppm, Rosenthal et al. 2015; 2803 ppm, Marty 2012) and calculated melting curves for these compositions (Fig. 4.9). We then selected the MIs with the highest MgO and lowest ILE concentrations from each sample, and used source CO_2/Ba estimates of 40, 60, 80 and 100 (lighter to darker colour circles in Fig. 4.9) to estimate a range of potential original magmatic CO_2 contents. Minimum and maximum initial CO_2 contents for El Hierro magmas are estimated at 0.9% and 4.2% respectively. These values correspond to mantle CO_2 between 203 and 675 ppm, similar to estimated carbon contents for OIB mantle (Rosenthal et al., 2015) and bulk silicate Earth (Hirschmann, 2016). Using the reconstructed MI CO_2 contents together with CO_2 melting models (Fig. 4.9), a more conservative estimate of 120-300 ppm source CO_2 is derived, which also overlaps with the Hirschmann (2016) estimate (Fig. 4.9).

Our magmatic CO_2 estimates of 0.9-4.2 wt% indicate that a typical El Hierro eruption would emit 9-42 g CO_2 per kg of erupted magma. This is up to two orders of magnitude larger than the estimate for MORB magmas (0.27-3.9 g/kg, Cartigny et al. (2008)), and also larger than the 5.7 g/kg calculated for the 2014 Holuhraun eruption (Bali et al., 2018) or the 7.5 g/kg for the 1783 Laki eruption (Hartley et al., 2014), Iceland. However, it is comparable to the estimates of 3.5±1.4 wt% CO_2 (21-49 g/kg) for Piton de la Fournaise, Réunion (Boudoire et al., 2018). These results emphasise that volatile emissions from volcanoes are not uniform globally: relatively smaller systems, such as ocean islands with enriched mantle source signatures (e.g. Canary Islands, Cape Verde, Cook Islands, St. Helena, Azores) can contribute disproportionately more to global CO_2 fluxes than their size would indicate.

If we assume that the sulfur contents of the most primitive MIs (Fig. 4.6) represent undegassed melts, then the primary melt is estimated to contain 3500-4500 ppm S. This melt S content can be modelled by 2-8% melting of a mantle with 265-450 ppm S, if a bulk distribution coefficient $D^{S}_{peridotite/melt}$ = 0.062 is used; similarly to CO_2 and Ba or Nb, S is thought to behave similarly to Dy during magmatic processes (Saal et al., 2002).). This value is calculated assuming S has distribution coefficients similar to Dy in olivine, orthopyroxene and clinopyroxene (McKenzie and O'Nions, 1991), and is incompatible (D=0.001) in garnet. We note that mineral/melt partitioning is unlikely to dictate S behaviour during melting, which is more likely controlled by the availability of accessory sulfides and oxygen fugacity. A lower estimate of 240-340 ppm S in the source mantle can be calculated from the highest S/Dy measured in the MIs (370-530) and assuming a Dy concentration of 0.6378 ppm (Hofmann, 1988). Most estimates of primitive mantle sulfur fall between 120 ppm and 310 ppm (Palme and O'Neill, 2003; Lyubetskaya and Korenaga, 2007), while DMM contains around 90-150 ppm S. Our calculations suggest that the El Hierro mantle source represents the S-rich end of primitive mantle estimates, or could be even more enriched.

Our melt inclusion Cl/K values of 0.04-0.10 are consistent with melts derived from a primitive mantle source, which are expected to have Cl/K=0.11±0.05 Palme and O'Neill (2003). However, our MI F/Nd values of 18-57 are higher than the 19±7 expected for primitive mantle-derived melts (Palme and O'Neill, 2003). Assuming K=258 ppm and Nd=1.19 ppm for the primitive mantle (Hofmann, 1988), we calculate F and Cl concentrations of 20-67 ppm and 13-26 ppm, respectively, for the El Hierro mantle source.

Volatile recycling beneath the western Canary Islands

Our data demonstrate that El Hierro eruptions are fed by magmas that are C-, S- and F-rich in comparison with other oceanic islands like Hawaii (Moussallam et al., 2016; Anderson and Poland, 2017), and have volatile concentrations that closely resemble magmas erupting at intra-continental rift settings such as Erebus or the East African rift system (Oppenheimer et al., 2011; Moussallam et al., 2014; Hudgins et al., 2015).

Our calculated F content for the El Hierro mantle source, 20-63 ppm, is elevated compared to primitive mantle. This F enrichment is accompanied by relatively low source Cl of 13-26 ppm, which rules out crustal or seawater assimilation. We suggest that the F enrichment is best explained by the presence of a recycled crustal component in the source. This is in accordance with previous results from HIMU-type OIBs from the Pacific Ocean (Cabral et al., 2014) and from the Azores (Rose-Koga et al., 2017), where elevated F/Nd in MIs was interpreted as a signature originating from recycled material in the mantle source. Subducting slabs tend to retain most of their F during dehydration, while Cl is fluid-mobile and is typically lost to escaping fluids (Kendrick et al., 2014). Recycled lithospheric components in the mantle should therefore have high F/Cl, which is then reflected in melts produced from this lithology. The sulfur concentration in the mantle source might be less important than fO_2 in controlling melt sulfur contents. El Hierro magmas have been suggested to be more oxidised than typical OIB mantle (Longpré et al., 2014, 2017), which could be a key factor in controlling the S content of the primitive melts.

Our upper estimate of 675 ppm CO_2 in the El Hierro mantle falls within the 600±200 ppm estimated for an OIB mantle source (Rosenthal et al., 2015). However, our estimate of mantle carbon is based on CO_2/Ba ratios of 40-100 in the source, lower than the CO_2/Ba of 133±44 suggested by Rosenthal et al. (2015) for OIB mantle. It is therefore possible that the El Hierro mantle could be significantly enriched in carbon. Excess carbon could originate from recycled subducted components, which would be consistent with Os and O-isotopic data indicating the presence of altered basalts and gabbros in the source region beneath the western Canary Islands (Day et al., 2009). Carbon could be present in the source mantle as recycled carbonates like magnesite or Ca-rich dolomites, which have been suggested to be stable during slab subduction (Dasgupta

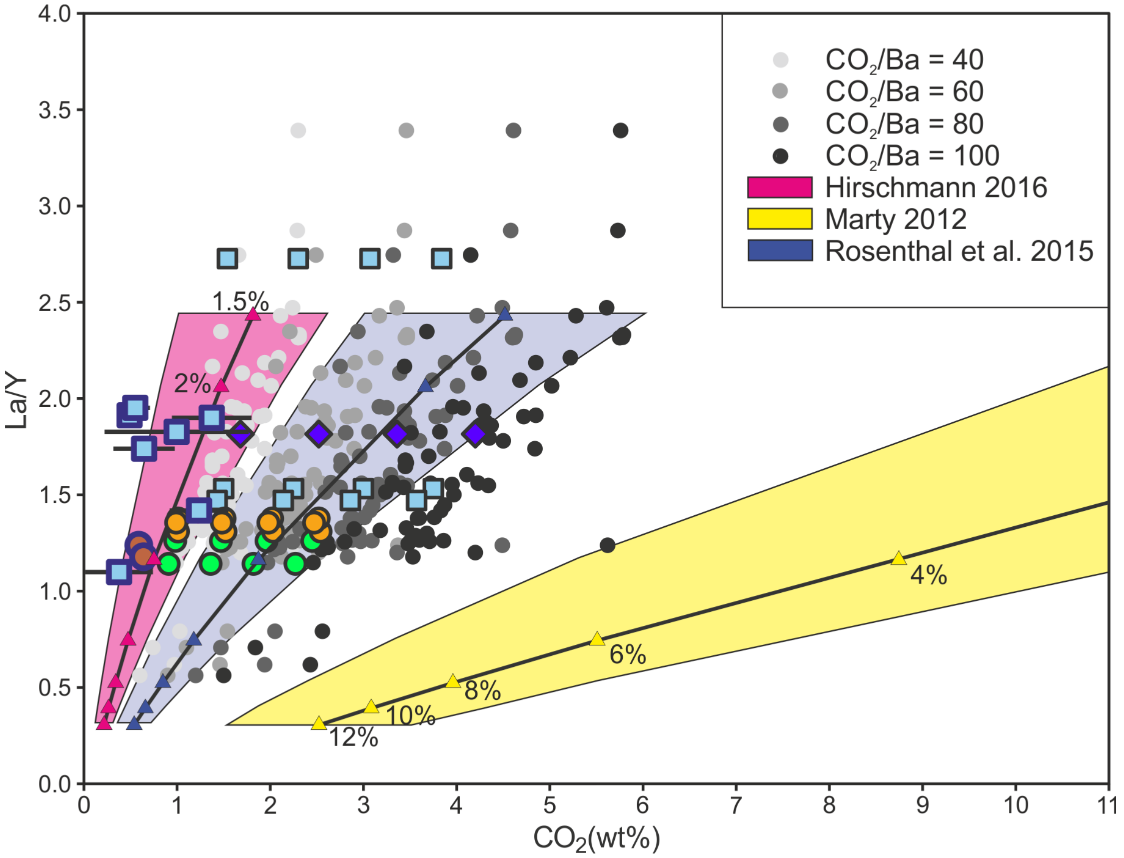

Figure 4.9: Estimates of original melt inclusion CO_2 contents, calculated using measured Ba concentrations and assuming a range of CO_2/Ba values (40, 60, 80 and 100) for primary mantle-derived melts, plotted against measured La/Y values. Assuming a primitive mantle Ba content of 6.75 ppm, these CO_2/Ba ratios correspond to source CO_2 contents of 270, 405, 540 and 675 ppm respectively. The melt inclusion dataset is plotted in grey, where darker shade means a higher source CO_2/Ba ratio was used to calculate the undegassed melt CO_2 content. Large, coloured symbols with black outlines (symbols as in Fig. 4.4) show calculated CO_2 contents for the least-evolved melt inclusions from each sample location, identified by their high MgO, low ILE contents and high host olivine Fo mol%. Higher CO_2 at identical La/Y means higher input CO_2/Ba values for these points. Large symbols with blue outlines show measured CO_2 and La/Y for melt inclusions with reconstructed (glass plus bubble) total CO_2 contents. Black curves show primary melt CO_2 concentrations produced by melting a primitive mantle source, calculated using different published mantle carbon concentrations (Marty, 2012; Rosenthal et al., 2015; Hirschmann, 2016); labelled triangle symbols show the partial melt fraction. The shaded coloured fields for each melting model represent the uncertainty in the starting mantle carbon content.

and Hirschmann, 2010; Dorfman et al., 2018). Recycled carbonates are thought to melt around ~300 km, forming carbon-rich fluids which induce silicate melting in recycled oceanic crustal material. The silicate and carbonatite melts produced then enrich the surrounding mantle in ILEs and volatiles, ultimately forming a heterogeneous, volatile-and carbon-rich mantle source beneath El Hierro. These results strengthen previous observations at other OIBs (Cabral et al., 2014), that the character of the mantle source plays a crucial role in influencing volcanic volatile fluxes from OIBs: similar levels of CO_2 and S enrichment are expected at other OIBs with enriched trace element and isotopic composition both in the case of neighbouring islands chains (Cape Verde, Azores, St. Helena) and globally (e.g. Cook Islands).

Long-term volatile flux estimates from El Hierro

Currently around 77 km^2, or 29% of El Hierro's land surface, is covered by material from platform-forming rift volcanism. The total thickness of these lavas and scoria deposits varies significantly across El Hierro, from >50 m in the El Golfo embayment and at Tanganasoga to <10 m in the south-west of the island. Taking an average thickness of 20 m for PFE rift lavas and tephras, as is observed in outcrops along coastal segments, a total erupted volume of 1.54×10^9 m^3 can be estimated for El Hierro in the last 20 ka. This volume of magma would degas 112±73 Gt CO_2 and 35.2±2.3 Tg of SO_2 based on our estimates of 9-42 g CO_2 and 3.5-4.5 g S content per kg of erupted melt. This would correspond to a time-averaged annual flux of 5.6±3.6 Gg/yr CO_2 and 1.76±0.23 Gg/yr SO_2, assuming platform-forming rift volcanism represent the last 20 ka activity of El Hierro (Carracedo et al., 2001). This is at least an order of magnitude lower than the diffuse CO_2 emissions of 66-358 Gg/yr (1σ uncertainty) measured in the weeks preceding the 2011-2012 eruption Melián et al. (2014); however, this is not surprising given the low eruption frequency at El Hierro, meaning that CO_2 emissions are not expected to remain constant over time. This time-averaged CO_2 flux for El Hierro is comparable with the expected CO_2 flux from 10-84 km of mid-ocean ridge, calculated using the global MORB CO_2 flux of Cartigny et al. (2008) and a global mid-ocean ridge length estimate of 70,000 km (Macdonald et al., 1991). It is two orders of magnitude lower than the 2150-5950 Gg/yr CO_2 estimate for the Magadi–Natron basin (Lee et al., 2016), located in the southern part of the East African rift system in the proximity of active carbonatitic and trachytic volcanoes. Thus, while our calculated time-averaged volatile fluxes are low compared to continental rift volcanoes, El Hierro magmas appear to have a high volatile-carrying capacity in comparison with other oceanic islands, with even small-volume eruptions capable of emitting substantial masses of volatiles into the atmosphere.

4.6 Conclusions

Olivine- and clinopyroxene-hosted melt inclusions from young El Hierro basanites show considerable variability in trace element contents and ratios, and some of the highest CO_2, S and F contents measured in MIs from oceanic islands to date. Major element systematics suggest that MIs are trapped at all stages along the crystallization path. Some primitive eruptions carry Fo-rich olivines hosting high-MgO MIs, while others produced more evolved clinopyroxene- and oxide-saturated magmas. Melt inclusion incompatible trace element ratios like La/Yb are significantly variable even within single eruptions, indicating that MIs were trapped from several magma batches that evolved separately from one another (Fig. 4.10). Trace element variability likely formed by mantle processes, e.g. variable melting degree of the mantle source. Since the variability in trace element ratios occurs in MIs with similar major element compositions and does not decrease with decreasing host olivine Fo content or clinopyroxene Mg#, they must represent melt batches formed either by different melting degrees, or by melting a heterogeneous mantle source. We propose a magmatic system comprising multiple interconnected sills (Stroncik et al., 2009; Klügel et al., 2015) whereby, during eruptions, multiple sills are tapped and mixed to produce a magma with a crystal cargo hosting MIs with highly variable trace element characteristics.

In this extensive plumbing system, various processes influence volatile systematics

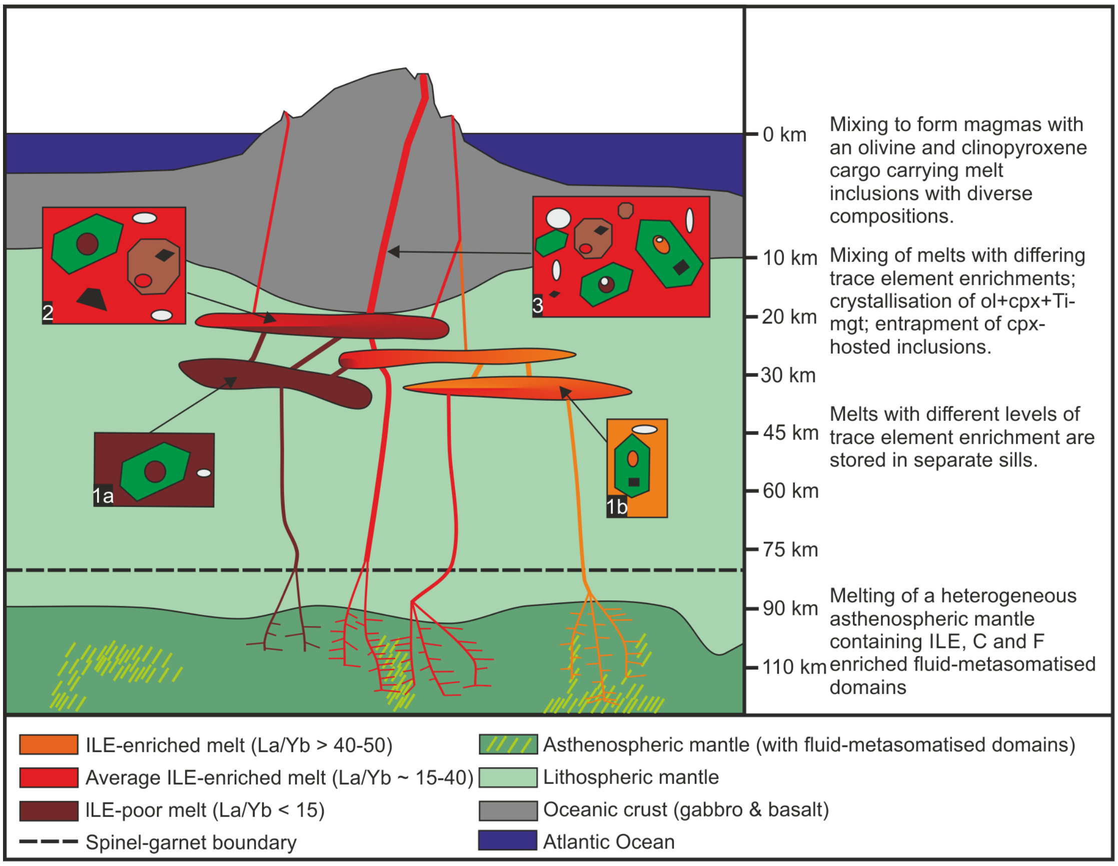

Figure 4.10: Schematic cartoon summarising the melt generation and evolution of El Hierro basanites. Primary melts form in the asthenospheric mantle, sampling a heterogeneous source containing a recycled oceanic lithospheric component that is enriched in incompatible lithophile elements (ILE), F, and possibly C and S. These melts ascend through the lithospheric mantle and start exsolving CO_2 at pressures >1 GPa. Partially degassed magmas are then stored within a multi-level storage system of interconnected sills. The sills can store magmas that are variably enriched in ILEs and volatiles, represented by boxes 1a and 1b (orange to dark red colours represent enrichment). Melts evolve separately within their storage reservoirs, trapping melt inclusions with differing La/Y. As the liquids evolve they become saturated in Ti-rich magnetite and clinopyroxene (box 2) and continue to degas CO_2 together with H_2O and S. Eruptions are eventually fed by melts pooled from multiple sills, which carry a crystal cargo that hosts melt inclusions trapped from variably degassed melts and with highly variable ILE ratios (box 3).

of the melt, both within the whole system and inside the melt inclusions. Up to 85% of melt inclusion CO_2 may be sequestered into inclusion-hosted bubbles formed by post-entrapment degassing during storage. Reconstructed total MI CO_2 concentrations (glass plus bubble) are >1.0 wt%, corresponding to volatile saturation pressures up to 700 MPa. Melt inclusion CO_2/Ba values of <31 are significantly lower than expected for undegassed, mantle-derived magmas, indicating that El Hierro magmas exsolved considerable CO_2 prior to inclusion trapping. Original melt CO_2 contents are likely between 0.9 and 4.2 wt%, with the precise value dependent on the mantle carbon content and melting degree. El Hierro MIs have high F concentrations and F/Nd values, which we suggest reflects a mantle source enriched in F relative to primitive mantle, most probably a recycled oceanic lithospheric component. Calculated sulfur and carbon contents for the mantle source are at the upper limit of published estimates for primitive mantle. Recycled C and S in the Canary Island mantle would provide a possible explanation for the formation of a trace element-enriched, heterogeneous mantle source beneath El Hierro, whereby volatile-induced melting of recycled crustal eclogites or pyroxenites metasomatises and enriches the asthenospheric mantle. Original melt CO_2 estimates presented here indicate eruptions of El Hierro, and more widely small oceanic islands where the presence of recycled crustal material in the mantle source is common, can contribute disproportionally more volatiles than their Icelandic or MORB counterparts. Our results demonstrate the usefulness of melt inclusions as a tool for tracing volatile recycling into the mantle, the importance of alkaline basaltic volcanism to fluxes of deep volatiles into the environment, and the influence of subduction-related volatile recycling to the mantle on global oceanic island volatile emissions.

Chapter 5

Instrumental mass fractionation during sulfur isotope analysis with secondary ion mass spectrometry in natural and synthetic glasses

5.1 Abstract

Sulfur stable isotopes are among the most commonly studied isotope systems in geochemistry. While sulfur isotope analysis of materials such as bulk rock samples, gases, and sulfide grains are routinely carried out, analyses of silicate glasses such as those formed in volcanic systems are relatively scarce in the literature. Despite a number of attempts in recent years to analyse sulfur isotopes from volcanic and experimentally produced glasses by secondary ion mass spectrometry (SIMS), the effects of instrumental mass fractionation (IMF) during analysis remain poorly understood. In this study we have used more than 600 sulfur isotope analyses of nine different glasses to characterise matrix effects that arise during sulfur isotope analysis of glasses by SIMS.

Samples were characterised for major element composition, sulfur contents, and sulfur isotope ratios by independent methods. Our glasses contain between 500 and 3400 ppm sulfur and cover a wide compositional range, including low-silica basanite, rhyolite, and phonolite, allowing us to investigate composition-dependent IMF. We use SIMS in multi-collection mode and use a Faraday cup/electron multiplier detector configuration to achieve analytical uncertainties of 0.7‰ to 2‰ (2σ) on measured δ^{34}S. We find composition-dependent matrix effects cause an offset of -12‰ to +1‰ between bulk sulfur isotope ratios and those measured by SIMS. Instrumental mass fractionation logarithmically correlates with glass sulfur contents and with a multivariate regression model that combines glass Al, Na, and K contents. Both regression methods are capable of predicting IMF with high accuracy: 91% (ln(S)) and 92% (Al-Na-K) of our analyses can be reproduced within 2σ external analytical uncertainty after a correction for composition-dependent IMF is applied. The process driving IMF is challenging to identify. We hypothesise that ionic bonded alkali-sulfur complex molecules form during sample-beam interaction, fractionating ^{34}S and ^{32}S and driving composition-dependent IMF. Our results demonstrate that the use of multiple, well-characterised standards is required to calibrate SIMS instruments prior to sulfur isotope analyses of unknown silicate glasses. Matrix effects related to glass Al-Na-K contents are of particular importance for felsic systems, where alkali and aluminium concentrations can vary considerably more than in mafic magmas.

5.2 Introduction

Sulfur, along with hydrogen and carbon, is one of the most abundant volatile elements present in magmatic systems and strongly influences a number of processes in melts and associated fluids. It primarily controls enrichment processes in various ore deposits at ocean floors and in magmatic hydrothermal systems (e.g. Seo et al., 2009; Simon and

Ripley, 2011), and plays a key role in modulating magmatic redox conditions during melt evolution and degassing (e.g. Marini et al., 2011; Moussallam et al., 2016, 2019; Longpré et al., 2017). H_2S and SO_2 formed during magma degassing are major constituents of many volcanic plumes, and can pose a significant hazard to human life due to their highly toxic nature. Understanding how sulfur behaves in magmatic systems from the melt source to the surface is essential if scientists are to provide better estimates on volcanic sulfur budgets and determine the source of sulfur in magmatic and hydrothermal systems.

Analytical tools such as electron probe microanalysis (EPMA) and secondary ion mass spectrometry (SIMS) are widely used to quantify sulfur contents in glasses down to < 100 ppm, and bulk-rock analysis of sulfur and its isotopes are a relatively routine procedures using spectroscopic methods and mass spectrometers. However, microanalyses of sulfur isotopes in glasses are relatively scarce in the literature, with only a few recent attempts made to determine sulfur isotopic ratios in melt inclusions, matrix glasses (Black et al., 2014; Beaudry et al., 2018), and experimental charges (Fiege et al., 2014). Such datasets have the potential to provide valuable insight into processes including sulfur degassing in magmas, sulfide ore formation in various geological settings, and the large scale and/or long term geochemical cycle of sulfur on the Earth.

Sulfur stable isotope ratios by convention are expressed as $\delta^{34}S$ (in ‰), calculated as:

$$\delta^{34}\mathrm{S}(‰) = ((^{34}\mathrm{S}/^{32}\mathrm{S})_{\mathrm{unk}}/(^{34}\mathrm{S}/^{32}\mathrm{S})_{\mathrm{V\text{-}CDT}} - 1) * 1000 \tag{5.1}$$

where $^{34}S/^{32}S_{unk}$ is the sulfur isotope ratio measured in the unknown and $^{34}S/^{32}S_{V\text{-}CDT}$ is the sulfur isotope ratio of the hypothetical V-CDT standard ($^{34}S/^{32}S = 0.0441626$, Ding et al. 2001). Microanalysis of any isotope ratio requires the use of a calibrated microanalytical tool. One of the most commonly used technique for isotope microanalysis in Earth sciences is SIMS. It is well documented that isotope analysis in glasses by SIMS is complicated by compositional matrix effects (or instrumental mass fractionation, IMF) for many isotope systems, including hydrogen (Hauri et al., 2006), boron (Rosner et al., 2008), oxygen (Eiler et al., 1997; Hartley et al., 2012), and chlorine (Manzini et al., 2017).

To investigate the effect of silicate glass chemistry on S isotope ratios measured by SIMS we require a set of glasses whose bulk δ^{34}S values have been accurately and precisely measured using an independent method. These glasses should cover a wide range of compositions and bulk sulfur contents so chemical components controlling IMF can be identified. Natural volcanic samples do not usually fit these criteria as they tend to degas most of their sulfur during magma ascent, with only a few hundred ppm sulfur remaining dissolved in the melt by the time of eruption. In addition, natural glasses are often chemically inhomogeneous, making them unsuitable for use as standard material. Experimentally produced glasses made in a high pressure and temperature apparatus offer alternative means to obtain homogeneous materials with bulk sulfur contents up to several thousands ppm. Sulfur isotope compositions of experimental charges can be determined the same way as for bulk rocks, using isotope ratio mass spectrometry (IRMS) after chemical extraction of sulfur. However, experiments typically produce only small volumes of material, which complicates bulk analysis and assessment of internal homogeneity.

Here we use a set of six experimental and three natural glasses with known major element compositions and sulfur isotope ratios to investigate composition-dependent IMF during sulfur isotope analysis of glasses by SIMS. Using glass chemistry and physical parameters, such as glass density, we perform simple linear, non-linear, and multivariate regression modelling to determine which parameters correlate with observed IMF. The best possible approach to sulfur isotope analysis in glasses using SIMS is discussed based on the results of the statistical modelling. We emphasise the importance of calibration using a range of standards covering the compositional range of the unknown silicate glasses before and during sulfur isotope measurements by SIMS.

5.3 Glass samples used for sulfur isotope analysis

We have used a set of nine glasses to investigate composition-dependent IMF (Fig. 5.1). Three of the nine glasses (A35, A36, and STAP) are natural subglacially erupted natural basalts from Iceland containing between 500-1600 ppm sulfur. The remaining six glasses are synthetic, and were melted under high pressure to keep sulfur dissolved in the glass. These synthetic glasses were made using powders of natural rock samples as opposed to a mixture of pure oxides and are therefore representative of natural magma compositions. The natural rock samples were selected to cover as wide a range of chemical components as possible (Fig. 5.1). Backscattered electron images of all the nine glasses are provided in the supplementary material.

5.3.1 Experimental procedures for synthetic glasses

Synthetic, sulfur-containing glasses were made using a internally heated pressure vessel (IHPV) at Leibniz Universität Hannover. Starting materials included two lava samples from the Canary Islands (Mg-rich basanite TNR14-01 and low-Mg basanite EGT17-01), two lava samples from Lacher See, Eifel Volcanic Field (nephelinite LS-17980 and phonolite LS-17985), one lava sample from Hawaii (picrite HAW-16095), and an obsidian from Lipari (LIP-17714). Glass major element compositions are presented in Fig. 5.1 and Table 5.1.

Samples were first ground into powders, then melted at 1200 to 1400 °C in a 1-atmosphere furnace and quenched into glass to produce a homogeneous, devolatilised material. The glasses were powdered again, and doped with various amounts of $CaSO_4$ with known sulfur isotope composition ($\delta^{34}S = 11.1 \pm 0.4‰$, see chapter three for the description of bulk sulfur isotope ratio analyses). The mix was dried in a furnace at 500

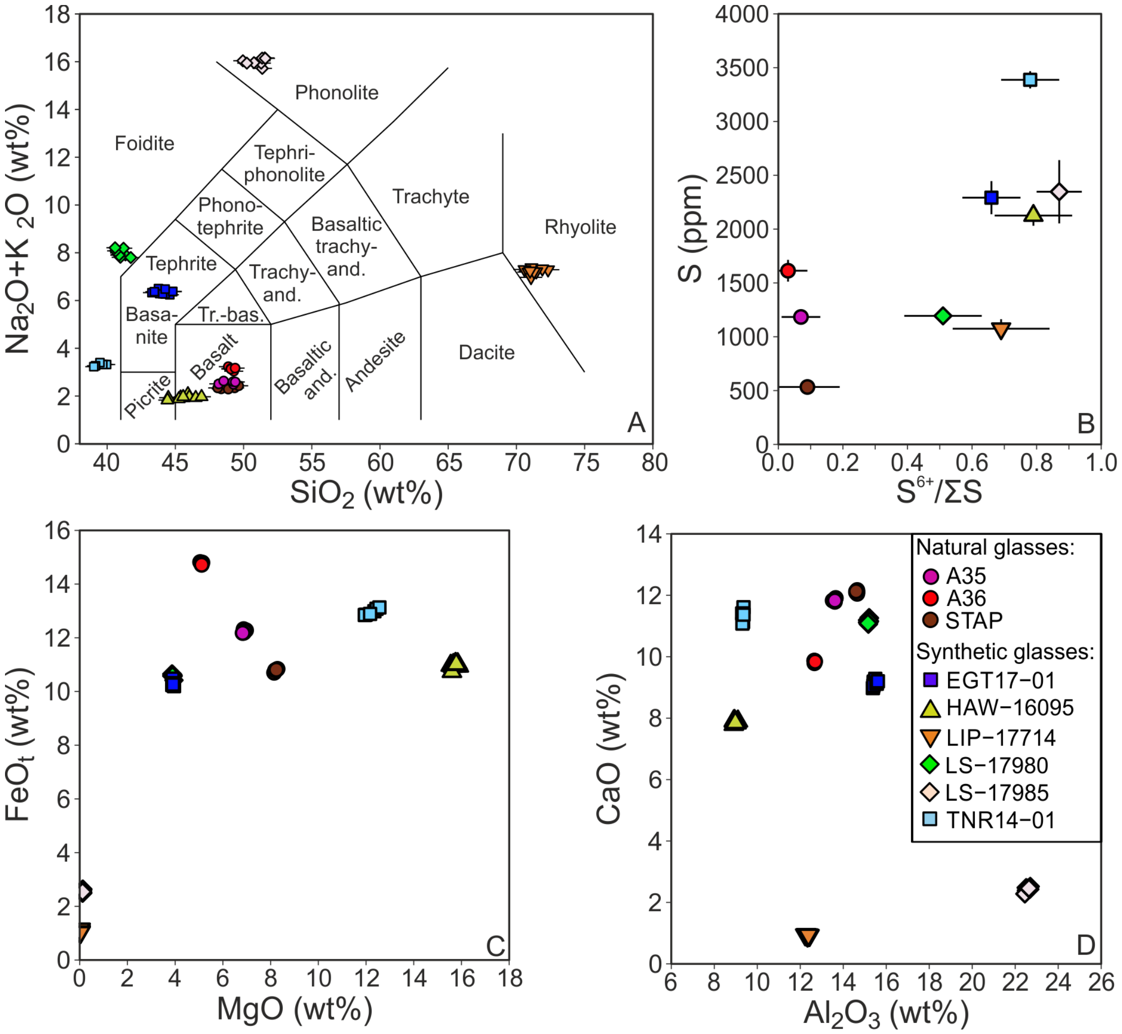

Figure 5.1: (A) Compositions of synthetic and natural glasses used here as sulfur isotope standards on a total alkali vs. silica diagram (Le Bas et al., 1986a). Most glasses are mafic in composition apart from a rhyolite (LIP-17714) and a phonolite (LS-19785). (B) Sulfur content of the glasses vs. $S^{6+}/\sum S$ ratio: synthetic glasses are dominated by oxidised S^{6+} while natural glasses are more reduced and contain mostly S^{2-}. (C) Total FeO vs. MgO and (D) CaO vs. Al_2O_3 diagrams indicate the glasses cover a wide compositional range for these elements. Error bars are 1σ standard deviation.

°C for 3 hours to remove absorbed water on the surface.

Between 132 and 185 mg of the sample powders were placed in $Au_{80}Pd_{20}$ capsules, along with 6-7 mg of H_2O, corresponding to 4 to 4.5 wt% concentration. The addition of water was required to lower the sample liqudus temperature and to set fO_2 conditions to highly oxidising (~FMQ+4) to prevent sulfide saturation and sulfur loss to capsules.

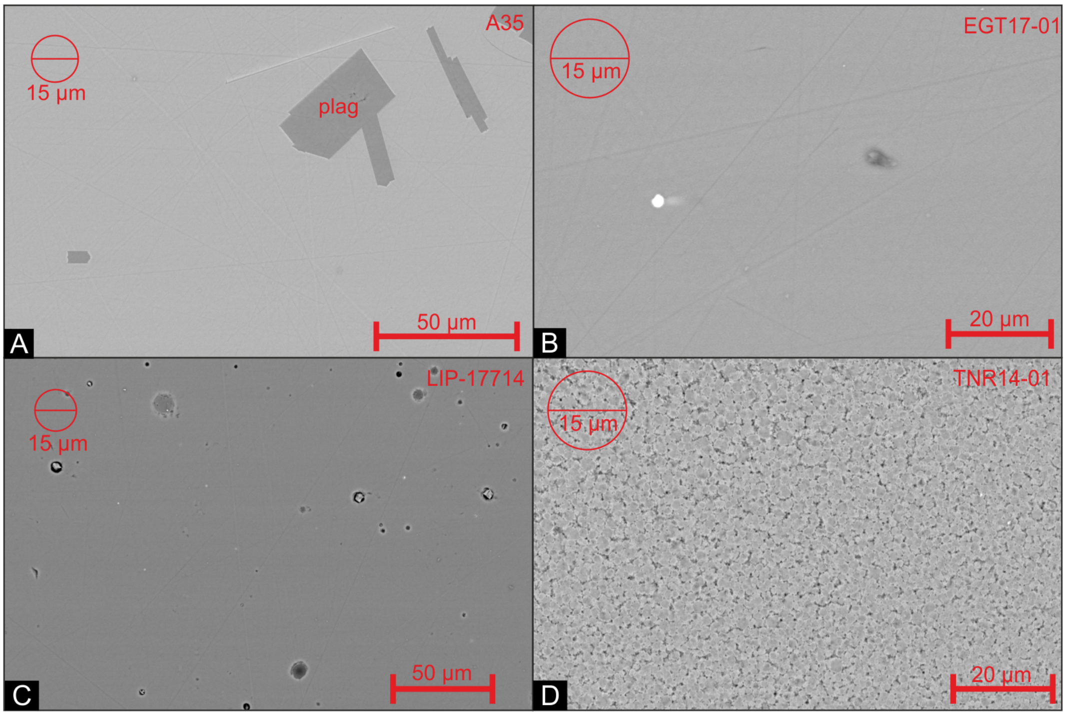

Figure 5.2: Large magnification backscattered electron images of selected glasses used in this study. In (A) natural subglacial glass A35 is shown, which contains minor amount of plagioclase, usually less than a 100 μm in size. The glass phase in natural samples has a homogeneous appearance. In (B-D) experimental glasses EGT17-01, LIP-17714, and TNR14-01 are shown. Sample EGT17-01 (B) is a glass with a homogeneous appearance; bright spot in (B) is caused by a small fragment of the AuPd capsule. Sample LIP-17714 (C) contains bubble-like vesicles <10 μm in size (larger vesicles are present in LS-17985, see supplementary SEM images for more detail). Some chips of TNR14-01 (D) have textures that appear to be devitrified; however grains, which may be small crystallites, are smaller than the SIMS spot size indicated by the red circle (approximately 15 μm). A similar feature is also present in LS-17980, with smaller nodules (see supplementary SEM images provided in the appendix).

IHPV experiments were carried out at 1300 °C and 300 MPa using an Ar pressure medium. The duration of experiments was two hours, after which capsules were drop-quenched to a room-temperature Cu plate while still under pressure. Capsules were then opened with a diamond saw and the glass was gently crushed and removed from the capsules using pliers. Smaller chips were used for bulk δ^{34}S analyses, while larger chips were set aside to be used for SIMS analyses.

Synthetic glasses produced during the experiments have a glassy appearance. High magnification backscattered electron (BSE) images reveal that while some samples have a perfect glassy texture (HAW-16095, EGT17-01), others contain some amount of smaller vesicles (mostly LS-17985). In some chips of LS-17980 and TNR14-01 devitrification can be observed (Fig. 5.2); however nodules observed in the glass are smaller than the SIMS spot size, and therefore may be suitable as standards (Fig. 5.2). Natural, Icelandic subglacial glasses sometime contain crystals of plagioclase (A35, A36) or olivine (STAP), but these can be easily avoided during analyses; the texture of the glass phase in the natural samples is homogeneous. More detail, including high-resolution BSE images of all the glasses is provided in the supplementary material of the thesis.

5.4 Analytical techniques

Major-, minor element, and sulfur concentrations of synthetic and natural glasses were measured using a Cameca SX100 electron microprobe (EPMA) at the University of Manchester. The following standards were used during glass analyses, with on-peak counting times in parentheses: Si (40 s), Na (80 s), and Al (80 s): jadeite; Ca (30 s): wollastonite; Mg (80 s): periclase; Cl (30 s): sodalite; S (40 s): anhydrite; P (30 s): apatite; K (30 s): potassic feldspar; Ti (30 s): rutile; Mn (80 s); tephroite; Fe (80 s): fayalite. Beam current was set at 3 nA for Si to avoid detector oversaturation, resulting in 330 and 720 cps/nA signal and an average 1.4 wt% counting statistic error (2σ) on SiO_2 concentrations. Other elements were measured using a 20 nA beam current. Beam diameter was set a 15 μm. A time-dependent intensity correction was applied for Na to account for loss due to volatilisation. Analytical error of measured S concentrations, based on counting statistics of the measured signal, was between 100 and 130 ppm, while the standard deviation of multiple measurements on various glass chips was between 90 to 170 ppm (2σ). Glass $S^{6+}/\sum S$ ratios were measured using the same EPMA using the method described in chapter three of the thesis. The S^{2-} (61414) and the S^{6+} (61445) peak positions were determined by scanning over a pyrite and an anhydrite standard, respectively. Two background positions were measured simultaneously. The background count rate was subtracted from the S^{2-} and S^{6+} peak counts. Background subtracted count rates were then divided, and $S^{6+}/\sum S$ ratios of the glasses were calculated relative to the ratios measured on pyrite ($S^{6+}{}_{peak}/S^{2-}{}_{peak} = 0.656\pm0.028$, 2σ) and anhydrite ($S^{6+}{}_{peak}/S^{2-}{}_{peak} = 1.313\pm0.034$, 2σ) standards, assuming $S^{6+}/\sum S$ and $S^{6+}{}_{peak}/S^{2-}{}_{peak}$ both change linearly. Uncertainties of major element contents and $S^{6+}/\sum S$ ratios are given in table 5.1.

Glass $Fe^{3+}/\sum Fe$ ratios were determined using wet chemistry and colorimetry at the Leibniz Universität Hannover following the procedures described by Schuessler et al. (2008). Between 4 and 17 mg of glass was reacted with NH_4VO_3, H_2SO_4 and HF. In summary, V^{5+} oxidised Fe^{2+} originating from the glass during dissolution into Fe^{3+} by producing oxidation-resistant V^{4+}. Fe^{2+} and V^{5+} were later regenerated from Fe^{3+} and V^{4+} produced during the previous reaction by adding boric acid to the solution. Fe^{2+} was then reacted with 2:2'bipyridyl to form Fe(II)-2:2'bipyridyl, which has a strong absorption band in the visible spectrum. Absorption of Fe^{2+} was measured first by colorimetry. After the measurement Fe^{2+}, hydroxylamine hydrochloride was added to the solution, reducing all Fe to Fe^{2+}. Absorption is measured again to determine total Fe content. The ratio of the two absorption values is used to get $Fe^{2+}/\sum Fe$, which is then converted to the more commonly used $Fe^{3+}/\sum Fe$ format. This method has an uncertainty of ~0.02-0.08 (2σ) in $Fe^{3+}/\sum Fe$ (table 5.1).

Three natural Icelandic glasses and three other synthetic glasses were analysed for their H_2O content by transmission micro-FTIR, using a Perkin Elmer Spotlight-400 instrument at the University of Manchester equipped with a mercury-cadmium-telluride (MCT) detector. We used the Beer-Lambert law to quantify H_2O contents in the samples, which requires sample thickness and molar absorptivity to be known. Glass chips were made into thin (30-120 μm) double-polished wafers. Thickness of the wafers was determined using a manual Miyamoto micrometer, which has a nominal precision of ±2

μm. Absorbance spectra of the glasses were recorded between 7000 cm^{-1} to 600 cm^{-1} to include H_2O peaks at 5200 and 1630 cm^{-1} and OH^- peaks at 4500 and 3550 cm^{-1}. Between three to eight spectra were taken from each sample. Absorbance from each spectrum was determined after manually subtracting the background from the peaks. H_2O contents were quantified using molar absorptivities taken from Mercier et al. (2010). Molar absorptivity values were varied based on the number of non-bridging oxygens per total oxygen atom (NBO/T): for TNR14-01 molar absorptivities of 43.96, 0.56 and 0.58 were used for the 3550, 4500 and 5200 cm^{-1} peak, respectively, while for all other mafic glasses molar absorptivities of 62.8, 0.62 and 0.67 were used. For hydrous experimental glasses, H_2O concentrations are calculated by adding together concentrations derived from the 5200 cm^{-1} H_2O and 4500 cm^{-1} OH^- peaks. For low (<1 wt%) H_2O glasses from Iceland the water content was determined using the absorbance of the 3550 cm^{-1} peak, which was taken as total H_2O.

Sulfur isotopic composition of the anhydrite used to add sulfur to the experimental charges was measured at the Godwin Laboratory, University of Cambridge, using a Thermo Finnegan Delta V Plus isotope ratio mass spectrometer (IRMS). Sulfur from the anhydrite was extracted as H_2S using Thode's solution, i.e. HI-H_2PO_3-HCl mixture, under a constant flow of N_2 gas. The extraction procedure took approximately three hours. H_2S was precipitated in Zn-acetate as ZnS, which was then reacted with $AgNO_3$ to form Ag_2S. The resulting Ag_2S precipitate was dried, combusted into SO_2 at 1030 °C in a flash element analyser and analysed for δ^{34}S.

Bulk sulfur isotope composition of our synthetic glasses were measured using a Thermo-electron MAT 253 IRMS at Massachusetts Institute of Technology. Samples masses were between 21 and 47 mg. Total sulfur was extracted from the glass samples using tin(II)-strong phosphoric acid (Kiba reagent; Sasaki et al. 1979) under a constant flow of N_2 gas. H_2S produced during the reaction was precipitated in Zn-acetate solution and as ZnS, which was later reacted with $AgNO_3$ to form Ag_2S. The Ag_2S precipitates were then dried, placed in aluminium foil and fluorinated in nickel reaction vessels for 8 hours at 300 °C. The resulting SF_6 was then purified by gas chromatography, going through a column packed with 5 Å molecular sieve and HayeSep Q. Gas pressures of the purified SF_6 were measured before isotopic analysis. Repeated analyses of a mid-ocean ridge glass sample (ALV4055-B6) using the same extraction method and the same instrument indicate that a precision of ±0.5 ‰ (2σ) in $\delta^{34}S$ can be reached for glass samples using this extraction procedure. Repeated analyses of international reference sulfide material (IAEA-S1) have yielded $\delta^{34}S$ precisions of 0.26‰ for 2 mg Ag_2S (n = 28, Ono et al. 2012) and 0.43‰ (2σ) for 40–130 μg Ag_2S (n = 13, Fortin et al. 2019).

Bulk sulfur isotope composition of natural, sulfur-containing Icelandic glasses A35, A36, and STAP (Fig. 5.1) were measured using the same Kiba extraction procedure, carried out at the University of Iceland. Sulfur isotope analysis were then carried out using the same Thermo-electron MAT 253 IRMS at the Massachusetts Institute of Technology as for the synthetic glasses. The larger mass of natural samples meant multiple extractions (3 to 4) could be carried out on larger amounts of extracted sulfur. Around 2 mg of the extracted Ag_2S was converted to SF_6, purified and measured using the same procedure as for the synthetic glasses. Repeated analysis of A35 (n = 3), A36 (n = 3) and STAP (n = 4) indicate a 2σ reproducibility of 0.06‰, 0.93‰, and 0.75‰, respectively using the Kiba extraction method.

5.4.1 SIMS analytical conditions and data processing

Sulfur isotopes in the synthetic and natural glasses were measured by secondary ion mass spectrometry at the Edinburgh Ion Microprobe Faility (EIMF) at the University of Edinburgh in November 2019. Samples were mounted in epoxy and gold-coated prior to analysis. $^{34}S/^{32}S$ ratios in glasses were determined using a Cameca IMS-1270 instrument operated in multi-collection mode. A Cs^+ primary ion beam with an accelerating voltage of 10 kV and a beam current of 2-3.7 nA was used for analytical sessions 2 to 13. A smaller 0.9-1.3 nA primary beam current was used during the first analytical session. Primary beam diameter was set at 10-15 μm. A low-energy flood electron gun was used to compensate for positive charge build up on the sample surface. Secondary ions were accelerated with 10 kV from the sample surface into the mass spectrometer. Secondary ions were passed through a 60 μm transfer lens and entrance slit, followed by a 400 μm contrast aperture and finally a 2000 μm field aperture. Sulfur isotopes were analysed as $^{34}S^-$ using an electron multiplier (EM) and $^{32}S^-$ using a Faraday cup (FC-L1) to optimise counting statistics on both isotope species. Mass resolution was set at ~3600 to distinguish between isobaric interferences on mass ~32 ($^{32}S^-$, $^{16}O_2^-$, $H^{31}P^-$) and ~34 ($^{34}S^-$, $^{16}O^{18}O^-$). Before each analysis the sample surface was pre-sputtered for 60 s, followed by a secondary ion beam alignment using dynamic transfer plates. Both $^{32}S^-$ and $^{34}S^-$ ions were measured for 20 cycles, with each cycle comprised of 4 seconds. This configuration resulted in count rates of 6×10^5 to 1.17×10^7 for $^{32}S^-$ and 2.9×10^4 to 5.26×10^5 for $^{34}S^-$ per cycle, with count rate standard errors varying between 0.05 to 2.17% for both isotopes. Total analysis time, including pre-sputtering, was ~3.5 minutes per measurement.

Drift and EM deadtime correction of sulfur isotope ratios

Due to the high count rate of up to 5.26×10^5 counts per cycle on the EM detector, a large deadtime correction was applied on the ^{34}S count rate. Deadtime correction is calculated as

$$N_{\mathrm{corr}} = N_{\mathrm{meas}}/(1 - N_{\mathrm{meas}} * \tau) \tag{5.2}$$

where N_{corr} is the deadtime-corrected counts, N_{meas} is the uncorrected counts and τ is the deadtime (in seconds). The deadtime correction on the Cameca IMS-1270 is electronically set: during the analytical session it was determined to be 51 ns. As shown in equation 5.2, the size of the deadtime correction is count rate dependent, and its value changes with variable glass sulfur content. Therefore, EM deadtime was manually measured to test if the electronically set deadtime is correct by analysing the A35 glass (which is a glass with intermediate S content) using different entrance slit sizes, resulting in a deadtime of 47.6 ns. The difference between the electronically set and measured EM deadtime changes $^{34}S/^{32}S$ ratios for A35 by 0.00002, equal to difference of 0.5 ‰ in $\delta^{34}S$. As this change is significant with respect to analytical errors (Fig. 5.3) data were reprocessed using equation 5.2 and the 47.6 ns deadtime.

Sulfur isotope analysis of the samples was usually carried out in blocks of 14, with each block consisting of four primary drift standard analyses, followed by five analyses of two different glass samples. EGT17-01 was used as the primary drift standard as it has perfect glassy texture, and a relatively high sulfur content (2292 ppm). Analyses were carried out in 14 sessions, with a new session starting after each instance of sample exchange or beam shutdown. All 14 session are affected by instrumental drift, evidenced by a systematic decrease in measured $^{34}S/^{32}S$ ratios in the primary drift standard. For each session, instrumental drift was corrected using a linear regression procedure to restore the primary drift standard measurements to a constant $^{34}S/^{32}S$ ratio. Further details of the drift correction procedure are provided in the supplementary material. R^2 of the linear regression fits varied between 0.71 and 0.99 (see supplementary Fig. S1 given in supplementary text file). The weaker correlations are associated with sessions where measured instrumental drift was small (<0.001 change in $^{34}S/^{32}S$).

Internal and external precision of SIMS analyses

Combined analytical uncertainty of our sulfur isotope analysis by SIMS is comprised of the counting statistic error on the detectors determined from the variation of count rates during the 20 cycles, the error associated with the drift correction which we define as the standard deviation measured on the primary drift standard for each session, and the precision of the bulk analysis of our glasses. The first two are the internal analytical precision, while all three combined make up the external error. Assuming that the three different errors are independent of each other the combined internal and external standard uncertainty (in ‰ δ^{34}S) can be calculated as

$$\sigma_{\text{comb, internal}} = \sqrt{(\sigma_{\text{count}}/\bar{x}_{\text{dcorr}})^2 + (\sigma_{\text{drift}}/\bar{x}_{\text{dcorr}})^2} * |\bar{x}_{\text{dcorr}}| \tag{5.3}$$

and

$$\sigma_{\text{comb, external}} = \sqrt{(\sigma_{\text{count}}/\bar{x}_{\text{dcorr}})^2 + (\sigma_{\text{drift}}/\bar{x}_{\text{dcorr}})^2 + (\sigma_{\text{IRMS}}/\bar{x}_{\text{dcorr}})^2} * |\bar{x}_{\text{dcorr}}| \tag{5.4}$$

where $\sigma_{\text{comb, internal}}$ and $\sigma_{\text{comb, external}}$ are the internal and external combined standard uncertainties, σ_{count} is the counting statistics error, σ_{drift} is the standard deviation measured on the primary drift standard EGT17-01, σ_{IRMS} is the error of the bulk IRMS analyses, and $\bar{x}_{\text{dcorr}}$ is the drift-corrected S isotope ratio while $|\bar{x}_{\text{driftcorr}}|$ is its absolute value (all units ‰ δ^{34}S). The error of the bulk IRMS analysis was assumed to be 0.25 ‰ (1σ) in our error calculations for all glasses.

Precision of sulfur isotope ratio analyses is primarily determined by the measured count rate and hence sulfur concentrations of the glass. Once the count rate decreases below 5×10^5 on the faraday cup for ^{32}S analytical error starts increasing exponentially on both detectors (Fig. 5.3). At higher count rates the combined uncertainty is primarily controlled by the error associated with the drift correction, which varies between 0.19 and 0.69‰. When errors associated with the drift correction are small and count rate is $>5 \text{ x } 10^5$, the analytical uncertainty achieved by SIMS may be below 0.7 ‰ approaching the error of the IRMS analyses. Our lowest combined uncertainty is less than a half of the 1.6‰ reported by Black et al. (2014) for sulfur isotope measurements by SIMS. Fiege et al. (2014) reported 0.52‰ reproducibility on a MORB glass, similar to our drift correction errors; however, they did not provide combined analytical uncertainty. Our error propagation calculations show that if the optimal conditions of high count rate and no or small instrumental drift are met, multi-collector SIMS and bulk IRMS

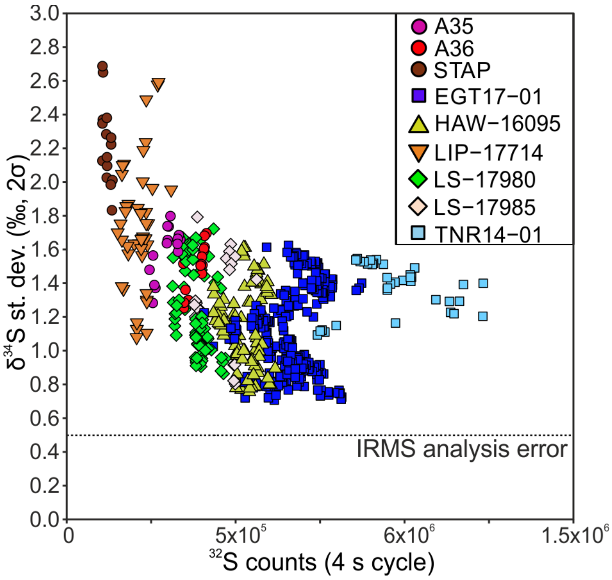

Figure 5.3: Combined analytical error of sulfur isotope measurements using SIMS, expressed in $\delta^{34}S$ (‰), plotted against ^{32}S count rate measured on a Faraday cup (FC, 4 second cycle). Combined 2σ uncertainty is between 0.7 and 1.6‰ when count rate is above 5 x 10^5, while at <5 x 10^5 combined uncertainty increases rapidly. This indicates that the total error at low count rate is limited by the counting statistics error and hence low sulfur concentrations in the glass rather than other factors such as precision of the bulk IRMS measurements.

analyses have comparable analytical uncertainty in measured $^{34}S/^{32}S$ ratios. Therefore SIMS offers a feasible way of discriminating permil-level changes in sulfur isotope ratios on the lengthscale of tens of microns in silicate glasses.

5.5 Results

5.5.1 Major element composition and sulfur content of glasses

Major element composition of the glasses measured by EPMA are presented in Fig. 5.1 and Table 5.1. The three natural Icelandic glasses are all basaltic in composition, while experimental glasses cover a wider compositional range, including alkaline basalts, a phonolite, and a rhyolite. The nine glasses cover an SiO_2 range of 39.5 to 71.3 wt%. Alkali contents are also variable, with Na_2O and K_2O contents between 1.6 to 7.7 wt%

Table 5.1: Compositions of synthetic and natural glasses. Values are in wt% if not otherwise stated. Icelandic glass $Fe^{3+}/\sum Fe$ ratios are based on Laki melt inclusions from Hartley et al. (2017). Sulfur contents measured by SIMS are calculated from ^{32}S cps/nA (see Results section for more detail). H_2O mass balance (mb) values are based on the weight of H_2O added to capsules prior to IHPV experiments. Uncertainty given in every even column is 2σ. NM: not measured. NA: not applicable.

Sample	**A36**		**STAP**		**A35**		**LS-17980**		**HAW-16095**		**TNR14-01**		**LS-17985**		**EGT17-01**		**LIP-17714**	
Type	natural glass		natural glass		natural glass		synthetic gl.		synthetic gl.		synthetic gl.		synthetic gl.		synthetic gl.		synthetic gl.	
	AVG	2σ	**AVG**	2σ	**AVG**	2σ	**AVG**	2σ	**AVG**	2σ	**AVG**	2σ	**AVG**	2σ	**AVG**	2σ	**AVG**	2σ
SiO_2	**49.1**	*0.4*	**48.9**	*1.3*	**48.9**	*1.1*	**41.0**	*0.7*	**45.6**	*1.6*	**39.5**	*0.7*	**51.0**	*0.6*	**44.1**	*1.1*	**71.3**	*1.0*
TiO_2	**3.050**	*0.007*	**1.620**	*0.035*	**1.645**	*0.019*	**2.355**	*0.046*	**1.889**	*0.025*	**3.937**	*0.033*	**0.290**	*0.005*	**3.162**	*0.056*	**0.064**	*0.015*
Al_2O_3	**12.67**	*0.03*	**14.63**	*0.06*	**13.60**	*0.11*	**15.18**	*0.07*	**8.98**	*0.13*	**9.33**	*0.05*	**22.60**	*0.09*	**15.48**	*0.15*	**12.34**	*0.14*
FeO(t)	**14.78**	*0.07*	**10.79**	*0.10*	**12.24**	*0.12*	**10.58**	*0.13*	**10.96**	*0.17*	**12.97**	*0.24*	**2.58**	*0.06*	**10.32**	*0.17*	**1.07**	*0.10*
FeO	**11.82**		**8.63**		**9.79**		**3.26**		**4.22**		**4.41**		**0.82**		**4.38**		**0.50**	
Fe_2O_3	**3.28**		**2.40**		**2.72**		**8.14**		**7.49**		**9.51**		**1.96**		**6.60**		**0.64**	
MnO	**0.24**	*0.02*	**0.19**	*0.018*	**0.21**	*0.015*	**0.30**	*0.015*	**0.16**	*0.017*	**0.18**	*0.019*	**0.23**	*0.012*	**0.21**	*0.012*	**0.04**	*0.010*
MgO	**5.10**	*0.068*	**8.22**	*0.109*	**6.89**	*0.101*	**3.89**	*0.057*	**15.73**	*0.218*	**12.24**	*0.497*	**0.12**	*0.003*	**3.90**	*0.044*	**0.03**	*0.010*
CaO	**9.85**	*0.07*	**12.11**	*0.09*	**11.85**	*0.10*	**11.15**	*0.14*	**7.87**	*0.08*	**11.29**	*0.41*	**2.43**	*0.07*	**9.14**	*0.17*	**0.94**	*0.03*
Na_2O	**2.74**	*0.14*	**2.06**	*0.12*	**2.37**	*0.12*	**4.55**	*0.29*	**1.57**	*0.14*	**2.32**	*0.18*	**7.69**	*0.22*	**4.51**	*0.14*	**3.33**	*0.24*
K_2O	**0.41**	*0.006*	**0.28**	*0.010*	**0.19**	*0.008*	**3.44**	*0.041*	**0.38**	*0.016*	**0.99**	*0.097*	**8.32**	*0.178*	**1.85**	*0.059*	**3.90**	*0.056*
P_2O_5	**0.32**	*0.060*	**0.21**	*0.042*	**0.15**	*0.045*	**1.15**	*0.062*	**0.20**	*0.030*	**0.69**	*0.047*	**0.05**	*0.015*	**1.24**	*0.086*	**0.01**	*0.020*
S (ppm, EPMA)	**1614**	*202*	**534**	*74*	**1184**	*104*	**1194**	*125*	**2126**	*190*	**3387**	*160*	**2347**	*294*	**2292**	*308*	**1075**	*177*
S (ppm, SIMS)	**1322**	*132*	**407**	*31*	**1008**	*51*	**1337**	*256*	**1859**	*259*	**3183**	*754*	**1579**	*119*	**2292**	*212*	**728**	*154*
Cl (ppm)	**150**	*88*	**181**	*84*	**87**	*58*	**142**	*57*	**7**	*82*	**26**	*69*	**933**	*57*	**138**	*63*	**110**	*89*
H_2O (mb)	**NA**		**NA**		**NA**		**4.28**		**4.42**		**4.03**		**4.12**		**4.28**		**4.54**	
H_2O (FTIR)	**0.70**	*0.09*	**0.37**	*0.09*	**0.28**	*0.04*	**3.37**	*1.20*	**2.66**	*0.61*	**5.65**	*1.75*	**NM**		**NM**		**NM**	
Total	**99.32**		**99.59**		**98.64**		**98.70**		**98.50**		**98.44**		**99.67**		**98.87**		**97.63**	
$Fe^{3+}/\sum Fe$	**0.20**		**0.20**		**0.20**		**0.69**	*0.03*	**0.61**	*0.03*	**0.66**	*0.03*	**0.68**	*0.02*	**0.58**	*0.03*	**0.54**	*0.08*
$S^{6+}/\sum S$	**0.03**	*0.11*	**0.09**	*0.20*	**0.07**	*0.12*	**0.51**	*0.24*	**0.79**	*0.24*	**0.78**	*0.17*	**0.87**	*0.07*	**0.66**	*0.19*	**0.69**	*0.29*
$\delta^{34}S$ (‰)	**-0.68**	*0.5*	**-1.10**	*0.75*	**-0.49**	*0.06*	**9.38**	*0.50*	**11.28**	*0.50*	**11.58**	*0.50*	**8.76**	*0.25*	**10.96**	*0.50*	**11.96**	*0.50*

and 0.7 to 8.3 wt%, respectively. Total alkali content is up to 16.0 wt% in the phonolitic glass (LS-17985). Total FeO contents of the glasses are between 1.1 and 14.8 wt%. In Icelandic glasses Fe is mainly present as Fe^{2+} ($Fe^{3+}/\sum Fe = 0.20$, based on Laki melt inclusion data, Hartley et al. 2017), while experimental glasses are considerably more oxidised, with $Fe^{3+}/\sum Fe$ ratios between 0.58 and 0.69. Glass MgO contents are between 0.03 and 17.7 wt%, covering most reasonable silicate glass compositions (Fig. 5.1C). Glass CaO and Al_2O_3 contents are between 0.94-12.1 wt% and 9.3-22.6 wt%, respectively (Fig. 5.1D). H_2O content of Icelandic subglacial glasses is between 0.3 and 0.7 wt%. Based on mass balance, synthetic glasses have 4.0 to 4.5 wt% H_2O. FTIR analyses from the three glasses indicate water contents may have changed during high-pressure and temperature experiments: H_2O content for HAW-16095 was 2.6 wt%, 1.6 wt% lower then the amount of water added. The other two glasses have H_2O of 3.4 wt% (LS-17980) and 5.7 wt% (TNR14-01), within error of the mass balance-based H_2O contents.

Sulfur concentrations in the glasses, measured by EPMA, range between 534 and 3378 ppm, covering most natural magmatic samples. Glass sulfur contents were also extrapolated from the SIMS ^{32}S count rates. The count rate measured for each cycle was converted to counts per second (cps) and divided by the primary beam current to calculate ^{32}S cps/nA for each analysis. The average cps/nA measured on EGT17-01 in each session was assumed to be equal to 2292 ppm sulfur, i.e. the S content of EGT17-01 measured by EPMA. Standard deviation of sulfur contents measured by SIMS are generally higher than errors of EPMA measurements, as SIMS-based sulfur contents often vary between session. The largest session-by-session variation is observed for TNR14-01. Mafic glass S contents measured by EPMA and by SIMS are within 2σ uncertainty. For the rhyolitic and phonolitic glass a constant offset can be observed between SIMS- and EPMA-derived sulfur contents: this difference may be caused by matrix effects, as our primary drift standard is an alkali basalt. Such matrix effects may be accounted for by measuring ^{32}S/O$_2$ or ^{32}S/^{30}Si ratios. In the synthetic glasses, glass sulfur contents based on ^{32}S/O$_2$ ratios measured in April 2019 using the same SIMS instrument correlate better sulfur contents measured by EPMA when compared with sulfur contents derived from $_{32}$S count rate (see supplementary spreadsheet that contains sulfur isotope data for standard glasses).

Sulfur speciation varies significantly between the nine glasses (Fig. 5.1B). Natural Icelandic glasses are dominated by S^{2-}, with $S^{6+}/\sum S < 0.1$. Experimental glasses are more oxidised, with $S^{6+}/\sum S$ between 0.51 and 0.87. This offers an opportunity to test whether oxidation state of sulfur influences the measured sulfur isotope ratio during SIMS analysis, which has not been previously investigated in detail.

5.5.2 Sulfur isotopic composition of glasses and observed IMF

Bulk sulfur isotope ratios measured by IRMS in the glasses are reported in table 5.1. Four experimental glasses have δ^{34}S between 11.0‰ and 12.0‰, close to that of the anhydrite used to add the sulfur to the samples (11.1‰). Exceptions are phonolite glass LS-17985 (8.8‰), and nephelinite glass LS-17980 (9.4‰); both glasses have a lighter isotopic composition than the anhydrite. However, these glasses contained sulfur after initial melting of the rock powders in a 1 atm furnace (see supplementary spreadsheets for starting compositions), which could be the cause of the difference in δ^{34}S. Compositions of natural Icelandic glasses are similar to those determined recently for MORB (-1.3‰ Labidi et al. 2013), with δ^{34}S between -0.4‰ and -1.6‰.

During SIMS sulfur isotope analysis each glass was analysed in blocks of five to determine whether they are sufficiently homogeneous to be used as primary calibration standards. After excluding analyses with anomalous counts for either isotope (too low or too high count rate compared to previous analysis, large counting statistic error) the remaining 602 glass analyses were averaged by session for each sample. Largest variability is observed the rhyolitic LIP-17714 glass which has a 2σ standard deviation between 1.3‰ and 1.8‰ in the five sessions it was measured (Fig. 5.4). This reproducibility is similar to the combined uncertainty of individual measurements, which is between 1‰ and 2.6‰ for LIP-17714 (Fig. 5.3). In session 9, LS-17985 had a standard deviation of 2.8‰, indicating the presence of isotopic heterogeneity. In the other glasses reproducibility during a session is between 0.3 and 1.4‰ (Fig. 5.4), either smaller than or similar to the combined standard error (Fig. 5.3). Low variability of measured δ^{34}S indicates glasses used in this study are suitable as SIMS primary standards.

Instrumental mass fractionation for sulfur isotopes can be expressed in ‰ using the following equation:

$$IMF(‰) = ((^{34}S/^{32}S)_{\mathrm{meas}} - (^{34}S/^{32}S)_{\mathrm{real}})/(^{34}S/^{32}S)_{\mathrm{real}} * 1000 \tag{5.5}$$

where $(^{34}\mathrm{S}/^{32}\mathrm{S})_{\mathrm{meas}}$ is the drift-corrected sulfur isotope ratio and $(^{34}\mathrm{S}/^{32}\mathrm{S})_{\mathrm{real}}$ is the sulfur isotope ratio measured by an independent technique not affected by matrix effects. We find significant IMF between glasses with different composition and sulfur content (Fig.

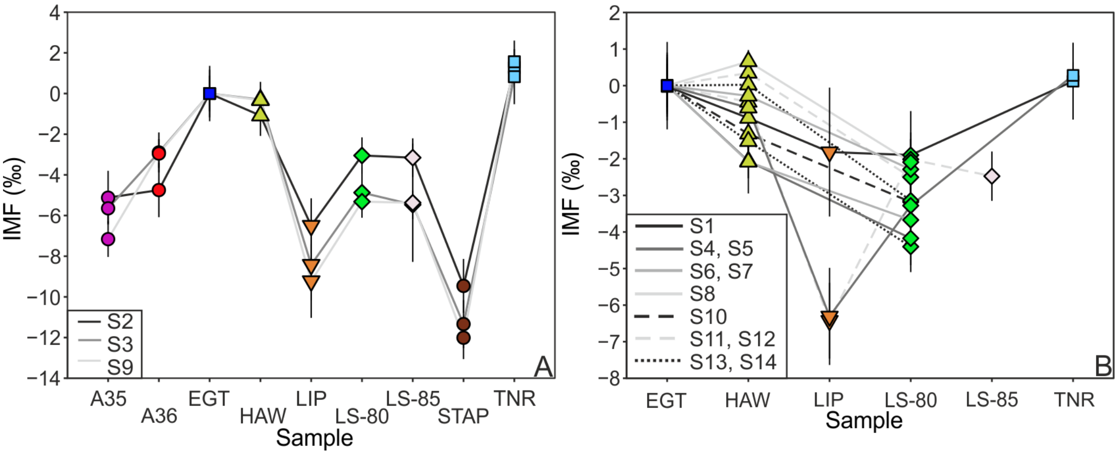

Figure 5.4: Diagrams showing instrumental mass fractionation values between different sessions, calculated relative to the primary drift standard EGT17-01, which is fixed at 0. In (A) sessions during which all nine glasses were measured are shown, while in (B) data from all other sessions are presented. Symbols are the same as in Figs. 5.1 and 5.2. Errors are 2σ standard deviation for each glass by session. EGT17-01, HAW-16095, and LS-17980 were measured in all 14 sessions. Note the difference in y-axis scale between (A) and (B).

5.4). Compared to our primary drift standard EGT17-01 most glasses display a negative IMF, as large as -12‰ in the case of STAP. The only exception is TNR14-01, which has a positive IMF of +1‰ relative to EGT17-01. A significant variability in IMF can be observed between different sessions: HAW-16095 and LS-17980 have IMF between -2.5 to +1‰ and -4.5 to -2‰, respectively (Fig. 5.4B). A significant difference can be observed between the IMF measured for LIP-17714 during session 1 and other sessions: IMF in session 1 is considerably lower (-2‰) compared to other sessions (between -6‰ and -8‰, Fig. 5.4). Natural Icelandic glasses all display a negative IMF, with the largest values observed for the sulfur-poor STAP glass, between -9.5 and -12‰. Both LS-17980 (basanite) and LS-17985 (phonolite) have similar IMF, varying between -5‰ and -2‰.

5.6 Discussion

If instrumental mass fractionation is controlled by the chemistry or the physical properties of the samples, such as density, a correlation should be observed between these parameters and observed IMF (Deloule et al., 1991; Eiler et al., 1997; Hauri et al., 2006; Hartley et al., 2012). If a correlation exists between IMF and one or more chemical/physical parameter, IMF can be predicted and corrected for in materials with an unknown isotope composition. IMF can be calculated for *n* linear predictors as

$$IMF = m_1 * x_1 + m_2 * x_2 + m_3 * x_3 + ... + m_\mathrm{n} * x_\mathrm{n} + c \tag{5.6}$$

where $\mathrm{m_1}$ to $\mathrm{m_n}$ are the slopes of the regression for each parameter, $\mathrm{x_1}$ to $\mathrm{x_n}$ are the values of parameters 1 to n, and c is a constant. The number of predictors should be kept to a minimum, as their number is limited by the number of predicted values, in this case by the number of standards used to calculate IMF. In the discussion we explore possible correction methods for composition-dependent IMF during sulfur isotope analysis of glasses by SIMS using simple univariate linear, multivariate linear, and non-linear regression models.

5.6.1 Univariate linear models between glass composition and IMF

Univariate linear models are the simplest way to correct for composition-dependent IMF. For the purpose of statistical modelling, we used data collected during sessions 2, 3, and 9. In these sessions data were collected from all nine glass standards (Fig. 5.4A). Results of univariate linear models are presented in Fig. 5.5. Linear regression modelling was carried out separately for all glass compositions (Fig. 5.5B) and for mafic glasses only (A35, A36, EGT17-01, HAW-16095, LS-17980, and TNR14-01, Fig. 5.5A). In both cases, the best correlation is between IMF and glass sulfur content (Fig. 5.5). When all glass standards are used, R^2 between IMF and sulfur contents

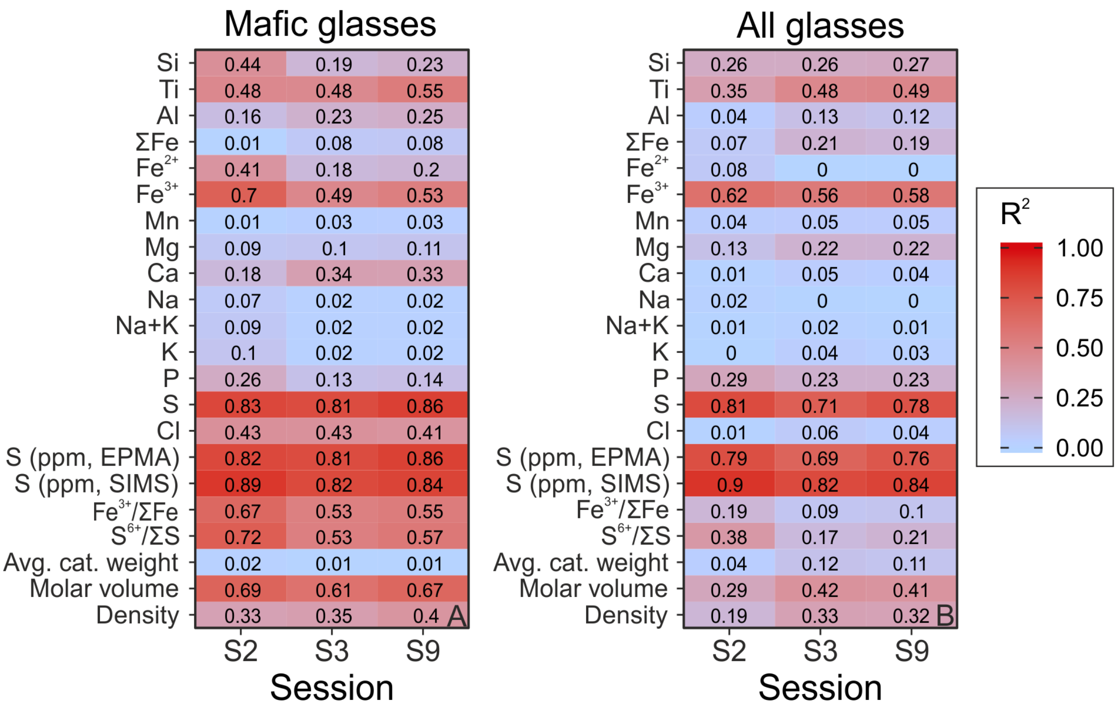

	S2	S3	S9
Si	0.44	0.19	0.23
Ti	0.48	0.48	0.55
Al	0.16	0.23	0.25
ΣFe	0.01	0.08	0.08
Fe^{2+}	0.41	0.18	0.2
Fe^{3+}	0.7	0.49	0.53
Mn	0.01	0.03	0.03
Mg	0.09	0.1	0.11
Ca	0.18	0.34	0.33
Na	0.07	0.02	0.02
Na+K	0.09	0.02	0.02
K	0.1	0.02	0.02
P	0.26	0.13	0.14
S	0.83	0.81	0.86
Cl	0.43	0.43	0.41
S (ppm, EPMA)	0.82	0.81	0.86
S (ppm, SIMS)	0.89	0.82	0.84
$Fe^{3+}/\Sigma Fe$	0.67	0.53	0.55
$S^{6+}/\Sigma S$	0.72	0.53	0.57
Avg. cat. weight	0.02	0.01	0.01
Molar volume	0.69	0.61	0.67
Density	0.33	0.35	0.4

	S2	S3	S9
Si	0.26	0.26	0.27
Ti	0.35	0.48	0.49
Al	0.04	0.13	0.12
ΣFe	0.07	0.21	0.19
Fe^{2+}	0.08	0	0
Fe^{3+}	0.62	0.56	0.58
Mn	0.04	0.05	0.05
Mg	0.13	0.22	0.22
Ca	0.01	0.05	0.04
Na	0.02	0	0
Na+K	0.01	0.02	0.01
K	0	0.04	0.03
P	0.29	0.23	0.23
S	0.81	0.71	0.78
Cl	0.01	0.06	0.04
S (ppm, EPMA)	0.79	0.69	0.76
S (ppm, SIMS)	0.9	0.82	0.84
$Fe^{3+}/\Sigma Fe$	0.19	0.09	0.1
$S^{6+}/\Sigma S$	0.38	0.17	0.21
Avg. cat. weight	0.04	0.12	0.11
Molar volume	0.29	0.42	0.41
Density	0.19	0.33	0.32

Figure 5.5: R^2 values calculated using simple linear regression models for mafic glasses (A) and all glasses (B), using data collected during sessions 2, 3, and 9. During these sessions all nine glasses were analysed. Linear regression models were calculated using atomic cation fractions of the glasses, normalised to 1. Molar volume (cm^3/mol) and density (g/cm^3) of the glasses are calculated using the method of Lange (1997)

measured by EPMA are 0.69 to 0.79 (Fig. 5.5). This increases to an R^2 of 0.82 to 0.9 if SIMS sulfur contents are used, indicating IMF best correlates with ^{32}S count rate. If sulfur is expressed as cations rather than by weight (ppm), R^2 is between 0.71 to 0.81. Other chemical and physical parameters have a weaker correlation: after sulfur, IMF is best correlated with Fe^{3+} cations, with R^2 values of 0.56 to 0.62. Similar results are obtained using only mafic glasses: sulfur correlates well with IMF. For mafic glasses IMF also correlates with $Fe^{3+}/\sum Fe$ ratios, $S^{6+}/\sum S$ ratios, and the molar volume of the glass, calculated using the method of Lange (1997). Nonetheless, R^2 values for these parameters are generally below 0.7 (Fig. 5.5A).

Simple univariate regression models indicate that glass sulfur concentration might play a major role in controlling IMF during sulfur isotope analysis by SIMS. Correlations between the bulk concentration and isotopic IMF of the same element have been documented for hydrogen/deuterium analyses in glasses by SIMS (Hauri et al., 2006).

Previous studies have not observed IMF during sulfur isotope analysis of glasses by SIMS because only one standard material was used for calibration (Gurenko et al., 2006; Black et al., 2014; Beaudry et al., 2018). Studies of sulfur isotopes measured by SIMS using multiple glass standards are rare: Fiege et al. (2014) presented analyses of sulfur isotopes from 11 glasses, including basaltic, andesitic and rhyolitic compositions with known bulk sulfur isotope ratios, and found no evidence of composition-dependent IMF, albeit using glasses covering a smaller sulfur content range between 521-1830 ppm. Based on data presented in their paper and using our equation 5.5, we calculate that six of the 11 glasses studied by Fiege et al. (2014) have larger IMF than their reported 2σ uncertainty of 0.52‰. IMF is up to 3.8‰ in their dataset. While Fiege et al. (2014) use a linear regression between SIMS and bulk δ^{34}S data, which is close to unity with a constant instrumental bias of 1.84‰ to correct their data no discussion is provided on the cause of the difference between SIMS and bulk δ^{34}S for some of their glasses. The analytical procedures used in Fiege et al. (2014) are different compared to those used in this work: their analyses were carried out in single-collector mode using two EM detectors. Different analytical conditions could be the cause of different observations regarding IMF during sulfur isotope analysis in glasses.

5.6.2 Multivariate and non-linear models

It is possible that instrumental mass fractionation is not controlled by a single parameter, but rather a combination of different parameters are required to explain observed variation in measured and true isotopic ratios (e.g Deloule et al., 1991; Vielzeuf et al., 2005; Manzini et al., 2017). Non-linear correlations between IMF and various parameters also have been observed, such as for δ^{18}O analyses in olivines (Eiler et al., 1997),

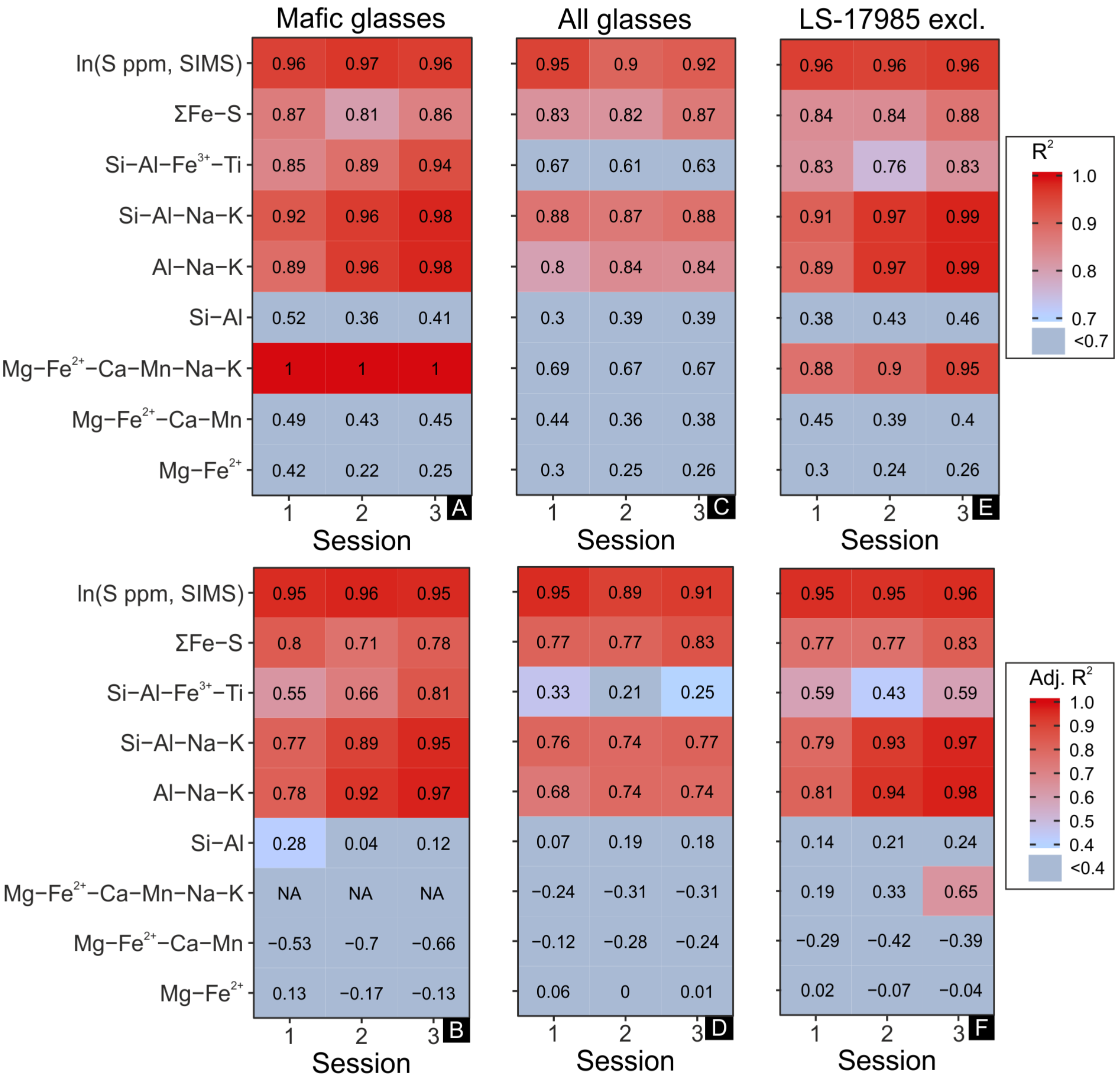

	Mafic glasses			All glasses			LS-17985 excl.		
Session	1	2	3	1	2	3	1	2	3
ln(S ppm, SIMS)	0.96	0.97	0.96	0.95	0.9	0.92	0.96	0.96	0.96
ΣFe−S	0.87	0.81	0.86	0.83	0.82	0.87	0.84	0.84	0.88
Si−Al−Fe^{3+}−Ti	0.85	0.89	0.94	0.67	0.61	0.63	0.83	0.76	0.83
Si−Al−Na−K	0.92	0.96	0.98	0.88	0.87	0.88	0.91	0.97	0.99
Al−Na−K	0.89	0.96	0.98	0.8	0.84	0.84	0.89	0.97	0.99
Si−Al	0.52	0.36	0.41	0.3	0.39	0.39	0.38	0.43	0.46
Mg−Fe^{2+}−Ca−Mn−Na−K	1	1	1	0.69	0.67	0.67	0.88	0.9	0.95
Mg−Fe^{2+}−Ca−Mn	0.49	0.43	0.45	0.44	0.36	0.38	0.45	0.39	0.4
Mg−Fe^{2+}	0.42	0.22	0.25	0.3	0.25	0.26	0.3	0.24	0.26

	B			D			F		
Session	1	2	3	1	2	3	1	2	3
ln(S ppm, SIMS)	0.95	0.96	0.95	0.95	0.89	0.91	0.95	0.95	0.96
ΣFe−S	0.8	0.71	0.78	0.77	0.77	0.83	0.77	0.77	0.83
Si−Al−Fe^{3+}−Ti	0.55	0.66	0.81	0.33	0.21	0.25	0.59	0.43	0.59
Si−Al−Na−K	0.77	0.89	0.95	0.76	0.74	0.77	0.79	0.93	0.97
Al−Na−K	0.78	0.92	0.97	0.68	0.74	0.74	0.81	0.94	0.98
Si−Al	0.28	0.04	0.12	0.07	0.19	0.18	0.14	0.21	0.24
Mg−Fe^{2+}−Ca−Mn−Na−K	NA	NA	NA	−0.24	−0.31	−0.31	0.19	0.33	0.65
Mg−Fe^{2+}−Ca−Mn	−0.53	−0.7	−0.66	−0.12	−0.28	−0.24	−0.29	−0.42	−0.39
Mg−Fe^{2+}	0.13	−0.17	−0.13	0.06	0	0.01	0.02	−0.07	−0.04

Figure 5.6: Results (R^2 in A, C, E and adjusted R^2 in B, D, F) of non-linear and multivariate linear regression models using sulfur isotope data collected in sessions 2, 3, and 9. Calculations were performed using only mafic glasses (A-B), all glasses (C-D), and excluding LS-17985 (E-F). Note the colour scale difference between A, C, E and B, D, F. In B, NA indicates that adjusted R^2 for the Mg-Fe^{2+}-Ca-Mn-Na-K model is not applicable as the number of predictors is equal to the number of fitted values.

for δ^{18}O and δ^{13}C analyses in carbonates (Śliwiński et al., 2018), and for δ^{25}Mg analysis in olivines and pyroxenes (Fukuda et al., 2020).

We performed multivariate linear regression modelling using equation 5.6 various combinations of elements, reported in Fig. 5.6. Elements were combined on the basis of

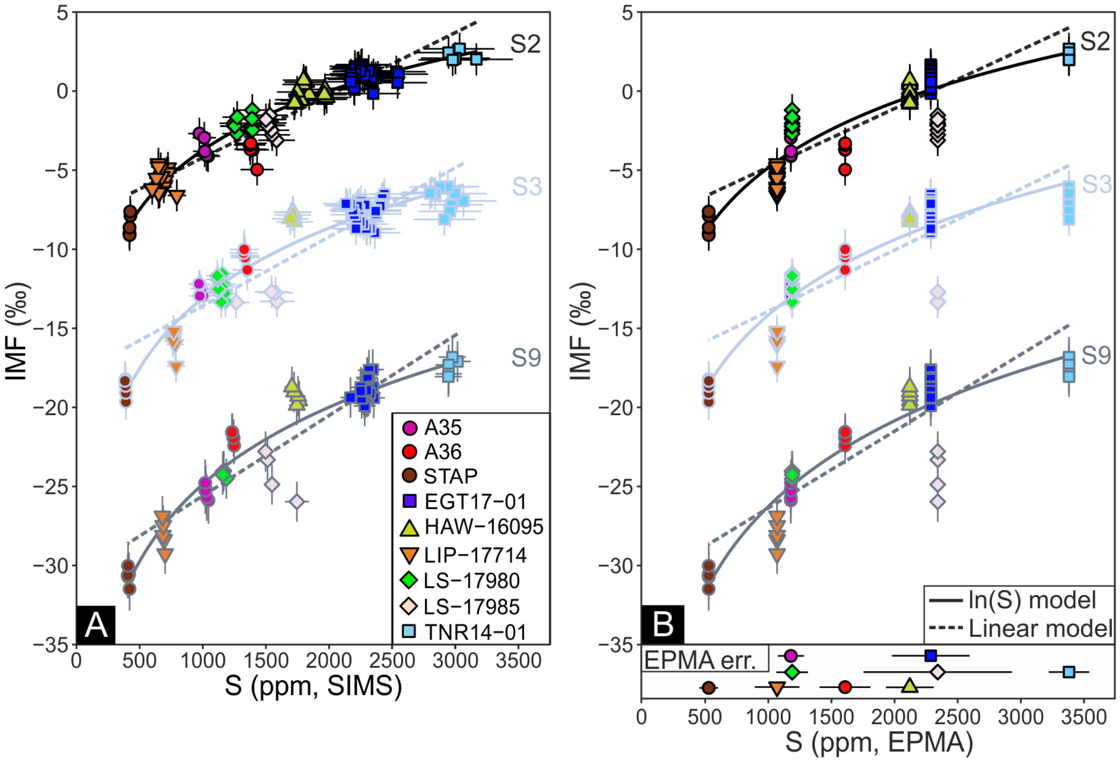

Figure 5.7: Results of linear and logarithmic regression modelling between observed IMF and sulfur concentration measured by SIMS (A), calculated using ^{32}S cps/nA relative to the sulfur content of EGT17-01 (2292 ppm S) and by EPMA (B) for sessions 2, 3, and 9. Errors of EPMA analysis are given in the top of (B). All errors are 2σ standard deviations. Logarithmic fit to the data estimates IMF considerably better as a function of S content than linear models. A large offset between S contents measured by SIMS and EPMA can be observed for the phonolitic (750 ppm) glass, which suggest ion yield of sulfur may be composition dependent, with less efficient ionisation observed in extremely alkali- and aluminium-rich glasses.

their structural position in the glass and their ion charge. We also calculated a logarithmic regression between IMF and glass sulfur (Fig. 5.7) to explore whether a significant improvement can be achieved compared to linear fits. Similar to univariate models, multivariate regression modelling was carried out for data collected during sessions 2, 3 and 9.

Multivariate regression models were calculated on three different samples sets: mafic glasses (Fig. 5.6/A,B), mafic glasses + rhyolite (including LIP-17714, but excluding phonolitic glass LS-17985; Fig. 5.6/C,D), and all nine glasses including the phonolitic glass LS-17985. A set of model calculations were performed excluding phonolitic glass

LS-17985 (Fig. 5.6/E,F) as we detected chemical heterogeneity measured sulfur contents between individual chips (Fig. 5.1B), with count rates often varying significantly between and during analyses.

The multivariate models combining alkalis, Al, and other elements such as Si and Ca show the largest increase in R^2 (Fig. 5.6).Univariate linear fits for Al, Na and K have R^2 <0.13 (Fig. 5.5B), while combining Al-Na-K in a trivariate regression model results in R^2 of 0.8 to 0.84 when all glasses are used (Fig. 5.6C). Adjusted R^2, which is an indicator of whether the addition of a new parameter into the model improves fits significantly, is 0.68 to 0.74 in case of the Al-Na-K model (Fig. 5.6D), a large improvement compared to univariate models. Other multivariate models such as Si combined with tetrahedral cations (Al, Fe^{3+}, Ti), or combinations of 2+ charged octahedral cations do not improve fits compared to univariate linear models, indicated by the decreasing adjusted R^2. Combining total Fe contents with sulfur improves R^2 and adjusted R^2, but this is minimal compared to the increase seen for the Al-Na-K model. Combining Al-Na-K with Si shows some improvement in R^2 and adjusted R^2, especially for data collected in session 2 (Fig. 5.6).

If modelling is performed after excluding LS-17985 from the dataset, R^2 of the Al-Na-K model increases significantly to 0.89-0.99 (Fig. 5.6E), providing a better fit than the univariate regression between IMF and SIMS sulfur contents (Fig. 5.5B). Addition of Si into the model at this point does not significantly increase the quality of the fit, indicated by the slight decrease in adjusted R^2 values (Fig. 5.6F). The cause of the large increase in R^2 for the Al-Na-K model after excluding LS-17985 is due to the extremely high alkali (up to 18 wt% Na_2O+K_2O) and Al_2O_3 (>20 wt%) contents of the phonolitic LS-17985 glass. Due to this extremely high alkali and Al content LS-17985 glass has the strongest leverage on the slopes of the Al-Na-K regression model.

A logarithmic fit between IMF and glass sulfur content provides a considerably better fit than the linear models. Logarithmic fits between IMF and SIMS-derived glass

Table 5.2: Results of selected regression models, including residuals, R^2 and adjusted R^2 values. These models provide the best fits for sulfur isotope data collected during sessions 2, 3, and 9.

Parameter	**Session**	**LS-17985 Included**	**Residuals**									**R^2**	**Adjusted R^2**
			A35	A36	EGT 17-01	HAW -16095	LIP -17714	LS -17980	LS -17985	STAP	TNR 14-01		
S (SIMS)	S2	Included	0.9	-0.9	0.4	1.1	0.2	1.1	0.2	-1.7	-1.2	**0.90**	**0.89**
S (SIMS)	S3	Included	1.3	1.8	0.2	2.6	-1.1	0.7	-1.5	-2.1	-1.9	**0.82**	**0.79**
S (SIMS)	S9	Included	0.2	2.6	0.1	2.6	-0.8	0.6	-1.5	-2.1	-1.7	**0.84**	**0.82**
S (SIMS)	S2	Not included	0.9	-0.8	0.4	1.1	0.2	1.1	NA	-1.7	-1.2	**0.90**	**0.89**
S (SIMS)	S3	Not included	1.1	1.6	0.0	2.4	-1.3	0.5	NA	-2.3	-2.1	**0.83**	**0.80**
S (SIMS)	S9	Not included	0.0	2.4	-0.1	2.4	-1.0	0.4	NA	-2.2	-2.0	**0.86**	**0.84**
ln(S, SIMS)	S2	Included	0.3	-1.7	0.4	0.5	0.4	0.3	-0.6	0.1	0.2	**0.95**	**0.95**
ln(S, SIMS)	S3	Included	0.7	0.8	0.3	1.9	-1.2	-0.1	-2.4	0.4	-0.4	**0.90**	**0.89**
ln(S, SIMS)	S9	Included	-0.6	1.6	0.2	1.8	-0.5	-0.3	-2.5	0.4	-0.1	**0.92**	**0.91**
ln(S, SIMS)	S2	Not included	0.2	-1.7	0.3	0.4	0.4	0.2	NA	0.0	0.1	**0.96**	**0.95**
ln(S, SIMS)	S3	Not included	0.5	0.5	-0.1	1.5	-1.4	-0.4	NA	0.3	-0.8	**0.96**	**0.95**
ln(S, SIMS)	S9	Not included	-0.9	1.2	-0.3	1.4	-0.7	-0.6	NA	0.4	-0.6	**0.96**	**0.96**
∑Fe-S	S2	Included	0.7	-1.3	1.5	1.0	-0.2	2.1	-0.6	-1.9	-1.2	**0.83**	**0.77**
∑Fe-S	S3	Included	0.5	0.2	1.8	2.0	0.5	0.9	-0.9	-2.8	-2.2	**0.82**	**0.77**
∑Fe-S	S9	Included	-0.3	0.5	1.7	2.0	0.4	1.1	-0.8	-2.4	-2.2	**0.87**	**0.83**
∑Fe-S	S2	Not included	0.8	-1.1	1.3	0.8	-0.7	2.1	NA	-1.8	-1.4	**0.84**	**0.77**
∑Fe-S	S3	Not included	0.7	0.5	1.5	1.8	-0.2	0.9	NA	-2.7	-2.5	**0.84**	**0.77**
∑Fe-S	S9	Not included	-0.2	0.8	1.5	1.9	-0.2	1.1	NA	-2.3	-2.4	**0.88**	**0.83**
Si-Al-Fe^{3+}-Ti	S2	Included	1.4	0.1	0.9	1.2	-0.3	-3.0	2.0	-3.3	1.0	**0.67**	**0.33**
Si-Al-Fe^{3+}-Ti	S3	Included	1.3	1.2	1.4	2.5	-0.6	-3.4	2.3	-4.7	0.0	**0.61**	**0.21**
Si-Al-Fe^{3+}-Ti	S9	Included	0.4	1.5	1.2	2.7	-0.6	-4.0	2.9	-4.6	0.4	**0.63**	**0.25**
Si-Al-Fe^{3+}-Ti	S2	Not included	2.3	-0.7	1.7	0.7	-0.3	-1.2	NA	-2.0	-0.7	**0.83**	**0.59**
Si-Al-Fe^{3+}-Ti	S3	Not included	2.4	0.4	2.4	1.9	-0.6	-1.3	NA	-3.1	-2.0	**0.76**	**0.43**
Si-Al-Fe^{3+}-Ti	S9	Not included	1.8	0.4	2.4	2.0	-0.6	-1.3	NA	-2.7	-2.1	**0.83**	**0.59**
Al-Na-K	S2	Included	1.4	-2.2	0.0	1.5	-1.9	-1.2	1.4	-0.1	1.2	**0.80**	**0.68**
Al-Na-K	S3	Included	1.3	-0.6	-0.3	2.2	-2.0	-2.3	2.0	-0.8	0.4	**0.84**	**0.74**
Al-Na-K	S9	Included	0.5	-0.3	-0.4	2.3	-2.5	-2.6	2.3	-0.2	0.9	**0.84**	**0.74**
Al-Na-K	S2	Not included	1.2	-2.6	0.7	0.5	-0.4	0.2	NA	0.0	0.5	**0.89**	**0.81**
Al-Na-K	S3	Not included	1.0	-1.1	0.6	0.9	0.1	-0.2	NA	-0.5	-0.6	**0.97**	**0.94**
Al-Na-K	S9	Not included	0.1	-1.0	0.7	0.7	0.0	-0.2	NA	0.0	-0.3	**0.99**	**0.98**
Al-Na-K-Ca	S2	Included	1.3	-1.9	0.4	1.6	-1.5	-1.8	1.4	-0.3	0.8	**0.81**	**0.62**
Al-Na-K-Ca	S3	Included	1.3	-0.7	-0.5	2.2	-2.2	-2.0	2.0	-0.7	0.6	**0.84**	**0.68**
Al-Na-K-Ca	S9	Included	0.5	-0.4	-0.5	2.3	-2.6	-2.5	2.3	-0.2	1.0	**0.84**	**0.67**
Al-Na-K-Ca	S2	Not included	1.1	-2.3	1.0	0.7	-0.1	-0.4	NA	-0.1	0.1	**0.90**	**0.78**
Al-Na-K-Ca	S3	Not included	1.0	-1.3	0.4	0.8	-0.1	0.1	NA	-0.5	-0.4	**0.97**	**0.93**
Al-Na-K-Ca	S9	Not included	0.2	-1.1	0.5	0.7	-0.2	0.0	NA	0.1	-0.2	**0.99**	**0.97**
Si-Al-Na-K	S2	Included	1.5	-1.5	0.9	0.8	-0.2	-1.9	0.7	-0.6	0.3	**0.88**	**0.76**
Si-Al-Na-K	S3	Included	1.4	0.0	0.4	1.7	-0.6	-2.8	1.4	-1.2	-0.3	**0.87**	**0.74**
Si-Al-Na-K	S9	Included	0.6	0.4	0.6	1.6	-0.7	-3.3	1.6	-0.8	-0.1	**0.88**	**0.77**
Si-Al-Na-K	S2	Not included	1.3	-2.1	1.0	0.4	0.1	-0.6	NA	-0.3	0.2	**0.91**	**0.79**
Si-Al-Na-K	S3	Not included	0.9	-1.2	0.5	0.9	0.0	-0.1	NA	-0.5	-0.6	**0.97**	**0.93**
Si-Al-Na-K	S9	Not included	0.2	-1.0	0.7	0.7	0.0	-0.3	NA	0.0	-0.3	**0.99**	**0.97**

sulfur contents have R^2 between 0.90-0.95 when all glasses are included in the fit, while R^2 is 0.96 if LS-17985 is excluded (Fig. 5.6, Table 5.2). A similar improvement can be observed for models using EPMA-derived glass sulfur concentrations. Linear models fail to fit IMF values measured in STAP and TNR14-01, with residuals close to -2‰. However, residuals for STAP and TNR14-01 decrease to ± 1‰ if a logarithmic model

Table 5.3: Results of IMF modelling using different correction methods. Glass δ^{34}S values are considered to be reproduced if after applying the IMF correction the resulting δ^{34}S is within the interval defined by the bulk δ^{34}S ± 1σ and 2σ combined external uncertainty calculated using equation 5.3.

Model	**Sessions**	**n**	**LS-17985**	**Reproduced (%)** 1σ	2σ
ln(S, EPMA)	All	602	Included	44.0%	72.9%
ln(S, EPMA)	All	579	Excluded	54.7%	84.6%
ln(S, SIMS)	All	602	Included	60.0%	89.0%
ln(S, SIMS)	All	579	Excluded	59.6%	91.2%
∑Fe-S	All	602	Included	57.6%	78.7%
∑Fe-S	All	579	Excluded	58.9%	81.7%
Al-Na-K	S1, S2, S3, S4, S9, S11	385	Included	43.6%	72.7%
Al-Na-K	S1, S2, S3, S4, S9	332	Excluded	61.4%	92.2%
Si-Al-Na-K	S2,S3,S9	242	Included	43.4%	75.6%
Si-Al-Na-K	S2,S3,S9	224	Excluded	33.9%	57.1%

is applied. (Table 5.2).

Multivariate and non-linear models clearly show that IMF arising during sulfur isotope analysis in glasses by SIMS is not best predicted by univariate linear models such as in case of oxygen isotope analysis, for which IMF is primarily controlled by silica contents (Hartley et al., 2012). IMF during sulfur isotope analysis of glasses by SIMS is best predicted by either a logarithmic fit to the sulfur concentration of the glasses or by a multivariate model using glass Al, Na, and K contents. The correlation between IMF and glass Al-Na-K concentrations could have important consequences for sulfur isotope analysis of glasses from silica-rich igneous systems, such as I- and S-type granites and rhyolites, which cover a wider range of Al and alkali contents compared to mafic magmas. The effects of instrumental mass fractionation and the use of appropriate standards must be further considered if the sulfur isotopic compositions of silica-rich melts are to be studied by SIMS.

5.6.3 Predicting instrumental mass fractionation using glass chemistry

To test which elements can be used predict IMF within analytical uncertainty, the δ^{34}S values of the analysed glasses were recalculated using modelled IMF values and compared with glass δ^{34}S measured by IRMS. As at least three different standard glasses were analysed in every session, models using one or two predictors can be applied to data collected in all of the 14 sessions (602 analyses in total). Models with more than two predictors can only be calculated for certain sessions (Table 5.3). If all nine glasses are used during model calculations, the best performing model is a logarithmic fit to the SIMS-derived sulfur contents (ln(S, SIMS)): 61% and 89% of analysis are reproduced within 1σ and 2σ external analytical uncertainty, respectively. Other models including total Fe-S, logarithmic fit using EPMA-derived S contents (ln(S, EPMA)), Al-Na-K, and Si-Al-Na-K only reproduce between 70% and 80 % of the data within 2σ analytical uncertainty (Table 5.3).

After excluding LS-17985 from the modelling procedure both the logarithmic model using sulfur content measured by EPMA and the multivariate model based on glass Al-Na-K concentrations reproduce a larger number of standards within the 2σ analytical uncertainty. The Al-Na-K model reproduces 92% of compositions within 2σ uncertainty, while the ln(S, SIMS) model reproduces 91% of compositions (Table 5.3). Both models could therefore serve as a potential correction method for composition-dependent IMF. The ln(S, SIMS) and ln(S, EPMA) models are comparable to each other if LS-17985 is excluded from the regressions. As shown in Fig. 5.8, the ln(S, EPMA) underestimates IMF for LS-17985 in sessions 2, 3, and 9 due to the significant difference between the measured S content by SIMS and by EPMA for this glass (Fig. 5.7).

While the ln(S, SIMS) model provides a good result in terms of reproducing the real δ^{34}S of our glass standard, it is not independent from the ^{34}S/^{32}S ratios measured

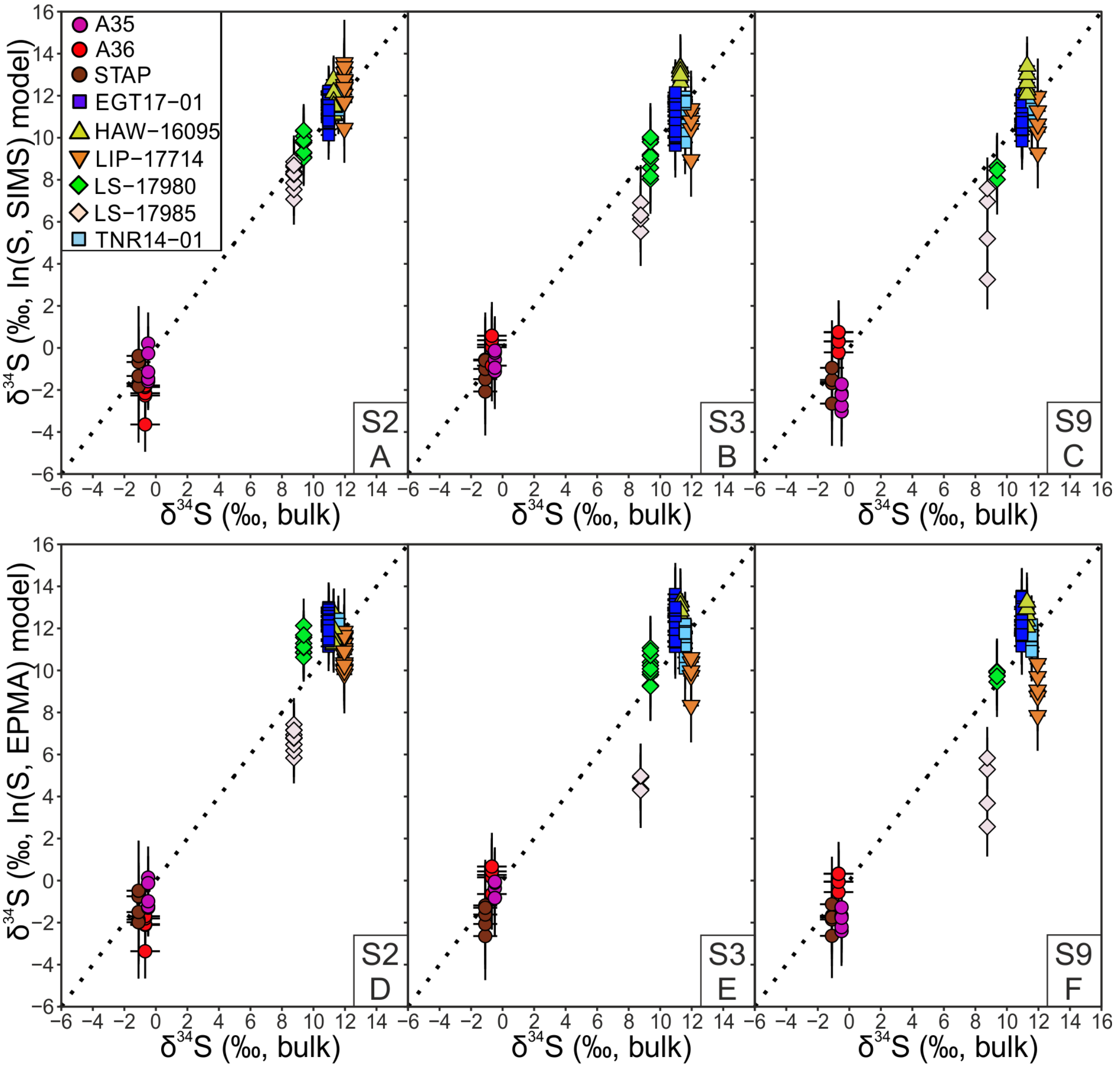

Figure 5.8: Fitted δ^{34}S values corrected for IMF using the ln(S) model plotted against bulk δ^{34}S of the glasses. In (A-C) IMF is calculated using SIMS sulfur contents (^{32}S cps/nA), while in (D-F) sulfur contents is measured by EPMA. The dotted lines show a 1:1 relationship. Each graph shows results for a different session (sessions 2, 3, and 9). Logarithmic models using EPMA- and SIMS-derived sulfur contents reproduce 59 and 87 % of the bulk δ^{34}S values within 2σ external uncertainty for data collected during sessions 2, 3, and 9, respectively. Error bars are 2σ uncertainty on both axes.

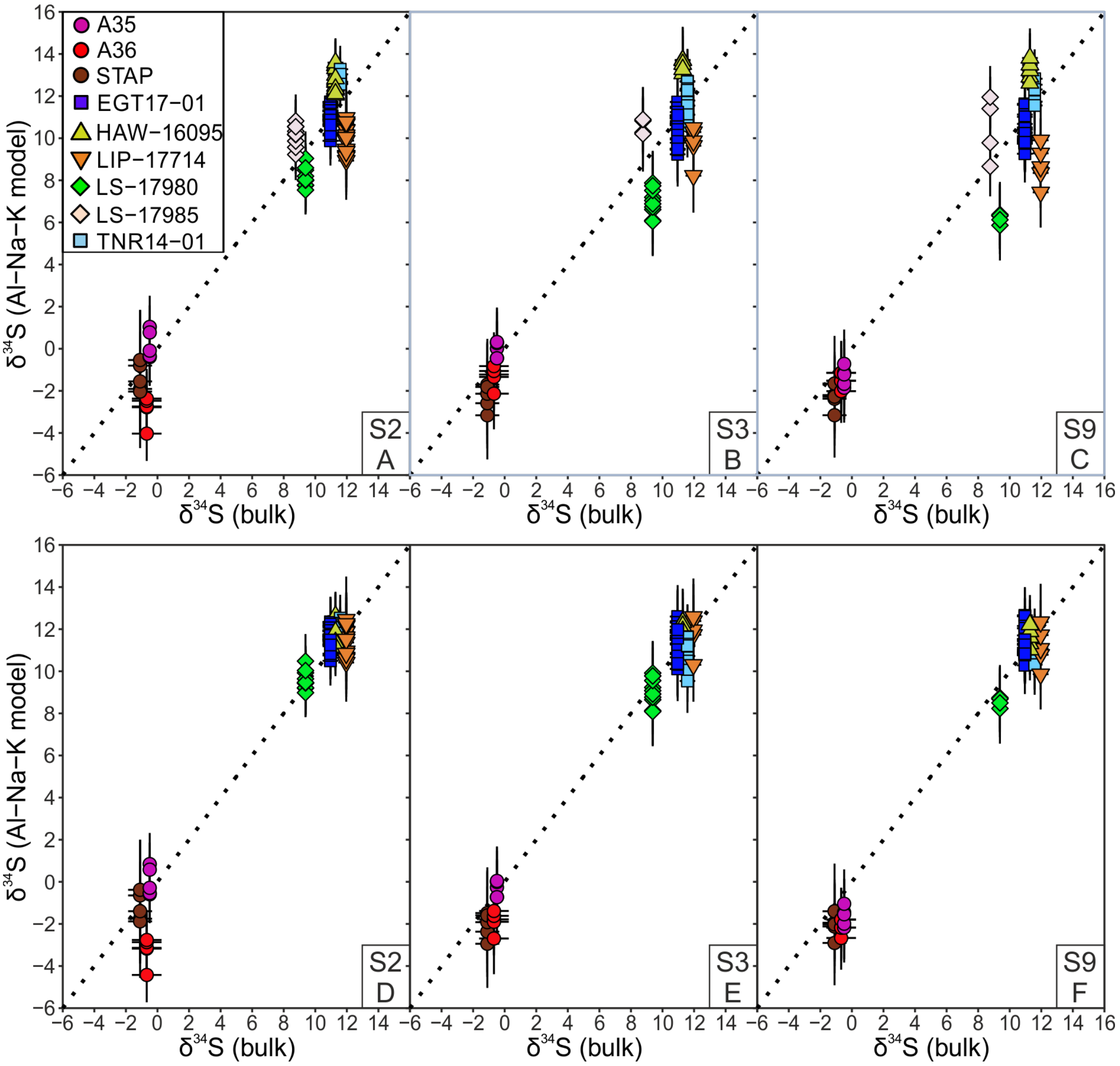

Figure 5.9: Fitted δ^{34}S values corrected for IMF using the Al-Na-K multivariate regression model plotted against glass bulk δ^{34}S. The dotted lines represent 1:1 relationship and session are the same as in Fig. 5.8. The top three graphs (A-C) show results using all glass analyses from the three session, while in the lower three graphs (D-F) LS-17985 was excluded. Using all glasses (A-C) 38% and 70% of the bulk δ^{34}S values are reproduced within 1σ and 2σ external uncertainty for the three session presented in this graph, respectively. The percentage of reproduced glass compositions increases to 58% (1σ) and 91% (2σ) when LS-17985 is excluded from the dataset.

by SIMS as it is based on the ^{32}S count rate. Therefore it cannot serve as a completely independent correction method for composition-dependent IMF during sulfur isotope analysis. The Al-Na-K model, after the exclusion of phonolitic glass LS-17985 from the dataset, reproduces standard compositions just as well as the ln(S, SIMS) model, and is completely independent of the SIMS analysis. Even with the phonolitic glass excluded, the Al-Na-K model is able to reproduce IMF for a large range of chemical compositions including alkali-rich and alkali-poor mafic volcanics, and a rhyolite. The phonolitic glass LS-17985 exerts a disproportionately large control over the correlation for this model due to its alkali- and Al-rich composition, hence this one glass can skew predicted IMF for other standards (Fig. 5.9). Furthermore, LS-17985 displays some signs of inter-fragment heterogeneity as seen in data from session 9 (Fig. 5.8C, F), which justifies its exclusion. However, it might be still appropriate as a matrix-matched standard for evolved alkali volcanics glasses. We find no significant improvement in either statistical parameters such as R^2 (Fig. 5.6) or in the number of analyses reproduced (Table 5.3) after adding new elements to the Al-Na-K correction scheme such as Ca and Si.

Session-by session variation in measured glass sulfur isotope ratios

Multivariate regression models, such as the Al-Na-K correction scheme, require the number of measured standards to be greater then a number of predictors (i.e. elements used in the fitting). This would require a large number of standards to be measured during each session. It is therefore important that the composition-dependent part of the IMF can be robustly predicted from one session to another, even after measuring just a few standards. Apart from IMF dependent on glass composition, the absolute value of measured ^{34}S/^{32}S by SIMS will be influenced by other factors related to the primary and secondary ion beams. The composition-independent part of the IMF should produce a constant offset in measured sulfur isotope ratios, evident from the near-parallel fits between glass sulfur content and IMF for session 2, 3, and 9 (Fig. 5.7).

Instrumental mass fractionation calculated using both the Al-Na-K multivariate regression model and the logarithmic fit to glass sulfur contents produces near-parallel fits when compared to measured IMF (supplementary Fig. S3 provided in the supplementary text). This indicates that these correction schemes provide a reliable way to predict composition-dependent IMF between different sessions; a few standards analysed regularly in each session are sufficient to obtain a good estimate for the constant offset in IMF that is composition-independent, but related to the ion beam. The calibration for composition-dependent IMF should be carried out before the analysis of unknown samples. Composition dependent IMF in our dataset stays constant for a relatively long (up to two weeks) time. As the multi-collector procedure used in this work only requires a short < 4 minute long analysis time per measurement this approach enables the acquisition of large datasets in a relatively short timeframe.

5.6.4 Possible causes of IMF during sulfur isotope analyses in glasses by SIMS

Processes controlling secondary ion formation during sample bombardment are not well understood, and cannot be predicted using current physical models (Hinton, 1995), therefore no process can be clearly implicated as the cause of the observed composition-dependent IMF. We find indication that secondary ion yield of sulfur in glasses is composition-dependent, based on the difference between sulfur contents measured by EPMA and the ^{32}S count rate during our analysis (Fig. 5.5). Our statistical analyses reveal that IMF correlates well with ln(S) and a multivariate regression model using Al-Na-K contents. It is possible these two correlations are not independent of each other.

Sulfur, Al, and alkali contents of the standard glasses could provide an explanation of what processes cause composition-dependent IMF in our dataset. Two glasses with the lowest observed IMF (HAW-16095 and TNR14-01, Fig. 5.4) relative to our primary drift correction standard EGT17-01 have the highest glass sulfur concentrations

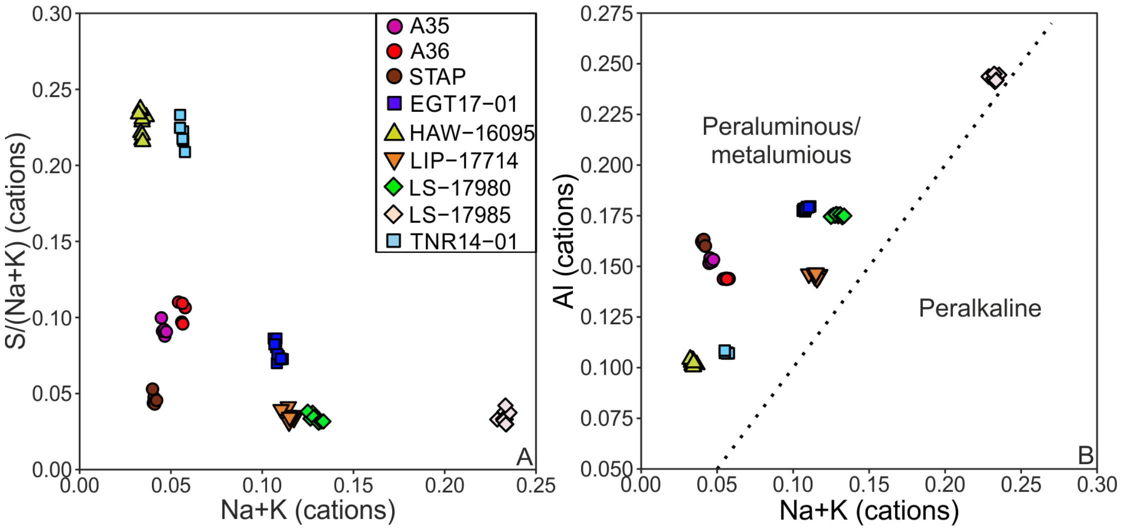

Figure 5.10: Atomic cation ratios of the glass standards. In (A) the amount of sulfur available to react with alkali elements (Na+K) during secondary ionisation relative to the alkali content of the glasses is shown. In (B) glass Al content is plotted against alkali total cations. In case of ionic bonds forming between Na^+/K^+ ions and S^- ions during beam-sample interaction would favour incorporating ^{34}S. In (A) glasses with similar Na+K content such as TNR14-01, HAW-16095, and the Icelandic glasses have more negative IMF as their S/(Na+K) ratio decreases, indicating that interaction between alkalis and sulfur might be limited by the amount of sulfur present in the ionised sample material. Symbol size is larger than 2σ error.

and lowest Al contents relative to their total alkali content (Fig. 5.1, 5.10). Natural Icelandic glasses have similar low alkali contents, but somewhat higher Al contents and lower sulfur to alkali ratios. However, natural Icelandic glasses have IMF between -3‰ to -12‰ (Fig. 5.4). LS-17980, a glass compositionally very similar to EGT17-01, has an average negative IMF of -3‰, with the only main difference between the two standards being the sulfur to alkali ratio (Fig. 5.10A). While this points to some degree of connection between IMF and sulfur to alkali ratios in the studied glasses, the correlation is not clear: EGT17-01 has a considerably lower S/(Na+K) ratio than HAW-16095, yet the latter sample has a negative IMF. Nonetheless, some relationship exists between IMF and S/(Na+K) at least for glasses with similar total alkali contents.

Alkalis such as Na and K both form 1+ ions, and both are highly reactive. During sulfur isotope analyses, secondary ions are analysed as $^{32}S^-$ and $^{34}S^-$, hence it is possible that negative sulfur ions interact with positively charged alkalis as the sample is ionised by the primary beam, producing complexes such as NaS and KS. As the electronegativity difference between alkalis and sulfur is relatively large (1.65 between S and Na, 1.76 between S and K) these bonds would be strongly ionic. If NaS and KS molecules form during beam-sample interaction they should preferentially incorporate heavier ^{34}S, as more complex, ionic bonded material favours the heavier isotopic species (Schauble, 2004). This would result in the loss of ^{34}S ions relative to ^{32}S that reach the detector, causing a decrease in measured ^{34}S/^{32}S and δ^{34}S. If ^{34}S is lost disproportionately during ion beam-sample interaction to alkali elements, that could serve as a possible explanation for the correlation between the Al-Na-K regression model and observed IMF. Nonetheless, no clear evidence can be found for such a process from glass alkali and sulfur contents. While glasses with low sulfur content and low S/(Na+K), such as LS-17980, do have a negative IMF compared to the primary drift standard EGT17-01, supporting the above hypothesis, glasses with low alkali contents such as the Icelandic glasses in our dataset also have negative IMF, indicating a loss of ^{34}S ions. This means that the formation of fewer alkali ions that are available to react with sulfur will not directly lead to more positive IMF values relative to EGT17-01. The role of Al in instrumental mass fractionation is less clear. Aluminium is inherently linked to Na and K in the glass structure (e.g. Mysen, 2005), hence Al content of the glass could have some effect on the ionisation of Na and K and subsequently influence the amount alkali-sulfur complex formation. A correlation can be observed between the relative amount of "lost" ^{32}S ions (calculated as the difference between EPMA- and SIMS-derived S contents) and glass (Na+K/Al) ratios (supplementary Fig. S4 provided in the text supplement of chapter five); however, this correlation is only evident in mafic glasses.

A possible test for the above hypothetical model is the measurement of KS$^-$ and NaS$^-$ count rates, ideally alongside ^{34}S/^{32}S ratios within glasses, which reveal any correlation between IMF and alkali-sulfur complex formation during sample beam interaction. However such measurements would be difficult to carry out in multi-collection mode due to the large mass difference between sulfur (masses 32 and 34), NaS (masses 55 and 57), and KS (masses 71 and 73) ions. Futher work would be required to better identify the causes of composition dependent IMF, possibly using a larger set of felsic glass standards, with highly variable Al and alkali contents, to investigate possible reactions between Al, alkalis, and sulfur during sample-beam interaction.

5.7 Conclusions

Sulfur isotope analyses of nine glass standards by multi-collector SIMS reveal significant composition-dependent instrumental mass fractionation effects in measured $^{34}S/^{32}S$ ratios. The magnitude of the IMF is up to -12‰ in some glasses, and is greater than the analytical uncertainty of 0.7-2 ‰ (2σ) at even low sulfur concentrations (< 600 ppm). This result is in contrast with previous studies where composition-dependent IMF during sulfur isotope was shown or assumed to be negligible. Multiple glass standards with known isotopic ratios covering at least the compositional range of unknown samples are required to investigate and accurately correct for composition-dependent IMF during multi-collector SIMS analysis of sulfur isotope ratios in glasses. Standard deviations measured for each session are lower then external uncertainty for eight of our nine glasses, hence they are suitable as primary standards; the one exception is our phonolitic glass, which displays heterogeneity both in terms of sulfur content and sulfur isotope composition above analytical uncertainty.

Statistical analyses including univariate, non-linear, and linear multivariate regression models reveal that observed IMF correlates logarithmically with glass sulfur content. A strong correlation is also observed between IMF and a multivariate regression model comprised of Al, Na, and K as predictors. After exclusion of our least reproducible phonolitic glass standard from the dataset we find that the ln(S) and the Al-Na-K multivariate regression models reproduce the bulk sulfur isotope ratios of the glasses for 91% (528 out of 579, 14 sessions) and 92% (306 out of 332, five sessions) of analyses within 2σ combined external uncertainty. We therefore recommend the use of the Al-Na-K multivariate regression model to correct for composition-dependent IMF as it is completely independent of the SIMS analysis and measured S isotope ratios, unlike the ln(S) regression model. Possible causes of IMF during sulfur isotope analysis of glasses may relate to complex ions forming between alkali elements and sulfur in the sample chamber during sample-beam interaction, although it is also possible that IMF is controlled by multiple factors not related to ion formation, such as atomic structure and coordination of various element such as alkalis and aluminium in the glass. Our standard set is useful to characterise composition-dependent IMF during multi-collector analysis of sulfur isotopes in glasses by SIMS, and can be used to predict IMF for a large range of mafic glass compositions, while also being applicable to certain silica-rich glasses such as alkali-rich rhyolites. Further work, involving a larger set of sulfur-containing felsic glasses would enable the better characterisation of IMF during sulufr isotope ratio analyses for silicic melts.

Chapter 6

Sulfur isotopes from El Hierro melt inclusions suggest recycled volatiles play a role in ocean island basalt melt generation

6.1 Abstract

El Hierro, located in the Western Canary Islands, erupts some one of the most sulfur- and carbon-rich basaltic magmas on the Earth. The cause of sulfur enrichment in these magmas can be either ascribed to low degree melting of a primtive mantle source or to the addition of volatiles into the mantle source from recycled, volatile-containing subducted slabs. Here we present sulfur isotope data from well-characterised El Hierro melt inclusions, matrix glasses, and lavas to decipher the origin of sulfur enrichment in these magmas. Using sulfur contents and sulfur isotope compositions together with trace element contents we estimate that El Hierro primary magmas contain around 5000

ppm S, have a δ^{34}S of 4±0.75‰, and their S/Dy ratio is 870±194, well above the ambient mantle estimates. Using these primitive melt S, Dy and δ^{34}S we estimate the sulfur content of the El Hierro mantle source to be around 700 ppm, which is more than two to 3.5 times that of the primitive mantle (200-350 ppm). The El Hierro mantle source is also enriched in ^{34}S compared to the upper mantle. This mantle source could have formed via metasomatic reactions between the ambient upper mantle and volatile-rich melts originating from previously subducted oceanic lithosphere that contained ~650 ppm sulfur. A proportion of the recycled sulfur was likely present as sulfate in the recycled slab that can deliver excess ^{34}S into the El Hierro mantle source. Our results indicate sulfate may not be completely mobilised in the subducting slab and transferred to the mantle wedge, but can be retained and recycled into the mantle. Recycled slabs containing S^{6+} could provide an effective way to add oxidised material into the mantle, causing widespread redox heterogeneity in the asthenosphere. Our results suggest oxidised sulfur likely plays a major role in the formation of low-fraction, fluid-rich melts that lower the mantle solidus and ultimately facilitate the generation of low-degree, silica deficient, and oxidised alkali ocean island basalts.

6.2 Introduction

Volatile elements exert significant control on every aspect of magmatism from melt generation to eruption dynamics. Therefore, to fully understand magmatic processes, reliable estimates of primary magmatic volatile contents are essential. The determination of primary magma volatile contents are hindered by their low solubility (carbon), fast diffusion (hydrogen), and saturation/immiscibility (sulfur) in many magmatic systems. While some mid-ocean ridge basalts (MORB) remain volatile undersaturated as they erupt on the ocean floor (Saal et al., 2002), many volatile-rich, subaerially erupted magmas are extremely degassed, retaining only a fraction of their original volatile contents.

Melt inclusions (MIs) provide a possible way to circumvent volatile loss through degassing. Entrapped at high pressure within their host crystals, MIs can often retain original magmatic volatile contents (e.g. Frezzotti, 2001; Métrich and Wallace, 2008), albeit many processes can alter melt inclusion volatile contents post-entrapment (Danyushevsky et al., 2002; Gaetani et al., 2012; Hartley et al., 2014; Venugopal et al., 2020).

Measurement of volatile element isotope ratios within MIs together with their concentrations can provide a valuable tool to identify processes that lead to volatile loss before or after entrapment. For example, diffusive H_2O loss can be identified, and possibly corrected for, using MI D/H ratios (Bucholz et al., 2013). A major limitation of this approach is the analytical challenge associated with microanalysis of volatile element isotopes in melt inclusions, most notably in the case of sulfur and carbon isotopes. Data on carbon isotopes in glasses are currently not available in the literature, while sulfur isotope data are scarce. In addition, the matrix effects associated with sulfur isotope measurements in glasses made by secondary ion mass spectrometry (SIMS) have often been left uncharacterised, or thought to be negligible (Black et al., 2014; Fiege et al., 2014; Beaudry et al., 2018), even though some analyses indicate they may be significant (Shimizu et al., 2019). Recent advances in characterising composition-dependent matrix effects during sulfur isotope analysis in glasses by SIMS makes high-precision analyses of $^{34}S/^{32}S$ ratios possible (see chapter 5 for more detail). Such analyses can enable scientists to detect and correct for sulfur degassing/saturation and to retrieve primary magma sulfur contents and sulfur isotope ratios. Furthermore, as sulfur isotopes are efficiently fractionated during surface processes, such as ocean floor alteration (Alt and Shanks, 2003, 2011), sulfur isotope ratios measured in MIs have the potential to provide valuable insight on the long-term sulfur cycle of the Earth (i.e. recycling during slab subduction) and volatile heterogeneity in the mantle. The sulfur isotopic composition of undegassed melts may help answer current major questions related to the long-term sulfur cycling, such as what phases and in what quantity is sulfur recycled into the mantle via subduction zones?

Here we present sulfur isotope ratios from young (< 20 ka) El Hierro tephra samples containing extremely carbon- and sulfur-rich melt inclusions which already have been characterised for trace and volatile elements (chapter four, Taracsák et al. 2019), together with the sulfur isotopic composition of El Hierro lava samples. Sulfur isotope data are used to estimate fractionation factors during sulfur degassing and to recalculate primary melt sulfur contents and isotope compositions. We have used sulfur data with trace element contents and melting models to estimate the sulfur content of the mantle source of El Hierro magmas. Our data provide new insights into the formation of volatile and trace element enriched OIBs, mantle redox conditions, and on the behaviour of sulfur in the long-term geochemical cycling of volatiles from the surface of the Earth to the mantle.

6.3 Samples and analytical methods

Melt inclusions and matrix glasses analysed for sulfur isotopes are all from glassy, rapidly quenched tephras collected from scoria deposits. Tephra samples used here are identical to those that were used in chapter four. Lava samples collected from flows that are connected to the scoria cones were also analysed for their bulk S isotope compositions. Samples represent the last 20 ka activity of El Hierro (i.e. the platform-forming rift volcanism stage, Carracedo et al. 2001). A number of melt inclusions used in this chapter are have already been presented in chapter four of the thesis, therefore major, trace, and volatile element data is available from these inclusions. However, a number of melt inclusions analysed for sulfur isotope ratios have not been presented in chapter four. These inclusions, after sulfur isotope ratio analyses, have been analysed for their major element, sulfur, and halogen contents by electron probe microanalysis (EPMA) using a Cameca SX100 instrument at the University of Manchester using the same analytical conditions that are presented in chapter three. Petrographic description of the lavas is provided in chapter seven, while melt inclusions petrography is provided in chapter four.

Sulfur isotope analysis of 10 lava samples was carried out at the Godwin Laboratory, University of Cambridge, using a Thermo Finnegan Delta V Plus GS-IRMS. Extraction of sulfur was carried out in two steps, first using HCl and $CrCl_2$, followed by extraction by Thode's solution. Full detail of the analytical procedures, including those used to measure bulk lava sulfur contents, are given in chapter three.

Sulfur isotope ratios of 67 melt inclusions and melt embayments (glass within crystals still connected to the melt via a thin channel, see chapter two section 2.5 for more detail on melt inclusion studies in general and chapter four section 4.3 for discription of melt inclusions used here) together with eight matrix glasses were measured at the NERC Ion Microprobe Facility at the University of Edinburgh. Analyses were carried out using a Cameca IMS-1270 instrument operated in multi-collector mode. We used a primary beam with 2-3.7 nA beam current, 10 μm diameter and 10 kV. After 60 s pre-sputtering, secondary ions were accelerated into the mass spectrometer at 10 kV. $^{32}S^{-}$ and $^{34}S^{-}$ ions were detected using a Faraday cup and an electron multiplier detector, respectively. Precision of SIMS sulfur isotope analyses are detailed in chapter five. The most S-poor matrix glasses and melt inclusions with <300 ppm S have an external analytical error of 2-3.7‰, while the most S-rich inclusions have analytical errors between 0.6‰ and 1‰ (2σ). Sulfur isotope data in this chapter is expressed in permil relative to V-CDT ($^{34}S/^{34}S$ = 0.044162589, Ding et al. 2001).

Instrumental mass fractionation (IMF) arising during sulfur isotope analysis of glasses by SIMS was corrected using a multivariate regression fit based on the Al, Na, and K contents of the glasses measured by EPMA. The correction method used here is extensively detailed in chapter five. Correction values were calculated using eight standards, two of which have similar composition to the unknown samples. Seven of the glasses used to correct IMF are mafic, and one is rhyolitic. Correlations between measured IMF and standard Al, Na, and K contents were used to model IMF for unknown El Hierro samples. Unknowns were corrected using two regression fits, collected during the first and second week of the analytical session, respectively. No significant difference in IMF-corrected δ^{34}S values can be observed for the El Hierro glasses depending on which regression fit is used, as the predicted IMF values calculated using Al-Na-K correction fits are close to parallel for each session (see supplementary material provided with chapter 5 for detail). To demonstrate the importance of IMF-correction for unknown sulfur isotope datasets, both uncorrected and corrected δ^{34}S values are provided in Fig. 6.1.

6.4 Results

El Hierro melt inclusions were corrected for post-entrapment crystallisation (PEC) using Petrolog3 (Danyushevsky and Plechov, 2011). Olivine was added or subtracted from the glass if the inclusion was found to be in disequilibrium with its host. This correction method requires knowledge of the original FeO content of the melt, which was estimated using a linear fit between Fe and Si content ($R^2 = 0.94$, see supplementary spreadsheet for chapter six) of previously published whole-rock and glass data from El Hierro not affected by PEC or diffusive Fe-loss. To calculate FeO from total Fe content, oxygen fugacity of the melt was assumed to be two log units above the fayalite-magnetite-quartz (FMQ) buffer (Moussallam et al. 2019, see chapter seven for more details on oxygen fugacity of El Hierro magmas). Glass $Fe^{3+}/\sum Fe$ ratios were calculated using the method of Kress and Carmichael (1991). Melt embayments were not corrected for either PEC or diffusive Fe-loss.

Sulfur contents of El Hierro melt inclusions and matrix glasses vary between 120

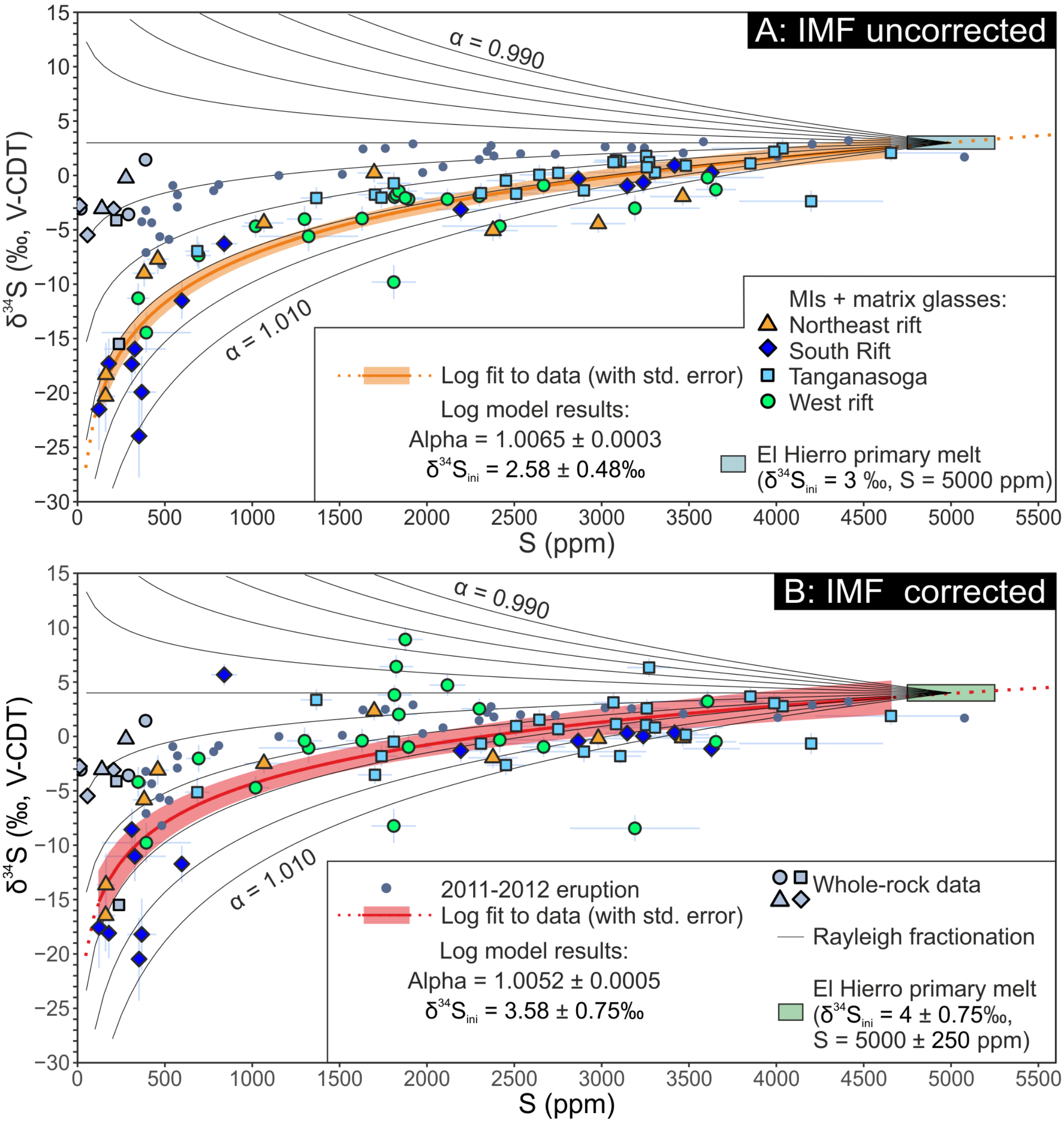

Figure 6.1: Sulfur isotope composition of El Hierro melt inclusions, matrix glasses, and lava samples plotted against S content measured by EPMA. Plot (A) shows IMF uncorrected MI and matrix glass data, while in (B) sulfur isotopic compositions have been corrected for IMF. Solid black lines are open system degassing curves calculated using Rayleigh fractionation and variable α values between 0.990 and 1.01 using 0.002 intervals. Orange (A) and red (B) lines are logarithmic fits to the melt inclusion and matrix glass data, while shaded areas represent one standard error of the fit. $\delta^{34}S_{ini}$ is the intercept of the logarithmic fit, interpreted as the sulfur isotopic composition of the melt at maximum melt inclusion S contents (4660 ppm), while alpha is the slope of the logarithmic fit, equal to the observed fractionation factor (see equation 6.2). Coloured rectangles represent the inferred El Hierro primary magma S contents and sulfur isotope composition. Glass and MI data for the 2011-2012 El Hierro eruption are from Beaudry et al. (2018), and are uncorrected for matrix effects. Error bars are 2σ.

and 4660 ppm (Fig. 6.1), ranging from close to totally degassed to highly undegassed with regards to sulfur. This sulfur content range is similar to that measured in MIs and matrix glasses from the 2011-2012 eruption of El Hierro (Longpré et al., 2017). Lava samples have considerably lower sulfur contents (<400 ppm) than melt inclusions, but are similar to the tephra matrix glasses (160-690 ppm).

Trace element contents and ratios in melt inclusions and matrix glasses are highly variable (see Taracsák et al. 2019 or chapter 4 for more detailed discussion on melt inclusions trace element contents): Dy varies between 6.0 and 12.7 ppm (Fig. 6.2), while Ce/Yb ratios are between 13 and 143, with lowest Ce/Yb observed in melt inclusions and matrix glasses erupted in the western rift of El Hierro (Fig. 6.3A). Melt inclusion and matrix glass S/Dy ratios are between 31 and 538 (Fig. 6.3). Major, trace, volatile element composition, together with sulfur isotope ratios, measured in MIs and matrix glasses are provided in the supplementary spreadsheet that contains all glass and whole rock data.

6.4.1 Sulfur isotopic compositions of El Hierro lavas, melt inclusions and glasses

El Hierro lavas have bulk δ^{34}S values between -15.5‰ and +1.4‰, with nine of the 10 samples falling between -5.5‰ and +1.4‰ (Fig. 6.1). Lavas are generally more enriched in ^{34}S than matrix glasses and degassed MIs with similar sulfur contents, which have δ^{34}S values <-7‰. The one exception is a lava sample with a δ^{34}S of -15.5‰ (Fig. 6.1).

δ^{34}S values measured in El Hierro melt inclusions and matrix glasses are between -20.5‰ and +8.1‰ after correction for composition-dependent IMF (Fig. 6.1B). The size of the IMF correction was between -12.1‰ and +5.5‰. IMF correction introduces larger scatter into the data that is not observed in the uncorrected δ^{34}S data; the latter has a stronger logarithmic relationship with S content ($R^2 = 0.85$) than the IMF corrected data ($R^2 = 0.60$). However, to our knowledge this is the first glass $\delta^{34}S$ dataset that has been systematically corrected for compositional matrix effects, hence it is possible that the larger scatter in the data reflects true natural variability rather than overcorrection. The Al-Na-K regression scheme used to correct the data has been demonstrated to reproduce bulk sulfur isotope compositions of mafic glass standards with high accuracy (see chapter 5). Sulfur isotope ratios measured in lavas, MIs, and matrix glasses are presented in the supplementary spreadsheets.

6.5 Discussion

6.5.1 Sulfur isotope fractionation during OIB degassing

As sulfur is degassed from the magmatic system it can cause fractionation in $\delta^{34}S$ between the gas and the melt. The fractionation factor α during sulfur degassing is known to vary significantly as a function of sulfur speciation in the melt and the gas phase, hence α is inherently linked to the oxygen fugacity (fO_2) of the system (Sakai et al., 1982; Marini et al., 2011; Liotta et al., 2012; Fiege et al., 2014). The logarithmic correlation between $\delta^{34}S$ and sulfur content in El Hierro MIs and glasses indicates that $\delta^{34}S$ is primarily controlled by open-system degassing (Fig. 6.1). Stable isotope fractionation during open-system degassing can be modelled using the following equation (Rayleigh distillation):

$$({}^{34}S/{}^{32}S)_m = ({}^{34}S/{}^{32}S)_i * F^{\alpha\text{-}1} \qquad (6.1)$$

where ${}^{34}S/{}^{32}S_m$ and ${}^{34}S/{}^{32}S_i$ are the sulfur isotope ratios in the final and the initial melt, F is the fraction of sulfur remaining in the melt (calculated as S_{melt}/S_{max}), and α is the fractionation factor between gas and melt. Rearranging this equation into a logarithmic format results in:

$$ln({}^{34}S/{}^{32}S)_m = ln({}^{34}S/{}^{32}S)_i + (\alpha - 1) * \ln(F) \qquad (6.2)$$

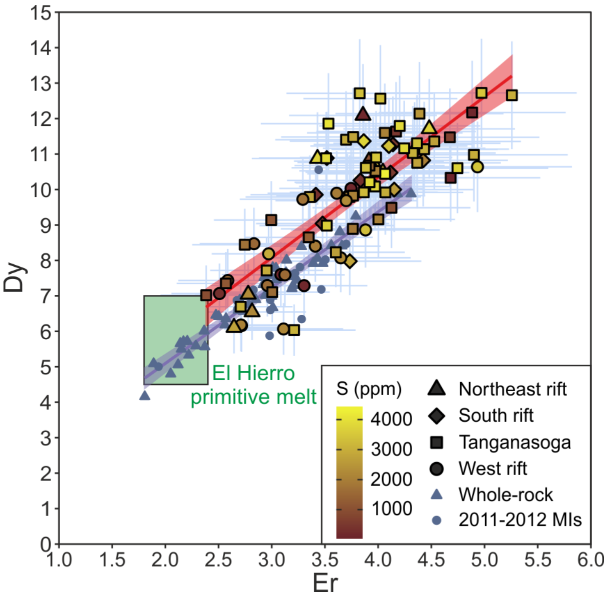

Figure 6.2: Dy versus Er content of El Hierro MIs, matrix glasses, and whole-rock samples taken from the literature. Linear regressions are fitted to MI and matrix glass data measured in the same samples as the sulfur isotope data (red line, data from Taracsák et al. 2019) and to whole-rock and MI (2011-2012 eruption, Longpré et al. 2017) data previously published from different El Hierro samples (purple line). Erbium correlates the best with Dy in El Hierro samples (R^2 is 0.85 for the purple line and 0.66 for the red line), therefore Er is the most suitable element to estimate the possible range of primary Dy contents in El Hierro magmas, represented by the green rectangle. Lowest primary magma Dy estimates are 4.5 ppm based on whole-rock samples while upper estimate is 7 ppm based on the Dy content of most Er poor MIs. Least evolved whole-rock samples (Mg-number >67) have Dy between 4.8 and 6.7 ppm. Error bars are 2σ.

Using equation 6.2, a fit between the logarithm of the melt $^{34}S/^{32}S$ ratio and the logarithm of the S_{melt}/S_{max} content can be used to determine the value of α-1, which is the slope, and $\ln(^{34}S/^{32}S)_i$, which is the intercept in equation 6.2.

Using a fit between the logarithm of the IMF-corrected El Hierro MI and matrix glass S isotope ratios and logarithm of their S contents an α of 1.0052±0.0005 can be derived, which is represented by the red curve in Fig. 6.1B on a non logarithmic plot. Recent estimates of sulfur isotope fractionation factors between gas and melt vary between 0.9985 and 1.0067, decreasing at higher fO_2 (Fiege et al., 2014). The modelled α value of 1.0052 indicates that degassing occurred at fO_2 conditions around FMQ+1. Note that this values would represent an average fO_2, as its value changes with sulfur degassing, cooling, ascent, and crystallisation (fO_2 evolution of El Hierro magmas is discussed in chapter seven). This is consistent with the fO_2 of FMQ+0.9 to FMQ+1.1 recorded by matrix glass S-speciation (data is provided in chapter seven) and the results of ilmenite-magnetite oxybarometry (~ FMQ+1.6) from the 2011-2012 eruption (Longpré et al., 2014), but ~1 log unit more reducing than estimates for undegassed El Hierro primary melts (Moussallam et al. 2019; also see chapter seven for more detail).

We also modelled fractionation factors using the method described by Marini et al. (2011), which utilises the temperature dependence of α between oxidised and reduced sulfur species in gas and melt (H_2S-S^{2-} and SO_2-SO_4^{2+}, Sakai et al. 1982; Miyoshi et al. 1984; Taylor 1986). This method requires the knowledge of SO_2/H_2S and SO_4^{2+}/S^{2-} ratios in the gas and melt during degassing. We calculated a degassing path using DCompress (Burgisser et al., 2015) which provides estimates for both gas SO_2/H_2S and melt SO_4^{2+}/S^{2-} ratios. Starting pressure, temperature, fO_2, H_2O content, and CO_2 content for the degassing model was set at 700 MPa, 1150 °C, FMQ+2, 2 wt%, and 1 wt%, respectively. Pressure and temperature and fO_2 values are based on clinopyroxene-melt thermobarometry and spinel-olvine oxybarometry data (see chapter seven for more detail), while H_2O and CO_2 contents are based on results presented in chapter four. Using this modelling approach α values close to 1.0049 can be estimated for most of the degassing path, which is within the error of our 1.0052±0.0005 estimate.

Magmatic oxygen fugacity is affected by degassing and fractional crystallisation. In the case of El Hierro a decrease in fO_2 can be observed with S degassing (Longpré et al., 2017; Moussallam et al., 2019), which could lead to an increase in α (Fiege et al., 2014) as the melt evolves and degasses. Our estimate for α represents the average value throughout the whole of the degassing process. Changes in α as a function of melt fO_2 could explain the large scatter of δ^{34}S observed at ~2000 ppm S content in our dataset (Fig. 6.1/B).

Most El Hierro lava samples have a notably heavier isotopic composition than degassed glasses, with lava samples plotting along the α = 1.002 fractionation curve (Fig. 6.1). Decoupling between matrix glasses and lavas may be connected to the crystallisation or separation of sulfide in the groundmass material, which can be observed in lava samples, but are uncommon in tephras. ^{34}S may partition preferentially into sulfides that form during the crystallisation of lava groundmass microlites. However, fractionation factors between sulfides and silicate melt have not been precisely measured to date, hence the cause of this difference is challenging to explain with the currently available data.

6.5.2 Sulfur budget of El Hierro primary melts and their mantle source: recycled versus primordial sulfur

The sulfur contents of primary magmas erupting in mid-ocean ridge or ocean island settings are thought to be limited by the sulfur concentration at sulfide saturation (SCSS) of the melt, which is strongly dependent on pressure, melt composition (Liu et al., 2007; Fortin et al., 2015; Nash et al., 2019), and fO_2 (Jugo et al., 2010). As the mantle is relatively reducing (Ballhaus, 1993; Williams et al., 2005), sulfur will be stored as sulfide in the asthenosphere. The SCSS will exhibit a primary control on melt S contents for MORBs and OIBs (Ding and Dasgupta, 2017, 2018), causing MORBs and various OIBs to have similar primary melt sulfur contents between 1000-2000 ppm (Saal et al., 2002; Vigouroux et al., 2009; Sides et al., 2014; Shimizu et al., 2016; Rose-Koga et al., 2017). Magmas erupting in arc settings, due to the more oxidising conditions in the sub-arc mantle (Kelley and Cottrell, 2009), can contain sulfur in excess of 4000 ppm (Zimmer et al., 2010), well above literature SCSS estimates (Liu et al., 2007; Jugo et al., 2010; Fortin et al., 2015).

At El Hierro, MIs from platform forming rift volcanics contain up to 4660 ppm sulfur, while MIs from the 2011-2012 eruption contain up 5080 ppm (Longpré et al., 2017). Therefore the sulfur contents of El Hierro magmas are more akin to the most sulfur-rich arc magmas than typical MORB or Hawaiian magmas (Fig. 6.3). Most sulfur-rich MIs have the heaviest δ^{34}S values: 16 out of 20 MIs with S contents above 3000 ppm have δ^{34}S between -0.7‰ and +3.7‰ (Fig. 6.1B). As the S contents of El Hierro MIs and matrix glasses is controlled by open-system degassing, indicated by the logarithmic relationship between S δ^{34}S (Fig. 6.1), and it is possible to recalculate the S content and isotopic composition of the primary melt through equation 6.2.

Sulfur is known to partition effectively into fluids from silicate melt at high pressure (Jégo and Dasgupta, 2014). The high CO_2 contents observed in El Hierro magmas cause fluid saturation at depth below the crust-mantle boundary (Taracsák et al., 2019), which may facilitate some sulfur to partition into the fluid phase from the melt. Therefore we suggest that our most S-rich MI at 4660 ppm may be already slightly degassed, and that El Hierro primary magmas contain around 5000±250 ppm sulfur, i.e. similar to the most S-rich melt inclusions from the 2011-2012 eruption (Longpré et al., 2017). Extending the logarithmic fit in Fig. 6.1B to 5000 ppm S results in a primary melt δ^{34}S value of +4.0±0.75‰, which is within error of the fitted δ^{34}S value at maximum MI sulfur content (+3.58±0.75‰, Fig. 6.1B). This estimate is considerably higher than the upper mantle estimate of -1.28±0.33‰ (DMM, Labidi et al. 2013), and is in line with the estimate of a δ^{34}S value of +3‰ based on MIs from the 2011-2012 eruption of El Hierro (Beaudry et al., 2018).

Sulfur and Dy contents of melt inclusions are often used together to decipher primary melt and mantle source sulfur contents, as they are thought to behave similarly during mantle melting and melt evolution, i.e. have similar distribution coefficients during melting and crystallisation, at mid-ocean ridges (Saal et al., 2002; Shimizu et al., 2016). While such a connection has been established for MORBs, which form through ~20 % melting of spinel peridotite, it may be less evident for OIBs, as melting degrees at ocean islands are highly variable, and the source is often garnet peridotite. During

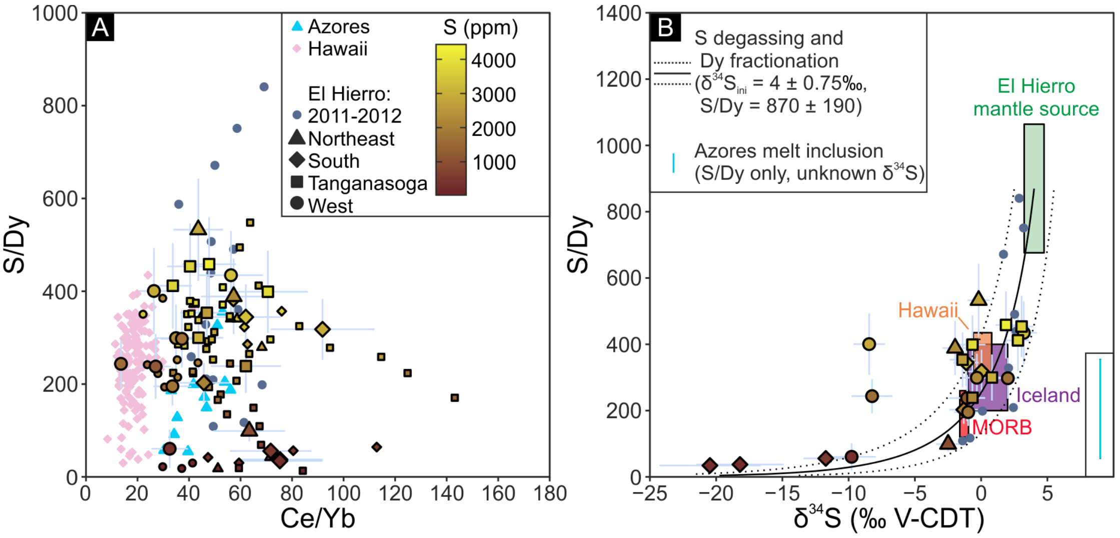

Figure 6.3: S/Dy ratios of glasses and melt inclusions from El Hierro plotted against Ce/Yb (A), including various literature data from other ocean islands. Hawaii MI data are from Sides et al. (2014); the Azores MI data is taken from Rose-Koga et al. (2017). Melt inclusion data from the 2011-2012 eruption of El Hierro are from Longpré et al. (2017). Larger symbols in (A) represent MIs from which sulfur isotope data are available, smaller symbols are data from the same samples published by Taracsák et al. (2019) (i.e. data in chapter 4). In (B) S/Dy is plotted against $\delta^{34}S$. S/Dy ratios for Iceland are from Bali et al. (2018). MORB S/Dy ratios are based on a sulfur content of 1200±150 ppm (Ding and Dasgupta, 2017) and a Dy content of 6.3±2.1 ppm (Hofmann, 1988), while $\delta^{34}S$ are taken from Labidi et al. (2013). Sulfur isotopic compositions of Icelandic and Hawaiian magmas are based on $\delta^{34}S$ values measured in lavas (Sakai et al., 1982; Torssander, 1989). $\delta^{34}S$ values for the El Hierro 2011-2012 melt inclusions are from Beaudry et al. (2018). The El Hierro mantle source is based on a 5000±250 ppm primary melt S content, 5.75±1.25 ppm Dy content, and a $\delta^{34}S$ of +4.0±0.75‰. Solid black line is a model combining open-system sulfur degassing and Dy fractionation. Sulfur degassing is modelled using the α value in Fig. 6.1B, and assumes 99% degassing at the final step, while Dy fractionation is modelled using a 5.75 ppm starting and 12 ppm final Dy content. Dashed lines represent the model error (2σ). Error bars for symbols are 2σ.

melting in the presence of garnet Dy can be retained in the residue, while the partitioning of sulfur will be controlled by the fraction of sulfide in the source and fO_2 conditions (Ding and Dasgupta, 2017, 2018; Mungall et al., 2006), both of which can be variable in OIB mantle sources. However, due to the large number of both S and Dy analyses from El Hierro, S/Dy ratios may still provide a robust estimate of mantle S contents. As trace element data are available for some of the melt inclusions analysed for S isotopes (Fig. 6.2, 6.3; see chapter four for detailed discussion of El Hierro melt inclusion trace element contents), S/Dy of the El Hierro primary magmas can be determined. Dysprosium contents in El Hierro magmas are controlled by fractional crystallisation alone (Fig. 6.2). However, due to fluid saturation in the early stages of magma evolution, measured melt inclusion S and Dy contents are decoupled from each other and may not be representative of the primary melt and the mantle source. The Dy content and its possible variability in the primary melt can be estimated by fitting a linear regression between Dy and an element that partitions similarly during crystallisation, such as Er (Fig. 6.2). Using MI, glass and whole-rock data, El Hierro primary melt Dy contents can be estimated at 5.75±1.25 ppm, with whole-rock samples indicating somewhat lower primary Dy content than MIs (Fig. 6.2). A similar range can be obtained by considering whole-rock samples with Mg numbers > 0.67 (Mg number defined as Mg/(Mg+Fe^{2+})): Dy contents of these samples are between 4.8 and 6.7 ppm.

Our primary melt S and Dy contents give a S/Dy ratio of 870±194, which is considerably higher than estimates for MORB mantle and also higher than S/Dy ratios measured in MIs from other OIBs (Fig. 6.3B). El Hierro primary melt S/Dy is also higher than those measured in El Hierro MIs, which are below 600; only three inclusions from the 2011-2012 eruption have S/Dy ratios that are comparable to our estimate (Fig. 6.3A). Concurrent open-system S degassing and a change in melt Dy content caused by silicate crystallisation reproduces observed El Hierro MI S/Dy and δ^{34}S values well, apart from two outlier compositions from the western rift (Fig. 6.3B). Therefore, while most El Hierro MIs have S/Dy ratios similar to those of Icelandic or Hawaiian MIs, due to the early fluid saturation and the decoupling between S and Dy many inclusions already record lower S/Dy than those of the primary melt.

Using primary melt S/Dy estimate of 870±194 for El Hierro and a primitive mantle Dy content of 0.674 ppm a mantle S content of 586±143 ppm can be derived. This is >300 ppm higher than primitive mantle estimates of 200-350 ppm S (McDonough and Sun, 1995; Palme and O'Neill, 2003; Lyubetskaya and Korenaga, 2007). Such mantle

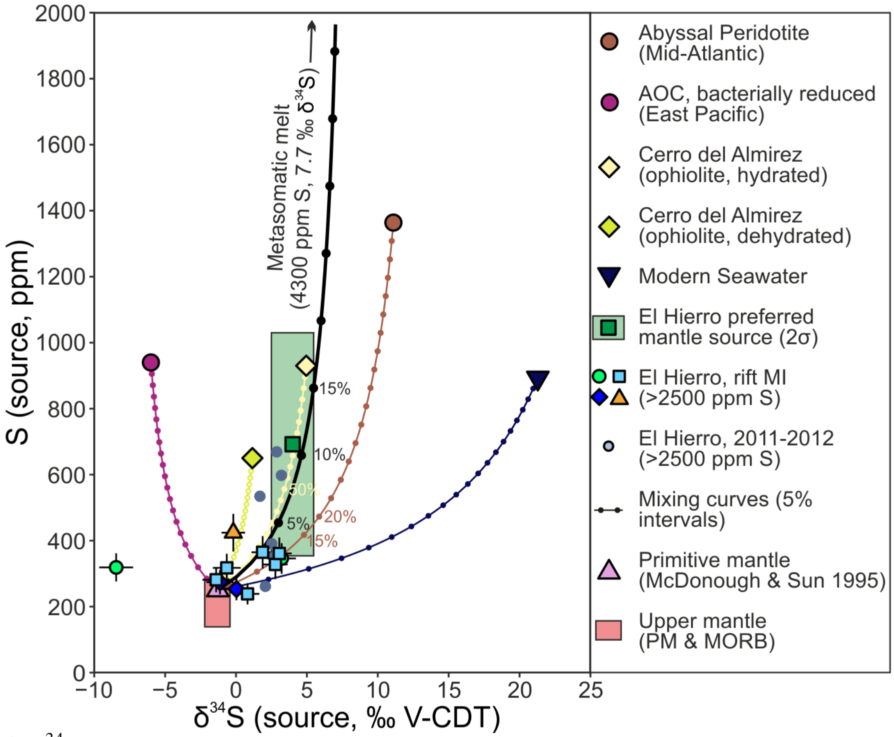

Figure 6.4: δ^{34}S-total S mixing models between various possible sulfur reservoirs including upper mantle, primitive mantle, and multiple recycled components (values are averages for each location): bacterially reduced altered oceanic crust (Alt and Shanks, 2011), hydrothermally altered abyssal peridotite (Alt and Shanks, 2003), and ophiolites (Alt et al., 2012). Mantle δ^{34}S is from Labidi et al. (2013); MORB and primitive mantle S contents are estimated at 195±45 ppm (Ding and Dasgupta, 2017) and 250±50 ppm (McDonough and Sun, 1995) respectively (1σ). The El Hierro mantle source is estimated to contain 692±169 ppm S (1σ), assuming a mantle source with 0.796 ppm Dy and no S-Dy fractionation during melting. The El Hierro mantle S content and isotope composition is best modelled by the addition of 5-15% of metasomatic melt formed by melting a recycled oceanic lithosphere containing 80% abyssal hydrothermally altered peridotite and 20% altered oceanic crust (black curve).

S contents, together with the enrichment of heavy ^{34}S in the mantle source of El Hierro, requires large quantities of recycled S to be present in the source.

Radiogenic (Sr, Nd, Pb, Os) and oxygen isotope data of whole-rock samples suggest that around 5-10% recycled oceanic lithosphere is present in the Western Canary Island mantle source containing variable proportions of altered oceanic crust (AOC) and lithospheric mantle (Day et al., 2010). This recycled component may provide an explanation for the elevated mantle S contents. Available data on AOC and abyssal peridotites indicate they contain between 900 and 1300 ppm S (Alt and Shanks, 2003, 2011), while ophiolites contain around 600 to 900 ppm S, depending on the level of sulfur loss caused by metamorphism (Alt et al., 2012). They can also cover a wide range in δ^{34}S (Fig. 6.4). Based on mixing models a hydrated ophiolite can explain El Hierro mantle source S contents and S isotope composition if the mantle source contains more than 50% recycled ophiolite component, which is well above the 5-10% suggested by other isotope systems (e.g Day et al., 2010) or by melting modelling (see chapter four, Fig 4.9). To achieve sufficient S enrichment with the addition of ~10% recycled material an intermediate process would be required that effectively extracts sulfur from the recycled oceanic lithosphere.

If the recycled oceanic lithosphere containing S and C undergoes volatile-fluxed melting at a depth ~300 km (Dasgupta and Hirschmann, 2006), the resulting melt could sufficiently enrich the surrounding asthenosphere in sulfur through metasomatic reaction. Furthermore, if the recycled oceanic lithosphere contains mostly sulfur originating from heavy, seawater-derived sulfate it could also explain the enrichment of ^{34}S in the mantle source (Fig. 6.4). By melting a recycled oceanic lithosphere containing ~650 ppm S similar to dehydrated ophiolite (Alt et al., 2012) by 15%, and assuming total consumption of S during the process from both sulfate and sulfide, a melt with ~4300 ppm S can be produced (Fig.6.4). The isotopic composition of this melt will be dependent of the source of S in the recycled material (bacterial vs. hydrothermal). The El Hierro mantle source δ^{34}S value of ~4‰ and the elevated S contents can be reproduced by the addition of 5-15% metasomatic melt with ~4300 ppm S, formed from a source containing 80% hydrothermally altered lithospheric mantle with a δ^{34}S of 11.1‰ (Alt and Shanks, 2003) and 20% bacterially altered oceanic crust with a δ^{34}S of -6.0‰ (Alt and Shanks, 2011), resulting in a bulk recycled lithosphere δ^{34}S of 7.7‰ (Fig. 6.4). The addition of 5-15% metasomatic melt into the upper mantle is in line with previous estimates of the amount of recycled component in the Western Canary Islands (Day et al., 2010), while also explaining modelled sulfur contents and sulfur isotope ratios.

The addition of a metasomatic melt would also change the Dy content of the mantle source, hence using a Dy representative of an un-metasomatised primitive mantle could be incorrect to calculate mantle source S contents from S/Dy ratios. The Dy content of the metasomatic melt can be calculated using the same parameters as used for sulfur, i.e. assuming a uniform 15% melting degree for a recycled oceanic lithosphere containing 80% lithospheric mantle and 20% AOC. The lithospheric mantle composition is approximated using abyssal peridotite compositions (Niu, 2004), while AOC Dy content is represented by natural ecolgite xenolith Dy contents (Barth et al., 2001). The addition of 10% of such melt into a primitive mantle results in a mantle source Dy content of 0.796 ppm, an 18% increase over the primitive mantle. Using this Dy content we estimate a mantle source sulfur content for El Hierro at 692±169 ppm, which is more than 400 ppm above primitive mantle estimates (Fig. 6.4). These results clearly point to recycled sulfur being present in the Western Canary Island mantle source. Intermediate reactions between the ambient mantle and the recycled material are required to reproduce the sulfur systematics of the mantle, as observed S enrichment cannot be reproduced by direct addition of eclogitic lithologies alone. This is in accordance with previous results from the Canary Islands which suggested solid-state reactions between a peridotitic mantle and recycled oceanic crust are required to produce silica deficient magmas erupting at the Canary Islands (Herzberg, 2011). In our model we propose melt-rock reactions instead of solid state reactions, as this would concentrate sulfur, and other volatiles, more effectively in the Canary Islands mantle source.

A possible alternative explanation for the elevated sulfur content of El Hierro magmas is enrichment through low degree melting of a primitive mantle (Longpré et al., 2017; Taracsák et al., 2019). Trace element ratios indicate that El Hierro, and Canary Islands magmas more generally, formed by 2 to 8% melting of a garnet peridotite dominated mantle (Gurenko et al., 2006; Day et al., 2010; Taracsák et al., 2019). To reproduce 5000 ppm primary melt S contents at El Hierro, total sulfur extraction from mantle sulfides would be required from a primitive mantle with 250 ppm sulfur after just 5% melting. This melting degree would not necessarily cause sulfide exhaustion during mantle melting, as that would require 8 to 22% melting (Ding and Dasgupta, 2017), albeit total sulfide loss from the mantle has been proposed at lower melting degrees (4%) in the case of more oxidising mantle conditions (Mungall et al., 2006) that are applicable for the Canary Islands and El Hierro. However, highly siderophile element contents of lavas support partial sulfide retention in the mantle source of El Hierro magmas based on the relative depletions of Os, Ir, and Ru (stored in refractory mono-sulfide solution) compared to Re, Pd, and Pt (mostly stored in interstitial sulfides, Day et al. 2010), which makes it unlikely that melt S enrichment can originate from a primitive mantle source alone.

6.5.3 From slab subduction to ocean island volcanism: recycled volatiles in the generation of OIB melts and the cycling of sulfur in the mantle

Volatile elements play a crucial part in melt generation in the mantle as they lower the solidus of silicate assemblages by >100 C° (Hart and Gaetani, 2006; Dasgupta et al., 2007; Green et al., 2010). The transfer of volatiles into the mantle via subduction zones is still a topic of considerable interest with many unknowns (Evans et al., 2012; Jégo and Dasgupta, 2014; Kelemen and Manning, 2015; Plank and Manning, 2019). Our results show the El Hierro mantle contains excess sulfur enriched ^{34}S compared to normal upper mantle, which indicates recycling of S into the asthenosphere at subduction zones may be an effective process, as previously suggested (Farquhar et al., 2002; Evans, 2012; Jégo and Dasgupta, 2014; Walters et al., 2020). In our model calculations we use a bulk recycled oceanic lithosphere S content of 650 ppm. If on average the upper section of the oceanic lithosphere contains around 1200-1300 ppm S in the oceanic crust and altered lithospheric mantle (Alt and Shanks, 2003; Ding and Dasgupta, 2017) that would mean at least 50% of S entering subduction zones is recycled into the deeper mantle, and less than half is released into the mantle wedge. This is consistent with the 60% recycling efficiency estimate by Jégo and Dasgupta (2014), but is somewhat lower than the 83% given by (Evans, 2012). The presence of excess heavy sulfur in the El Hierro mantle source indicates some of the recycled S is derived from seawater sulfur, most likely from hydrothermally altered upper lithosphere. ^{34}S is enriched in the sulfate phase in the altered oceanic lithosphere (Alt and Shanks, 2003; Alt et al., 2012). High ^{34}S/^{32}S ratios in El Hierro MIs is a strong indication that sulfate can be recycled into the OIB mantle source. This is in contrast with previous observations in metamorphosed rocks in which anhydrite breakdown is expected during blueschist and eclogite facies metamorphism (Tomkins and Evans, 2015); thermodynamic modelling also supports sulfate breakdown during high T and P metamorphism (Walters et al., 2020). Experiments carried out on sulfur-doped MORB at various fO_2 conditions indicate residual anhydrite may be recycled into the mantle if insufficient amounts of hydrous fluid are available to cause total anhydrite dissolution (Jégo and Dasgupta, 2014). Our data indicate that sulfur originally stored as sulfate in the slab potentially survives the subduction process and is transferred back into the mantle.

Sulfate recycling into the deeper mantle at subduction zones could be an important pathway for oxidised material transfer into the deeper spheres of the Earth, and could be one of the major causes of elevated fO_2 observed in some OIBs (Moussallam et al., 2019). Following subduction and slab detachment the recycled lithosphere is heated by the surrounding hotter mantle. Loss of recycled volatiles via metasomatic melt and/or fluid formation could transfer considerable amounts of S^{6+} into the asthenosphere, resulting in localised oxidation of mantle domains around the subducted slab. Excess sulfur could play a key role in the formation of low degree volatile- and trace element-enriched OIB melts as it can decrease the solidus of the mantle assemble and facilitate the melting of silicates. Such processes would have of critical importance in terms of understanding thermal properties of the mantle beneath ocean islands, such as the Canary Islands, where low-fraction melting is observed (< 8%). It is possible that a thermal anomaly may not be essential to produce extractable volumes of melt in the asthenosphere at these locations. Instead, the addition of oxidising, volatile-rich metasomatic material into the asthenospheric mantle could induce melting. Volatiles alone, however, would not be able to explain magmatism at ocean islands such as Hawaii, Reunion, or Iceland, where melting degree estimates for tholeiites are often above 10%. Our results point to the dual nature of OIB formation in the mantle instead of a single thermal origin: in some cases melting is primarily driven by thermal anomalies, while in other cases it is driven by volatile addition to the mantle from recycled subducted materials.

6.6 Conclusions

Young, undegassed El Hierro melt inclusions and matrix glasses exhibit extremely high sulfur concentrations coupled with ^{34}S enrichment above normal upper mantle values. δ^{34}S values and S content of glasses and MIs indicate magmatic sulfur contents are controlled by open-system degassing. After correcting for the effect of degassing, we estimate El Hierro primary magmas contained approximately 5000 ppm S, and their δ^{34}S was close to +4‰, significantly heavier than the most recent estimates of the upper mantle of -1.3‰.

El Hierro primary magmas have a S/Dy ratio of 870±194. Assuming Dy and S behave similarly during garnet peridotite melting, this corresponds to a mantle sulfur content of 692±169 ppm. This mantle sulfur content is > 400 ppm above primitive mantle estimates, meaning that the El Hierro mantle source contains excess sulfur. A possible source of this sulfur is recycled slabs containing ~650 ppm S. Sulfur from the recycled slab is concentrated by the formation of metasomatic, volatile-rich melts which react with the surrounding mantle, enriching it in sulfur. The addition of 5-15% of this metasomatic melt is sufficient to reproduce our modelled mantle S content and δ^{34}S values. We find that <50% of S is released from the subducting slab into the mantle wedge and more than half of sulfur is effectively recycled into the deeper spheres of the Earth. ^{34}S enrichment of El Hierro magmas points to recycling of seawater-derived, hydrothermally formed sulfate in the slab, and indicates that anhydrite may not undergo complete breakdown in the subducting slab during blueschist-eclogite facies metamorphism. The recycling of oxidised sulfur into the asthenosphere at subduction zones has potential implications for the redox budget of the mantle source of oxidised ocean island basalts, and could contribute to widespread redox heterogeneity in the mantle. Our results suggest that addition of oxidised sulfur into the mantle through metasomatic melts may be a driver of melting and ocean island volcanism at some locations such as the Canary Islands.

Chapter 7

The role of mantle metasomatism in the generation of volatile-rich OIBs, revealed by oxygen fugacity and temperature estimates from primitive magmas feeding El Hierro, Canary Islands

7.1 Abstract

Recent studies investigating volatile systematics in ocean island volcanoes indicate widespread enrichment of volatiles both in the erupting magmas and their mantle source. At El Hierro in the Western Canary Islands, magmas with exceptionally high CO_2 and S contents have been erupting throughout the Holocene. This volatile enrichment has previously been ascribed to undegassed primitive mantle or recycled lithospheric material in the

melting region. Here we present oxygen fugacity data, combined with estimates of magmatic temperature, mantle potential temperature and melting pressure for El Hierro to evaluate redox and temperature conditions in the early stages of melt evolution. Oxybarometry from olivine-hosted spinel inclusions yield melt oxygen fugacities between FMQ+2 and FMQ+3, suggesting that El Hierro magmas are highly oxidised compared to Icelandic or Hawaiian magmas. Aluminium-in-olivine thermometry yields near-liquidus temperature estimates of 1300±30 °C (1σ), slightly hotter than previous estimates from mid-ocean ridge basalts (MORB). Melting pressure estimates for the Canary Islands range between 0.5 and 6.0 GPa. The average mantle potential temperature for the broader Canary Archipelago is estimated at 1443±21 °C (80% confidence interval, n=17), which overlaps with the average potential temperature estimated for adjacent mid-ocean ridge segments (1427±2°C, n=474). The uncertainties in calculated mantle potential temperatures associated with alkaline Canary Islands magmas are considerably larger than for locations mostly erupting tholeiitic magmas; this is mostly likely due the presence of a significant pyroxenite and volatile-enriched peridotite component in the Canary Islands mantle source. Based on the oxidised nature of El Hierro primitive magmas, their high C and S contents, MORB-like liquidus temperatures, and mantle potential temperatures similar to adjacent ridge segments, we propose a model for melt generation beneath the Canary Islands that does not require elevated mantle temperatures. In this model, mantle upwelling beneath the Canary Islands is driven by buoyant, oxidised, and volatile-metasomatised material that accumulated close to the mantle transition zone during past subduction events. The upwelling material undergoes decompression melting in the upper asthenosphere, producing SiO_2-, S- and C-rich oxidised melts that react with the surrounding ambient mantle, oxidising the silicate assemblage and causing volatile enrichment. Trace and volatile element-enriched magmas erupting at El Hierro form by low-degree melting of this oxidised, volatile-rich mantle material. The HIMU (high $^{238}U/^{204}Pb$) signature of El Hierro magmas could be enhanced by the fluid-mobile behaviour of uranium in oxidised conditions, which enriches the source mantle in ^{238}U compared to locations where oxidised, volatile-rich melts/fluids in the mantle source are less common. Our data indicate that elevated mantle temperature as an explanation for magmatism at El Hierro, and the Canary Islands in general, is questionable, as the combined effects of high volatile content and elevated temperature would result in more widespread magmatism than the observed low magma flux. We propose that melt generation from a metasomatised, oxidised, volatile-enriched mantle could explain magmatism at other ocean islands, such as Cape Verde, that erupt compositionally similar magmas to the Canary Islands at low magma fluxes.

7.2 Introduction

Magmatic processes such as melt generation, magma storage, and volatile degassing, are fundamentally controlled by temperature (T), pressure (P) and redox (or oxygen fugacity, fO_2) conditions. Magmatic volatile contents and oxygen fugacity are often linked: sulfur solubility is primarily controlled by the oxygen fugacity of magmas through redox reactions (e.g. Jugo et al., 2005, 2010; Nash et al., 2019), while oxygen fugacity is directly linked to hydrogen fugacity and hence melt H_2O content (e.g. Taylor et al., 1992). H_2O-rich magmas, such as those erupted subduction-related volcanic arcs, are generally more oxidised (>FMQ+2, two log units above the fayalite-magnetite-quartz buffer) than magmas erupting at mid-ocean ridges (FMQ to FMQ+0.5; Kelley and Cottrell 2009; Cottrell and Kelley 2011; Evans et al. 2012; O'Neill et al. 2018; Zhang et al. 2018). The link between oxidation state and magmatic volatile content is well established in subduction-related arc magmas (e.g. Kelley and Cottrell, 2009), but it is less well understood for ocean island basalts (OIBs). For many OIBs both magmatic fO_2 conditions and volatile contents remain poorly constrained, even though both provide important information about melt generation at these locations.

Studies of crystal-hosted melt inclusions from various ocean islands including the Azores, Canary Islands, Hawaii, Réunion and Iceland show that ocean island basalts exhibit widespread enrichment in carbon and sulfur (e.g. Dixon et al., 1997; Métrich et al., 2014; Anderson and Poland, 2017; Longpré et al., 2017; Boudoire et al., 2018; Taracsák et al., 2019; Tucker et al., 2019). Carbon and sulfur are present in a wide range of oxidation states (+4 to 0 and +6 to -2, respectively) in minerals, and could play a significant role in controlling mantle and primary melt oxygen fugacity (Rielli et al., 2017). Previous studies found elevated fO_2 between FMQ+1 and FMQ+2, higher than typical mid-ocean ridge basalts (MORB), in erupted products from OIBs such as Cape Verde, the Canary Islands, and Hawaii (Moussallam et al., 2016, 2019; Brounce et al., 2017). However, these results are based on matrix glass and melt inclusion analyses where fO_2 may have been affected by magmatic processes including reduction during S degassing (e.g. Longpré et al., 2017; Moussallam et al., 2019), and electron exchange between S and Fe during quenching (Nash et al., 2019). Melt inclusions often record fO_2 conditions after extensive crystallisation, and are prone to fO_2 re-equilibration following entrapment (e.g. Danyushevsky et al., 2000; Gaetani et al., 2012; Bucholz et al., 2013; Hartley et al., 2017). Oxygen fugacity estimates derived from $Fe^{3+}/\sum Fe$ or $S^{6+}/\sum S$ ratios measured in glasses either by electron microprobe or X-ray near edge spectroscopy (XANES) may also be affected by electron-sample interactions and photo reduction or oxidation (e.g. Wilke et al., 2011; Cottrell et al., 2018; Hughes et al., 2018). These syn- and post-magmatic modifications mean that fO_2 measured in melt inclusions and glasses is unlikely to reflect the true primary melt oxidation state. An alternative window into early magmatic fO_2 is to examine olivine-hosted spinel crystals (Ballhaus et al., 1991; Evans et al., 2012), which have the potential to record magmatic fO_2 at the earliest stages of crystallisation and prior to the onset of degassing.

This work focuses on the island of El Hierro in the Western Canary Islands, a good example of an ocean island erupting small volumes of volatile-rich, basanitic magmas with a HIMU-like isotopic composition ($^{206}Pb/^{204}Pb>19$). The presence of volatile-rich magmas beneath El Hierro, and more generally the Western Canary Islands, is well documented (Longpré et al., 2017; Walowski et al., 2019; Taracsák et al., 2019). However, whether or not this volatile enrichment is caused by a volatile-rich mantle source, or by purely low melting degrees of a primitive mantle source remains unclear. Assessing evidence for these potential volatile enrichment sources is important to further constrain the origin of Canary Island volcanism, a topic that has been long discussed in the literature (e.g. Hoernle et al., 1995; Anguita and Hernán, 2000; Lundstrom et al., 2003) and is still subject to debate (Van Den Bogaard, 2013; Zaczek et al., 2015; Fullea et al., 2015; Belay et al., 2019).

In this study we use whole-rock, mineral, melt inclusion (MI), and matrix glass compositions, alongside MI and matrix glass sulfur speciation data, to reconstruct the P-T-fO_2 conditions at various stages in the magmatic system beneath El Hierro. We calculate olivine, clinopyroxene and spinel crystallisation temperatures using established olivine-melt, clinopyroxene-melt and aluminium-in-olivine (olivine-spinel) thermometers. We use rhyolite-MELTS modelling to calculate liquid lines of descent for El Hierro magmas and to calculate phase saturation temperatures of different minerals, and compare saturation temperatures with the results of the mineral-melt thermometers. We use PRIMELT3 (Herzberg and Asimow, 2015) together with the method of Lee et al. (2009) to estimate mantle potential temperature (T_p) and melting pressure. The evolution of magmatic fO_2 for El Hierro magmas is explored from source to surface using olivine-hosted spinel inclusion compositions, as well as MI and matrix glass sulfur speciation. By reconstructing near-liquidus temperatures and fO_2 conditions of El Hierro magmas, we highlight the importance of volatile addition and subsequent metasomatism-driven oxidation in the asthenospheric mantle source. Placing these results in a global context, our model for the generation of volatile-enriched, oxidised melts is applicable to other low melt flux OIBs with HIMU-like composition.

7.3 Samples and Methods

Tephra and lava samples were collected from El Hierro from the locations indicated in chapter 2 of the thesis (Fig. 2.2). Sample locations were chosen to be representative of the volcanic activity of the last 20 ka. Tephra samples were collected from fresh glassy scoria deposits. Where possible, lava samples were collected from flows that are related the scoria cones. Lava samples were prepared into petrographic thin sections, while tephra samples were crushed, sieved, and washed, then mounted into epoxy resin. Olivine crystals containing glassy melt inclusions were picked from the tephra samples and mounted in epoxy. Resin mounts were ground to expose the sample surface and then polished for petrographic and geochemical analysis.

El Hierro is dominated by mafic alkaline volcanics such as basanites (olivine-rich alkaline basalt) and tephrites (olivine-poor alkaline basalts) and the young platform-forming rift lavas and tephras studied in this thesis are no exception: they are dominantly basanites and tephrites (Table 2.1). A less common rock type found on El Hierro is ankaramite, a highly porphyritic, clinopyroxene- and olivine-rich volcanic rock sometimes found in ocean arc settings (Green et al., 2004). Ankaramites can be found at the Tanganasoga volcano and at some scoria cones of the southern and western rift zone both as lava and as tephra. Tanganasoga ankaramites often contain clinopyroxenes as large as 2 cm in diameter. Young, platform-forming rift lavas and tephras have identical mineralogy (including mineral texture) and textural features apart from differences in volcanic glass content: tephras generally contain fewer microphenocryst and groundmass crystals since they cooled more rapidly than lavas.

Figure 7.1 (next page): Photomicrographs of young alkaline basalts from El Hierro. (A) is an ankaramite sample from Tanganasoga, showing euhedral olivine and clinopyroxene crystals in a clinopyroxene-rich groundmass. (B) is an aphyric lava sample from the northwestern part of El Hierro. (C) is a typical crystal clot of clinopyroxene, Fe-Ti oxide and olivine in a Tanganasoga ankaramite. Basanite sample (D) from the eastern part of El Hierro, containing inclusion-rich euhedral olivine phenocrysts. (E) is a sector-zoned clinopyroxene phenocryst from Tanganasoga. (F) is a basanite sample from Montañita Negra with euhedral olivine and concentrically zoned clinopyroxene (F). All photomicrographs were taken in plane-polarised light, except E and F which are cross-polarised light images.

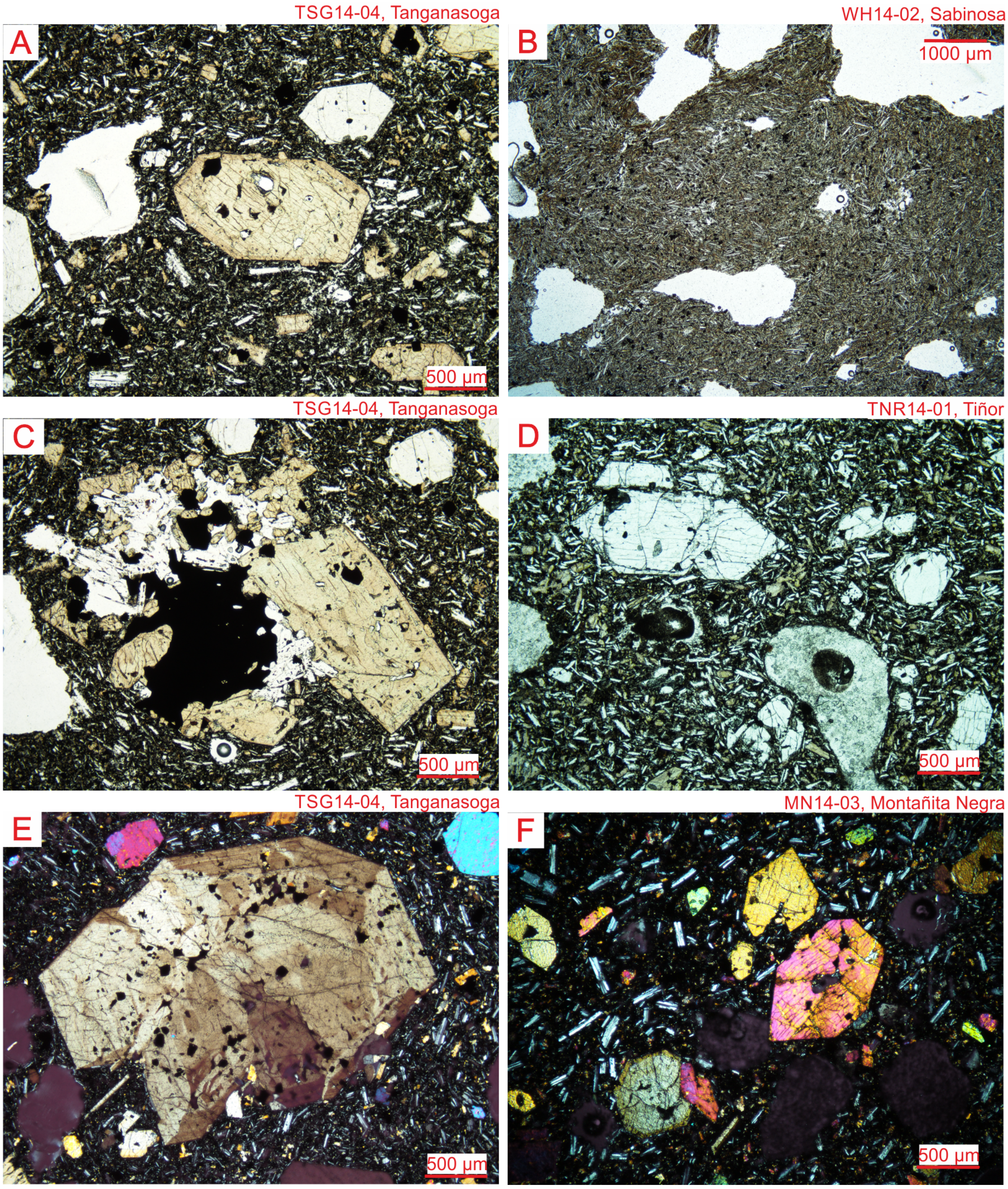
TSG14-04, Tanganasoga
A
500 µm
WH14-02, Sabinosa
B
1000 µm
TSG14-04, Tanganasoga
C
500 µm
TNR14-01, Tiñor
D
500 µm
TSG14-04, Tanganasoga
E
500 µm
MN14-03, Montañita Negra
F
500 µm

El Hierro lavas contain between 0 to ~25 vol% olivine crystals (Fig. 7.1). Some lava samples are aphyric (Fig. 7.1B) and likely more fractionated than basanitic samples (Fig. 7.1F). Lavas have intersertal textures with small amounts of glass still present in the matrix together with oxides, plagioclase, and clinopyroxene. *Sensu stricto* basanites are olivine-phyric (Fig. 7.1D) and contain little to no large clinopyroxene crystals, while ankaramite samples have high clinopyroxene content, sometimes up to 50 vol%. Olivines do not display zoning in backscattered electron images apart from a thin (~10 μm) iron-rich rim around edges (Fig. 7.2). Under plane-polarised light concentric zoning can be observed in some clinopyroxenes (Fig. 7.1C), while cross-polarised light images reveal common sector-zoning in clinopyroxene (Fig. 7.1E). However, these zoning features are weak or cannot be observed in backscattered electron images (Fig. 7.2B). Ti-magnetite crystals are common in ankaramitic samples (Fig. 7.1A, C, Fig. 7.2B). Crystal clots of olivine, clinopyroxene and oxides can be found in ankaramites, but not in basanites. Both olivines and clinopyroxenes contain inclusions of oxide crystals: these are Fe-Ti rich oxides in clinopyroxenes, while olivines also contain a number of Cr-rich spinel inclusions. These inclusions provide some information on the crystallisation sequence in the samples: Cr-rich spinels are one of the earliest phases to form from the melt and are only hosted in olivines, suggesting olivines likely crystallised before clinopyroxenes, as the latter only contain Fe-Ti oxide inclusions formed later in the crystallisation sequence.

The largest olivine crystals in basanites are around 1 mm in diameter, while ankaramitic olivines are considerably larger (up to 2-3 mm). In ankaramites clinopyroxene crystals are often present as megacrysts up to 2 cm in diameter. Larger Ti-magnetite crystals are euhedral or sometime skeletal. Both olivines and clinopyroxenes are dominantly euhedral, indicating that they are phenocrysts, autocrysts, or antecrysts rather than mantle or crustal xenocrysts that have been picked up during magma ascent. Chemical compositions of zoned clinopyroxene cores and rims are both Ti-augite and Ti-diopsides

(Fig. 7.3), making it unlikely they are xenocrysts from the lithospheric mantle or crustal gabbros, which are usually Ti-poor diopsides or Ti-poor augites.

Major and minor element analysis of mineral phases and glasses was carried out using a CAMECA SX100 EPMA at the University of Manchester, using the analytical conditions described in chapter 3 of the thesis. Fourteen powdered whole-rock samples were analysed for major elements by X-Ray Fluorescence at the University of Edinburgh using a Panalytical PW2404 instrument, following the procedure described by Passmore et al. (2012) and references therein. Samples were fused with lithium borate into glass pellets prior to analyses.

7.3.1 Methods of P-T-fO_2 estimation

Olivine-melt thermometry

To calculate the crystallisation temperatures of the studied olivines, we used the olivine-melt thermometer presented in equation 22 of Putirka (2008b). This thermometer is based on Mg-Fe^{2+} partitioning between olivine and melt. To test whether equilibrium conditions between olivine and melt compositions are met, we estimated K_d $^{Mg\text{-}Fe}$ based on averaged El Hierro whole-rock, matrix glass and melt inclusion compositions using the method of Gee and Sack (1988). K_d $^{Mg\text{-}Fe}$ was estimated at 0.313±0.035, 0.288±0.033 and 0.291±0.026 (3σ) for matrix glasses, melt inclusions and whole-rock samples, respectively. Calculated K_d $^{Mg\text{-}Fe}$ was compared to measured K_d $^{Mg\text{-}Fe}$ for each olivine-melt pair to determine whether they were in equilibrium. Generally, olivine cores were paired with whole-rock samples, and melt inclusions and rims with matrix glasses. A total of 83 out of 230 olivine-glass pairs matched our equilibrium criteria for

---

Figure 7.2 (next page): Backscattered electron images of platform-forming rift lavas, showing a basanite (A) from the northeastern rift (same area imaged as Fig. 7.1D) and an ankaramite from the Tanganasoga volcano (B), showing the same area seen in Fig. 7.1A. Red labels indicate olivine (ol), clinopyroxene (cpx), Ti-Fe oxide crystals (ox), and glass (gl). Typical, small Cr-rich spinel can be seen in the labelled olivines in both (A) and (B), while in the large clinopyroxene crystal, typical Ti-Fe oxide inclusions are present.

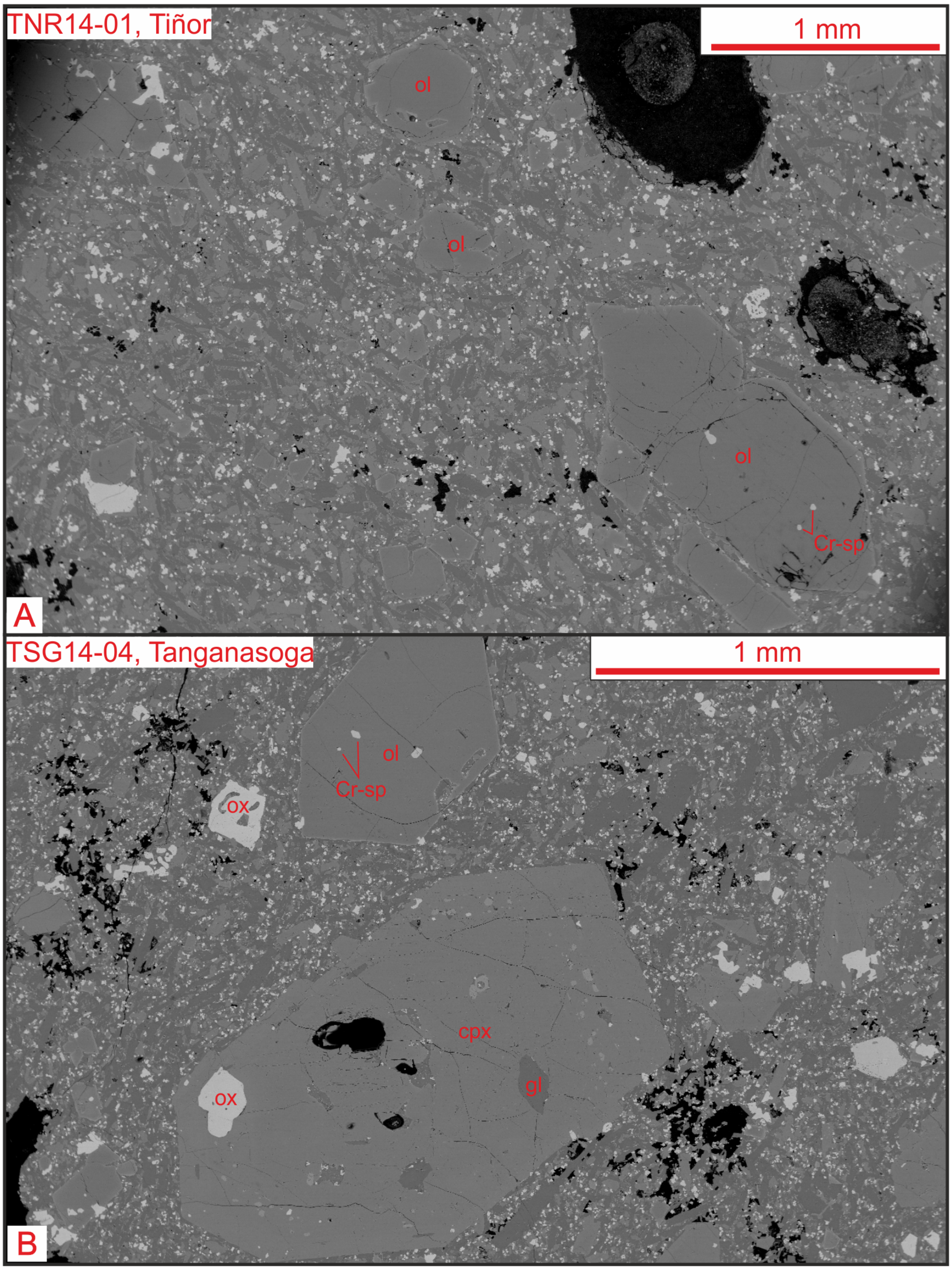
TNR14-01, Tiñor
1 mm
ol
ol
ol
Cr-sp
A
TSG14-04, Tanganasoga
1 mm
ol
Cr-sp
ox
cpx
gl
ox
B

K_d $^{Mg\text{-}Fe}$. Olivine-melt thermometry data are provided in the supplementary material.

Clinopyroxene-melt thermobarometry

Crystallisation pressures and temperatures of clinopyroxenes in the studied samples were calculated using the barometer of Neave and Putirka (2017) and the thermometer presented in equation 33 of Putirka (2008b). The barometer is based on the pressure dependence of Na (jadeite) in clinopyroxene, while the thermometer uses Mg-Fe^{2+} partitioning between clinopyroxene and melt. Equilibrium conditions were tested by comparing measured clinopyroxene-melt K_d $^{Mg\text{-}Fe}$ and clinopyroxene components (DiHd, CaTs and EnFs; Putirka 2008b) with predicted values based on melt composition. For K_d $^{Mg\text{-}Fe}$, a variation of 0.27±0.06 was allowed, while for predicted and observed DiHd, CaTs and EnFs components a difference of 0.06, 0.03 and 0.03 was accepted, respectively. A total of 119 out of 181 clinopyroxene analyses were paired with equilibrium melt compositions. In most cases, both crystals cores and rims are in equilibrium with matrix glass and MI compositions, but not with lava whole-rock compositions.

Temperature and fO_2 estimation using olivine-hosted chromian spinel inclusions

Olivine-hosted spinel inclusions, together with their hosts, were used for both aluminium-in-olivine thermometry (referred to as olivine-spinel thermometry hereafter; Wan et al. 2008; Coogan et al. 2014) and olivine-spinel oxybarometry (Ballhaus et al., 1991). Olivine-spinel thermometry data is based on the temperature dependence of aluminium partitioning between olivine and spinel, while olivine-spinel oxybarometry is based on the reaction fayalite = magnetite + quartz (i.e. the reaction defining the FMQ buffer) and uses Fe^{3+}, Fe^{2+}, Al and Cr content of spinels and the fayalite content of olivine to estimate fO_2. Only spinels with >13 wt% Cr_2O_3 and <7.5 wt% TiO_2 were used for the calculations, as early-crystallising spinels are most Cr-rich while Ti-rich spinels grow much later, after extensive cooling and crystallisation. Spinel Fe^{3+} contents were estimated based on stoichiometry (Droop, 1987). We identified a total of 22 olivine-spinel pairs suitable for calculations. Olivine-spinel thermometry calculations were carried out using the equation of Coogan et al. (2014) with uncertainties estimated using the published parameter errors, resulting in errors between ±80 and 110 °C. Olivine-spinel fO_2 estimates were calculated using the method of Ballhaus et al. (1991) and the more recent oxybarometer of Nikolaev et al. (2016). Initial pressure for the calculations was set at 600 MPa, representative of average storage depths beneath El Hierro (e.g. Stroncik et al., 2009; Klügel et al., 2015) while input temperatures were taken from the results of the olivine-spinel thermometer. The oxybarometer was developed for orthopyroxene-saturated systems and forsterite-rich olivines. To account for the absence of orthopyroxene in the El Hierro magmatic system, a silica activity correction has to be applied (Ballhaus et al., 1991). We used the method of Beattie (1993) to calculate the silica activity for orthopyroxene-bearing mantle xenoliths found in El Hierro lavas, which represents the silica activity of the mantle source and of primitive whole-rock lava compositions. The difference in silica activity between xenoliths and erupted lavas was then multiplied by three (Ballhaus et al., 1991) and applied as a correction to our olivine-spinel derived fO_2 values. The correction was -0.207 log units, which is within the nominal error of the oxybarometer (±0.4 log units, Ballhaus et al. (1991)). We find a systematic difference of around 1.3 log units in calculated fO_2 between the Ballhaus et al. (1991) and Nikolaev et al. (2016) oxybarometers. However, this difference is within the 1σ error of the oxybarometer of Nikolaev et al. (2016), which is ~1.5 log units for El Hierro olivine-spinel pairs. Due to the lack of oxidised experiments used to calibrate the oxybarometer of Nikolaev et al. (2016), we favour the Ballhaus et al. (1991) method for our calculations, which is calibrated to the magnetite-hematite buffer (around ΔFMQ+5).

Sulfur speciation within olivine-hosted melt inclusions

Sulfur in basaltic glasses can be present as either S^{2-} or as SO_4^{2-}. The ratio of these two species can be determined by using XANES or EPMA (Carroll and Rutherford, 1988; Wilke et al., 2011). Sulfur speciation can be determined by EPMA by exploiting a shift in the S K_α peak position that is dependent on S oxidation state. By analysing the two endmember oxidation states in pyrite and anhydrite standards, the magnitude of the peak shift can be measured. Glasses containing both S^{2-} and S^{6+} species have a S K_α peak position that falls between the two endmember values; this shift is proportional to the ratio of S^{6+} to S^{2-} (Carroll and Rutherford, 1988). The shift in the peak position can be measured using two different methods: by scanning over the S K_α peak during each analysis for both unknowns and standards, or by using multiple crystals together fixed at the position of the S^{2-} peak, the S^{6+} peak (Wilke et al., 2011), and possibly at two background positions. The intensity ratio of the S^{6+} and S^{2-} peaks is proportional to the $S^{6+}/\sum S$ ratio. While the scanning approach is more widely used, we adopted the latter method due to the availability of four PET crystals. Detectors measuring at fixed crystal positions provide more reliable results than scans due to shorter measurement times (30-60 s using fixed crystals opposed to 120 s during scans), minimising any of photo reduction or oxidation that is thought to alter $S^{6+}/\sum S$ ratios measured with EPMA (Jugo et al., 2010). Sulfur speciation analyses of melt inclusions and glasses were made using a Cameca SX100 instrument, with a 15 μm beam diameter, and a 20 nA beam current for 60 seconds. Reproducibility of the ratio of S^{6+} and S^{2-} peaks were 2.3 % for pyrite and 1.9 % for anhydrite during the analytical session. A time dependent intensity correction was enabled during analyses: this allowed us observe changes in intensity on each spectrometer within 10 s intervals, revealing any reduction or oxidation caused by the electron beam interacting with the sample.

7.4 Results

7.4.1 Whole-rock geochemistry

The whole-rock compositions of young El Hierro lavas generally fall within the basanite/tephrite field of the TAS diagram (Le Bas et al., 1986b). Notable exceptions are the ankaramitic samples from Tanganasoga and the Southern rift zone, which lie in the picrite and to the left of the picrite field, respectively. The Mg# of whole-rock samples is between 0.51 and 0.71, where Mg# is calculated as Mg / (Mg + Fe^{2+}) using a $Fe^{2+}/\sum Fe$ ratio of 0.74 based on primitive melt fO_2 estimates of (Moussallam et al., 2019) (ΔFMQ+2). Most samples having Mg#>0.65. Aphyric lavas from the Western rift zones have low Mg#, higher SiO_2 and alkali contents than phyric lavas from other locations.

7.4.2 Mineral Chemistry

Clinopyroxene

El Hierro clinopyroxenes have Mg# (calculated as Mg / (Mg + $\sum$Fe) * 100) between 68 and 83 (Fig. 7.3A). Their Ca content is relatively constant as a function of Mg#, while Ti content increases with decreasing Mg# (Fig. 7.3B, C). The compositional distribution is not uniform between locations: clinopyroxene Mg# is more restricted in samples from Tanganasoga and the Southern rift ankaramite samples (Fig. 7.3A). Megacrysts from the Tanganasoga ankaramite show strong optical sector zoning but do not display marked compositional zoning: 31 of 36 analyses of these clinopyroxene megacrysts have Mg# of 77.5±1 and TiO_2 contents of 3.0±0.3 wt%. Clinopyroxene cores have higher Mg# and lower Ti cation numbers than crystal rims (Fig. 7.3B).

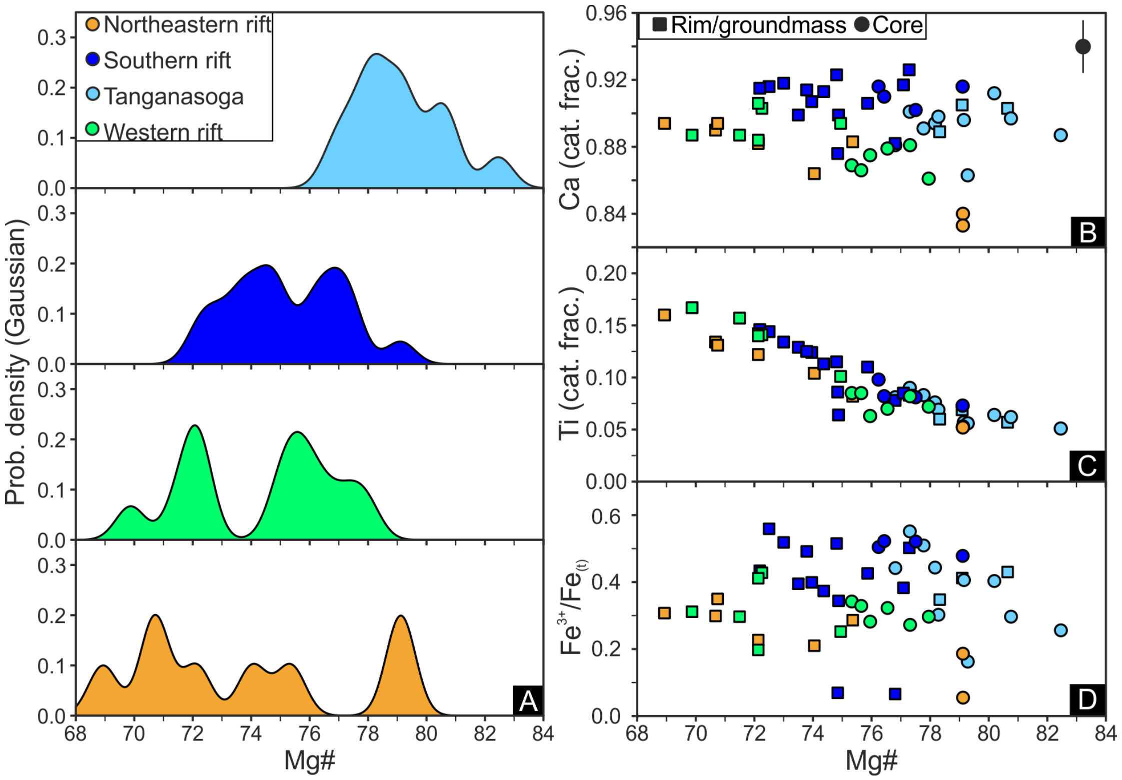

Figure 7.3: Compositions of El Hierro clinopyroxenes. (A) Mg-number (calculated using total Fe) kernel density estimates for the three rifts of El Hierro and Tanganasoga volcano. Clinopyroxenes from Tanganasoga have higher and less diverse Mg# than the three other rifts. (B) Clinopyroxene Ca cation contents (normalised to four cations) are broadly constant over the whole Mg# range, although a small increase in Ca can be observed with decreasing Mg# in samples from the North-eastern and Western rift. (C) Titanium contents increase with decreasing Mg#. (D) $Fe^{3+}/\sum Fe$ ratios cover a wide range between 0.1 and 0.6, and do not correlate with Mg#. For all locations, clinopyroxene rims have lower Mg# than and higher Ti than crystal cores. The error bar in (B) indicates the 2σ analytical uncertainty measured on the Smithsonian Cr-Augite standard between sessions; in (C) the error bars are smaller than symbol size. Fe^{3+} is estimated on a stoichiometric basis using the method of Droop (1987).

Olivine

Olivines in tephra and lava samples from El Hierro have compositions between Fo_{74} and Fo_{84}, although with distinctive compositional peaks for samples from different locations (Fig. 7.4A). Olivines from the Tanganasoga ankaramites show a narrow compositional range around Fo = 79±1, while Fo>82 olivines are restricted to samples from the rift arms of El Hierro. For all locations, olivine NiO content decreases with decreasing Fo, from 0.3 to 0.1 wt% (2360 ppm to 790 ppm Ni) (Fig. 7.4B). Most olivine cores and

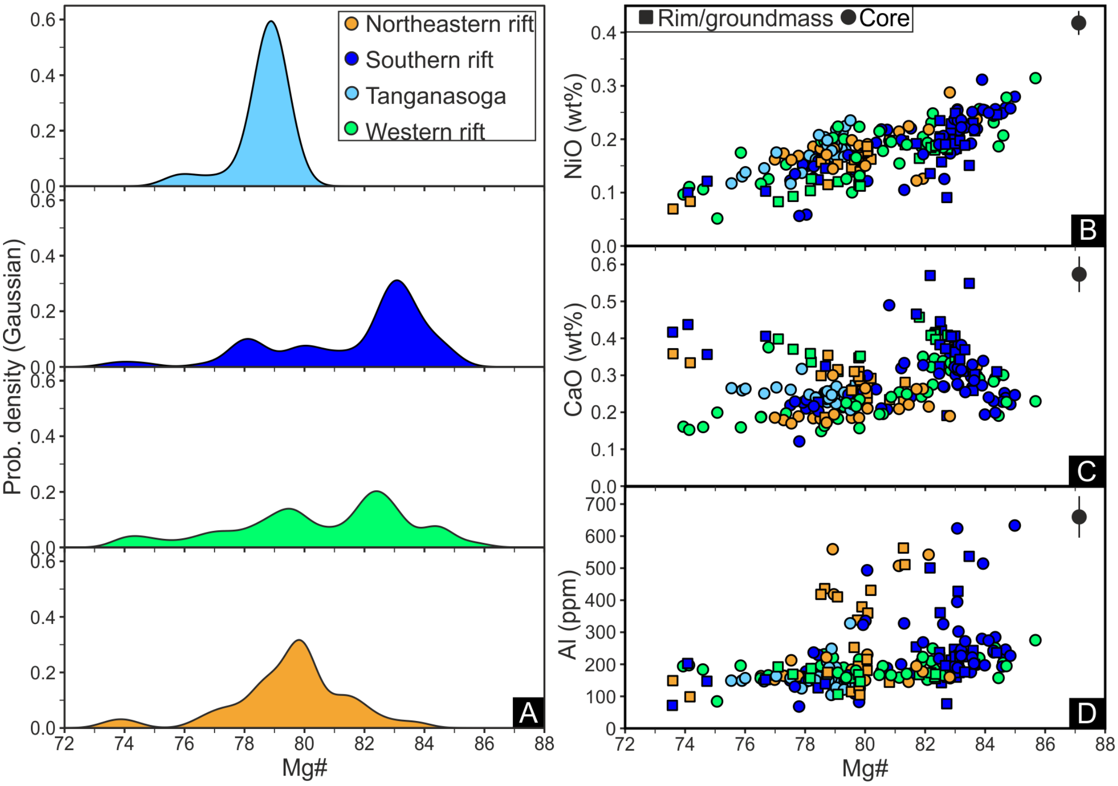

Figure 7.4: (A) Compositions of El Hierro olivines shown on kernel density estimate diagrams as a function of forsterite content (expressed here as Mg-number, Mg#). Samples from the Western and Southern rifts show a relatively wide range of olivine compositions, while Tanganasoga olivines converge to a value of 79±1. (B) Olivine NiO contents decrease with decreasing Mg#, as expected during crystallisation. (C) and (D) show CaO and Al (in ppm) content of olivines plotted against Mg#. There is no statistically significant correlation between Fo and Ca or Al content. The highest variability in olivine Al content is observed in more forsteritic olivine (Fo_{80}). High Al contents are usually rims, which could result from some amount of glass being present within the analytical volume sampled by EPMA. Across all sample locations, olivine rims typically have higher CaO and lower NiO contents than their cores. The error bars in (B)-(D) indicate 2σ analytical uncertainties measured on the San Carlos olivine standard between sessions.

rims have Al contents between 100-300 ppm, although some analyses show Al content up to 650 ppm (Fig. 7.4D). There is a very weak correlation between Fo and Al content (R^2 = 0.20, after removing data with Al>300 ppm). Olivine cores generally contain between 0.1 and 0.4 wt% CaO, while rims have higher CaO contents of 0.3-0.6 wt%, Fig. 7.4C).

Spinel

Compositions of olivine- and clinopyroxene-hosted spinel inclusions, spinel phenocrysts and spinels found in glomerocrysts (or crystal clots) are shown in Fig 7.5. The term 'spinel' here refers to all oxides with a spinel or inverse spinel crystallographic structure, including spinel *sensu stricto* ($MgAl_2O_4$), chromite, magnetite, ulvöspinel, and their solid solutions. Spinel Mg# is Mg / (Mg + Fe^{2+}), with Fe^{2+} and Fe^{3+} calculated on a stoichiometric basis (Droop, 1987). The spinels have Mg# between 0.13 and 0.55. Spinel $Fe^{3+}/\sum Fe$ ratios are between 0.44 and 0.83, and decrease with decreasing Mg# (Fig. 7.5C). There is an increase in Fe^{3+}/Al ratio and a decrease in Cr# (Cr# = Cr/(Cr+Al)) with decreasing spinel Mg# (Fig. 7.5D, E). Spinel TiO_2 contents are between 3.9 and 26.4 wt%. It has to be noted that many of our original spinel analyses have low totals, down to 93 wt%, which is attributed to the relatively high Fe^{3+} content of the spinels. As we calculated $^{3+}$ on a stoichiometric basis, errors of Fe^{3+}/Fe^{2+} ratios in spinels with Fe^{3+}-rich composition, hence low original totals, will be considerably larger than in Fe^{2+}-rich spinels with close to 100% original totals.

7.4.3 T, P and fO_2 estimates in the El Hierro magmatic system

Various temperature, pressure and oxygen fugacity estimates are shown in Fig. 7.6 (clinopyroxene-melt and olivine-melt), Fig. 7.7 (fO_2 based on melt inclusion and glass S speciation), and Fig. 7.9 (olivine-spinel thermometer and oxybarometer). Olivine-melt and olivine-spinel temperature estimates are compared in Fig. 7.8. Clinopyroxene-melt thermobarometry calculations indicate crystallisation temperature and pressures between 1110-1220 °C and 370-1020 MPa (Fig. 7.6/A). The highest crystallisation temperatures and pressures are from the western rift of El Hierro (T >1200 °C), while at other locations temperatures are mostly restricted to 1120-1200 °C. The lowest crystallisation temperatures are from Tanganasoga at 1130±10 °C (1σ standard deviation). The

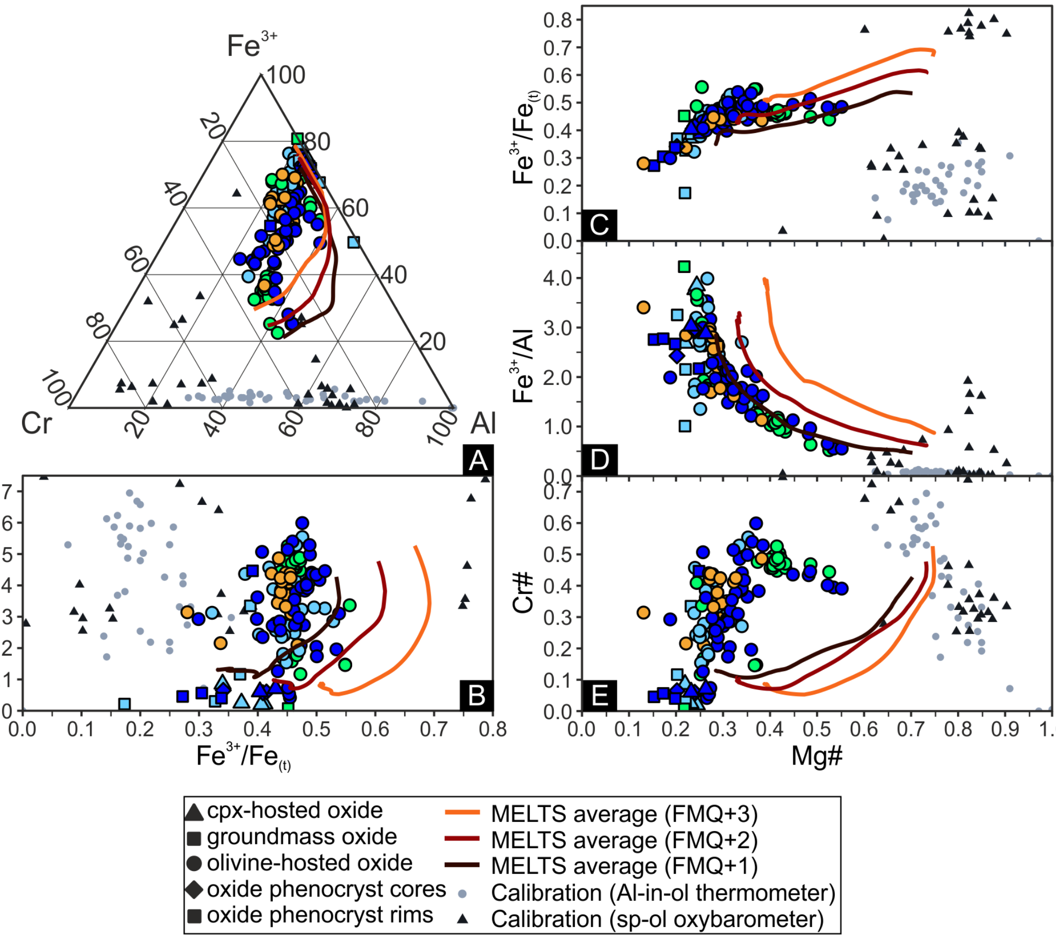

Figure 7.5: (A) Compositions of El Hierro spinel inclusions on a Cr-Al-Fe^{3+} ternary diagram. Small symbols show the composition of spinels used to calibrate the thermometer of Wan et al. (2008) and Coogan et al. (2014), and the oxybarometer of Ballhaus et al. (1991). (B) Cr# (calculated as Cr/(Cr+Al)) is plotted against $Fe^{3+}/\sum Fe$ ratios. In (C), (D) and (E) $Fe^{3+}/\sum Fe$, Fe^{3+}/Al and Cr# are plotted against spinel Mg# (calculated as Mg/(Mg+ Fe^{2+})). Most El Hierro spinels have Mg# of 0.1-0.4, with a smaller population having Mg#>0.4. The latter group is characterised by high Cr# (0.4-0.6), and low Fe^{3+}/Al. Coloured lines show crystallisation models calculated in rhyolite-MELTS, and indicate the compositions of spinels predicted to crystallise from primitive El Hierro melts under different starting magmatic fO_2 conditions.

uncertainty of the clinopyroxene-melt thermometer is ±40 °C (Putirka, 2008b). Crystallisation pressures from all El Hierro samples are 730±120 MPa (1σ standard deviation); no significant variability is observed between different locations within the island. The uncertainty of the clinopyroxene-melt barometer is ±120 MPa (Neave and Putirka, 2017). Clinopyroxene rim compositions record both lower pressures and temperatures than cores, but the number of rim analyses is significantly smaller. The returned pressures are equivalent to crystallisation at 15-35 km depth using the pressure-depth conversation of Longpré et al. (2014), i.e. lower crust to upper lithospheric mantle.

The most probable olivine-melt equilibrium temperature of 1150 °C (Fig. 7.6B) overlaps with the clinopyroxene-melt equilibrium temperatures. However, olivines record a larger range of temperatures than the clinopyroxenes, at 1070 to 1250 °C for the whole dataset. The highest temperatures are recorded in Fo_{84} olivines found in high-Mg# lavas from the Western rift zone. Tanganasoga olivines record temperatures similar to clinopyroxenes, with T_{avg} of 1150±20 °C (1σ standard deviation). The published error of the olivine-melt thermometer is ±30 °C (Putirka, 2008b).

Melt inclusions and groundmass glasses have $S^{6+}/\sum S$ of 0.00 to 0.74. Using the relationship between $\log(S^{6+}/S^{2-})$ and fO_2 established by Jugo et al. (2010), where $(\log(S^{6+}/S^{2-}) = 2.16 * fO_2 - 2.42$ (in ΔFMQ units; see their figure 9), this corresponds to fO_2 between FMQ+0.2 and FMQ+1.3. Groundmass glasses show little variation in fO_2, with values between FMQ+0.8 and FMQ+1.0 (Fig. 7.7). Melt inclusions cover a wider fO_2 range, with lower fO_2 values <FMQ+0.6 restricted to melt inclusions with H_2O<1.1 wt% (Fig. 7.7A).

Olivine-hosted spinel inclusions were used in this study to estimate both temperature and fO_2 conditions of the magmatic system during the early stages of crystallisation (Fig. 7.8), up to the co-saturation of spinel and olivine (Fig. 7.9). Average olivine-spinel equilibrium temperatures for El Hierro is 1300 °C, approximately 150 °C higher than

---

Figure 7.6 (next page) : Results of (A) clinopyroxene-melt thermobarometry, and (B) olivine-melt thermometry calculations on P-T, Fo vs. temperature and on kernel density estimate diagrams. Blue lines in (A) show anhydrous and hydrous solidii calculated using the parameterisation of Katz et al. (2003). Red and black lines in (B) show results of rhyolite-MELTS crystallisation modelling (average compositions based on seven samples. Both thermometers predict crystallization over a temperature interval from 1100-1250 °C. The most probable crystallization temperature is at 1150-1200 °C, coinciding with the main crystallisation phase predicted by rhyolite-MELTS. Pressure estimates are between 400-1000 MPa, inferring upper mantle storage (crust-mantle boundary estimate at El Hierro is indicated with a dashed line). Calibration uncertainties are ±36 °C for the olivine-melt thermometer, and ±46 °C and ±120 MPa for the clinopyroxene-melt thermobarometer (Putirka, 2008b; Neave and Putirka, 2017).

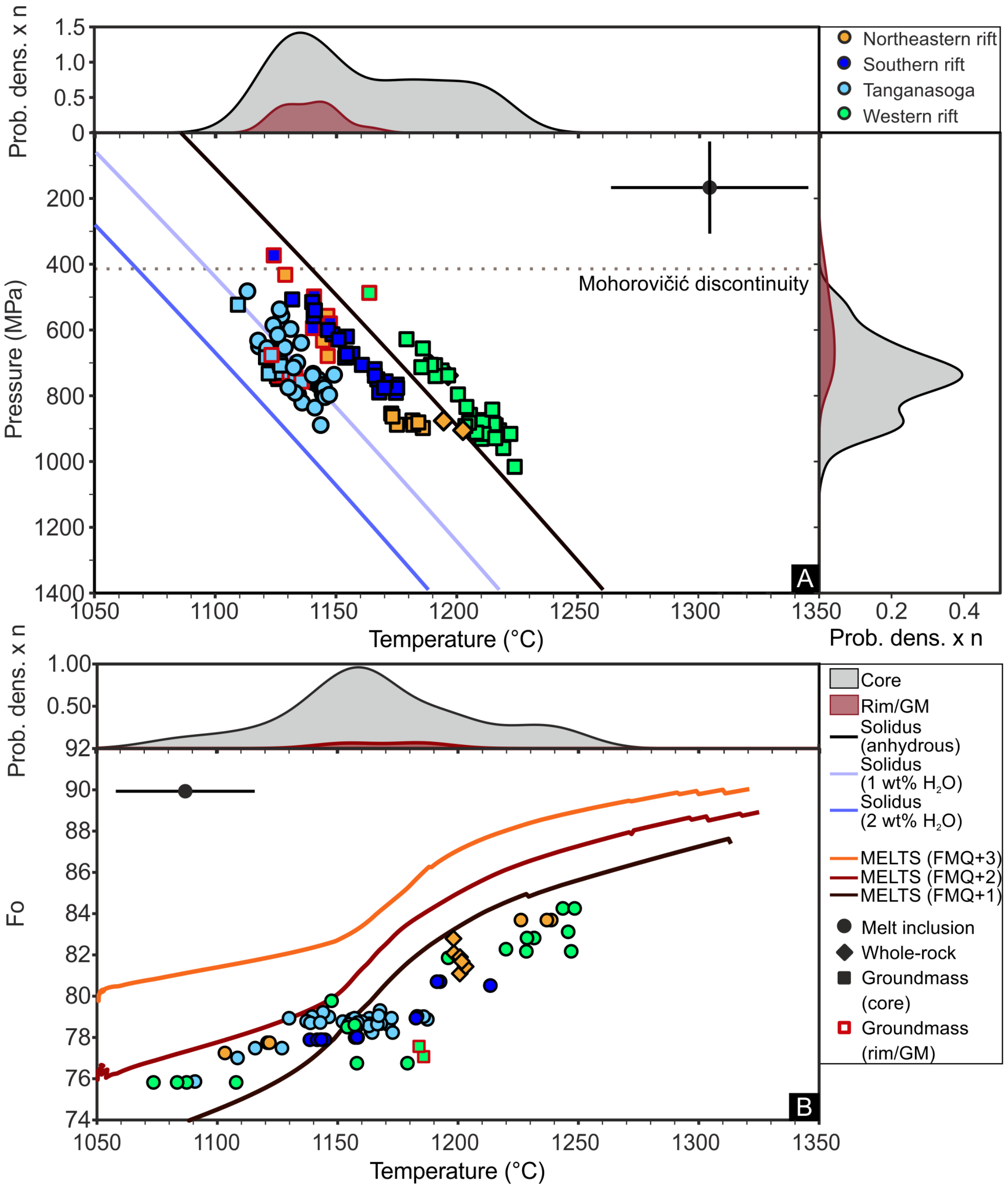

olivine-melt and clinopyroxene-melt equilibrium temperature (Fig. 7.8A). Most spinels with high Cr_2O_3 and low TiO_2 contents suitable for the olivine-spinel co-saturation temperature and fO_2 calculations are from Mg-rich material from the Western rift of El Hierro. Oxygen fugacity estimates for El Hierro spinels are between FMQ+1.7 and

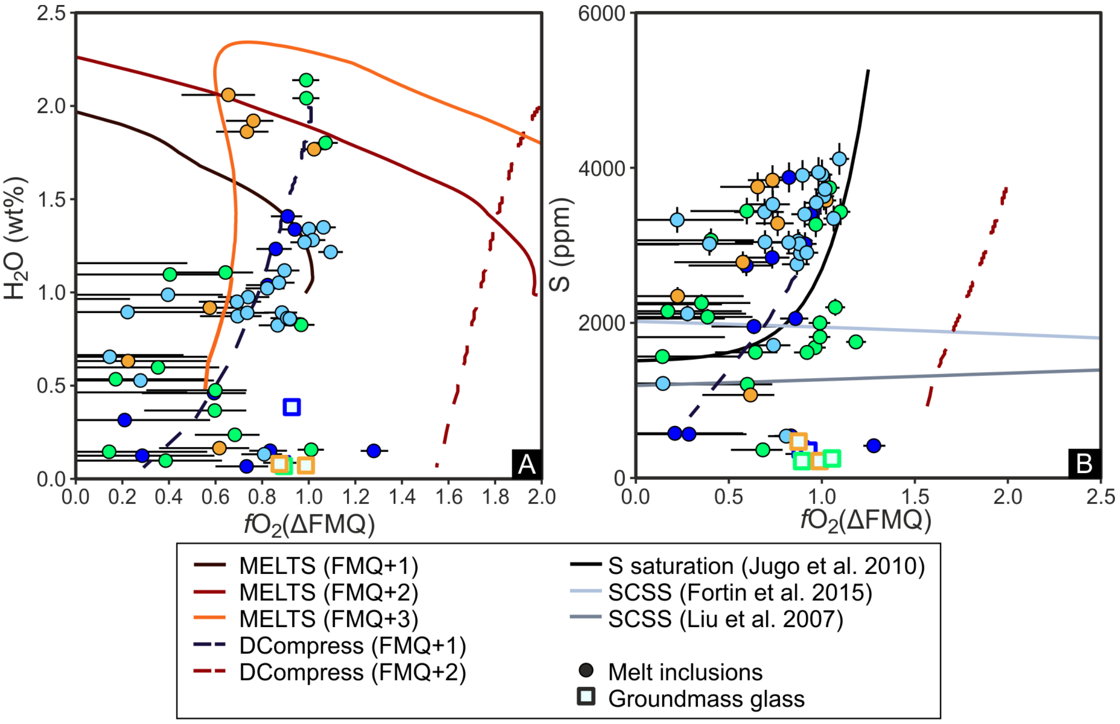

Figure 7.7: (A) H_2O and (B) S contents of El Hierro melt inclusions plotted against fO_2 values determined using sulfur speciation data. Solid lines in (A) show the evolution of melt H_2O content during crystallization and degassing for a melt with an initial 1 wt% H_2O, calculated using rhyolite-MELTS. Dashed lines are degassing pathways calculated in D-Compress (Burgisser et al., 2015), using 1150 °C and 350 MPa as starting parameters (melt composition was taken from Taracsák et al. 2019). The melt inclusion composition and fO_2 data are best described by H_2O degassing from a melt with initial 2 wt% H_2O at FMQ+1 using D-Compress. Rhyolite-MELTS calculations also produce a similar fO_2-H_2O pathway to the data, i.e. the one with a primary melt starting fO_2 of FMQ+3 and initial H_2O content of 1 wt%, which increases to 2 wt% after crystallisation before ascent and degassing. Solid lines in (B) show sulfur saturation curves from Jugo et al. (2010). Melt inclusion S concentrations indicate S oversaturation in case of every model, regardless if the model takes the presence of both S^{6+} and S^{2-} in the melt into account (Jugo et al., 2010) or only S^{2-} (Liu et al., 2007; Fortin et al., 2015)

FMQ+2.9 (Fig. 7.8D). Average fO_2 at the western rift is 2.5±0.3 (1σ) log units above the FMQ buffer. Two primitive (i.e. ones with a high Cr and a low Ti content) spinels from the Northeast rift and one primitive spinel from Tanganasoga return fO_2 estimates of ΔFMQ+2.8 and ΔFMQ+2.4 respectively, suggesting that there is no difference in melt fO_2 between locations. The nominal error of the oxybarometer is ±0.4 log units, Ballhaus et al. (1991).

7.5 Discussion

7.5.1 Pressures and temperatures of crystallisation and storage in the El Hierro magmatic systems

Spinel, olivine and clinopyroxene appear on the liquidus at different stages of magmatic evolution (Fig. 7.9). By using a range of mineral-melt and mineral-mineral thermobarometers, it is possible to determine the evolution of magmatic temperature as crystallisation proceeds. In this work, we use temperature estimates from three independent methods to constrain the temperature pathway of El Hierro magmas. To put these temperatures in context of magma evolution, we compare these results with rhyolite-MELTS modelling.

Crystallisation pressures beneath El Hierro have been determined previously from submarine samples dredged along the three rift axes (Stroncik et al., 2009), from products of the 2011-2012 eruption (e.g. Longpré et al., 2014) and from Tanganasoga ankaramite clinopyroxene megacrysts (Longpré, 2009). The crystallisation pressures of 500-900 MPa reported in previous studies correspond well with the pressures calculated for young rift volcanics in this study, indicating that El Hierro has been fed by a magma plumbing system constructed by vertically extensive interconnected dykes and sills starting just beneath the crust (15-33 km), with little to no intermediate magma accumulation present at crustal levels.

To interpret and connect our various temperature and oxygen fugacity estimates, we constructed a two-step crystallisation model using rhyolite-MELTS 1.2.0, which is optimised for mafic magmas with a mixed H_2O-CO_2 fluid present (Gualda et al., 2012; Ghiorso and Gualda, 2015). The modelling consisted of an isobaric equilibrium crystallisation stage from the liquidus temperature to 1150 °C at 600 MPa, followed by a decompressional “ascent” stage with dP/dT = 6 MPa/°C, during which pressure was decreased to near-surface conditions and temperature decreased to 1050 °C, the lowest temperature recorded in our dataset (Fig. 7.9). The isobaric pressure and temperature conditions were chosen based on clinopyroxene barometry and olivine-melt thermometry results, since these are interpreted to record the stalling depth and temperature at the final stages of deep crystallisation in the plumbing system. The ascent stage of the crystallisation model represents the magma moving through the crust without further shallow storage; no record of such storage is preserved by any mineral-melt barometers. Whole-rock compositions from the platform-forming rift volcanics of El Hierro, published by Carracedo et al. (2001) (CIHI30) and Day et al. (2010) (JMDD EH01) together with five new whole-rock data presented in this paper were chosen as input liquid compositions. These starting compositions were chosen to represent most of the chemical variation in El Hierro whole-rock samples in the literature. Crystallisation models were generated using starting oxygen fugacities of FMQ+1, FMQ+2 and FMQ+3 for every sample, covering the fO_2 range calculated using melt inclusion S-speciation and olivine-spinel equilibria. Initial CO_2 concentrations were set at 0.6-0.75 wt%, while initial H_2O concentration was taken as 1 wt% (Weis et al., 2015; Taracsák et al., 2019). Calculations assume equilibrium crystallisation and closed-system degassing which are likely the predominant processes for prolonged and deep magma storage at El Hierro.

Theoretically, olivine-hosted spinels should record near-liquidus or early crystallisation temperatures (Coogan et al., 2014), as Cr-rich spinels tend to be one of the earliest crystallising phases. MELTS modelling suggests that primitive El Hierro magmas first saturate in spinel at temperatures between 1320 and 1400 °C, with higher magmatic fO_2 conditions yielding higher spinel crystallisation temperatures (Fig. 7.9D, E, F). Spinel is followed by the onset of olivine crystallisation at 1300-1320 °C. At this stage spinels can be trapped within growing olivine crystals, making this the highest recordable equilibrium temperature by the thermometer, assuming spinels can re-equilibrate with the melt until they are enclosed in the olivine. The olivine saturation temperatures

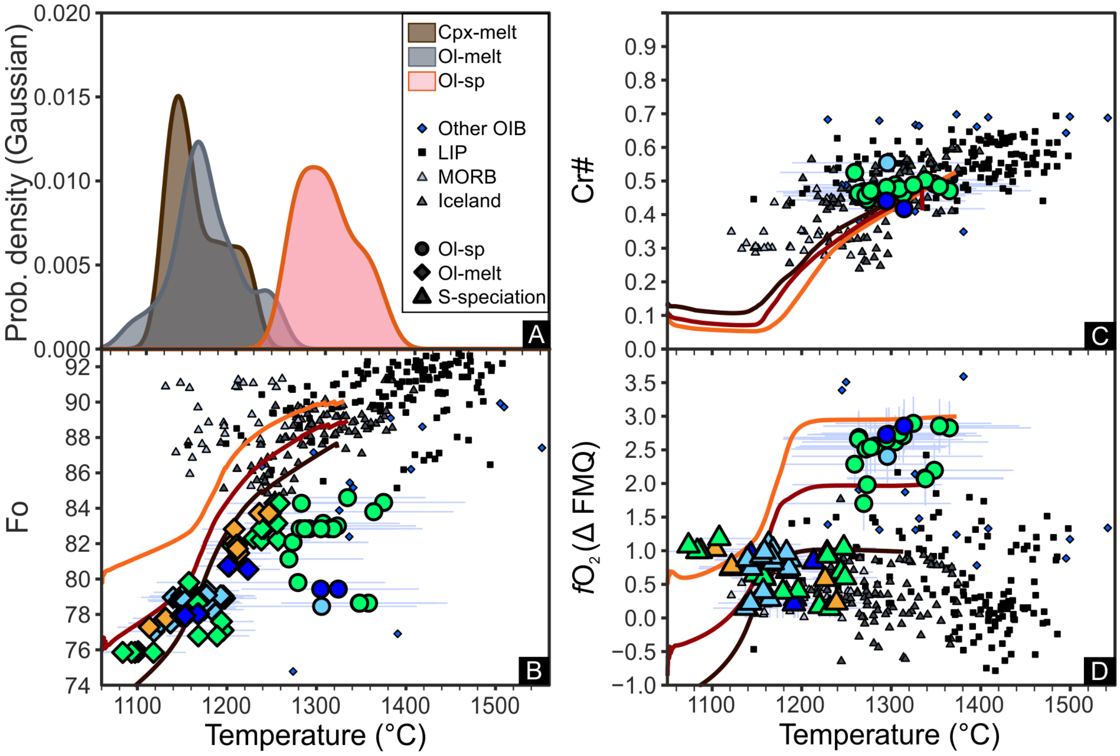

Figure 7.8: (A) Results from clinopyroxene-melt, olivine-melt and ol-sp thermometers summarized on a kernel density estimate diagram, each colour indicating estimates using separate methods. While clinopyroxene-melt and olivine-melt crystallisation temperatures overlap, the ol-sp thermometer recovers 100 °C higher temperatures, close to the liquidus predicted by MELTS. (B-D) Fo content of olivines hosting spinel inclusions, Cr# of selected high-Cr_2O_3 spinels, and fO_2 values based on ol-sp pairs and olivine-hosted melt inclusion S-speciation data are plotted against temperature (ol-sp thermometer results for spinel-based data, olivine-melt thermometer results for melt inclusion based fO_2). Colour scheme of the symbols, and the rhyolite-MELTS crystallisation pathways (solid lines) is identical to that used in Figs. 7.7 and 7.8. Small symbols are T and fO_2 estimates calculated using previously published olivine and spinel compositions, with a full list of references provided in the main text and in the supplementary material.

predicted by rhyolite-MELTS are consistent with our average olivine-spinel crystallisation temperatures of 1300 °C at El Hierro. Maximum temperature calculated using the olivine-spinel thermometer at El Hierro is 1365 °C. El Hierro olivine-spinel crystallisation temperatures are higher than those recovered for MORB (T_{avg} = 1190 °C, T_{max} = 1270 °C, Coogan et al. 2014), similar to average temperatures recovered from Iceland (T_{avg} = 1290 °C, T_{max} = 1374 °C, Spice et al. 2016; Matthews et al. 2016), and are somewhat lower than temperatures calculated from the few published olivine-spinel pairs from Hawaii and Réunion (T_{avg} = 1355 °C, T_{max} = 1540 °C, Sobolev and Nikogosian 1994). While the olivine-spinel thermometer is not specifically calibrated for the high Ti and Fe^{3+} contents characteristic of El Hierro spinels (Wan et al., 2008; Coogan et al., 2014) (Fig. 7.5), the output of the thermometer is well matched by rhyolite-MELTS modelling, suggesting that the thermometer can provide a robust method for estimating near-liquidus temperatures in alkaline basaltic systems.

Olivine saturation is followed by the appearance of clinopyroxene at 1240-1260 °C in our rhyolite-MELTS calculations (Fig. 7.9). In the models, significant crystallisation of clinopyroxene (20-30 %) and spinel (5-12 %) accompanied by olivine occurs after cooling below 1220 °C until reaching 1150 °C, i.e. the end of the isobaric crystallisation stage (Fig. 7.8 and 7.9). Olivine-melt and clinopyroxene-melt crystallisation temperatures predominantly record the temperature range where most of the crystallisation occurs in the magmatic system (Fig. 7.8) rather than the early stages of magma evolution.

We observe a strong discrepancy between observed olivine Fo contents at high temperatures (>1200 °C) and Fo contents predicted by rhyolite-MELTS, especially for crystallisation under the most oxidising conditions (Fig. 7.6B). This large difference in modelled and measured Fo contents of spinel-hosting olivines is present at any given temperature (Fig. 7.8). We also find differences between observed and modelled Mg# of El Hierro spinels at a given Al/Fe^{3+} ratio or Cr#, even though measured spinels capture most of the range in trivalent cation ratios predicted by rhyolite-MELTS (Fig. 7.5C, D). A shift in observed spinel Mg# and $Fe^{3+}/\sum Fe$ towards values similar to those calculated by rhyolite-MELTS with a starting fO_2 of FMQ+1 (i.e. increased Fe^{2+}, Fig. 7.5B) and low olivine Fo contents compared to modelled values can be explained by the exchange of Mg and Fe^{2+} cations between olivine, spinel and the surrounding melt via diffusion (e.g. Ozawa, 1984; Costa et al., 2008). Subsolidus re-equilibration, via

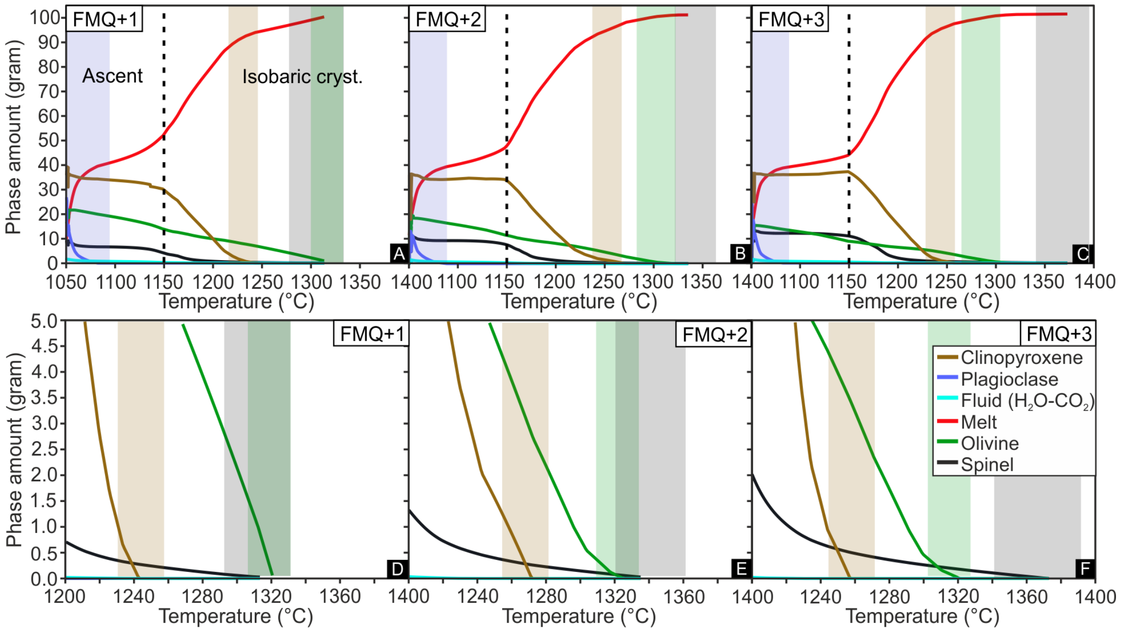

Figure 7.9: Modal abundance of crystallising phases predicted by rhyolite-MELTS modelling, plotted against temperature assuming various starting fO_2. A-C shows results for the whole temperature interval of crystallisation, while D-F show results for the early stages of crystallisation. On the y-axis, total mass of melt on the liquidus is between 99.6 and 101.2 grams; this is due to the whole-rock compositions not normalised to a 100% prior to model calculations. The dashed line in A-C indicates the transition between an initial stage of isobaric cooling and a later stage of fast ascent with dP/dT = 6 MPa/°C. Coloured boxes indicate the range of initial saturation temperatures for spinel (grey), olivine (green), clinopyroxene (brown) and plagioclase (blue). Saturation temperatures of spinel and hence liquidus temperature increases, while olivine saturation temperatures decrease, with more oxidising fO_2. Clinopyroxene saturation temperatures are not affected by fO_2. Feldspar only crystallises at lower temperatures and pressures, consistent with petrological observations that plagioclase is only common as a groundmass phase in El Hierro lavas.

diffusion of Fe^{2+} and Mg, between Cr-rich spinels and the olivine hosts would also provide and explanation for the offset between measured and modelled spinel Fe^{2+} contents (Lehmann, 1983). While olivine crystals and spinel inclusions initially formed in Mg-rich magmas, storage in the extensive plumbing system beneath El Hierro (e.g. Stroncik et al., 2009; Klügel et al., 2015) could have allowed sufficient time for the host olivine crystals to be mixed into more evolved melts with lower Mg#, such that diffusive exchange between melt and crystals perturbed the original olivine Mg-Fe^{2+} systematics and hence also changed the $Fe^{3+}/\sum Fe$ in the spinel inclusions. The lack of zoning in large olivine phenocrysts (Fig. 7.10), and the low variability of Mg# in clinopyroxene megacrysts (Mg# between 76 and 80 in >1 cm crystals; Longpré 2009) indicates that magmas feeding El Hierro eruptions were not significantly variable in their major element compositions. Another possible explanation for the lack of chemical zoning is that individual magma storage reservoirs were well mixed, and that there was sufficient time for Mg-Fe^{2+} to be reset both in the olivine crystals and olivine-hosted spinel inclusions. In this scenario, measured olivine Mg-Fe^{2+} ratios would represent melt composition just before ascent (Fig. 7.6). On the other hand, trivalent cations in spinels (Fe^{3+}, Cr, Al) are likely to record a composition in equilibrium with the original melt (Fig. 7.5C), as these elements diffuse considerably slower than Fe^{2+} and Mg in olivine (Chakraborty, 2010; Spandler and O'Neill, 2010) and are more robust to changes in the surrounding melt Cr, Al and Fe^{3+} content, and external fO_2 changes during melt evolution.

To explore the timeframe required to reset the Mg-Fe^{2+} systematic of olivines, we carried out diffusion modelling whereby a primitive unzoned olivine is stored in a more evolved surrounding melt. The aim of the modelling was to determine the timescale over which the compositional variation across a 0.5 mm and a 1 mm olivine becomes less variable than the Fo variability measured in profiles through our olivines, i.e. ±1 mol% Fo. We assume a simple one-dimensional model for a planar source with semi-infinite boundary conditions (Fig. 7.10). We used diffusion coefficients applicable to the a- and b-axis of the olivine, along which diffusion is six times slower than along the c-axis (Dohmen and Chakraborty, 2007). Therefore calculations yield maximum estimates of the re-equilibration time for a three-dimensional crystal. Two time estimates were calculated: one at 1150 °C and FMQ+1.5, representative of the calculated olivine crystallisation temperatures in samples from Tanganasoga, and one at 1250 °C and FMQ+2.5, representative of forsterite-rich olivines from the western rift. Starting olivine compositions of Fo_{83} and Fo_{88} were taken from the rhyolite-MELTS model with high starting fO_2 (FMQ+3) at 1150 or 1250 °C, while observed average Fo contents of

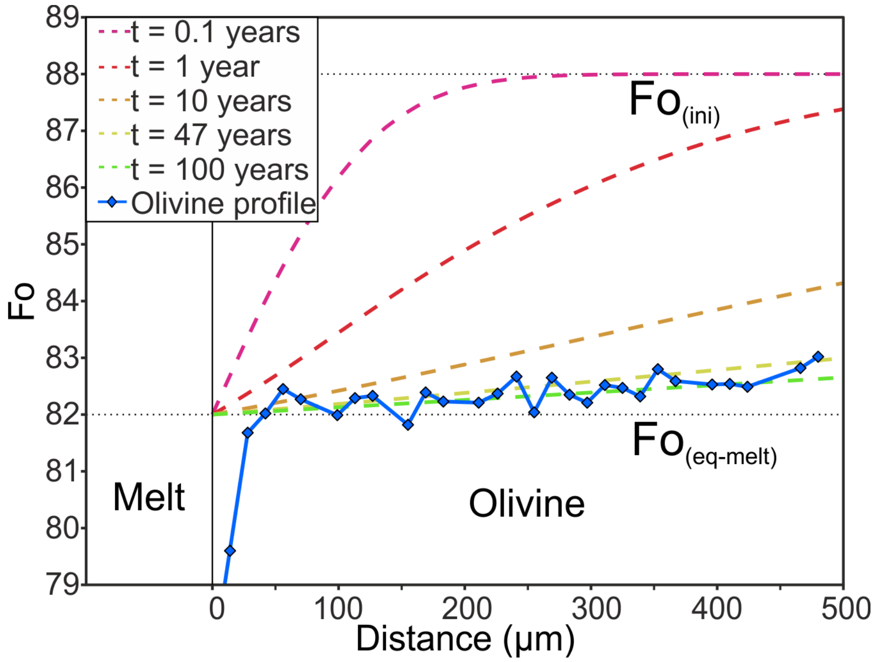

Figure 7.10: A simple one-dimensional olivine diffusion model at 1250 °C and fO_2 of FMQ+2.5) for a 1 mm diameter crystal. The model calculations (dashed lines) are compared with a measured profile (solid line with symbols indicating the measurement spots) of an olivine from the Northwestern rift zone. The measured olivine profile shows a near-constant core composition of 82-83 mol% Fo which probably grew during storage in the upper mantle. The 20 μm rim is considerably less forsteritic and likely crystallised during magma ascent just prior eruption. The near-flat Fo_{82-83} olivine core profile could be formed by diffusive re-equilibration between an initial Fo_{88} olivine and a more evolved surrounding carrier melt over a period of approximately 47 years under the specified magma storage conditions.

Fo_{79} and Fo_{82} were used as the final olivine compositions. Our diffusion calculations indicate that at 1150 °C it would take a maximum of 460 years for an initially unzoned Fo_{83} olivine to reach a composition of Fo_{79} with variability of <1 mol%, i.e. the typical olivine composition in crystal-rich Tanganasoga samples (Fig. 7.4). This timeframe decreases to 47 years at 1250 °C for an initial Fo_{88} olivine to reach a composition of Fo_{82} typical of samples from the western rift (Fig. 7.10). Diffusion modelling results indicate that, while storage times close to half a millennium could be needed to re-equilibrate olivines in our crystal-rich samples, more primitive magmas stored in the upper mantle can fully re-equilibrate olivine Mg-Fe^{2+} contents with their surrounding melts within a few decades.

7.5.2 Redox evolution of El Hierro magmas from mantle to surface.

Primitive ocean island basalts have typical oxygen fugacities between FMQ+1 and FMQ+2, intermediate between MORB (~FMQ) and island arc basalts (>FMQ+2, Ballhaus 1993; Williams et al. 2005; Evans et al. 2012; Berry et al. 2018). Recent advances in $Fe^{3+}/\sum Fe$ and $S^{6+}/\sum S$ ratio measurements in matrix glasses and melt inclusions indicate that there is significant change in fO_2 during magma ascent, mainly due to sulfur degassing (Brounce et al., 2017; Moussallam et al., 2016, 2019). Crystallisation may also affects oxygen fugacity, most notably during crystallisation of Fe^{3+}-rich spinel, as shown in our rhyolite-MELTS modelling (Fig. 7.10D). If Fe^{3+}-rich spinel crystallisation precedes the earliest stages of melt inclusion trapping, it may be the case that neither melt inclusions nor matrix glasses record the primary melt fO_2 and hence cannot be used to draw conclusions on mantle source fO_2.

Cr-rich spinel inclusions hosted in olivines are a good alternative to melt inclusions in determining magmatic fO_2. Spinels are commonly used for oxybarometry calculations in mantle xenoliths (e.g. O'Neill and Wall, 1987; Ballhaus, 1993), and these oxybarometers can be applied to magmatic spinels when certain compositional criteria, introduced in section 7.3.1 of this thesis, are met (Ballhaus, 1993; Evans et al., 2012). Oxygen fugacities recovered from our entire sample suite range between FMQ+1.7 and FMQ+2.9, while if only samples from the Western rift zone are taken into account, its 2.5±0.3 log units above the FMQ buffer (Fig. 9/D). These values are a minimum of 1.5 log unit higher than MORB (Cottrell and Kelley, 2011; Berry et al., 2018). They represent some of the highest magmatic fO_2 determined previously from OIBs, and more closely resemble arc magmas (Evans et al., 2012). Our olivine-spinel oxybarometry estimates indicate more oxidising conditions than $Fe^{3+}/\sum Fe$ data measured in volatile-rich melt inclusions from El Hierro (fO_2 up to FMQ+1.5) and Lanzarote (around FMQ+1) (Moussallam et al., 2019). However, based on observed degassing trends, Moussallam et al. (2019) estimated primary melt fO_2 to be around or above FMQ+2 at El Hierro.

This is in good agreement with our olivine-spinel fO_2 estimates, indicating that olivine-spinel pairs are well suited to record early magmatic fO_2.

Melt inclusion and matrix glass sulfur speciation data record less oxidising conditions than olivine-hosted spinel inclusions: FMQ+0.2 to FMQ+1.3 for melt inclusions, and FMQ+1 in matrix glasses (Fig. 7.7). We used D-Compress (Burgisser et al., 2015) and rhyolite-MELTS to explore the expected variation in melt fO_2 during crystallisation and degassing (Fig. 7.7, 7.8). Variation in melt inclusion oxidation state broadly follows H_2O degassing trends modelled using a starting fO_2 of FMQ+1 and H_2O content of 2 wt% (see chater four for discussion on volatile contents, Taracsák et al. 2019). The degassing trend predicted by rhyolite-MELTS assuming a primary melt H_2O content of 1 wt% and FMQ+3 starting fO_2 also reproduces the observed variation, due to the extensive decrease in magma fO_2 during the main crystallisation phase at 1150-1200 °C, which precedes water degassing. The rhyolite-MELTS model links the high oxidation state recorded by spinels with the more reduced melt inclusions: while spinels record early near-liquidus fO_2 conditions of FMQ+1.7 to FMQ+2.9, melts trapped by MIs and matrix glasses are more reduced due to subsequent degassing and crystallisation of Fe^{3+}-rich phases such as spinel with a high magnetite component. Even if melt inclusions are trapped at early phases of crystallisation, fast diffusion of Fe^{2+} through olivine via point defects can reset melt inclusion fO_2 within hours to days at magmatic temperatures (Gaetani et al., 2012), causing melt inclusions to record more reducing conditions than spinels.

Spinels are prone to Mg-Fe^{2+} re-equilibration with the surrounding magma and with the host olivines, even under subsolidus conditions, in our samples as indicated by Mg# and Al/Fe^{3+} systematics of the spinels compared to rhyolite-MELTS modelling. The best fit to the data is provided by a rhyolite-MELTS model with a starting fO_2 of FMQ+1 (Fig. 7.5C). Therefore it is necessary to evaluate the effect of Mg-Fe^{2+} exchange on our calculated fO_2 values. By assuming an ideal spinel composition of $(Mg_{0.5}Fe^{2+}{}_{0.5})$

$(Al_{0.4}Cr_{0.8}Fe^{3+}{}_{0.4})O_4$ hosted in a Fo_{85} olivine we carried out a simple test to determine the effect of changes in pressure, temperature and chemical composition of the spinel and its host olivine on calculated fO_2 values. Input parameters in the oxybarometer equation of Ballhaus et al. (1991) were varied individually in order to assess which exert the strongest control on calculated fO_2. The largest change is caused by varying the Fe^{3+} content of the spinel: a decrease of 0.2 in $X(Fe^{3+})$, i.e. $Fe^{3+}/(Fe^{3+}+Cr+Al)$, in the spinel translates to a 1.2 log unit decrease in calculated fO_2. The second largest effect is changing the Fo content of the olivine with a ~0.13 log unit decrease resulting from changing Fo by 1 mol% (i.e. changing Fo by 5 mol% yields calculated fO_2 values within two times the nominal error of the oxybarometer). Changing the spinel Mg# by 0.2 only changes fO_2 by 0.3 log units, i.e. within the error of the oxybarometer. Therefore, as the fO_2 values calculated using the olivine-spinel oxybarometer are mostly governed by trivalent cations that diffuse slowly through olivine, olivine-spinel oxybarometry can be used to estimate of early magmatic fO_2 with a < 0.7 log unit accuracy even in samples that may have been affected by diffusive re-equilibration due to long storage at high temperatures.

7.5.3 Mantle temperature and fO_2 at El Hierro, and its implications on melt genesis of HIMU ocean island basalts.

Mantle potential temperatures and melting pressures beneath El Hierro

Mantle potential temperature calculations are commonly used to assess the temperature difference between the mantle sources of mid-ocean ridges and intraplate magmas (e.g. Herzberg and Asimow, 2008; Putirka, 2008a; Lee et al., 2009). To evaluate the melting conditions beneath El Hierro and the Canary Islands, and to compare them with melting processes beneath other regions, we carried out potential temperature (T_p, i.e. the temperature of the mantle upon the inception of melting projected adiabatically to

P = 0 GPa) calculations on a large dataset of literature whole-rock compositions. We compiled 4951 samples with MgO > 8 wt% taken from the GeoROC and PetDB (2019 May) databases, and used PRIMELT3 Herzberg and Asimow (2015) to calculate Tp (Fig 7.11). Mantle melting pressures and temperatures for the same sample set were also calculated using the method of Lee et al. (2009). In summary, PRIMELT3 calculates mantle potential temperature by projecting magma compositions in a olivine-quartz-anortite ternary and MgO-FeO systems, and derived a primitive magma and melt fraction from these, while temperature and pressure in the Lee et al. (2009) model is derived from magma Si, Mg, Ca and water (H) contents. The literature dataset includes samples from: (1) the Canary Islands, Cape Verde, St. Helena and the Cook-Austral Islands, representing OIBs with HIMU or HIMU-like Pb-isotopic compositions and low eruption rates (if still active); (2) Hawaii and Réunion, representing OIBs with high eruption rates and widespread tholeiitic volcanism; (3) MORB from the middle segment of the Atlantic ridge (between latitudes of 1°S to 37°N); and (4) Icelandic samples, representing E-MORB. We also include a number of whole rock compositions from the North Atlantic Igneous Province (NAIP), as this is one of the few locations where Tp and Al-in-olivine thermometer results can be compared (Coogan et al., 2014; Spice et al., 2016). References for the whole-rock compositions used to calculate T_p are provided in the supplementary material.

Input Fe^{2+}/Fe^{3+} ratios were calculated using the method of Kress and Carmichael (1991) at representative fO_2 values for HIMU-like OIB (FMQ+2), Hawaii and Réunion (FMQ+1.5), Iceland and MORB (FMQ+0.5). For the Lee et al. (2009) model a mantle olivine composition of Fo_{90} was assumed. Initial olivine $K_d{}^{Mg\text{-}Fe}$ was estimated for each location based on average melt composition Gee and Sack (1988).

Results from the PRIMELT3 calculations were filtered using the inbuilt error codes: samples where clinopyroxene fractionation or accumulation was indicated were filtered out as a first step. Samples were also removed where extreme mantle olivine forsterite content (Fo<84 and Fo>94) or a source composition not handled well was predicted by PRIMELT3 (i.e. samples with inferred pyroxenite or volatile-rich peridotite in the source). Errors relating to source composition were most common at ocean island localities erupting HIMU magmas, where volatile-rich peridotite in the mantle source was often inferred. No whole-rock data satisfied the above mentioned criteria from St. Helena or the Cook-Austral Islands, and only 2 % of compositions remained after filtering from our Canary Islands (17 in total from 677, none from El Hierro) and Cape Verde (9 from 638) datasets. A volatile-rich peridotite source was indicated for 201 Canary Island (18 from El Hierro), 296 Cape Verde, nine St. Helena (out of 26), and 14 Cook-Austral Island (out of 27) whole-rock compositions. Combining all our data from ocean islands erupting HIMU-like magmas, 80% of the whole-rock data are unsuitable for T_p estimation due to volatile-rich peridotite being inferred in their mantle source. For our Atlantic MORB dataset, 43% (484 out of 1128) of whole-rock compositions fit all the criteria.

Previous studies of the Canary Islands have suggested elevated temperatures (~1450 °C) compared to ambient mantle (1300-1400 °C) (Herzberg and Asimow, 2008, 2015; Fullea et al., 2015). Our average mantle potential temperature estimates calculated using PRIMELT3 for the Canary Island overlap with these estimates at 1444±21 °C (n = 17, errors reported in this section are 80% confidence intervals of the average) (Fig. 7.9). However, this value overlaps with our average T_p estimate for Mid-Atlantic MORB, which is 1427±2 °C (n = 484). Therefore, our potential temperature estimates do not provide conclusive evidence that the mantle beneath the Canary Islands has elevated temperatures compared to Atlantic MORB. A similar observation can be made for the Cape Verde Islands. Average T_p at Cape Verde is 1423±8 °C (n = 9), indistinguishable from Atlantic MORB. In contrast to the Canary Islands and Cape Verde, Icelandic potential temperature estimates are 70 °C higher than Atlantic MORB, at T_p = 1497±5 °C (n = 150), providing robust evidence for a hotspot origin in agreement with recent

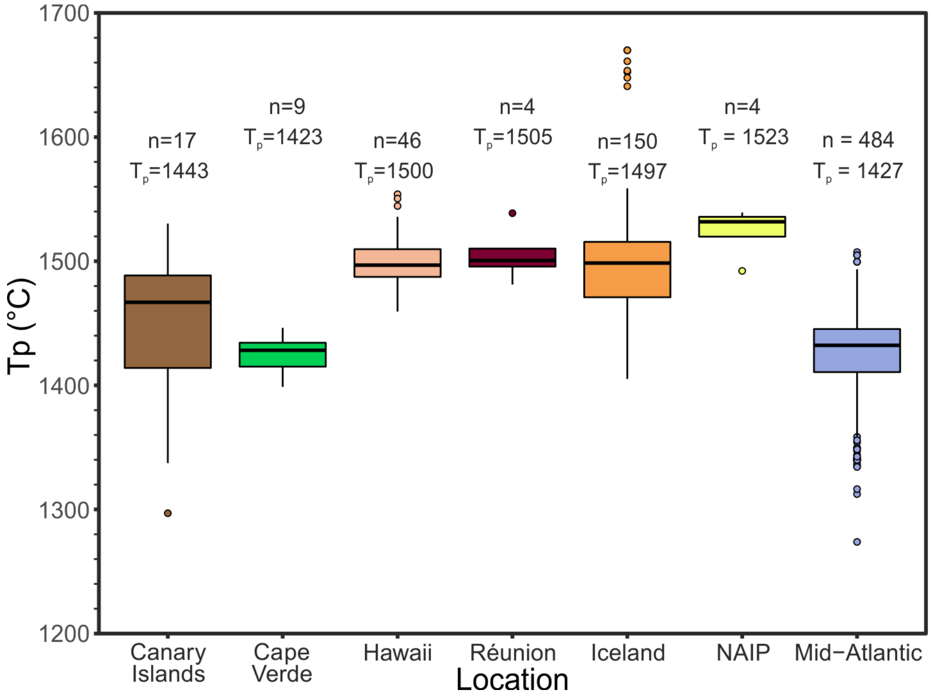

Figure 7.11: Mantle potential temperatures calculated using PRIMELT3 (Herzberg and Asimow, 2015) for various locations and geodynamic settings: OIB with HIMU affinity (Canary Islands Cape Verde); other OIB (Hawaii, Réunion); MORB (only including Atlantic Ocean samples between latitudes 1°S and 37°N along the present ridge); enriched-MORB (Iceland); and magmas associated with large igneous provinces (North Atlantic Igneous Province). Above the boxplots, T_p indicates the average value in °C, while n is the number of samples used. Whole-rock samples where the PRIMELT3 indicate any error messages were filtered, including clinopyroxene accumulation/fractionation and source composition, resulting in filtering between 95% and 98% of samples from any OIB location. T_p range for the Canary Islands overlap with previous estimates of Herzberg and Asimow (2008), while Atlantic MORB T_p is 60 °C higher than for East Pacific Rise MORB. Cape Verde samples overlap with Atlantic MORB, while average T_p is 20 °C higher at the Canary Islands, i.e. within the error of the method (40 °C). Locations like Hawaii, Reunion and Iceland have 70-80 °C higher T_p compared to MORB; in the case of Iceland, T_p presented here overlaps with other recent estimates (e.g. Shorttle et al., 2014; Matthews et al., 2016).

studies (Shorttle et al., 2014; Matthews et al., 2016; Spice et al., 2016).

Melting temperature and pressure calculations using the method of Lee et al. (2009) suggest that Canary Island and El Hierro magmas have higher predicted T_p than MORB by 50 and 90 °C, respectively (Fig. 7.12). The estimated Canary Islands T_p of 1460 °C is intermediate between MORB (1410 °C) and Iceland (1510 °C, Fig. 7.12C), and more closely resembles other HIMU-type OIBs such as those erupting on Cape Verde (Fig. 7.12B). There is a large spread in melting temperature values at a given pressure for both Canary Island and Cape Verde magmas, causing a large uncertainty in estimating T_p, as opposed to MORB or Iceland which have a narrow P-T path (Fig. 7.12B, C). Melting pressures for the Canary Islands magmas and other OIBs with HIMU affinity are between 1-6 GPa, lower than what would be expected for magmas generated under a thick oceanic lithosphere (Fig. 7.12B). The P-T paths of HIMU OIBs are not near-parallel to melting isopleths, as is the case Icelandic basalts and MORB (Fig. 7.12C) or OIBs where tholeiitic magmas are common, such as Hawaii (Fig. 7.12D). This makes T_p estimates from HIMU OIB unreliable. In our calculations, mantle olivine Fo contents were set uniformly at 90; however, it is possible that olivine forsterite content in the enriched HIMU-mantle is lower due to the addition of melt from subducted eclogites which have lower MgO but higher FeO and SiO_2 contents (e.g. Pertermann and Hirschmann, 2003). It is also possible that a refractory source such as Depleted MORB Mantle (DMM), could have higher mantle forsterite content than 90 due to previous melt depletion events. Decreasing the source olivine forsterite content with 1 mol% would decrease calculated temperatures by approximately 20-30 °C, or cause the opposite effect if Fo is increased. This further complicates T_p estimation for HIMU OIBs, since their mantle source is commonly thought to contain recycled crustal materials (e.g. Hofmann, 1997; Stracke et al., 2005; Day et al., 2010). It is therefore challenging to compare mantle potential temperatures between HIMU OIBs and the ambient upper mantle.

Due to the multiple challenges in obtaining reliable T_p estimates for the Canary Islands, the T_p values presented here likely to have large uncertainties. These uncertainties arise either because some mantle source lithologies are not fully incorporated into models (PRIMELT3 calculates primary melt composition and melting degree based on experiments on anhydrous peridotite KR-4003, Walter 1998), causing issues with calibration when e.g. volatile-rich peridotite is in the source (Herzberg and Asimow, 2008, 2015), or from uncertainty in input parameters such as mantle olivine forsterite content

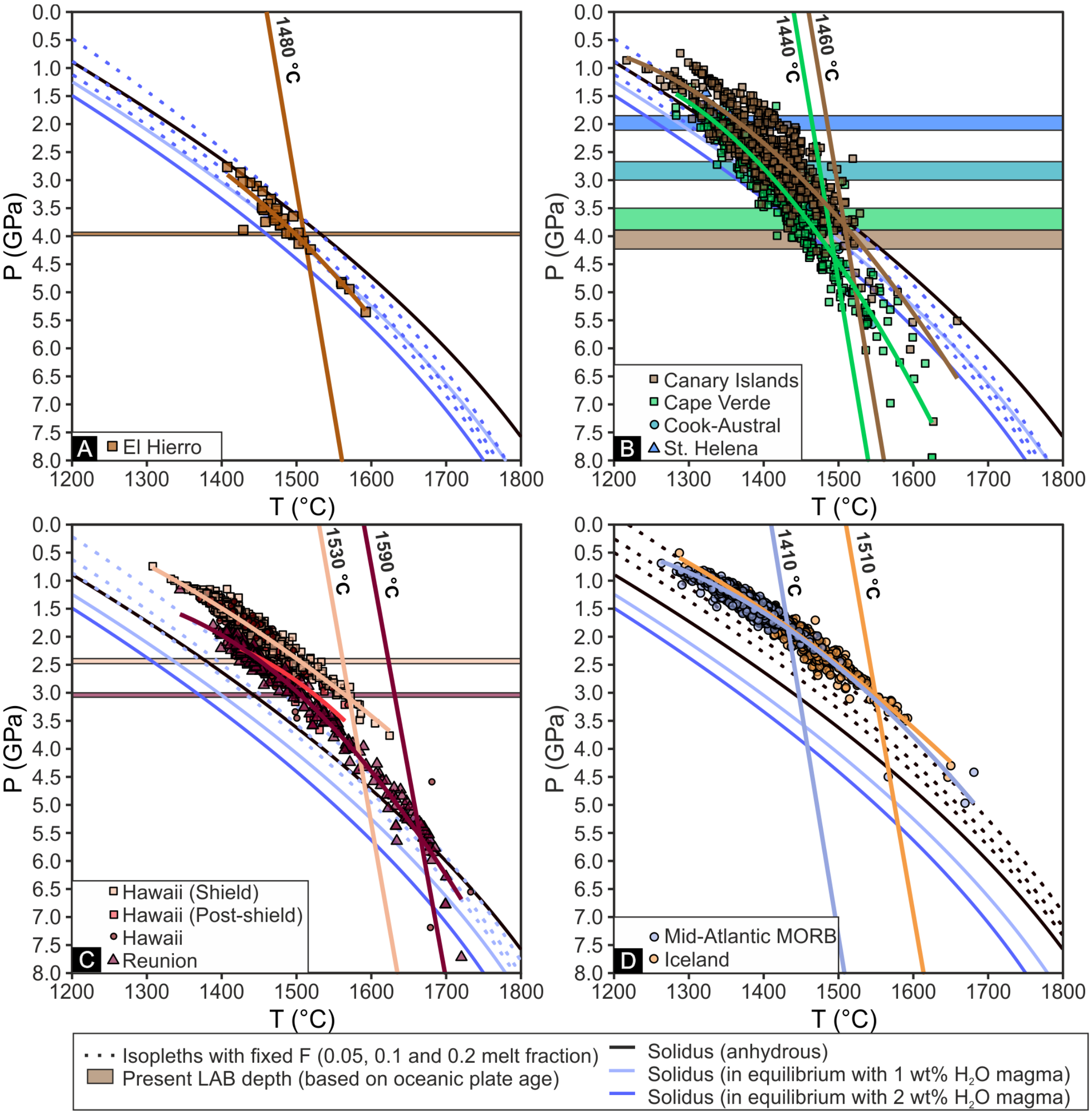

Figure 7.12: Melting temperatures and pressures for global OIB and MORB localities, calculated using the model of Lee et al. (2009). Horizontal coloured lines indicate the depth of the lithosphere-asthenosphere boundary (LAB) beneath each location, calculated using the half-space cooling model of Steinberger and Becker (2018) and seafloor ages of Müller et al. (2008). Coloured near-vertical lines are mantle adiabats corresponding to the best possible T_p estimates for each location, based on the sample P-T paths and their intersections with the anhydrous and hydrous solidi of Katz et al. (2003). El Hierro and other HIMU affinity OIBs show much lower melting pressures, down to 1 GPa, than the depth of the LAB in the region. This is most prominent for the Canary Islands and Cape Verde, both of which formed over Jurassic oceanic lithosphere. Melting pressures are also lower than expected in Hawaii and Réunion; in the case of Hawaii shield-stage lavas, this discrepancy is explained by thermal erosion of the LAB Lee et al. (2009), which could also occur beneath Réunion. Mantle T_p estimates are considerably (>100 °C) higher at Iceland Hawaii, and Réunion than at mid-ocean ridges, while Cape Verde and Canary Island samples are only 30-50 °C higher than MORB.

such as in the case of the Lee et al. (2009) model.

Our calculations yield T_p estimates for Iceland, Hawaii and Réunion that are ∼80-100°C higher than MORB, consistent with previous studies (Falloon et al., 2007; Herzberg and Asimow, 2008, 2015; Lee et al., 2009; Matthews et al., 2016). However, it is challenging to evaluate if there is a real difference in mantle temperature beneath ocean islands erupting basalts with HIMU affinity and ambient mantle (Fig. 7.11, 7.12). While PRIMELT3 gives 20 °C higher average temperature for the Canary Islands compared to Mid-Atlantic MORB, this difference is both within the statistical uncertainty of the average values, and within the error of the method itself (±42 °C, Herzberg and Asimow 2015). We note that our Mid-Atlantic MORB T_p estimate is at least 20 °C higher than the ambient MORB temperature of presented by Herzberg et al. (2007), and 80 °C higher than T_p estimate of 1344 °C for Siqueiros MORB from the East Pacific Rise Herzberg and Asimow (2015) calculated using PRIMELT3. However, it is possible that temperature differences exist between the ambient mantle temperature beneath the Mid-Atlantic and the East-Pacific ridges.

Olivine-spinel thermometry could provide an alternative way to estimate mantle source temperature, as it records near-liquidus conditions from which mantle temperature can be derived (Matthews et al., 2016). Olivine-spinel co-saturation temperature estimates for El Hierro (1300±20 °C) are higher than temperatures calculated for MORB (<1270 °C; Coogan et al. 2014), generally lower than estimates from LIPs (Fig. 7.8), and overlap with data from Iceland (Matthews et al., 2016; Spice et al., 2016), the latter ranging from 1180 to 1400 °C (Fig. 7.9). Olivine-spinel thermometry results have been used to estimate mantle potential temperatures for MORB and Icelandic magmas, where the geotherm of the ascending asthenosphere provides a good control on the decrease in magma temperature from mantle source to surface (Matthews et al., 2016). However, for the Canary Islands, the decrease in magma temperature from the asthenospheric mantle source to the upper mantle plumbing system is much harder to define, due to the presence of 80 km-thick lithospheric mantle beneath the Canary Islands (Fig 7.12): there will be an unknown amount of heat exchange between the melt and the lithospheric mantle. The shape of the geotherm close to the lithosphere-asthenosphere boundary and the decrease in magma temperature before olivine-spinel co-saturation is reached add further uncertainties to such calculations. Nonetheless, based on the data presented here, there is no clear indication of excess mantle temperatures beneath the Canary Islands or Cape Verde compared to ambient, Mid-Atlantic MORB mantle. However, PRIMELT3 modelling does suggest a widespread, volatile-rich peridotitic mantle source for OIBs with a HIMU isotopic signature from locations in the Atlantic and Pacific oceans. This volatile-rich material likely plays a major role in melt generation beneath these ocean islands.

Oxidising conditions and volatiles as a driving force of magmatism beneath the Canary Islands

Near-liquidus oxygen fugacity estimates of FMQ+2 to FMQ+3 indicate that El Hierro could represent an oxidised OIB endmember locality (Fig. 7.8C). This oxidation state is 1-3 logfO_2 units higher than MORB (FMQ, e.g. Berry et al. 2018) or Icelandic magmas (FMQ+0.5, Shorttle et al 2015), and is similar to arc basalts (Evans et al., 2012). This indicates that a highly oxidised component is present in the El Hierro mantle source (Fig. 7.8). High fO_2 at El Hierro is coupled with high magmatic volatile contents, most notably S and C (Longpré et al., 2017; Taracsák et al., 2019). It has been suggested that both S and C play a key role in generating high-fO_2 melts beneath island arcs through redox reactions between a reduced, mantle silicate assemblage and an oxidised, slab-derived fluids rich in carbon and sulfur (Rielli et al., 2017)

Both S and C have been shown to be partially recycled into the mantle during subduction (Evans, 2012; Plank and Manning, 2019). If recycled into the asthenosphere, oxidised S and C could play a crucial role in mantle redox reactions and influence the oxidation state of the mantle source of ocean island basalts. If subducting slabs stall at the density boundaries in the mantle transition zone, it is possible that significant amounts of recycled and oxidised C and S could be released from the slab at this depth (Fig 7.13A). Volatiles can be either released from the slab by melting it as it is heated by its surroundings, or by the breakdown of volatile-rich phases. This volatile enrichment and subsequent mantle metasomatism could be an explanation for low p- and s-wave velocities often found at these depths (Fukao et al., 1992; Revenaugh and Sipkin, 1994; Wolfe et al., 2009), which is a prominent feature beneath the Canary Islands (French and Romanowicz, 2015). Volatile-rich mantle formed at the mantle transition zone can eventually become buoyant and begin to upwell towards the surface (Thompson et al., 2015; Long et al., 2019; Yang and Faccenda, 2020).

This volatile-rich upwelling material will transport metasomatised peridotite, recycled lithospheric material and excess volatiles into the shallower asthenosphere, where further melting will occur due to decompression and phase instability (e.g. at the boundary of carbonate stability at 300 km depth; Dasgupta and Hirschmann 2006, 2010). This melt, enriched in volatiles (S, C and possibly H_2O) and incompatible elements, will react

---

Figure 7.13 (next page) : Model for melt generation beneath the Canary Islands, and for low melting degree HIMU-type OIBs. In (A), a hypothetical subduction event transports oceanic lithospheric material to the asthenosphere. The partially devolatilised below the mantle wedge, but still contains F, S and possibly C and H_2O, in sulfates, carbonates and nominally anhydrous minerals when it reaches the transition zone at 410 km. Increase in mantle density at the transition zone causes some, if not all, of the subducted material to stall and accumulate at the base of the asthenosphere. As it is heated by the surrounding mantle, it starts releasing its remaining volatiles and becomes mixed into the ambient mantle. Mantle convection transports the subducted lithosphere and metasomatised mantle within the asthenosphere, until it becomes buoyant and forms a volatile-rich mantle upwelling (B) containing excess S, C and H_2O either within minerals and/or as low-fraction interstitial melt. In (C) the process of mantle metasomatism is detailed. A volatile-rich metasomatic agent added to a primitive mantle material reacts with olivine to form orthopyroxene, clinopyroxene, and possibly sulfides and diamonds due to its high S and C content. During this process, the reduction of S^{6+} and C^{4+} to S^{2-} and C^0 oxidises the silicate assemblage. This oxidised mantle material melts to generate the most trace element-enriched and oxidised melts beneath El Hierro, which then mix with less enriched melts derived from the top of the lithosphere or from less-enriched mantle domains. These melts mix and equilibrate during storage at 400-1000 MPa, before erupting on the surface.

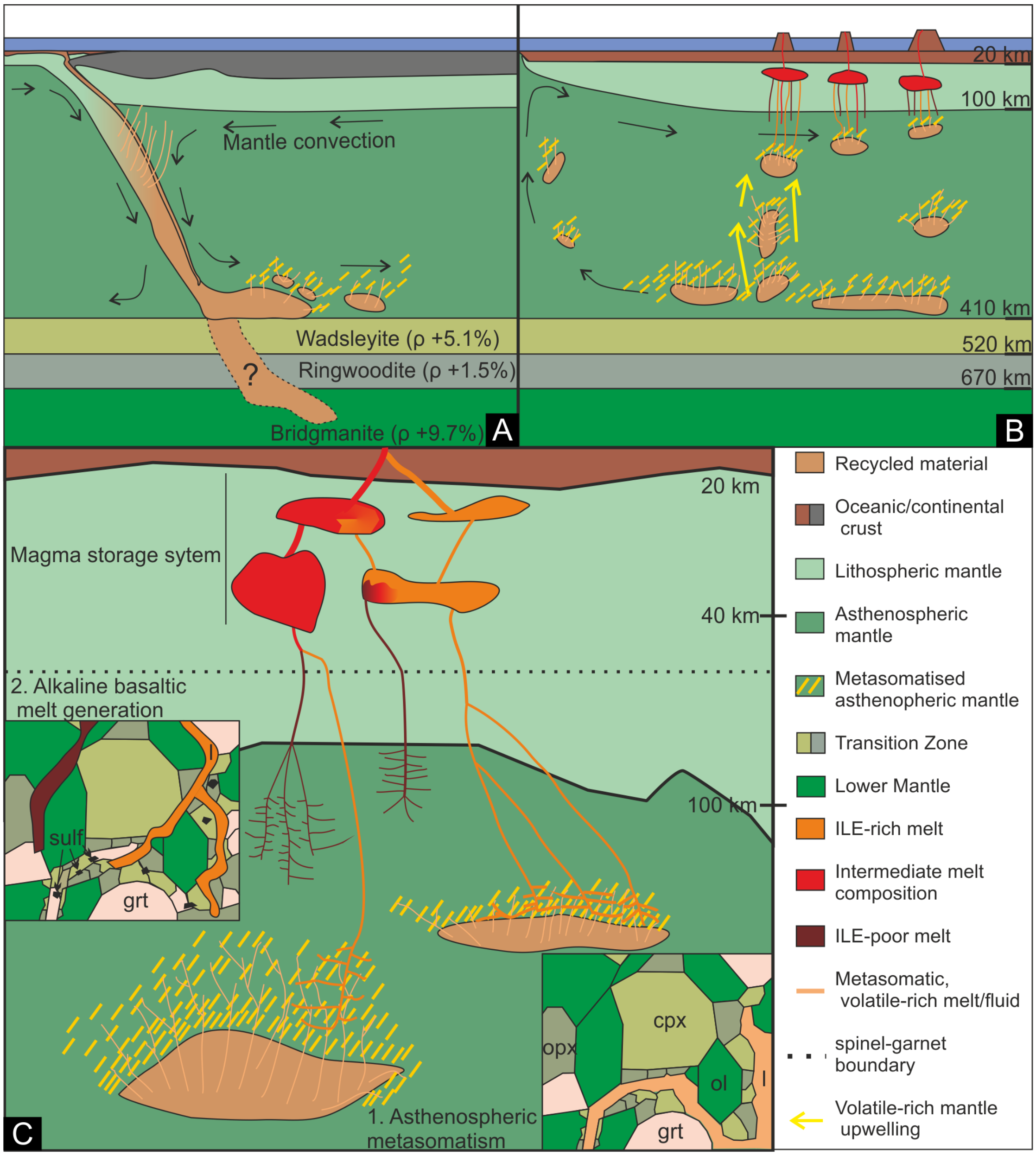
Mantle convection
Wadsleyite (ρ +5.1%)
Ringwoodite (ρ +1.5%)
?
Bridgmanite (ρ +9.7%)
A
20 km
100 km
410 km
520 km
670 km
B
20 km
Magma storage sytem
40 km
2. Alkaline basaltic melt generation
l
sulf
grt
100 km
cpx
opx
ol
l
grt
1. Asthenospheric metasomatism
C
Recycled material
Oceanic/continental crust
Lithospheric mantle
Asthenospheric mantle
Metasomatised asthenopheric mantle
Transition Zone
Lower Mantle
ILE-rich melt
Intermediate melt composition
ILE-poor melt
Metasomatic, volatile-rich melt/fluid
spinel-garnet boundary
Volatile-rich mantle upwelling

with the upper asthenosphere and enrich it in S and C, oxidise the silicate assemblage via redox reactions (as the sulfate- and carbonate-rich melt “freezes” it will form reduced phases stable in the upper asthenosphere e.g. diamonds and sulfides), increase the modal proportion of pyroxenes compared to olivine, and decrease the solidus of the upper asthenosphere (Fig. 7.13C). A similar scenario has been proposed for melt generation beneath intracontinental basalts in Southern China where buoyancy is provided by excess volatiles in the plume, rather than excess temperatures (Kuritani et al., 2019), while magmatism at the island of Bermuda has been recently explained by volatile-rich, recycled material upwelling from the mantle transition zone (Mazza et al., 2019). Melts originating from metasomatic veins within the lithosphere, formed by reactions of a fluid-rich melt and lherzolitic mantle (i.e. in a similar manner than in Fig. 7.13), have been proposed as a possible explanation for alkali basaltic volcanism at ocean islands (Pilet et al., 2008), albeit with melt-rock reactions and melt generation occurring at much shallower depth than in our model.

Our proposed model could explain magmatism at the Canary Islands without a significant mantle thermal anomaly, and could account for some issues that arise from the classic thermal plume model originating from the core-mantle boundary, including the low eruption rate of Canary Island volcanoes at sporadic locations, and the absence of compositional trends between islands compared to that observed in Hawaii (i.e. SiO_2-rich tholeiites erupting on Lanzarote during the post-shield stage, while alkaline magmas erupt on Tenerife, La Palma and El Hierro during the shield building stage, just above the inferred position of the plume). The sporadic nature of eruptions in the Canary Islands can be explained by volcanic activity being restricted to areas with a higher proportion of volatile-rich mantle in the source, producing extractable ($>1\%$ melt fraction) volumes of melt. Compositional variability (tholeiitic vs alkaline) on some islands, like Gran Canaria and Lanzarote, can be explained by various volatiles being heterogeneously distributed in the source: CO_2-rich magmas will be Si-poor, while H_2O rich magmas are Si-rich (e.g. Grove et al., 2006; Dasgupta and Hirschmann, 2010). Therefore, widespread alkaline volcanism at the Canary Islands can be attributed to excess S and C in the mantle source being a common feature. Sub-lithospheric seismic anomalies observed beneath the Canary Islands (e.g. Fullea et al., 2015) can be explained by the addition of low-fraction volatile-rich fluids and/or melts, as opposed to excess temperatures of 100 °C, as volatile-rich fluids decrease seismic wave speed. A broad seismic velocity anomaly of up to -1.7% $\delta V_s/V_s$ at depths just above 500 km (French and Romanowicz, 2015), i.e. the top of the mantle transition zone also fits well within our model, as the upwelling of a volatile-enriched, buoyant mantle originates at this depth (Fig. 7.13A). A mantle temperature close to ambient Atlantic MORB mantle beneath the Canary Islands could also explain the low eruption rate compared to Hawaii and Réunion, as high mantle temperatures would be expected to produce elevated magma fluxes at the Canary Islands. Some features of our model are similar to the "blob" model of Hoernle and Schmincke (1993b), most notably the presence of a fusible material mixed with refractory material in the asthenospheric mantle. Our model also includes a broad mantle upwelling beneath the Canary Islands, as has been suggested previously (e.g. Fullea et al., 2015). However, a major difference in our model compared to previous works is that magmatism is primarily driven by mantle heterogeneity and volatile enrichment as opposed to excess mantle temperatures.

Addition of slab-derived metasomatic agents to the OIB source mantle originating from the transition zone has been proposed as a model for magmatism for Bermuda (Mazza et al., 2019), a location that erupted basalts with a similar isotopic signature to those erupting on El Hierro and the Canary Islands in general. The model presented in figure 7.13 for El Hierro could be applicable to other locations that have similar characteristics like a low melt flux and magmas with HIMU-like Pb-isotopic composition, such as Cape Verde and St Helena in the Atlantic Ocean or the Cook Islands in the Pacific Ocean. Oxidising conditions in slab-derived melts and fluids could facilitate the extraction of uranium causing high ^{238}U/^{204}Pb in the source compared to OIBs with less metasomatised material in their source. Therefore, the model presented here is an alternative to the previously proposed deep mantle origin (e.g. Kogiso et al., 1997; Takamasa et al., 2009; Jackson et al., 2018) for the HIMU mantle endmember.

7.6 Conclusions

We have used a combination of mineral-melt and mineral-mineral thermometers, barometers and oxybarometers to probe the conditions of melt generation and storage beneath El Hierro, Canary Islands. Pressure estimates based on cpx-melt barometry indicate storage depths of 15-35 km corresponding to uppermost mantle, consistent with data from previous studies of El Hierro. Near-liquidus melts have a temperature of 1300 °C. Temperature during magma storage is between 1100-1250 °C, coinciding with the main phase of crystallisation, which was dominated by clinopyroxene and oxides. Rhyolite-MELTS modelling confirms the relationship between phase saturation and estimated crystallisation temperatures. Olivine-hosted spinel inclusions preserve a near-primary magmatic fO_2 of 2.3±0.4 log units above the FMQ buffer. Melt inclusions and matrix glasses record more reducing conditions due the combined effects of crystallisation, degassing and resetting of fO_2 via Mg-Fe^{2+} diffusion in melt inclusions. The lack of chemical zoning in olivine phenocrysts suggests prolonged storage of decades to centuries for crystal-rich magmas beneath El Hierro. Long magma storage durations could also cause extensive re-equilibration of Mg-Fe systematics observed in spinel inclusions in olivines.

Average mantle potential temperature estimates from the Canary Islands (and Cape Verde) are not statistically different from Mid-Atlantic MORB, albeit only 2% of whole-rock compositions return robust T_p estimates according to model criteria. Melting pressures for El Hierro are between 2.5-5 GPa, and 0.5-6 GPa for the Canary Islands archipelago, in both cases predicting a shallower melting region than would be expected based on the depth of the lithosphere-asthenosphere boundary at >4.0 GPa. Differences in melting pressure estimates and large uncertainties in potential temperature calculations are likely caused by the lack of experimental data available for volatile-rich alkaline basalts with which to calibrate mantle melting models, making it challenging to evaluate mantle thermal conditions beneath the Canary Islands. We find no strong and conclusive evidence for elevated temperatures beneath the Canary Islands, and more generally for ocean island erupting magmas with a HIMU affinity. However, based on the large proportion (80%) of HIMU OIBs predicted to have a volatile-rich peridotite source, our results suggest that widespread and heterogeneous volatile enrichment is present in the mantle source of these ocean islands globally.

Combining high primary oxygen fugacity estimates with previous observations of high S and C contents, we propose a model for melt generation at El Hierro (Fig. 7.13). Our model involves a volatile-enrichment driven mantle upwelling from the mantle transition zone, incorporating previously metasomatised mantle and recycled lithosphere. This upwelling material likely contains a low fraction of a melt or fluid phase that can account for the low velocity anomalies found in the asthenospheric mantle. Volatile-rich material upwelling into the upper asthenosphere can react with the surrounding asthenospheric mantle and cause oxidation of the silicate assemblage while also decreasing the solidus temperature and enriching the mantle in volatiles such as carbon and sulfur. We propose that the oxidised, carbon- and sulfur-rich basanites found on El Hierro form by the low-degree melting of this mantle source. This model of melt generation is applicable to other ocean island locations where magmatic activity and magma chemistry is similar to that of El Hierro, and suggests a dual nature of OIB formation on Earth; either driven by deep thermal plumes, or by shallower melting processes in a heterogeneous, volatile-rich mantle.

Chapter 8

Final concluding remarks

In my thesis I combine melt inclusion volatile and trace element contents with isotope microanalysis data and thermometric and oxybarometric calculations to decipher melting conditions and magma evolutionary processes at the island of El Hierro. Results of melt inclusion major, trace, and volatile element analyses indicate that El Hierro, throughout the last 20 ka, has been exclusively fed by mafic alkali magmas that have a similar major element composition. Relatively homogeneous major element contents are accompanied by highly variable lithophile trace element ratios between different samples, which indicates that magmas are formed by the melting of a heterogeneous mantle source or by variable melting degrees. Trace element ratios observed in El Hierro melt inclusions can be reproduced by 2% to 8% melting of a primitive mantle source. In terms of melting degrees El Hierro is more akin to intracontinental basalts (e.g. Jung et al., 2006; McGee et al., 2013) than ocean island basalts such as Hawaii, where melting degree often reach > 10% (e.g. Feigenson et al., 2003). Volatile element concentrations measured within El Hierro melt inclusions are extremely high: most notably carbon, sulfur and fluorine. Low melt inclusion CO_2/Ba ratios indicate that at the time of entrapment the melt was already partially degassed. Further loss of CO_2 into a fluid phase occurred within melt inclusions post-entrapment: up to 85% of the CO_2

may be hosted in the fluid phase within melt inclusions. Elevated F/Nd ratios combined with mantle-like Cl/K ratios indicate that the El Hierro mantle source is enriched in F compared to Cl, which is in accordance with the presence of some recycled oceanic lithosphere in the mantle source of the magmas. While S/Dy ratios in melt inclusions are high, no clear indication can be found of sulfur enrichment in the mantle source of El Hierro based on volatile and trace element systematics alone; sulfur enrichment may be ascribed to a sulfur-rich mantle, or to low melting degrees. Carbon enrichment of the mantle cannot be clearly identified either due to extensive, deep CO_2 degassing at pressures exceeding 1 GPa.

Sulfur isotope ratios measured in melt inclusion and matrix glass from the same samples, using a novel analytical approach by multi-collector SIMS developed as part of this thesis, reveal that El Hierro primary melts have heavier δ^{34}S than normal upper mantle values. These results are similar to those derived from melt inclusions from the 2011-2012 eruption of El Hierro (Beaudry et al., 2018). Using degassing and melting modelling, the sulfur content of El Hierro primary melt and mantle source are estimated at 5000 ppm and ~700 ppm, respectively. This mantle source S content is well above primitive mantle estimates (McDonough and Sun, 1995; Palme and O'Neill, 2003). Mantle sulfur contents together with the enrichment in ^{34}S in the melt inclusions indicate that the El Hierro mantle contains sulfur originating from recycled oceanic lithosphere. The enrichment of sulfur in El Hierro melts is best explained by melting of a mantle source previously metasomatised by volatile-rich melts of a recycled oceanic crust-lithosphere mixture. Sulfur isotope analysis of melt inclusions provides a powerful tool for tracing long-term volatile cycling, and can be used to uncover processes that bulk sulfur and trace element analysis alone cannot accomplish.

Temperature, pressure, and oxygen fugacity estimates from El Hierro indicate long, deep magma storage in the uppermost mantle prior to eruption. Up to 400 years long storage episodes enabled the chemical re-equilibration of crystals and melt inclusions with the surrounding melt. Therefore, temperatures and oxygen fugacities recorded by melt inclusions and olivine crystals do not preserve the early stages of magmatic evolution. Only Cr-rich spinel inclusions record early temperature and oxygen fugacity conditions, and even spinel Mg-Fe^{2+} contents are partially reset through diffusion. Olivine-spinel pairs record high oxygen fugacities, comparable to those measured in island arc settings (Evans et al., 2012; Kelley and Cottrell, 2012). Potential temperature estimates are unreliable for most Canary Island magmas; the few samples that produce reliable estimates do not clearly support a thermal plume origin for the Canary Islands, as average potential temperature estimates overlap with those estimated for Atlantic mid-ocean ridge basalts.

The results presented in chapter four, six and seven provide strong evidence that El Hierro and more broadly speaking the Canary Islands is fed by some of the most volatile-rich ocean island magmas on Earth. They have significantly higher CO_2, sulfur and fluorine when compared with Hawaiian magmas (Sides et al., 2014). The volatile enrichment can be ascribed to the presence of previously subducted and recycled oceanic lithosphere in the mantle source, which has also been identified by radiogenic and stable isotope ratios measured in whole rock samples at the Western Canary Islands (Marcantonio et al., 1995; Day et al., 2010). This recycled material must retain some of its original volatile budget particularly F and S; it may contain recycled carbon as well. Heavy sulfur enrichment in melt inclusions, combined with high primary magma oxygen fugacity estimates, point to an oxidised mantle source that formed by the addition of sulfate-containing melts into the ambient mantle. This sulfate was reduced to sulfide as it mixed into the ambient upper mantle, and subsequently oxidised the silicate assemblage. Therefore, some sulfate may be retained in the oceanic lithosphere during subduction and transferred back into the deeper part of the mantle; this is contrary to previous assumptions of complete sulfate dissolution and transfer into the mantle wedge during subduction (Tomkins and Evans, 2015; Walters et al., 2020).

Recycled volatiles in the mantle source provide a good explanation for the composition of magmas erupting on the Canary Islands. They also explain the lack of features that are associated with ocean islands that form above thermally driven mantle plumes, such as an age progression parallel with plate movement, or positive bathymetric and geoid anomalies. At the same time, a volatile-metasomatised mantle also explains features that have previously been used to argue for elevated mantle temperatures at the Canary Islands, such as low seismic wave velocities in the mantle beneath El Hierro (Fullea et al., 2015; French and Romanowicz, 2015). Volatile-fluxed melting of recycled oceanic crustal material and subsequent metasomatism of the surrounding asthenosphere would result in the addition of volatiles into the El Hierro mantle source. This volatile addition decreases the solidus of the mantle (Dasgupta and Hirschmann, 2010; Green et al., 2010), resulting in low degree partial melting and the formation of volatile-rich, silica-undersaturated melts. The observations presented in the thesis suggest that a thermal anomaly is not essential to explain melt generation at the Western Canary Islands. Instead, the Canary Islands, and El Hierro in particular, are a good example of an ocean island where volatiles play a more important role in melt generation than a temperature anomaly.

Results presented here are relevant beyond volcanism the Canary Islands. They point to the dual nature of ocean island volcanism: at some locations, such as the Canary Islands, Cape Verde, and the Azores, magmatism can be driven primarily by volatiles that have been transferred into the mantle via subduction. At other locations, such as Hawaii and Réunion, this is less likely, as melt production at these locations is higher than what could be explained by low-degree, volatile-induced melting. Nonetheless, heterogeneity, and volatile heterogeneity in particular, may still influence the chemical composition of magmas at all ocean islands and beyond. For example recycled volatiles originating from subducted slabs may effect volcanism at mid-ocean ridges, causing compositional variation (e.g. Liu and Liang, 2017). The transfer of subducted lithoshepric material containing oxidised volatiles, such as sulfates, could be a pathway for oxidised material to enter the asthenosphere and the deeper mantle.

Currently, El Hierro and the Western Canary Islands is among the most studied ocean islands in terms of volatile geochemistry (Longpré et al., 2017; Beaudry et al., 2018; Taracsák et al., 2019; Walowski et al., 2019) along with Hawaii (e.g. Sides et al., 2014; Tucker et al., 2019; Wieser et al., 2020). Volatile element data is relatively scarce from other ocean island locations, including those with low melt flux and prominent HIMU isotopic character. Acquisition of volatile element data from melt inclusions at these locations is hindered by their inaccessibility and sample quality: many of these islands have not erupted in the past few million years, hence collection of fresh tephra samples in not straightforward. Improvements in homogenisation techniques using controlled environments, such gas-flow heating stages or piston cylinder re-homogenisation experiments (Mironov et al., 2015) could provide the way forward in the analysis of volatile contents in older ocean island basalts. Further work is required at many other locations to confirm if other low-melt flux ocean islands exhibit similar features as El Hierro in terms of volatile content and volatile stable isotope ratios. A potential target area is the Cape Verde Islands, share many features with the Canary Islands: poor age progression with plate movement, carbonatites present on the surface, exclusively alkali volcanism, and low melt flux. Ocean island characterised by high melt flux and eruption rate, such as Réunion, should also be targeted to confirm or disprove ideas presented here on the different causes of melt generation at various ocean islands.

Bibliography

Abratis, M., Schmincke, H. U., and Hansteen, T. (2002). Composition and evolution of submarine volcanic rocks from the central and western Canary Islands. *International Journal of Earth Sciences*, 91(4):562–582.

Alt, J. C., Garrido, C. J., Shanks, W. C. I., Turchyn, A., Padrón-Navarta, J. A., Sánchez-Vizcaíno, V. L., Pugnaire, M. T. G., and Marchesi, C. (2012). Recycling of water, carbon, and sulfur during subduction of serpentinites: A stable isotope study of cerro del almirez, spain. *Earth and Planetary Science Letters*, 327:50–60.

Alt, J. C. and Shanks, W. C. (2011). Microbial sulfate reduction and the sulfur budget for a complete section of altered oceanic basalts, IODP Hole 1256D (eastern Pacific). *Earth and Planetary Science Letters*, 310(1-2):73–83.

Alt, J. C. and Shanks, W. C. I. (2003). Serpentinization of abyssal peridotites from the MARK area, Mid-Atlantic Ridge: sulfur geochemistry and reaction modeling. *Geochimica et cosmochimica Acta*, 67(4):641–653.

Ancochea, E., Hernán, F., Huertas, M., Brändle, J., and Herrera, R. (2006). A new chronostratigraphical and evolutionary model for La Gomera: implications for the overall evolution of the Canarian Archipelago. *Journal of Volcanology and Geothermal Research*, 157(4):271–293.

Anderson, D. L. (2000). The thermal state of the upper mantle; No role for mantle plumes. *Geophysical Research Letters*, 27(22):3623–3626.

Anderson, K. R. and Poland, M. P. (2017). Abundant carbon in the mantle beneath Hawai‘i. *Nature Geoscience*, 10:704.

Anguita, F. and Hernán, F. (2000). The Canary Islands origin: a unifying model. *Journal of Volcanology and Geothermal Research*, 103(1–4):1–26.

Anguita, F. and Hernán, F. (1975). A propagating fracture model versus a hot spot origin for the Canary Islands. *Earth and Planetary Science Letters*, 27(1):11–19.

Aparicio, A., Tassinari, C. C., García, R., and Araña, V. (2010). Sr and Nd isotope composition of the metamorphic, sedimentary and ultramafic xenoliths of Lanzarote (Canary Islands): Implications for magma sources. *Journal of Volcanology and Geothermal Research*, 189(1-2):143–150.

Araña, V. and Ortiz, R. (1991). The Canary Islands: Tectonics, magmatism and geodynamic framework. In Kampunzu, A. B. and Lubala, R. T., editors, *Magmatism in Extensional Structural Settings: The Phanerozoic African Plate*, pages 209–249. Springer Berlin Heidelberg, Berlin, Heidelberg.

Ariskin, A. A. and Barmina, G. S. (1999). An empirical model for the calculation of spinel-melt equilibria in mafic igneous systems at atmospheric pressure: 2. Fe-Ti oxides. *Contributions to Mineralogy and Petrology*, 134(2):251–263.

Aulinas, M., Gimeno, D., Fernandez-Turiel, J. L., Font, L., Perez-Torrado, F. J., Rodriguez-Gonzalez, A., and Nowell, G. M. (2010). Small-scale mantle heterogeneity on the source of the Gran Canaria (Canary Islands) Pliocene–Quaternary magmas. *Lithos*, 119(3–4):377–392.

Bali, E., Hartley, M., Halldórsson, S., Gudfinnsson, G., and Jakobsson, S. (2018). Melt inclusion constraints on volatile systematics and degassing history of the 2014–2015 Holuhraun eruption, Iceland. *Contributions to Mineralogy and Petrology*, 173(9).

Ballhaus, C. (1993). Redox states of lithospheric and asthenospheric upper mantle. *Contributions to Mineralogy and Petrology*, 114(3):331–348.

Ballhaus, C., Berry, R. F., and Green, D. H. (1991). High pressure experimental calibration of the olivine-orthopyroxene-spinel oxygen geobarometer: implications for the oxidation state of the upper mantle. *Contributions to Mineralogy and Petrology*, 107(1):27–40.

Balogh, K., Ahijado, A., Casillas, R., and Fernández, C. (1999). Contributions to the chronology of the Basal Complex of Fuerteventura, Canary Islands. *Journal of Volcanology and Geothermal Research*, 90(1–2):81–101.

Barth, M. G., Rudnick, R. L., Horn, I., McDonough, W. F., Spicuzza, M. J., Valley, J. W., and Haggerty, S. E. (2001). Geochemistry of xenolithic eclogites from West Africa, Part I: a link between low MgO eclogites and Archean crust formation. *Geochimica et Cosmochimica Acta*, 65(9):1499–1527.

Beattie, P. (1993). Olivine-melt and orthopyroxene-melt equilibria. *Contributions to Mineralogy and Petrology*, 115(1):103–111.

Beaudry, P., Longpré, M.-A., Economos, R., Wing, B. A., Bui, T. H., and Stix, J. (2018). Degassing-induced fractionation of multiple sulphur isotopes unveils post-Archaean recycled oceanic crust signal in hotspot lava. *Nature communications*, 9(1):1–12.

Belay, I. G., Tanaka, R., Kitagawa, H., Kobayashi, K., and Nakamura, E. (2019). Origin of ocean island basalts in the West African passive margin without mantle plume involvement. *Nature Communications*, 10(1):3022.

Berry, A. J., Stewart, G. A., O'Neill, H. S. C., Mallmann, G., and Mosselmans, J. F. W. (2018). A re-assessment of the oxidation state of iron in MORB glasses. *Earth and Planetary Science Letters*, 483:114–123.

Black, B. A., Hauri, E. H., Elkins-Tanton, L. T., and Brown, S. M. (2014). Sulfur isotopic evidence for sources of volatiles in Siberian Traps magmas. *Earth and Planetary Science Letters*, 394:58–69.

Boudoire, G., Rizzo, A. L., Di Muro, A., Grassa, F., and Liuzzo, M. (2018). Extensive CO_2 degassing in the upper mantle beneath oceanic basaltic volcanoes: First insights from Piton de la Fournaise volcano (La Réunion Island). *Geochimica et Cosmochimica Acta*, 235:376–401.

Brounce, M., Stolper, E., and Eiler, J. (2017). Redox variations in Mauna Kea lavas, the oxygen fugacity of the Hawaiian plume, and the role of volcanic gases in Earth's oxygenation. *Proceedings of the National Academy of Sciences*, 114(34):8997.

Bucholz, C. E., Gaetani, G. A., Behn, M. D., and Shimizu, N. (2013). Post-entrapment modification of volatiles and oxygen fugacity in olivine-hosted melt inclusions. *Earth and Planetary Science Letters*, 374:145–155.

Burgisser, A., Alletti, M., and Scaillet, B. (2015). Simulating the behavior of volatiles belonging to the C–O–H–S system in silicate melts under magmatic conditions with the software D-Compress. *Computers & Geosciences*, 79:1–14.

Burton, M. R., Sawyer, G. M., and Granieri, D. (2013). Deep carbon emissions from volcanoes. *Reviews in Mineralogy and Geochemistry*, 75(1):323–354.

Cabral, R. A., Jackson, M. G., Koga, K. T., Rose-Koga, E. F., Hauri, E. H., Whitehouse, M. J., Price, A. A., Day, J. M., Shimizu, N., and Kelley, K. A. (2014). Volatile cycling of H_2O, CO_2, F, and Cl in the HIMU mantle: A new window provided by melt inclusions from oceanic hot spot lavas at Mangaia, Cook Islands. *Geochemistry, Geophysics, Geosystems*, 15(11):4445–4467.

Canales, J. and Dañobeitia, J. J. (1998). The Canary Islands swell: a coherence analysis of bathymetry and gravity. *Geophysical Journal International*, 132(3):479–488.

Carracedo, J., Day, S., Guillou, H., Rodríguez Badiola, E., Canas, J., and Pérez Torrado, F. (1998). Hotspot volcanism close to a passive continental margin: the Canary Islands. *Geological Magazine*, 135(5):591–604.

Carracedo, J., Guillou, H., Nomade, S., Rodríguez-Badiola, E., Pérez-Torrado, F., Rodríguez-González, A., Paris, R., Troll, V., Wiesmaier, S., Delcamp, A., and Fernández-Turiel, J. (2011). Evolution of ocean-island rifts: The northeast rift zone of Tenerife, Canary Islands. *GSA Bulletin*, 123(3-4):562–584.

Carracedo, J. C., Badiola, E. R., Guillou, H., de la Nuez, J., and Torrado, F. P. (2001). Geology and volcanology of La Palma and El Hierro, Western Canaries. *Estudios Geológicos*, 57(5-6):175–273.

Carracedo, J. C., Troll, V. R., Zaczek, K., Rodríguez-González, A., Soler, V., and Deegan, F. M. (2015). The 2011–2012 submarine eruption off El Hierro, Canary Islands: New lessons in oceanic island growth and volcanic crisis management. *Earth-Science Reviews*, 150:168–200.

Carroll, M. R. and Rutherford, M. J. (1988). Sulfur speciation in hydrous experimental glasses of varying oxidation state; results from measured wavelength shifts of sulfur X-rays. *American Mineralogist*, 73(7-8):845–849.

Cartigny, P., Pineau, F., Aubaud, C., and Javoy, M. (2008). Towards a consistent mantle carbon flux estimate: Insights from volatile systematics (H_2O/Ce, δD, CO_2/Nb) in the North Atlantic mantle (14 N and 34 N). *Earth and Planetary Science Letters*, 265(3-4):672–685.

Chakraborty, S. (2010). Diffusion Coefficients in Olivine, Wadsleyite and Ringwoodite. *Reviews in Mineralogy and Geochemistry*, 72(1):603–639.

Coello, J., Cantagrel, J.-M., Hernán, F., Fúster, J.-M., Ibarrola, E., Ancochea, E., Casquet, C., Jamond, C., Díaz de Téran, J.-R., and Cendrero, A. (1992). Evolution of the eastern volcanic ridge of the Canary Islands based on new K-Ar data. *Journal of Volcanology and Geothermal Research*, 53(1):251–274.

Coogan, L. A., Saunders, A. D., and Wilson, R. N. (2014). Aluminum-in-olivine thermometry of primitive basalts: Evidence of an anomalously hot mantle source for large igneous provinces. *Chemical Geology*, 368:1–10.

Costa, F., Dohmen, R., and Chakraborty, S. (2008). Time Scales of Magmatic Processes from Modeling the Zoning Patterns of Crystals. *Reviews in Mineralogy and Geochemistry*, 69(1):545–594.

Cottrell, E. and Kelley, K. A. (2011). The oxidation state of Fe in MORB glasses and the oxygen fugacity of the upper mantle. *Earth and Planetary Science Letters*, 305(3):270–282.

Cottrell, E., Lanzirotti, A., Mysen, B., Birner, S., Kelley, K. A., Botcharnikov, R., Davis, F. A., and Newville, M. (2018). A Mössbauer-based XANES calibration for hydrous basalt glasses reveals radiation-induced oxidation of Fe. *American Mineralogist*, 103(4):489–501.

Danyushevsky, L. V. (2001). The effect of small amounts of H_2O on crystallisation of mid-ocean ridge and backarc basin magmas. *Journal of Volcanology and Geothermal Research*, 110(3-4):265–280.

Danyushevsky, L. V., Della-Pasqua, F. N., and Sokolov, S. (2000). Re-equilibration of melt inclusions trapped by magnesian olivine phenocrysts from subduction-related magmas: petrological implications. *Contributions to Mineralogy and Petrology*, 138(1):68–83.

Danyushevsky, L. V., McNeill, A. W., and Sobolev, A. V. (2002). Experimental and petrological studies of melt inclusions in phenocrysts from mantle-derived magmas: an overview of techniques, advantages and complications. *Chemical Geology*, 183(1–4):5–24.

Danyushevsky, L. V. and Plechov, P. (2011). Petrolog3: Integrated software for modeling crystallization processes. *Geochemistry Geophysics Geosystems*, 12(7):1–32.

Dasgupta, R. and Hirschmann, M. M. (2006). Melting in the Earth's deep upper mantle caused by carbon dioxide. *Nature*, 440(7084):659–662.

Dasgupta, R. and Hirschmann, M. M. (2010). The deep carbon cycle and melting in Earth's interior. *Earth and Planetary Science Letters*, 298(1):1–13.

Dasgupta, R., Hirschmann, M. M., and Smith, N. D. (2007). Partial melting experiments of peridotite + CO_2 at 3 GPa and genesis of alkalic ocean island basalts. *Journal of Petrology*, 48(11):2093–2124.

Day, J. M. D. and Hilton, D. R. (2011). Origin of ^{3}He/^{4}He ratios in HIMU-type basalts constrained from Canary Island lavas. *Earth and Planetary Science Letters*, 305(1–2):226–234.

Day, J. M. D., Pearson, D. G., Macpherson, C. G., Lowry, D., and Carracedo, J.-C. (2009). Pyroxenite-rich mantle formed by recycled oceanic lithosphere: Oxygen-osmium isotope evidence from Canary Island lavas. *Geology*, 37(6):555–558.

Day, J. M. D., Pearson, D. G., Macpherson, C. G., Lowry, D., and Carracedo, J. C. (2010). Evidence for distinct proportions of subducted oceanic crust and lithosphere in HIMU-type mantle beneath El Hierro and La Palma, Canary Islands. *Geochimica et Cosmochimica Acta*, 74(22):6565–6589.

Day, S., Carracedo, J., Guillou, H., and Gravestock, P. (1999). Recent structural evolution of the Cumbre Vieja volcano, La Palma, Canary Islands: volcanic rift zone reconfiguration as a precursor to volcano flank instability? *Journal of Volcanology and Geothermal Research*, 94(1-4):135–167.

De Hoog, J. C., Gall, L., and Cornell, D. H. (2010). Trace-element geochemistry of mantle olivine and application to mantle petrogenesis and geothermobarometry. *Chemical Geology*, 270(1):196 – 215.

Deegan, F. M., Troll, V. R., Barker, A. K., Harris, C., Chadwick, J. P., Carracedo, J. C., and Delcamp, A. (2012). Crustal versus source processes recorded in dykes from the Northeast volcanic rift zone of Tenerife, Canary Islands. *Chemical Geology*, 334:324–344.

Deloule, E., Albarede, F., and Sheppard, S. M. (1991). Hydrogen isotope heterogeneities in the mantle from ion probe analysis of amphiboles from ultramafic rocks. *Earth and Planetary Science Letters*, 105(4):543–553.

Dieterich, J. H. (1988). Growth and persistence of Hawaiian volcanic rift zones. *Journal of Geophysical Research: Solid Earth*, 93(B5):4258–4270.

Ding, S. and Dasgupta, R. (2017). The fate of sulfide during decompression melting of peridotite–implications for sulfur inventory of the morb-source depleted upper mantle. *Earth and Planetary Science Letters*, 459:183–195.

Ding, S. and Dasgupta, R. (2018). Sulfur inventory of ocean island basalt source regions constrained by modeling the fate of sulfide during decompression melting of a heterogeneous mantle. *Journal of Petrology*, 59(7):1281–1308.

Ding, T., Valkiers, S., Kipphardt, H., De Bievre, P., Taylor, P., Gonfiantini, R., and Krouse, R. (2001). Calibrated sulfur isotope abundance ratios of three IAEA sulfur isotope reference materials and V-CDT with a reassessment of the atomic weight of sulfur. *Geochimica et Cosmochimica Acta*, 65(15):2433–2437.

Dixon, J. E. (1997). Degassing of alkalic basalts. *American Mineralogist*, 82(3-4):368–378.

Dixon, J. E., Clague, D. A., Wallace, P., and Poreda, R. (1997). Volatiles in alkalic basalts form the North Arch Volcanic Field, Hawaii: extensive degassing of deep submarine-erupted alkalic series lavas. *Journal of Petrology*, 38(7):911–939.

Dohmen, R. and Chakraborty, S. (2007). Fe-Mg diffusion in olivine II: point defect chemistry, change of diffusion mechanisms and a model for calculation of diffusion coefficients in natural olivine. *Physics and Chemistry of Minerals*, 34(6):409–430.

Dorfman, S. M., Badro, J., Nabiei, F., Prakapenka, V. B., Cantoni, M., and Gillet, P. (2018). Carbonate stability in the reduced lower mantle. *Earth and Planetary Science Letters*, 489:84–91.

Droop, G. T. R. (1987). A general equation for estimating Fe^{3+} concentrations in ferromagnesian silicates and oxides from microprobe analyses, using stoichiometric criteria. *Mineralogical Magazine*, 51(361):431–435.

Duncan, R. A. (1981). Hotspots in the Southern Oceans — an absolute frame of reference for motion of the Gondwana continents. *Tectonophysics*, 74(1):29–42.

Edgar, C. J., Wolff, J. A., Nichols, H. J., Cas, R. A. F., and Martı, J. (2002). A complex Quaternary ignimbrite-forming phonolitic eruption: the Poris Member of the Diego Hernández Formation (Tenerife, Canary Islands). *Journal of Volcanology and Geothermal Research*, 118(1–2):99–130.

Edmonds, M., Sides, I. R., Swanson, D. A., Werner, C., Martin, R. S., Mather, T. A., Herd, R. A., Jones, R. L., Mead, M. I., Sawyer, G., Roberts, T. J., Sutton, A. J., and Elias, T. (2013). Magma storage, transport and degassing during the 2008-10 summit eruption at Kilauea Volcano, Hawaii. *Geochimica et Cosmochimica Acta*, 123:284–301.

Eiler, J. M., Graham, C., and Valley, J. W. (1997). SIMS analysis of oxygen isotopes: matrix effects in complex minerals and glasses. *Chemical Geology*, 138(3-4):221–244.

Evans, K. (2012). The redox budget of subduction zones. *Earth-Science Reviews*, 113(1):11 – 32.

Evans, K., Elburg, M., and Kamenetsky, V. (2012). Oxidation state of subarc mantle. *Geology*, 40(9):783–786.

Falloon, T. J., Green, D. H., and Danyushevsky, L. V. (2007). *Crystallization temperatures of tholeiite parental liquids: Implications for the existence of thermally driven mantle plumes*, volume 430, page 0. Geological Society of America.

Farquhar, J., Wing, B., McKeegan, K., Harris, J., Cartigny, P., and Thiemens, M. (2002). Mass-independent sulfur of inclusions in diamond and sulfur recycling on early Earth. *Science*, 298(5602):2369–2372.

Feigenson, M. D., Bolge Louise, L., Carr Michael, J., and Herzberg Claude, T. (2003). REE inverse modeling of HSDP2 basalts: Evidence for multiple sources in the Hawaiian plume. *Geochemistry, Geophysics, Geosystems*, 4(2).

Fialin, M., Wagner, C., Métrich, N., Humler, E., Galoisy, L., and Bézos, A. (2001). $Fe^{3+}/\Sigma Fe$ vs. Fe L α peak energy for minerals and glasses: Recent advances with the electron microprobe. *American Mineralogist*, 86(4):456–465.

Fiege, A., Holtz, F., Shimizu, N., Mandeville, C. W., Behrens, H., and Knipping, J. L. (2014). Sulfur isotope fractionation between fluid and andesitic melt: an experimental study. *Geochimica et Cosmochimica Acta*, 142:501–521.

Fitton, J. (2007). The OIB paradox. *Geological Society of America Special Paper*, 430:387–412.

Fortin, M.-A., Riddle, J., Desjardins-Langlais, Y., and Baker, D. R. (2015). The effect of water on the sulfur concentration at sulfide saturation (SCSS) in natural melts. *Geochimica et Cosmochimica Acta*, 160:100–116.

Fortin, M.-A., Watson, E. B., Stern, R. A., and Ono, S. (2019). Experimental characterization of diffusive and Soret isotopic fractionation of sulfur in a reduced, anhydrous basaltic melt. *Chemical Geology*, 510:10–17.

French, S. W. and Romanowicz, B. (2015). Broad plumes rooted at the base of the Earth's mantle beneath major hotspots. *Nature*, 525(7567):95–99.

Frey, F., Garcia, M., Wise, W., Kennedy, A., Gurriet, P., and Albarede, F. (1991). The evolution of mauna kea volcano, hawaii: petrogenesis of tholeiitic and alkalic basalts. *Journal of Geophysical Research: Solid Earth*, 96(B9):14347–14375.

Frezzotti, M.-L. (2001). Silicate-melt inclusions in magmatic rocks: applications to petrology. *Lithos*, 55(1-4):273–299.

Fukao, Y., Obayashi, M., Inoue, H., and Nenbai, M. (1992). Subducting slabs stagnant in the mantle transition zone. *Journal of Geophysical Research: Solid Earth*, 97(B4):4809–4822.

Fukuda, K., Beard, B. L., Dunlap, D. R., Spicuzza, M. J., Fournelle, J. H., Wadhwa, M., and Kita, N. T. (2020). Magnesium isotope analysis of olivine and pyroxene by SIMS: Evaluation of matrix effects. *Chemical Geology*, page 119482.

Fullea, J., Camacho, A. G., Negredo, A. M., and Fernández, J. (2015). The Canary Islands hot spot: New insights from 3D coupled geophysical–petrological modelling of the lithosphere and uppermost mantle. *Earth and Planetary Science Letters*, 409:71–88.

Gaetani, G. A. and Grove, T. L. (2013). *Experimental Constraints on Melt Generation in the Mantle Wedge*, pages 107–134. American Geophysical Union (AGU).

Gaetani, G. A., Grove, T. L., and Bryan, W. B. (1993). The influence of water on the petrogenesis of subduction-related igneous rocks. *Nature*, 365(6444):332.

Gaetani, G. A., O'Leary, J. A., Shimizu, N., Bucholz, C. E., and Newville, M. (2012). Rapid reequilibration of H_2O and oxygen fugacity in olivine-hosted melt inclusions. *Geology*, 40(10):915–918.

Gee, L. L. and Sack, R. O. (1988). Experimental Petrology of Melilite Nephelinites. *Journal of Petrology*, 29(6):1233–1255.

Gee, M. J. R., Watts, A. B., Masson, D. G., and Mitchell, N. C. (2001). Landslides and the evolution of El Hierro in the Canary Islands. *Marine Geology*, 177(3):271–293.

Geldmacher, J., Hoernle, K., Bogaard, P. v. d., Duggen, S., and Werner, R. (2005). New ^{40}Ar/^{39}Ar age and geochemical data from seamounts in the Canary and Madeira volcanic provinces: Support for the mantle plume hypothesis. *Earth and Planetary Science Letters*, 237(1–2):85–101.

Ghiorso, M. S. and Gualda, G. A. R. (2015). An H_2O–CO_2 mixed fluid saturation model compatible with rhyolite-MELTS. *Contributions to Mineralogy and Petrology*, 169(6):53.

Green, D., Schmidt, M., and Hibberson, W. (2004). Island-arc ankaramites: primitive melts from fluxed refractory lherzolitic mantle. *Journal of Petrology*, 45(2):391–403.

Green, D. H., Hibberson, W. O., Kovacs, I., and Rosenthal, A. (2010). Water and its influence on the lithosphere-asthenosphere boundary. *Nature*, 467(7314):448–451.

Green, D. H., Hibberson, W. O., Rosenthal, A., Kovács, I., Yaxley, G. M., Falloon, T. J., and Brink, F. (2014). Experimental study of the influence of water on melting and phase assemblages in the upper mantle. *Journal of Petrology*, 55(10):2067–2096.

Grove, T. L., Chatterjee, N., Parman, S. W., and Médard, E. (2006). The influence of H_2O on mantle wedge melting. *Earth and Planetary Science Letters*, 249(1):74–89.

Gualda, G. A. R., Ghiorso, M. S., Lemons, R. V., and Carley, T. L. (2012). Rhyolite-MELTS: a Modified Calibration of MELTS Optimized for Silica-rich, Fluid-bearing Magmatic Systems. *Journal of Petrology*, 53(5):875–890.

Guillou, H., Carracedo, J. C., and Duncan, R. A. (2001). K–Ar, 40Ar–39Ar ages and magnetostratigraphy of Brunhes and Matuyama lava sequences from La Palma Island. *Journal of Volcanology and Geothermal Research*, 106(3–4):175–194.

Guillou, H., Carracedo, J. C., Paris, R., and Torrado, F. J. P. (2004). Implications for the early shield-stage evolution of Tenerife from K/Ar ages and magnetic stratigraphy. *Earth and Planetary Science Letters*, 222(2):599–614.

Guillou, H., Carracedo, J. C., Torrado, F. P., and Badiola, E. R. (1996). K-Ar ages and magnetic stratigraphy of a hotspot-induced, fast grown oceanic island: El Hierro, Canary Islands. *Journal of Volcanology and Geothermal Research*, 73(1):141–155.

Gurenko, A., Hoernle, K., Hauff, F., Schmincke, H.-U., Han, D., Miura, Y., and Kaneoka, I. (2006). Major, trace element and Nd–Sr–Pb–O–He–Ar isotope signatures of shield stage lavas from the central and western Canary Islands: Insights into mantle and crustal processes. *Chemical Geology*, 233(1–2):75–112.

Hansteen, T. H., Klügel, A., and Schmincke, H.-U. (1998). Multi-stage magma ascent beneath the Canary Islands: evidence from fluid inclusions. *Contributions to Mineralogy and Petrology*, 132(1):48–64.

Hart, S., Hauri, E., Oschmann, L., and Whitehead, J. (1992). Mantle plumes and entrainment: isotopic evidence. *Science*, 256(5056):517–520.

Hart, S. R. (1984). A large-scale isotope anomaly in the Southern Hemisphere mantle. *Nature*, 309(5971):753–757.

Hart, S. R. and Gaetani, G. A. (2006). Mantle Pb paradoxes: the sulfide solution. *Contributions to Mineralogy and Petrology*, 152(3):295–308.

Hartley, M., Thordarson, T., Taylor, C., Fitton, J., et al. (2012). Evaluation of the effects of composition on instrumental mass fractionation during SIMS oxygen isotope analyses of glasses. *Chemical Geology*, 334:312–323.

Hartley, M. E., Maclennan, J., Edmonds, M., and Thordarson, T. (2014). Reconstructing the deep CO_2 degassing behaviour of large basaltic fissure eruptions. *Earth and Planetary Science Letters*, 393:120–131.

Hartley, M. E., Neave, D. A., Maclennan, J., Edmonds, M., and Thordarson, T. (2015). Diffusive over-hydration of olivine-hosted melt inclusions. *Earth and Planetary Science Letters*, 425:168–178.

Hartley, M. E., Shorttle, O., Maclennan, J., Moussallam, Y., and Edmonds, M. (2017). Olivine-hosted melt inclusions as an archive of redox heterogeneity in magmatic systems. *Earth and Planetary Science Letters*, 479:192–205.

Hauri, E. H., Shaw, A. M., Wang, J., Dixon, J. E., King, P. L., and Mandeville, C. (2006). Matrix effects in hydrogen isotope analysis of silicate glasses by SIMS. *Chemical Geology*, 235(3-4):352–365.

Herzberg, C. (2011). Identification of Source Lithology in the Hawaiian and Canary Islands: Implications for Origins. *Journal of Petrology*, 52(1):113–146.

Herzberg, C. and Asimow, P. D. (2008). Petrology of some oceanic island basalts: PRIMELT2.XLS software for primary magma calculation. *Geochemistry, Geophysics, Geosystems*, 9(9).

Herzberg, C. and Asimow, P. D. (2015). PRIMELT3 MEGA.XLSM software for primary magma calculation: Peridotite primary magma MgO contents from the liquidus to the solidus. *Geochemistry, Geophysics, Geosystems*, 16(2):563–578.

Herzberg, C., Asimow, P. D., Arndt, N., Niu, Y., Lesher, C. M., Fitton, J. G., Cheadle, M. J., and Saunders, A. D. (2007). Temperatures in ambient mantle and plumes: Constraints from basalts, picrites, and komatiites. *Geochemistry, Geophysics, Geosystems*, 8(2).

Hinton, R. W. (1995). Ion microprobe analysis in geology. In *Microprobe techniques in the earth sciences*, Mineralogical Society Series Volume 6. Chapman & Hall, London.

Hirschmann, M. M. (2016). Constraints on the early delivery and fractionation of Earth's major volatiles from C/H, C/N, and C/S ratios. *American Mineralogist*, 101(3):540–553.

Hirschmann, M. M., Kogiso, T., Baker, M. B., and Stolper, E. M. (2003). Alkalic magmas generated by partial melting of garnet pyroxenite. *Geology*, 31(6):481–484.

Hirschmann, M. M., Tenner, T., Aubaud, C., and Withers, A. C. (2009). Dehydration melting of nominally anhydrous mantle: The primacy of partitioning. *Physics of the Earth and Planetary Interiors*, 176(1–2):54–68.

Hoernle, K., Zhang, Y.-S., and Graham, D. (1995). Seismic and geochemical evidence for large-scale mantle upwelling beneath the eastern Atlantic and western and central Europe. *Nature*, 374(6517):34–39.

Hoernle, K. A. J. and Schmincke, H.-U. (1993a). The Petrology of the Tholeiites through Melilite Nephelinites on Gran Canaria, Canary Islands: Crystal Fractionation, Accumulation, and Depths of Melting. *Journal of Petrology*, 34(3):573–597.

Hoernle, K. A. J. and Schmincke, H.-U. (1993b). The role of partial melting in the 15-Ma geochemical evolution of Gran Canaria: A blob model for the Canary hotspot. *Journal of Petrology*, 34(3):599–626.

Höfer, H. E. and Brey, G. P. (2007). The iron oxidation state of garnet by electron microprobe: Its determination with the flank method combined with major-element analysis. *American Mineralogist*, 92(5-6):873–885.

Hofmann, A. W. (1988). Chemical differentiation of the Earth: the relationship between mantle, continental crust, and oceanic crust. *Earth and Planetary Science Letters*, 90(3):297–314.

Hofmann, A. W. (1997). Mantle geochemistry: the message from oceanic volcanism. *Nature*, 385(6613):219–229.

Hofmann, A. W., Jochum, K., Seufert, M., and White, W. M. (1986). Nb and Pb in oceanic basalts: new constraints on mantle evolution. *Earth and Planetary science letters*, 79(1-2):33–45.

Hofmann, A. W. and White, W. M. (1982). Mantle plumes from ancient oceanic crust. *Earth and Planetary Science Letters*, 57(2):421–436.

Hudgins, T. R., Mukasa, S. B., Simon, A. C., Moore, G., and Barifaijo, E. (2015). Melt inclusion evidence for CO_2-rich melts beneath the western branch of the East African

Rift: implications for long-term storage of volatiles in the deep lithospheric mantle. *Contributions to Mineralogy and Petrology*, 169(5):46.

Hughes, E. C., Buse, B., Kearns, S. L., Blundy, J. D., Kilgour, G., Mader, H. M., Brooker, R. A., Balzer, R., Botcharnikov, R. E., Di Genova, D., Almeev, R. R., and Riker, J. M. (2018). High spatial resolution analysis of the iron oxidation state in silicate glasses using the electron probe. *American Mineralogist*, 103(9):1473–1486.

Jackson, M. G., Becker, T. W., and Konter, J. G. (2018). Evidence for a deep mantle source for em and himu domains from integrated geochemical and geophysical constraints. *Earth and Planetary Science Letters*, 484:154–167.

Jégo, S. and Dasgupta, R. (2014). The fate of sulfur during fluid-present melting of subducting basaltic crust at variable oxygen fugacity. *Journal of Petrology*, 55(6):1019–1050.

Jugo, P. J., Luth, R. W., and Richards, J. P. (2005). An experimental study of the sulfur content in basaltic melts saturated with immiscible sulfide or sulfate liquids at 1300°C and 1.0 GPa. *Journal of Petrology*, 46(4):783–798.

Jugo, P. J., Wilke, M., and Botcharnikov, R. E. (2010). Sulfur K-edge XANES analysis of natural and synthetic basaltic glasses: Implications for S speciation and S content as function of oxygen fugacity. *Geochimica et Cosmochimica Acta*, 74(20):5926–5938.

Jung, C., Jung, S., Hoffer, E., and Berndt, J. (2006). Petrogenesis of Tertiary mafic alkaline magmas in the Hocheifel, Germany. *Journal of Petrology*, 47(8):1637–1671.

Jung, W.-Y. and Rabinowitz, P. D. (1986). Residual geoid anomalies of the North Atlantic Ocean and their tectonic implications. *Journal of Geophysical Research: Solid Earth*, 91(B10):10383–10396.

Katz, R. F., Spiegelman, M., and Langmuir, C. H. (2003). A new parameterization of hydrous mantle melting. *Geochemistry, Geophysics, Geosystems*, 4(9):1073.

Kelemen, P. B. and Manning, C. E. (2015). Reevaluating carbon fluxes in subduction zones, what goes down, mostly comes up. *Proceedings of the National Academy of Sciences*, 112(30):E3997–E4006.

Kelley, K. A. and Cottrell, E. (2009). Water and the Oxidation State of Subduction Zone Magmas. *Science*, 325(5940):605.

Kelley, K. A. and Cottrell, E. (2012). The influence of magmatic differentiation on the oxidation state of Fe in a basaltic arc magma. *Earth and Planetary Science Letters*, 329-330:109–121.

Kendrick, M. A., Jackson, M. G., Kent, A. J. R., Hauri, E. H., Wallace, P. J., and Woodhead, J. (2014). Contrasting behaviours of CO_2, S, H_2O and halogens (F, Cl, Br, and I) in enriched-mantle melts from Pitcairn and Society seamounts. *Chemical Geology*, 370:69–81.

Kendrick, M. A., Woodhead, J. D., and Kamenetsky, V. S. (2012). Tracking halogens through the subduction cycle. *Geology*, 40(12):1075–1078.

Klemme, S. and O'Neill, H. S. (2000). The near-solidus transition from garnet lherzolite to spinel lherzolite. *Contributions to Mineralogy and Petrology*, 138(3):237–248.

Klerkx, J. and de Paepe, P. (1971). Cape Verde Islands: evidence for a Mesozoic oceanic ridge. *Nature Physical Science*, 233(41):117–118.

Klügel, A., Hansteen, T. H., van den Bogaard, P., Strauss, H., and Hauff, F. (2011). Holocene fluid venting at an extinct Cretaceous seamount, Canary archipelago. *Geology*, 39(9):855–858.

Klügel, A., Longpré, M.-A., García-Cañada, L., and Stix, J. (2015). Deep intrusions, lateral magma transport and related uplift at ocean island volcanoes. *Earth and Planetary Science Letters*, 431:140–149.

Kogiso, T., Hirose, K., and Takahashi, E. (1998). Melting experiments on homogeneous mixtures of peridotite and basalt: application to the genesis of ocean island basalts. *Earth and Planetary Science Letters*, 162(1):45 – 61.

Kogiso, T., Tatsumi, Y., Shimoda, G., and Barsczus, H. G. (1997). High μ (HIMU) ocean island basalts in southern Polynesia: New evidence for whole mantle scale recycling of subducted oceanic crust. *Journal of Geophysical Research: Solid Earth*, 102(B4):8085–8103.

Koleszar, A., Saal, A., Hauri, E., Nagle, A., Liang, Y., and Kurz, M. (2009). The volatile contents of the Galapagos plume; evidence for H_2O and F open system behavior in melt inclusions. *Earth and Planetary Science Letters*, 287(3):442–452.

Kress, V. C. and Carmichael, I. S. E. (1991). The compressibility of silicate liquids containing Fe_2O_3 and the effect of composition, temperature, oxygen fugacity and pressure on their redox states. *Contributions to Mineralogy and Petrology*, 108(1):82–92.

Kuritani, T., Xia, Q.-K., Kimura, J.-I., Liu, J., Shimizu, K., Ushikubo, T., Zhao, D., Nakagawa, M., and Yoshimura, S. (2019). Buoyant hydrous mantle plume from the mantle transition zone. *Scientific Reports*, 9(1):6549.

Labidi, J., Cartigny, P., and Moreira, M. (2013). Non-chondritic sulphur isotope composition of the terrestrial mantle. *Nature*, 501(7466):208–211.

Lange, R. A. (1997). A revised model for the density and thermal expansivity of K_2O - Na_2O - CaO - MgO - Al_2O_3 - SiO_2 liquids from 700 to 1900 K: extension to crustal magmatic temperatures. *Contributions to Mineralogy and Petrology*, 130(1):1–11.

Langmuir, C. H., Klein, E. M., and Plank, T. (1992). Petrological Systematics of Mid-Ocean Ridge Basalts: Constraints on Melt Generation Beneath Ocean Ridges. In *Mantle Flow and Melt Generation at Mid-Ocean Ridges*, pages 183–280. American Geophysical Union.

Le Bas, M. J., Le Maitre, R. W., Streckeisen, A., and Zanettin, B. (1986a). A Chemical Classification of Volcanic Rocks Based on the Total Alkali-Silica Diagram. *Journal of Petrology*, 27(3):745–750.

Le Bas, M. J., Rex, D. C., and Stillman, C. J. (1986b). The early magmatic chronology of Fuerteventura, Canary Islands. *Geological Magazine*, 123(03):287–298.

Le Voyer, M., Asimow, P. D., Mosenfelder, J. L., Guan, Y., Wallace, P. J., Schiano, P., Stopler, E., and Eiler, J. (2014). Zonation of H_2O and F concentrations around melt inclusions in olivines. *Journal of Petrology*, 55(4):685–707.

Lee, C.-T. A., Luffi, P., Plank, T., Dalton, H., and Leeman, W. P. (2009). Constraints on the depths and temperatures of basaltic magma generation on Earth and other terrestrial planets using new thermobarometers for mafic magmas. *Earth and Planetary Science Letters*, 279(1–2):20–33.

Lee, H., Muirhead, J. D., Fischer, T. P., Ebinger, C. J., Kattenhorn, S. A., Sharp, Z. D., and Kianji, G. (2016). Massive and prolonged deep carbon emissions associated with continental rifting. *Nature Geoscience*, 9(2):145–149.

Lehmann, J. (1983). Diffusion between olivine and spinel: application to geothermometry. *Earth and Planetary Science Letters*, 64(1):123 – 138.

Liotta, M., Rizzo, A., Paonita, A., Caracausi, A., and Martelli, M. (2012). Sulfur isotopic compositions of fumarolic and plume gases at mount etna (italy) and inferences on their magmatic source. *Geochemistry, Geophysics, Geosystems*, 13(5).

Liu, B. and Liang, Y. (2017). The prevalence of kilometer-scale heterogeneity in the source region of MORB upper mantle. *Science advances*, 3(11):e1701872.

Liu, Y., Samaha, N.-T., and Baker, D. R. (2007). Sulfur concentration at sulfide saturation (SCSS) in magmatic silicate melts. *Geochimica et Cosmochimica Acta*, 71(7):1783–1799.

Long, X., Ballmer, M. D., Córdoba, A. M.-C., and Li, C.-F. (2019). Mantle melting and intraplate volcanism due to self-buoyant hydrous upwellings from the stagnant slab that are conveyed by small-scale convection. *Geochemistry, Geophysics, Geosystems*, 20(11):4972–4997.

Longpré, M.-A. (2009). *Consequences of giant landslides on ocean island magmatism: volcanic and geochemical evolution of the Teno massif, Tenerife, and El Hierro Island (Canary Archipelago)*. Phd thesis, Trinity College, University of Dublin.

Longpré, M.-A., Chadwick, J. P., Wijbrans, J., and Iping, R. (2011). Age of the El Golfo debris avalanche, El Hierro (Canary Islands): New constraints from laser and furnace ^{40}Ar/^{39}Ar dating. *Journal of Volcanology and Geothermal Research*, 203(1):76–80.

Longpré, M.-A., Klügel, A., Diehl, A., and Stix, J. (2014). Mixing in mantle magma reservoirs prior to and during the 2011–2012 eruption at El Hierro, Canary Islands. *Geology*, 42(4):315–318.

Longpré, M.-A., Stix, J., Klügel, A., and Shimizu, N. (2017). Mantle to surface degassing of carbon- and sulphur-rich alkaline magma at El Hierro, Canary Islands. *Earth and Planetary Science Letters*, 460:268–280.

Lowenstern, J. B. (2003). Melt inclusions come of age: volatiles, volcanoes, and Sorby's legacy. In *Developments in Volcanology*, volume 5, pages 1–21. Elsevier.

López, C., Blanco, M. J., Abella, R., Brenes, B., Cabrera Rodríguez, V. M., Casas, B., Domínguez Cerdeña, I., Felpeto, A., de Villalta, M. F., del Fresno, C., García, O., García-Arias, M. J., García-Cañada, L., Gomis Moreno, A., González-Alonso, E., Guzmán Pérez, J., Iribarren, I., López-Díaz, R., Luengo-Oroz, N., Meletlidis, S., Moreno, M., Moure, D., de Pablo, J. P., Rodero, C., Romero, E., Sainz-Maza, S., Sentre Domingo, M. A., Torres, P. A., Trigo, P., and Villasante-Marcos, V. (2012). Monitoring the volcanic unrest of El Hierro (Canary Islands) before the onset of the 2011–2012 submarine eruption. *Geophysical Research Letters*, 39(L13303):1–7.

Lundstrom, C. C., Hoernle, K., and Gill, J. (2003). U-series disequilibria in volcanic rocks from the Canary Islands: Plume versus lithospheric melting. *Geochimica et Cosmochimica Acta*, 67(21):4153–4177.

Lyubetskaya, T. and Korenaga, J. (2007). Chemical composition of Earth's primitive mantle and its variance: 1. Method and results. *Journal of Geophysical Research: Solid Earth*, 112(B3).

Macdonald, K. C., Scheirer, D. S., and Carbotte, S. M. (1991). Mid-ocean ridges: Discontinuities, segments and giant cracks. *Science*, 253(5023):986–994.

Maclennan, J. (2017). Bubble formation and decrepitation control the CO_2 content of olivine-hosted melt inclusions. *Geochemistry Geophysics Geosystems*, 18:597–616.

Manzini, M., Bouvier, A.-S., Barnes, J. D., Bonifacie, M., Rose-Koga, E. F., Ulmer, P., Métrich, N., Bardoux, G., Williams, J., Layne, G. D., et al. (2017). SIMS chlorine isotope analyses in melt inclusions from arc settings. *Chemical Geology*, 449:112–122.

Marcantonio, F., Zindler, A., Elliott, T., and Staudigel, H. (1995). Os isotope systematics of La Palma, Canary Islands: Evidence for recycled crust in the mantle source of HIMU ocean islands. *Earth and Planetary Science Letters*, 133(3):397–410.

Marini, L., Moretti, R., and Accornero, M. (2011). Sulfur Isotopes in Magmatic-Hydrothermal Systems, Melts, and Magmas. *Reviews in Mineralogy and Geochemistry*, 73(1):423–492.

Martí, J., Castro, A., Rodríguez, C., Costa, F., Carrasquilla, S., Pedreira, R., and Bolos, X. (2013a). Correlation of magma evolution and geophysical monitoring during the 2011–2012 El Hierro (Canary Islands) submarine eruption. *Journal of Petrology*, 54(7):1349–1373.

Martí, J., Pinel, V., López, C., Geyer, A., Abella, R., Tárraga, M., Blanco, M. J., Castro, A., and Rodríguez, C. (2013b). Causes and mechanisms of the 2011–2012 El Hierro (Canary Islands) submarine eruption. *Journal of Geophysical Research: Solid Earth*, 118(3):823–839.

Marty, B. (2012). The origins and concentrations of water, carbon, nitrogen and noble gases on Earth. *Earth and Planetary Science Letters*, 313-314:56–66.

Masson, D., Watts, A., Gee, M., Urgeles, R., Mitchell, N., Le Bas, T., and Canals, M. (2002). Slope failures on the flanks of the western Canary Islands. *Earth-Science Reviews*, 57(1-2):1–35.

Masson, D. G. (1996). Catastrophic collapse of the volcanic island of Hierro 15 ka ago and the history of landslides in the Canary Islands. *Geology*, 24(3):231–234.

Matthews, S., Shorttle, O., and Maclennan, J. (2016). The temperature of the Icelandic mantle from olivine-spinel aluminum exchange thermometry. *Geochemistry, Geophysics, Geosystems*, 17(11):4725–4752.

Mazza, S. E., Gazel, E., Bizimis, M., Moucha, R., Béguelin, P., Johnson, E. A., McAleer, R. J., and Sobolev, A. V. (2019). Sampling the volatile-rich transition zone beneath Bermuda. *Nature*, 569(7756):398–403.

McDonough, W. F. and Sun, S. s. (1995). The composition of the Earth. *Chemical Geology*, 120(3):223–253.

McDougall, I. and Schmincke, H. U. (1976). Geochronology of Gran Canaria, Canary Islands: Age of shield building volcanism and other magmatic phases. *Bulletin Volcanologique*, 40(1):57–77.

McGee, L. E., Smith, I. E. M., Millet, M.-A., Handley, H. K., and Lindsay, J. M. (2013). Asthenospheric control of melting processes in a monogenetic basaltic system: a case study of the Auckland Volcanic Field, New Zealand. *Journal of Petrology*, 54(10):2125–2153.

McKenzie, D. and O'Nions, R. (1991). Partial melt distributions from inversion of rare earth element concentrations. *Journal of Petrology*, 32(5):1021–1091.

Melián, G., Hernández, P. A., Padrón, E., Pérez, N. M., Barrancos, J., Padilla, G., Dionis, S., Rodríguez, F., Calvo, D., and Nolasco, D. (2014). Spatial and temporal variations of diffuse CO_2 degassing at El Hierro volcanic system: Relation to the 2011–2012 submarine eruption. *Journal of Geophysical Research: Solid Earth*, 119(9):6976–6991.

Mercier, M., Di Muro, A., Métrich, N., Giordano, D., Belhadj, O., and Mandeville, C. W. (2010). Spectroscopic analysis (FTIR, Raman) of water in mafic and intermediate glasses and glass inclusions. *Geochimica et Cosmochimica Acta*, 74(19):5641–5656.

Mironov, N., Portnyagin, M., Botcharnikov, R., Gurenko, A., Hoernle, K., and Holtz, F. (2015). Quantification of the CO_2 budget and H_2O–CO_2 systematics in subduction-zone magmas through the experimental hydration of melt inclusions in olivine at high H_2O pressure. *Earth and Planetary Science Letters*, 425:1–11.

Miyoshi, T., Sakai, H., and Chiba, H. (1984). Experimental study of sulfur isotope fractionation factors between sulfate and sulfide in high temperature melts. *Geochemical Journal*, 18(2):75–84.

Müller, R. D. and Roest, W. R. (1992). Fracture zones in the North Atlantic from combined Geosat and Seasat data. *Journal of Geophysical Research: Solid Earth*, 97(B3):3337–3350.

Müller, R. D., Sdrolias, M., Gaina, C., and Roest, W. R. (2008). Age, spreading rates, and spreading asymmetry of the world's ocean crust. *Geochemistry, Geophysics, Geosystems*, 9(4).

Montelli, R., Nolet, G., Dahlen, F. A., Masters, G., Engdahl, E. R., and Hung, S.-H. (2004). Finite-Frequency Tomography Reveals a Variety of Plumes in the Mantle. *Science*, 303(5656):338.

Moore, L. R., Gazel, E., Tuohy, R., Lloyd, A. S., Esposito, R., Steele-MacInnis, M., Hauri, E. H., Wallace, P. J., Plank, T., and Bodnar, R. J. (2015). Bubbles matter: An assessment of the contribution of vapor bubbles to melt inclusion volatile budgets. *American Mineralogist*, 100(4):806–823.

Morgan, W. J. (1971). Convection plumes in the lower mantle. *Nature*, 230(5288):42–43.

Morgan, W. J. (1983). Hotspot tracks and the early rifting of the Atlantic. *Tectonophysics*, 94:123–139.

Moussallam, Y., Longpré, M.-A., McCammon, C., Gomez-Ulla, A., Rose-Koga, E. F., Scaillet, B., Peters, N., Gennaro, E., Paris, R., and Oppenheimer, C. (2019). Mantle plumes are oxidised. *Earth and Planetary Science Letters*, 527:115798.

Moussallam, Y., Morizet, Y., and Gaillard, F. (2016). H_2O–CO_2 solubility in low SiO_2-melts and the unique mode of kimberlite degassing and emplacement. *Earth and Planetary Science Letters*, 447:151–160.

Moussallam, Y., Oppenheimer, C., Scaillet, B., Gaillard, F., Kyle, P., Peters, N., Hartley, M., Berlo, K., and Donovan, A. (2014). Tracking the changing oxidation state of Erebus magmas, from mantle to surface, driven by magma ascent and degassing. *Earth and Planetary Science Letters*, 393:200–209.

Métrich, N. and Rutherford, M. J. (1998). Low pressure crystallization paths of H_2O-saturated basaltic-Hawaiitic melts from Mt Etna: Implications for open-system degassing of basaltic volcanoes. *Geochimica et Cosmochimica Acta*, 62(7):1195–1205.

Métrich, N. and Wallace, P. J. (2008). Volatile abundances in basaltic magmas and their degassing paths tracked by melt inclusions. *Reviews in Mineralogy and Geochemistry*, 69:363–402.

Métrich, N., Zanon, V., Créon, L., Hildenbrand, A., Moreira, M., and Marques, F. O. (2014). Is the 'Azores hotspot'a wetspot? Insights from the geochemistry of fluid and melt inclusions in olivine of Pico basalts. *Journal of Petrology*, 55(2):377–393.

Mungall, J. E., Hanley, J. J., Arndt, N. T., and Debecdelievre, A. (2006). Evidence from meimechites and other low-degree mantle melts for redox controls on mantle-crust fractionation of platinum-group elements. *Proceedings of the National Academy of Sciences*, 103(34):12695–12700.

Mysen, B. (2005). Melt and Glass Structure: Basic Concepts. In Mysen, B. and Richet, P., editors, *Silicate Glasses and Melts*, volume 10 of *Developments in Geochemistry*, pages 101 – 129. Elsevier.

Nash, W. M., Smythe, D. J., and Wood, B. J. (2019). Compositional and temperature effects on sulfur speciation and solubility in silicate melts. *Earth and Planetary Science Letters*, 507:187–198.

Neave, D. A. and Putirka, K. D. (2017). A new clinopyroxene-liquid barometer, and implications for magma storage pressures under Icelandic rift zones. *American Mineralogist*, 102(4):777–794.

Neumann, E.-R., Wulff-Pedersen, E., Simonsen, S., Pearson, N., Martí, J., and Mitjavila, J. (1999). Evidence for fractional crystallization of periodically refilled magma chambers in Tenerife, Canary Islands. *Journal of Petrology*, 40(7):1089–1123.

Nikolaev, G. S., Ariskin, A. A., Barmina, G. S., Nazarov, M. A., and Almeev, R. R. (2016). Test of the Ballhaus–Berry–Green Ol–Opx–Sp oxybarometer and calibration of a new equation for estimating the redox state of melts saturated with olivine and spinel. *Geochemistry International*, 54(4):301–320.

Niu, Y. (2004). Bulk-rock major and trace element compositions of abyssal peridotites: implications for mantle melting, melt extraction and post-melting processes beneath mid-ocean ridges. *Journal of Petrology*, 45(12):2423–2458.

O'Neill, H. S. C., Berry, A. J., and Mallmann, G. (2018). The oxidation state of iron in Mid-Ocean Ridge Basaltic (MORB) glasses: Implications for their petrogenesis and oxygen fugacities. *Earth and Planetary Science Letters*, 504:152–162.

O'Neill, H. S. C. and Wall, V. J. (1987). The Olivine—Orthopyroxene—Spinel Oxygen Geobarometer, the Nickel Precipitation Curve, and the Oxygen Fugacity of the Earth's Upper Mantle. *Journal of Petrology*, 28(6):1169–1191.

O'Nions, R., Evensen, N., and Hamilton, P. (1979). Geochemical modeling of mantle differentiation and crustal growth. *Journal of Geophysical Research: Solid Earth*, 84(B11):6091–6101.

Ono, S., Keller, N. S., Rouxel, O., and Alt, J. C. (2012). Sulfur-33 constraints on the origin of secondary pyrite in altered oceanic basement. *Geochimica et Cosmochimica Acta*, 87:323–340.

Oppenheimer, C., Moretti, R., Kyle, P. R., Eschenbacher, A., Lowenstern, J. B., Hervig, R. L., and Dunbar, N. W. (2011). Mantle to surface degassing of alkalic magmas at Erebus volcano, Antarctica. *Earth and Planetary Science Letters*, 306(3):261–271.

Ozawa, A., Tagami, T., and Garcia, M. O. (2005). Unspiked K–Ar dating of the Honolulu rejuvenated and Ko ‘olau shield volcanism on O ‘ahu, Hawai ‘i. *Earth and Planetary Science Letters*, 232(1-2):1–11.

Ozawa, K. (1984). Olivine-spinel geospeedometry: Analysis of diffusion-controlled Mg-Fe^{2+} exchange. *Geochimica et Cosmochimica Acta*, 48(12):2597–2611.

Palme, H. and O'Neill, H. S. C. (2003). Cosmochemical estimates of mantle composition. *Treatise on Geochemistry*, 2:1–38.

Paris, R., Guillou, H., Carracedo, J. C., and Torrado, F. P. (2005). Volcanic and morphological evolution of La Gomera (Canary Islands), based on new K-Ar ages and magnetic stratigraphy: implications for oceanic island evolution. *Journal of the Geological Society*, 162(3):501–512.

Passmore, E., Maclennan, J., Fitton, G., and Thordarson, T. (2012). Mush Disaggregation in Basaltic Magma Chambers: Evidence from the ad 1783 Laki Eruption. *Journal of Petrology*, 53(12):2593–2623.

Pertermann, M. and Hirschmann, M. M. (2003). Anhydrous Partial Melting Experiments on MORB-like Eclogite: Phase Relations, Phase Compositions and Mineral–Melt Partitioning of Major Elements at 2-3GPa. *Journal of Petrology*, 44(12):2173–2201.

Pilet, S., Baker, M. B., and Stolper, E. M. (2008). Metasomatized Lithosphere and the Origin of Alkaline Lavas. *Science*, 320(5878):916.

Plank, T. and Manning, C. E. (2019). Subducting carbon. *Nature*, 574(7778):343–352.

Portnyagin, M., Almeev, R., Matveev, S., and Holtz, F. (2008). Experimental evidence for rapid water exchange between melt inclusions in olivine and host magma. *Earth and Planetary Science Letters*, 272(3-4):541–552.

Prægel, N.-O. and Holm, P. M. (2006). Lithospheric contributions to high-MgO basanites from the Cumbre Vieja Volcano, La Palma, Canary Islands and evidence for temporal variation in plume influence. *Journal of volcanology and geothermal research*, 149(3-4):213–239.

Pérez, N. M., Padilla, G. D., Padrón, E., Hernández, P. A., Melián, G. V., Barrancos, J., Dionis, S., Nolasco, D., Rodríguez, F., Calvo, D., and Hernández, I. (2012). Precursory diffuse CO_2 and H_2S emission signatures of the 2011–2012 El Hierro submarine eruption, Canary Islands. *Geophysical Research Letters*, 39(16):L16311.

Putirka, K. (2008a). Excess temperatures at ocean islands: Implications for mantle layering and convection. *Geology*, 36(4):283–286.

Putirka, K. D. (2005). Mantle potential temperatures at Hawaii, Iceland, and the mid-ocean ridge system, as inferred from olivine phenocrysts: Evidence for thermally driven mantle plumes. *Geochemistry, Geophysics, Geosystems*, 6(5).

Putirka, K. D. (2008b). Thermometers and Barometers for Volcanic Systems. *Reviews in Mineralogy and Geochemistry*, 69(1):61–120.

Revenaugh, J. and Sipkin, S. A. (1994). Seismic evidence for silicate melt atop the 410-km mantle discontinuity. *Nature*, 369(6480):474–476.

Rielli, A., Tomkins, A. G., Nebel, O., Brugger, J., Etschmann, B., Zhong, R., Yaxley, G. M., and Paterson, D. (2017). Evidence of sub-arc mantle oxidation by sulphur and carbon. *Geochemical Perspectives Letters*, 3(2):124–132.

Rose-Koga, E., Koga, K., Moreira, M., Vlastelic, I., Jackson, M., Whitehouse, M. J., Shimizu, N., and Habib, N. (2017). Geochemical systematics of Pb isotopes, fluorine, and sulfur in melt inclusions from São Miguel, Azores. *Chemical Geology*, 458:22–37.

Rosenthal, A., Hauri, E. H., and Hirschmann, M. M. (2015). Experimental determination of C, F, and H partitioning between mantle minerals and carbonated basalt, CO_2/Ba and CO_2/Nb systematics of partial melting, and the CO_2 contents of basaltic source regions. *Earth and Planetary Science Letters*, 412:77–87.

Rosner, M., Wiedenbeck, M., and Ludwig, T. (2008). Composition-Induced Variations in SIMS Instrumental Mass Fractionation during Boron Isotope Ratio Measurements of Silicate Glasses. *Geostandards and Geoanalytical Research*, 32(1):27–38.

Saal, A. E., Hauri, E. H., Langmuir, C. H., and Perfit, M. R. (2002). Vapour undersaturation in primitive mid-ocean-ridge basalt and the volatile content of Earth's upper mantle. *Nature*, 419(6906):451–455.

Sakai, H., Casadevall, T. J., and Moore, J. G. (1982). Chemistry and isotope ratios of sulfur in basalts and volcanic gases at Kilauea Volcano, Hawaii. *Geochimica et Cosmochimica Acta*, 46(5):729–738.

Salters, V. J. M. and Stracke, A. (2004). Composition of the depleted mantle. *Geochemistry, Geophysics, Geosystems*, 5(5).

Sasaki, A., Arikawa, Y., and Folinsbee, R. (1979). Kiba reagent method of sulfur extraction applied to isotopic work. *Chishitsu Chosajo Geppo*, 30(4):241–245.

Schauble, E. A. (2004). Applying stable isotope fractionation theory to new systems. *Reviews in Mineralogy and Geochemistry*, 55(1):65–111.

Schmincke, H.-U. (1982). Volcanic and chemical evolution of the canary islands. In von Rad, U., Hinz, K., Sarnthein, M., and Seibold, E., editors, *Geology of the Northwest African Continental Margin*, pages 273–306. Springer Berlin Heidelberg.

Schmincke, H.-U. (2004). *Volcanism*, volume 28. Springer Science & Business Media.

Schmincke, H.-U. and von Rad, U. (1979). Neogene evolution of Canary Island volcanism inferred from ash layers and volcaniclastic sandstones of DSDP Site 397 (Leg 47A). *Initial Reports of the Deep Sea Drilling Project*, 47:703–725.

Schuessler, J. A., Botcharnikov, R. E., Behrens, H., Misiti, V., and Freda, C. (2008). Amorphous Materials: Properties, structure, and durability: Oxidation state of iron in hydrous phono-tephritic melts. *American Mineralogist*, 93(10):1493–1504.

Seo, J. H., Guillong, M., and Heinrich, C. A. (2009). The role of sulfur in the formation of magmatic–hydrothermal copper–gold deposits. *Earth and Planetary Science Letters*, 282(1):323 – 328.

Shimizu, K., Saal, A. E., Myers, C. E., Nagle, A. N., Hauri, E. H., Forsyth, D. W., Kamenetsky, V. S., and Niu, Y. (2016). Two-component mantle melting-mixing model for the generation of mid-ocean ridge basalts: implications for the volatile content of the Pacific upper mantle. *Geochimica et Cosmochimica Acta*, 176:44–80.

Shimizu, K., Ushikubo, T., Murai, T., Matsu'ura, F., and Ueno, Y. (2019). In situ analyses of hydrogen and sulfur isotope ratios in basaltic glass using sims. *Geochemical Journal*, 53(3):195–207.

Shishkina, T. A., Botcharnikov, R. E., Holtz, F., Almeev, R. R., and Portnyagin, M. V.

(2010). Solubility of H_2O- and CO_2-bearing fluids in tholeiitic basalts at pressures up to 500MPa. *Chemical Geology*, 277(1):115–125.

Shorttle, O., Maclennan, J., and Lambart, S. (2014). Quantifying lithological variability in the mantle. *Earth and Planetary Science Letters*, 395:24–40.

Sides, I., Edmonds, M., Maclennan, J., Houghton, B. F., Swanson, D., and Steele-MacInnis, M. J. (2014). Magma mixing and high fountaining during the 1959 Kīlauea Iki eruption, Hawai 'i. *Earth and Planetary Science Letters*, 400:102–112.

Sigmarsson, O., Carn, S., and Carracedo, J. C. (1998). Systematics of U-series nuclides in primitive lavas from the 1730–36 eruption on Lanzarote, Canary Islands, and implications for the role of garnet pyroxenites during oceanic basalt formations. *Earth and Planetary Science Letters*, 162(1-4):137–151.

Sigmarsson, O., Laporte, D., Carpentier, M., Devouard, B., Devidal, J.-L., and Marti, J. (2013). Formation of U-depleted rhyolite from a basanite at El Hierro, Canary Islands. *Contributions to Mineralogy and Petrology*, 165(3):601–622.

Simon, A. C. and Ripley, E. M. (2011). The Role of Magmatic Sulfur in the Formation of Ore Deposits. *Reviews in Mineralogy and Geochemistry*, 73(1):513–578.

Simonsen, S., Neumann, E.-R., and Seim, K. (2000). Sr-Nd-Pb isotope and trace-element geochemistry evidence for a young HIMU source and assimilation at Tenerife (Canary Island). *Journal of Volcanology and Geothermal Research*, 103(1-4):299–312.

Sleep, N. H. (1990). Hotspots and mantle plumes: Some phenomenology. *Journal of Geophysical Research: Solid Earth*, 95(B5):6715–6736.

Śliwiński, M. G., Kitajima, K., Spicuzza, M. J., Orland, I. J., Ishida, A., Fournelle, J. H., and Valley, J. W. (2018). SIMS Bias on Isotope Ratios in Ca-Mg-Fe Carbonates

(Part III): δ^{18}O and δ^{13}C Matrix Effects Along the Magnesite–Siderite Solid-Solution Series. *Geostandards and Geoanalytical Research*, 42(1):49–76.

Sobolev, A. and Nikogosian, I. (1994). Petrology of long-lived mantle plume magmatism: Hawaii, Pacific and Reunion Island, Indian Ocean. *Petrology*, 2(2):111–144.

Sobolev, A. V., Hofmann, A. W., Sobolev, S. V., and Nikogosian, I. K. (2005). An olivine-free mantle source of Hawaiian shield basalts. *Nature*, 434(7033):590–597.

Spandler, C. and O'Neill, H. S. C. (2010). Diffusion and partition coefficients of minor and trace elements in San Carlos olivine at 1,300°C with some geochemical implications. *Contributions to Mineralogy and Petrology*, 159(6):791–818.

Spice, H. E., Fitton, J. G., and Kirstein, L. A. (2016). Temperature fluctuation of the Iceland mantle plume through time. *Geochemistry, Geophysics, Geosystems*, 17(2):243–254.

Staudigel, H. and Schmincke, H.-U. (1984). The pliocene seamount series of la palma/canary islands. *Journal of Geophysical Research: Solid Earth*, 89(B13):11195–11215.

Steele-Macinnis, M., Esposito, R., and Bodnar, R. J. (2011). Thermodynamic model for the effect of post-entrapment crystallization on the H_2O–CO_2 systematics of vapor-saturated, silicate melt inclusions. *Journal of Petrology*, 52(12):2461–2482.

Steele-MacInnis, M., Esposito, R., Moore, L. R., and Hartley, M. E. (2017). Heterogeneously entrapped, vapor-rich melt inclusions record pre-eruptive magmatic volatile contents. *Contributions to Mineralogy and Petrology*, 172(4):18.

Steinberger, B. and Becker, T. W. (2018). A comparison of lithospheric thickness models. *Tectonophysics*, 746:325–338.

Stillman, C. (1999). Giant Miocene landslides and the evolution of Fuerteventura, Canary Islands. *Journal of Volcanology and Geothermal Research*, 94(1-4):89–104.

Stracke, A., Hofmann, A. W., and Hart, S. R. (2005). FOZO, HIMU, and the rest of the mantle zoo. *Geochemistry, Geophysics, Geosystems*, 6(5).

Stroncik, N. A., Klügel, A., and Hansteen, T. H. (2009). The magmatic plumbing system beneath El Hierro (Canary Islands): constraints from phenocrysts and naturally quenched basaltic glasses in submarine rocks. *Contributions to Mineralogy and Petrology*, 157(5):593–607.

Takamasa, A., Nakai, S., Sahoo, Y., Hanyu, T., and Tatsumi, Y. (2009). W isotope compositions of oceanic islands basalts from French Polynesia and their meaning for core–mantle interaction. *Chemical Geology*, 260(1):37–46.

Taracsák, Z., Hartley, M. E., Burgess, R., Edmonds, M., Iddon, F., and Longpré, M. A. (2019). High fluxes of deep volatiles from ocean island volcanoes: Insights from El Hierro, Canary Islands. *Geochimica et Cosmochimica Acta*, 258:19–36.

Taylor, B. E. (1986). Magmatic volatiles; isotopic variation of C, H, and S. *Reviews in Mineralogy and Geochemistry*, 16(1):185–225.

Taylor, J. R., Wall, V. J., and Pownceby, M. I. (1992). The calibration and application of accurate redox sensors. *American Mineralogist*, 77(3-4):284–295.

Thirlwall, M., Jenkins, C., Vroon, P., and Mattey, D. (1997). Crustal interaction during construction of ocean islands: Pb-Sr-Nd-O isotope geochemistry of the shield basalts of Gran Canaria, Canary Islands. *Chemical Geology*, 135(3):233 – 262.

Thomas, L., Hawkesworth, C., Van Calsteren, P., Turner, S., and Rogers, N. (1999). Melt generation beneath ocean islands: A U-Th-Ra isotope study from Lanzarote in the Canary Islands. *Geochimica et Cosmochimica Acta*, 63(23-24):4081–4099.

Thompson, D., Hammond, J. O., Kendall, J.-M., Stuart, G., Helffrich, G., Keir, D., Ayele, A., and Goitom, B. (2015). Hydrous upwelling across the mantle transition zone beneath the Afar Triple Junction. *Geochemistry, Geophysics, Geosystems*, 16(3):834–846.

Tomkins, A. G. and Evans, K. A. (2015). Separate zones of sulfate and sulfide release from subducted mafic oceanic crust. *Earth and Planetary Science Letters*, 428:73–83.

Torssander, P. (1989). Sulfur isotope ratios of Icelandic rocks. *Contributions to Mineralogy and Petrology*, 102(1):18–23.

Troll, V. R., Klügel, A., Longpré, M., Burchardt, S., Deegan, F., Carracedo, J., Wiesmaier, S., Kueppers, U., Dahrén, B., and Blythe, L. (2012). Floating stones off El Hierro, Canary Islands: xenoliths of pre-island sedimentary origin in the early products of the October 2011 eruption. *Solid Earth*, 3(1):97–110.

Tucker, J. M., Hauri, E. H., Pietruszka, A. J., Garcia, M. O., Marske, J. P., and Trusdell, F. A. (2019). A high carbon content of the Hawaiian mantle from olivine-hosted melt inclusions. *Geochimica et Cosmochimica Acta*, 254:156–172.

Turner, S., Hoernle, K., Hauff, F., Johansen, T. S., Klügel, A., Kokfelt, T., and Lundstrom, C. (2015). ^{238}U – ^{230}Th – ^{226}Ra Disequilibria Constraints on the Magmatic Evolution of the Cumbre Vieja Volcanics on La Palma, Canary Islands. *Journal of Petrology*, 56(10):1999–2024.

Van Den Bogaard, P. (2013). The origin of the canary island seamount province-new ages of old seamounts. *Scientific Reports*, 3:2107.

Venugopal, S., Schiavi, F., Moune, S., Bolfan-Casanova, N., Druitt, T., and Williams-Jones, G. (2020). Melt inclusion vapour bubbles: the hidden reservoir for major and volatile elements. *Scientific Reports*, 10(1):1–14.

Vielzeuf, D., Champenois, M., Valley, J. W., Brunet, F., and Devidal, J. (2005). SIMS analyses of oxygen isotopes: matrix effects in Fe–Mg–Ca garnets. *Chemical Geology*, 223(4):208–226.

Vigouroux, N., Williams-Jones, A. E., Wallace, P., and Staudacher, T. (2009). The November 2002 eruption of Piton de la Fournaise, Réunion: tracking the pre-eruptive thermal evolution of magma using melt inclusions. *Bulletin of volcanology*, 71(9):1077.

Wallace, P. J., Kamenetsky, V. S., and Cervantes, P. (2015). Melt inclusion CO_2 contents, pressures of olivine crystallization, and the problem of shrinkage bubbles. *American Mineralogist*, 100(4):787–794.

Walowski, K. J., Kirstein, L. A., De Hoog, J. C. M., Elliott, T. R., Savov, I. P., and Jones, R. E. (2019). Investigating ocean island mantle source heterogeneity with boron isotopes in melt inclusions. *Earth and Planetary Science Letters*, 508:97–108.

Walter, M. J. (1998). Melting of Garnet Peridotite and the Origin of Komatiite and Depleted Lithosphere. *Journal of Petrology*, 39(1):29–60.

Walter, T. R., Troll, V. R., Cailleau, B., Belousov, A., Schmincke, H.-U., Amelung, F., and Vd Bogaard, P. (2005). Rift zone reorganization through flank instability in ocean island volcanoes: an example from Tenerife, Canary Islands. *Bulletin of Volcanology*, 67(4):281–291.

Walters, J., Cruz-Uribe, A., and Marschall, H. (2020). Sulfur loss from subducted altered oceanic crust and implications for mantle oxidation. *Geochemical Perspectives Letters*, 13:36–41.

Wan, Z., Coogan, L. A., and Canil, D. (2008). Experimental calibration of aluminum partitioning between olivine and spinel as a geothermometer. *American Mineralogist*, 93(7):1142–1147.

Wang, X., Chou, I. M., Hu, W., Burruss, R. C., Sun, Q., and Song, Y. (2011). Raman spectroscopic measurements of CO_2 density: Experimental calibration with high-pressure optical cell (HPOC) and fused silica capillary capsule (FSCC) with application to fluid inclusion observations. *Geochimica et Cosmochimica Acta*, 75(14):4080–4093.

Watkins, J. S. and Hoppe, K. (1979). Seismic reflection reconnaissance of the Atlantic margin of Morocco. *Deep Drilling Results in the Atlantic Ocean: Continental Margins and Paleoenvironment*, pages 205–217.

Watts, A. B., Peirce, C., Collier, J., Dalwood, R., Canales, J. P., and Henstock, T. J. (1997). A seismic study of lithospheric flexure in the vicinity of Tenerife, Canary Islands. *Earth and Planetary Science Letters*, 146(3):431–447.

Weis, F. A., Skogby, H., Troll, V. R., Deegan, F. M., and Dahren, B. (2015). Magmatic water contents determined through clinopyroxene: Examples from the Western Canary Islands, Spain. *Geochemistry, Geophysics, Geosystems*, 16(7):2127–2146.

Wieser, P. E., Jenner, F., Edmonds, M., Maclennan, J., and Kunz, B. E. (2020). Chalcophile elements track the fate of sulfur at Kīlauea Volcano, Hawai'i. *Geochimica et Cosmochimica Acta*, 282:245–275.

Wilke, M., Klimm, K., and Kohn, S. C. (2011). Spectroscopic Studies on Sulfur Speciation in Synthetic and Natural Glasses. *Reviews in Mineralogy and Geochemistry*, 73(1):41–78.

Williams, H. M., Peslier, A. H., McCammon, C., Halliday, A. N., Levasseur, S., Teutsch, N., and Burg, J. P. (2005). Systematic iron isotope variations in mantle rocks and minerals: The effects of partial melting and oxygen fugacity. *Earth and Planetary Science Letters*, 235(1):435–452.

Wilson, J. T. (1973). Mantle plumes and plate motions. *Tectonophysics*, 19(2):149–164.

Witham, F., Blundy, J., Kohn, S. C., Lesne, P., Dixon, J., Churakov, S. V., and Botcharnikov, R. (2012). SolEx: A model for mixed COHSCl-volatile solubilities and exsolved gas compositions in basalt. *Computers & Geosciences*, 45:87–97.

Wolfe, C. J., Solomon, S. C., Laske, G., Collins, J. A., Detrick, R. S., Orcutt, J. A., Bercovici, D., and Hauri, E. H. (2009). Mantle Shear-Wave Velocity Structure Beneath the Hawaiian Hot Spot. *Science*, 326(5958):1388.

Yang, J. and Faccenda, M. (2020). Intraplate volcanism originating from upwelling hydrous mantle transition zone. *Nature*, 579(7797):88–91.

Zaczek, K., Troll, V. R., Cachao, M., Ferreira, J., Deegan, F. M., Carracedo, J. C., Soler, V., Meade, F. C., and Burchardt, S. (2015). Nannofossils in 2011 El Hierro eruptive products reinstate plume model for Canary Islands. *Scientific Reports*, 5(1):7945.

Zhang, H. L., Cottrell, E., Solheid, P. A., Kelley, K. A., and Hirschmann, M. M. (2018). Determination of $Fe^{3+}/\sum Fe$ of XANES basaltic glass standards by Mössbauer spectroscopy and its application to the oxidation state of iron in MORB. *Chemical Geology*, 479:166–175.

Zimmer, M. M., Plank, T., Hauri, E. H., Yogodzinski, G. M., Stelling, P., Larsen, J., Singer, B., Jicha, B., Mandeville, C., and Nye, C. J. (2010). The role of water in generating the calc-alkaline trend: new volatile data for Aleutian magmas and a new tholeiitic index. *Journal of Petrology*, 51(12):2411–2444.

Zindler, A. and Hart, S. (1986). Chemical Geodynamics. *Annual Review of Earth and Planetary Sciences*, 14(1):493–571.

Zou, H. (1998). Trace element fractionation during modal and nonmodal dynamic melting and open-system melting: a mathematical treatment. *Geochimica et Cosmochimica Acta*, 62(11):1937–1945.

Appendix A

Supplementary material for research chapters

All supplementary files for thesis are provided in Mendeley Data titled "PhD Thesis Supplementary Material". Files for reviewers can be found under the following link:

dropbox link to supplementary

The datasets are under a 6 month embargo, until 19th December 2020. After that, the data can be accessed under the following DOI (newest version is version 2, which is embargoed until 8th March 2021):

10.17632/8y6s2ph9by.2

Supplementary file list (with description):

Supplementary text chapter4.docx:

Supplementary text for chapter four, including details of LLD calculation (carried out in Petrolog3, Fig. 4.4) and the effect of H_2O content on LLDs, melting modelling (Fig 4.8), and halogen data comparison (SIMS vs. EPMA).

Melt inclusion images annotated.pdf:

Annotated images of El Hierro melt inclusions used in the thesis, mostly taken using reflected light.

Supplementary text S-isotope-stds.docx:

Description of drift correction during SIMS sulfur isotope analyses, discussions on the Al-Na-K composition of glass standards used in chapter five, and demonstration of how reproducible the Al-Na-K IMF correction method is between different sessions.

supplementary SEM images S-isotope-stds.docx

Backscattered electron images of glasses used in chapter five as potential glass standards during sulfur isotope analyses by SIMS.

Supplementary spreadsheet S isotope std glasses.xlsx

Spreadsheets containing data presented in chapter five. Driftcorrection sheet contains drift correction calculations. S isotope data sheet contains sulfur isotope ratios measured in the 14 analytical sessions. Sulfur ppm April2019 contains $^{32}S/O_2$ ratios data, and glass S contents derived from those for the six synthetic glasses used in chapter five as standards. Glass starting comp sheet presents the starting composition of the samples before doping with sulfur (as anhydrite).

Supplementary spreadsheets melting models.xlsx

Two spreadsheets containing input parameters for melting models used to produce graphs in Fig 4.8 (melting model chapter 4) and 6.4 (melting model chapter six).

Supplementary spreadsheets MELTS T P fO2.xlsx

Seven spreadsheets containing various data used in chapter seven of the thesis. Contains input data for rhyolite-MELTS modelling, results of clinopyroxene-melt thermobarometry (Cpx-melt), olivine melt thermometry (ol-melt), spinel-olivine thermometry and oxybarometry (sp-ol), results of diffusion modelling (Fig. 7.10), PRIMELT3 (Herzberg and Asimow, 2015) potential temperature calculations (Fig. 7.11) and potential temperature and melting pressure estimates calculated using the method of (Lee et al., 2009).

Supplementary spreadsheets MI glass WHR.xlsx

Spreadsheets containing PEC uncorrected and PEC corrected data for melt inclusions. "MI data Taracsak et al 2019" are PEC corrected MI compositions used in chapter four, while "MI data PEC corr" sheet is data used in chapter 6 (PEC correction carried out using different oxygen fugacity hence there are minor differences between the two). Whole rock and sulfur speciation data are also provided here. DCompress modelling used in chapter six to estimate fractionation factors are also given in a sheet. Reconstructed CO_2 contents presented in chapter four (bubble measurement by Raman, glass by SIMS) are given in sheet CO2 glass+bubble.

Supplementary spreadsheets mineral chemisrty.xlsx

Mineral chemistry data presented in chapter seven (Figs. 7.3, 7.4 and 7.5). Secondary standard data measured during sessions and plotted in fig 3.1 (for olivines) are also provided.